RESIDUAL AND INTERNAL STRESS DEVELOPMENT RESULTING FROM PLASTIC DEFORMATION OF MULTI-PHASE ALLOYS

THE CASE OF PEARLITE

Jeroen TACQ

Members of the
Examination Committee

Prof. Dr. P. Wollants, chairman
Prof. Dr. M. Seefeldt, supervisor
Prof. Dr. B. Verlinden, supervisor
Dr. S. Van Petegem
Prof. Dr. Gil Sevillano
Prof. Dr. P. Jacques
Prof. Dr. P. Van Houtte
Prof. Dr. K. Vanmeensel
Prof. Dr. M. Seo

Dissertation presented in
partial fulfilment of the
requirements for the
degree of Doctor in
Materials Engineering

November 2015

Uitgegeven in eigen beheer, Jeroen TACQ, Geluveld

Acknowledgments

Een lange tijd op het departement Materiaalkunde (MTM) komt nu voor mij ten einde. Het is een mooie periode geweest, met – zoals dat altijd gaat – ook een paar minder makkelijke momenten. Doorheen dit alles hebben veel mensen mij bijgestaan, geholpen en ondersteund. In de eerste plaats wil ik mijn promotor Marc Seefeldt bedanken. Ik was altijd welkom op je bureau en we hebben er vele uren gepraat. Mijn werk heeft er vorm gekregen, maar er was ook tijd om over luchtigere dingen te praten. Bedankt om mijn verblijf aan MTM mede zo aangenaam te maken. Ik wil ook mijn co-promotor Bert Verlinden bedanken. Jouw input en positief kritische blik hebben mee geholpen om mijn werk extra diepgang te geven en het grotere geheel nooit uit het oog te verliezen. I would also like to thank the other members of my jury for taking the time to read my somewhat long manuscript and for their valuable input in improving the text.

Het Fonds Wetenschappelijk Onderzoek Vlaanderen (FWO) wil ik bedanken voor zijn financiële steun. De federale overheidsdienst wetenschapsbeleid Belspo onder IAP project 7/21 bedank ik voor het voorzien van een taalgrensoverschrijdend kader om aan onderzoek te doen. Het Europese NMI3-II programma bedankt ik voor de financiële steun die het mogelijk maakte onderzoek te doen aan verschillende neutronen en synchrotron diffractie instituten binnen Europa.

I did not perform the neutron and synchrotron diffraction experiments on my own. Many thanks go to the people who helped me: Steven Van Petegem and Tobias Panzner (PSI, Villigen), Manuela Klaus and Christoph Genzel (HZB, Berlin), Jan Pilch (NPI, Řež) and Michael Hofmann (MLZ). Special thanks also go to Martin Kriška for giving me the chance to participate in the experiments for his doctoral work and for providing me with the opportunity to build on his results. I would also like to thank Roumen Petrov and Leo Kestens for allowing me to cold roll my steel sheets at the UGent and Marnix for the practical implementation.

Zonder de deskundige hulp van het technisch en administratief personeel op MTM zou mijn doctoraat ook niet mogelijk geweest zijn. In het bijzonder wil ik Paul Crabbe, Louis Depre, Louis Kockaerts, Olivier Van Roey en Tom Van der Donck bedanken voor alles wat ze mij hebben geleerd en de tijd die ze in mijn experimenten hebben gestoken.

At MTM I had the great privilege to spend my days in office 91.49. I want to thank all the office buddies that came and went. You all made my stay at MTM into a good time. I will never forget the great time we had during our office drinks! The same is true for my great colleagues in the ASTRO-group. I hope to see many of you at the next ASTRO-café! And off course all the other friends I made at the department, thank you for making my stay at MTM an enjoyable time.

Uiteindelijk wil ik ook graag en vanuit de grond van mijn hart mijn ouders bedanken. Jullie hebben al van kindsbeen af een omgeving gecreëerd die studeren stimuleerde en mij altijd alle mogelijkheden gegeven om mij te ontwikkelen. Maar nog meer dan dat, hebben jullie altijd onvoorwaardelijk in mijn kunnen geloofd, zelfs als ik dat zelf niet altijd deed. Zonder jullie had ik nooit gestaan waar ik vandaag sta! Ik wil ook mijn broer bedanken voor de schitterende tijd die we samen in Leuven gedeeld hebben. Samen met jou heb ik één van de mooiste periodes van mijn leven mogen beleven. En daar ben ik dankbaar voor! En als laatste, maar eigenlijk als eerste, wil ik mijn vrouw bedanken. Je bent er altijd voor mij geweest. En zeker in het laatste jaar heb je mij door moeilijke momenten geholpen. Ik weet dat het ook voor jou niet altijd even makkelijk is geweest.

Bedankt aan iedereen, en veel leesgenot voor zij die verder raken dan deze pagina.

‘In times of change, learners inherit the earth; while the learned find themselves beautifully equipped to deal with a world that no longer exists.’

(Eric Hoffer, 1902-1983)

Abstract

Multiphase materials can have very interesting properties such as an exceptionally high strength combined with a good ductility. However, it is inevitable that during their production, especially when large plastic deformations are involved, residual stresses and strains will develop. These residual strains will in turn have an influence on the properties of the material. To be able to optimize the design of multiphase materials the residual stress and strain development needs to be understood.

In an effort to contribute to this understanding, the current work presents a fundamental study of, mainly, the micro-phase residual strain development. As a case study, pearlitic steel will be investigated. While it appears that everything should be known about steel by now, our knowledge is far from complete, especially when the cementite phase is considered. Basic properties such as its elastic constants remain the object of discussion and the question as to whether or not cementite undergoes strain hardening has not yet been answered.

The residual strain in both cold rolled and cold drawn pearlite was measured over a broad strain interval by means of various diffraction techniques. The microstructural evolution from both a morphological and crystallographic point of view was investigated by means of scanning electron microscopy and electron backscatter diffraction.

Pearlitic steel has a lamellar microstructure which can readily be idealized as a stack of flat ferrite and cementite plates. Based on this idealisation into a sandwich microstructure, a simple model was developed which could be used as a tool to analyse the experimental results. This approach allowed to come to an understanding of the residual strain development in terms of the in-situ deformation behaviour of the ferrite and cementite phases.

Three stages in the residual strain development were found. First there is a fast increase of the residual strain, which can be linked to the plastification of the cementite phase. Next there is a stage in which the residual strain saturates. This led to the conclusion that the cementite phase has to undergo some type of strain hardening. Finally, there is a stage in which the intergranular residual strain evolution becomes much more significant. This has been explained in terms of the development of a strong morphological and crystallographic texture.

Additionally, in-situ tensile tests under neutron diffraction have been performed on samples with different microstructures. These results, coupled with the observed significant reversal of strain broadening, led to the

conclusion that the real material does not deform according to an iso-strain model. Instead, the two phases can undergo different amounts of deformation. This realisation led to the postulation of significant strain gradients in the material, which can explain the observed reversal of strain broadening.

Finally, it was seen that the ferrite diffraction profiles become asymmetric at high rolling and drawing strains. To explain this, the idea of the development of a dislocation rich ferrite region at the lamellae interfaces is introduced. The existence of such an interface region also presents a convenient way to explain the cementite strain hardening behaviour in a non-classical way, i.e. not controlled by the storage and entanglement or pinning of cementite dislocation. Cementite strain hardening is rather considered to be the result of an increased difficulty to nucleate new dislocations.

Samenvatting

Meerfazige materialen kunnen interessante eigenschappen hebben, zoals een zeer hoge sterkte gecombineerd met een goeie ductiliteit. Het is echter onvermijdelijk dat er zich restspanningen en -rekken ontwikkelen tijdens de productie van dergelijke materialen, vooral wanneer er grote plastische vervormingen worden opgelegd aan het materiaal. Deze restspanningen en -rekken zullen op hun beurt een invloed hebben op de eigenschappen van het materiaal. Om het ontwerp van meerfazige materialen te kunnen optimaliseren moet de ontwikkeling van restspanningen en -rekken dus goed begrepen worden.

In een poging om hieraan bij te dragen, wordt in dit werk een fundamentele studie van voornamelijk de micro-fase restrekken gepresenteerd. Als een casestudie zal perlitisch staal worden onderzocht. Hoewel het kan lijken alsof alles nu wel geweten is over staal, is dit verre van de waarheid, zeker wanneer de cementiet fase in beschouwing wordt genomen. Zelfs de basis eigenschappen van cementiet, zoals de elastische constanten, zijn nog steeds niet eenduidig bepaald. Evenmin is er een antwoord op de vraag of cementiet vervormingsversteviging vertoont.

Met behulp van verschillende diffractie technieken werden de restrek in zowel koud gewalst als koud getrokken perliet gemeten over een breed vervormingsinterval. De microstructurele evolutie, zowel in termen van de morfologie als de kristallografie, werd onderzocht met raster elektronen microscopie en 'Electron backscatter diffraction'.

Perlitisch staal heeft een lamellaire microstructuur die kan worden geïdealiseerd als een stapel van vlakke ferriet en cementiet plaatjes. Deze vereenvoudiging tot een sandwich structuur liet toe een intuïtief model te ontwikkelen, dat gebruikt kon worden als gereedschap waarmee de experimentele resultaten werden geanalyseerd. Door deze aanpak liet toe de evolutie van de restrekken te begrijpen in termen van het in-situ vervormingsgedrag van de ferriet en cementiet fazen.

Er werden drie stadia onderscheidden in de restrek evolutie. In het eerste stadium is er een snelle toename van de restrek. Deze werd toegeschreven aan het plastisch worden van de cementiet fase. In het tweede stadium bereikt de restrek een saturatie niveau. Deze saturatie kon enkel verklaard worden indien een zekere vervormingsversteviging van de cementiet fase werd toegelaten. In het derde stadium wordt de ontwikkeling van restrekken ten gevolge van verschillen in kristallografische oriëntatie van de korrels veel prominenter. Dit kon verklaard worden door de ontwikkeling van een sterke kristallografische en morfologische textuur.

Monsters met verschillende microstructuren werden onderworpen aan een in-situ trektest onder neutronen diffractie. De bekomen resultaten, gekoppeld met een waargenomen reversibele vervormingsverbreding van de diffractie pieken, leidden tot de conclusie dat het werkelijke materiaal niet vervormt volgens een iso-vervormingsmodel. De twee fazen kunnen met andere woorden een verschillende vervorming ondergaan. Dit inzicht leidde tot het postuleren van de aanwezigheid van significante rekgradiënten doorheen het materiaal. Deze gradiënten kunnen op hun beurt de waargenomen reversibele vervormingsverbreding helpen verklaren.

Ten slotte werd vastgesteld dat de ferriet diffractie profielen asymmetrisch worden bij hoge wals- en draadtrekvervormingen. Om deze asymmetrie te verklaren werd de ontwikkeling van een dislocatierijke ferrietregio aan de interfasen geopperd. Het bestaan van een dergelijke interfaseregio maakt het ook mogelijk de vervormingsversteviging van cementiet te verklaren. Deze versteviging is niet het gevolg van de opslag en het vastlopen van dislocaties, zoals bij ‘klassieke’ materialen. De vervormingsversteviging van cementiet moet eerder beschouwd worden als het resultaat van de toegenomen moeilijkheid om nieuwe dislocaties te creëren in de cementiet lamellen.

List of symbols and abbreviations

α	ferrite phase
β	full width at half maximum
ε	strain, context dependent
ε_{ij}	ijth component of the strain tensor
ε_{eq}	Von Mises equivalent strain
ε^{hkl}	lattice strain for a particular set of crystallographic planes
ε_q	constant Voigt strain
ε_i^{tot}	the total strain in the ith phase
ε^L	loading strain
ε^{UL}	unloading strain
ε^{el}	elastic strain
ε^{pl}	plastic strain
$\Delta\varepsilon$	specific strain as defined in Fig. 7.1
ε^{relax}	relaxation strain as defined in Fig. 7.4
ε^{fit}	fitting strain as defined in Fig. 7.4
ε^{RS}	residual elastic strain
$\langle\varepsilon^{RS}\rangle$	average residual elastic strain
η	parameter describing the Lorentzian/Gaussian fraction in a Pseudo-Voigt profile
θ	cementite phase/diffraction angle
ν	Poisson's ratio
ρ	dislocation density
σ_y	yield stress
σ_{ij}	ijth component of the stress tensor
σ_{eq}	Von Mises equivalent stress
σ_{ij}^{t}	total stress
σ_{ij}^{M}	macroscopic stress
σ_{ij}^{μ}	microscopic stress
$\overline{\sigma_p}$	average stress in a grain family
σ_p^{i}	stress in all grains with a certain orientation
σ^L	loading stress
σ^{UL}	stress after unloading
σ^{RS}	residual stress
σ^{flow}	flow stress
σ^{app}	externally applied stress

$\Delta\sigma_{flow}$	difference in in-situ flow stress between ferrite and cementite at a certain externally applied strain
A_{hkl}	cubic anisotropy factor
Å	angstrom, 10^{-10}m
at%	atomic fraction, in percent
bcc	body centred cubic
C_{ij}	ijth element of the stiffness tensor
$\overline{C_{pq}^{V}}$	average stiffness tensor according to Voigt
C_{pq}^{i}	stiffness tensor for all grains with a certain orientation
D	diameter of wire
D_0	initial diameter of a drawn wire
D_1	diameter of a wire after drawing
DEC	diffraction elastic constant
d	lattice plane spacing
d_0	lattice plane spacing at zero strain
d_{hkl}	lattice plane spacing for a particular set of crystallographic planes
E_i	Young’s modulus of the ith phase
EBSD	electron backscatter diffraction
EPSC	elasto-plastic self-consistent
Fe_3C	cementite
FWHM	full width at half maximum
fcc	face centred cubic
g	a particular crystallographic orientation
HAB	high angle boundary
HC	high carbon
hkl	miller indices of a crystallographic plane
ILS	interlamellar spacing
IPF	inverse pole figure
IQ	image quality
k_1	constant in a Hall-Petch type relationship
keV	kilo electron volt
LAB	low angle boundary
LC	low carbon
MLZ	Heinz Maier-Leibnitz Zentrum
ND	normal direction
PSI	Paul Scherrer Institut

RD	rolling direction
RS	residual stress/strain
SEM	scanning electron microscopy
$\overline{S_{pq}^{hkl,R}}$	average compliant tensor according to Reuss
S_{pq}^{hkl}	stiffness tensor for all grains with a certain orientation
TD	transverse direction
TEM	transmission electron microscopy
TOF	time of flight
t	thickness of a rolled sheet
t_0	initial thickness of a rolled sheet
t_1	thickness of a sheet after rolling
V_α	volume fraction of the ferrite phase
V_θ	volume fraction of the cementite phase
V^i	volume fraction of grains with a certain orientation
vol%	volume fraction, in percent
W	energy spend on fitting phases together
wt%	weight fraction, in percent

Table of contents

1 General introduction

Many engineering materials consist of multiple phases. Often, it is the very presence of these multiple phases that gives the material superior properties as compared to the properties of the phases on their own. However, because of the different thermal and mechanical properties of each phase, internal and residual stress can develop in the material. Also changes in volume, associated with phase transformations can introduce residual stresses. These stresses will in turn have an impact on the properties of the material, such as the electrical conductivity, dimensional stability and mechanical strength. It is therefore essential to understand how and why internal and residual stresses develop in engineering materials, if we want to predict and improve their properties.

This field of study is obviously very wide and cannot possibly be covered in the scope of a single research project. In the current study, the development of internal and residual stresses as a result of deformation will be investigated. To focus the research further, it was opted to limit the experimental work to one specific material as a case-study. A couple of points which were considered in choosing the material of study were (i) the industrial relevance of the material, (ii) the scientific interest of the material, (iii) the ability to produce and/or process the material with the available equipment, (iv) the microstructure of the material and (v) the available knowledge and experimental data at the institute were the project is carried out. Finally, pearlitic steel was chosen as the material of study.

Pearlitic steel has a wide history of use as wire in rubber tire reinforcement, as filaments for the production of steel cords and as sawing wire for the production of wafers. It is its mechanical strength which makes it the material of choice for many applications. This mechanical strength in turn comes from the peculiar pearlitic microstructure consisting of alternating plates of relatively soft ferrite and hard, carbon rich cementite. The difference in mechanical properties between these two phases is responsible for the introduction of residual stresses. In order to increase the high strength of pearlite even further, the origin of these residual stresses must be understood in depth.

But also from a scientific point of view pearlitic steel is an immensely interesting material. A lot of fundamental questions regarding the origin of its mechanical properties remain unanswered, especially concerning the cementite phase. In 2013 around 1.65 billion tonnes of steel were produced world-wide [1], in which cementite is the most important secondary phase. Still, cementite’s most basic mechanical properties such as its elastic properties and mechanical strength have still not unambiguously been determined.

This study was started with as a purpose to investigate the mechanisms responsible for the development of internal and residual stresses as a result of deformation. However, throughout this work, it became clear that understanding the residual stress development is inextricably linked with understanding the in-situ mechanical properties and strain hardening behaviour of the individual phases. 'In-situ' meaning the way each phase behaves within the composite material. This can be very different from the ex-situ, bulk behaviour. In this text, a significant amount of attention will therefore also be paid to how pearlite deforms on a microscopic scale and how this may, qualitatively, translate into mechanical properties for the individual phases. Considering the lack of knowledge on cementite, special attention will be paid to this phase.

The residual stress and strain development over a large macroscopic strain interval have been studied by both cold drawing and cold rolling of pearlite. The residual lattice strains were determined using both X-ray and neutron diffraction techniques at various international institutes. The experimental results on cold drawing were part of M. Kriška's Ph.D. [2]. Additional experiments were performed on cold rolled pearlitic sheets in order to be able to compare wire and sheet. Because of the complex nature of the problem presented, a relatively simple, intuitive model was constructed with which the experimental data can be compared. It is this comparison which will prove to be instrumental in the development of a solid view on the origins of residual stress development, in terms of the in-situ mechanical properties of the constituting phases.

In Chapter 2 the terminology used in this work will first be explained, followed by a limited review of the literature on internal and residual stresses. Based on the conclusions drawn there, some open questions are identified and translated into the goals of this work (see section 2.7). In Chapter 3 pearlitic steel will be discussed in a bit more detail. Based on the available literature, a view on the deformation and strain hardening behaviour of pearlite is sketched. In Chapter 4 and 5 the performed experimental work is outlined. The material choice and the various applied experimental techniques are considered. The results of these experiments are presented in Chapter 6, along with a basic discussion of these results were this is possible without extensive cross-referencing to other results. The intuitive model used as a tool to analyse the experimental results is described in Chapter 7. Finally, in Chapter 8, all the insights gained from the experimental and modelling work are combined. A unified explanation for the observed residual stress development is presented. The authors view on pearlite's deformation behaviour, as based on the available evidence, is also described. The text finishes with an overview of the most important conclusions in Chapter 9 and some proposals for additional, future research in Chapter 10.

4

2 Internal and Residual stress and strain in multiphase alloys

This chapter will briefly introduce the reader to the concepts of internal and residual stress and strain. The chapter begins with an introduction to the nomenclature used in this work to describe different stresses and strains. In sections 2.2 and 2.3 some results from literature will be discussed. In section 2.3 the Fe-C system is emphasized because of this study's focus on pearlitic steel. Next, the relation between diffraction peak broadening and micro strains will be addressed, followed by a limited discussion on the consequences of internal and residual stresses. The chapter will be concluded by pointing out a number of open questions.

2.1 Classification of the types of stresses and strains

Most engineering materials are inhomogeneous, and their macroscopic mechanical properties will be a combination of the behaviour of the material's components and their interactions. These components can be different phases, regions with different composition or grains with different orientations. One way in which these components will interact is by creating internal and residual stresses and strains.

During the deformation of inhomogeneous materials, *internal stresses* will be generated as a result of the spatial inhomogeneity of elastic properties, yield stress and hardening rate. Internal stresses are present in the material while an external load is applied. After removal of the load and unloading of the sample, stresses might remain in the sample as a result of inhomogeneous plastic flow and elastic accommodation of the resulting plastic mismatch. They are present in the material although there is no external load and are called *residual* stresses and strain.

In the current work, the stresses and strains resulting from differences between phases and between differently oriented grains will be considered. The former will be termed *micro-phase stresses and strains*, while the latter will be referred to as *intergranular stresses and strains*. In order to maintain the stress equilibrium, these stresses need to average out over distances comparable to a few times the dimensions of the phases and grains, respectively.

The emergence of these stresses can qualitatively be understood from the sketch in Fig. 2.1. When a material consisting of a hard and a soft phase is strained, the soft phase wants to plastically deform more than the hard phase. However, in order to maintain geometrical compatibility, both phases have to undergo the same total deformation. In order to 'fit' both phases together again, a compressive residual stress is introduced in the soft phase and a tensile residual stress in the hard phase.

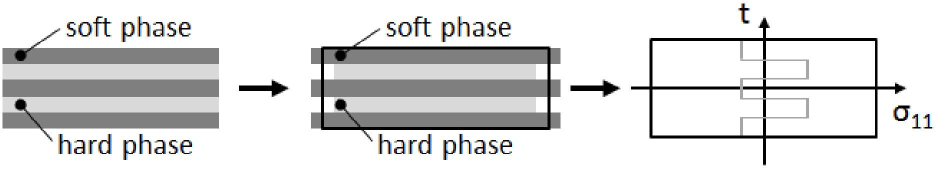

Fig. 2.1: Simplified illustration to qualitatively explain the emergence of micro-phase residual stresses and strains.

Stresses and strains in the material can also be introduced as a result of an inhomogeneous strain field. This is illustrated in Fig. 2.2 for the case of sheet rolling. The surface and core of the sheet will tend to deform differently, with the exact response depending on the deformation conditions [3]. If the surface plastically deforms more than the core, geometrical compatibility can be maintained by introducing compressive residual stresses at the surface and tensile stresses in the core of the sheet. To maintain stress equilibrium, these stresses have to average out to zero over the macroscopic sample dimensions. Therefore, these stresses will be termed *macro residual stresses*. Examples of macro residual stress profiles in cold drawn steel rods can be found in [4–6], but also surface treatments like shot peening can result in macroscopic stress profiles [7].

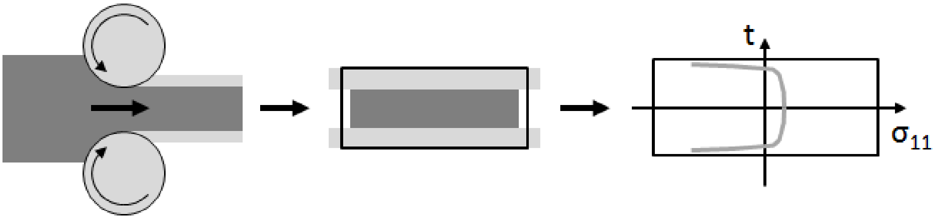

Fig. 2.2: Simplified illustration to qualitatively explain the emergence of macro residual stresses and strains.

Two specific examples where given to illustrate the origins of residual stresses. However, in general, it can be stated that residual stresses will develop whenever there is an inhomogeneous plastic strain field within a sample. A good introduction to the origin of macro- and microstresses is also given in the papers by Winholtz and Cohen [8] and by Hanabusa et al. [9]. The present work will focus on micro-phase and intergranular stresses.

2.2 Multiphase alloys and model systems

The development of micro-phase and intergranular stresses in a couple of interesting multiphase systems will be discussed in this section. Particular attention will be paid to the micro-phase stresses in Cu-Cr and Cu-Nb systems with a rod-like morphology, requiring co-deformation of the two phases present. Additionally, the intergranular stress development in two Fe-based alloys will be discussed. However, with respect to the current work, most attention will be paid to the Fe-C systems treated in section 2.3.

2.2.1 Micro-phase stresses and strains

Materials consisting of a hard and a soft phase will exhibit a specific pattern of internal micro-phase stress development during an in-situ tensile test. A good and illustrative example is given by Sinclair et al. for a directionally solidified Cu-Cr eutectic alloy [10,11]. The microstructure consists of fine Cr rods with a lath shape and a very high aspect ratio (>1000), embedded in a Cu matrix. The rods are oriented parallel to the solidification direction, which is also the loading direction. The rod alignment and their high aspect ratio forces both phases to co-deform, i.e. the total strain in both phases should be equal.

The <220> Cu lattice strain in the loading direction is shown in Fig. 2.3(a), together with the macroscopic stress-strain response (b). Due to the low Cr volume fraction (2%), the Cr lattice strain could only be recorded until yield of the Cr phase and is not shown here. Two deflection points can clearly be seen in both plots. The first one corresponds to the Cu yield point, the second to the Cr yield point. A similar result was obtained for a duplex stainless steel by Dakhlaoui et al. [12] and for a number of Fe-Cu alloys by Daymond et al. [13].

In the first stage, both phases are deforming elastically. If both phases have similar elastic constants, there will be no load transfer from one phase to the other. No residual stresses will remain after unloading. In the second stage, the Cu deforms plastically while the harder Cr remains elastic. As a result, load is transferred from the Cu to the Cr phase and the rate of increase of the lattice strain is decreased in the Cu phase, while it is increased in the Cr phase. If the material were to be unloaded, compressive residual elastic strains would remain in the Cu phase and tensile strains in the Cr phase. In the third stage, both phases co-deform plastically and the difference in lattice strain increase is again reduced. As a result, the build-up of internal stresses is also reduced. However, it can be seen that the rate of increase of the Cu lattice strain remains below that in the elastic region, suggesting that the Cr rods strain harden more than the Cu matrix and carry an increasing portion of the load. TEM studies showed a very low dislocation density in the Cr rods, indicating that the strain hardening of the Cr rods is a result of the difficulty with which dislocations can be nucleated at the phase boundary rather than a result of dislocation-dislocation interaction. It should be noted that a higher hardening rate in the hard phase is not a general feature, as the opposite is observed in the duplex stainless steel studied by Dakhlaoui et al. [12].

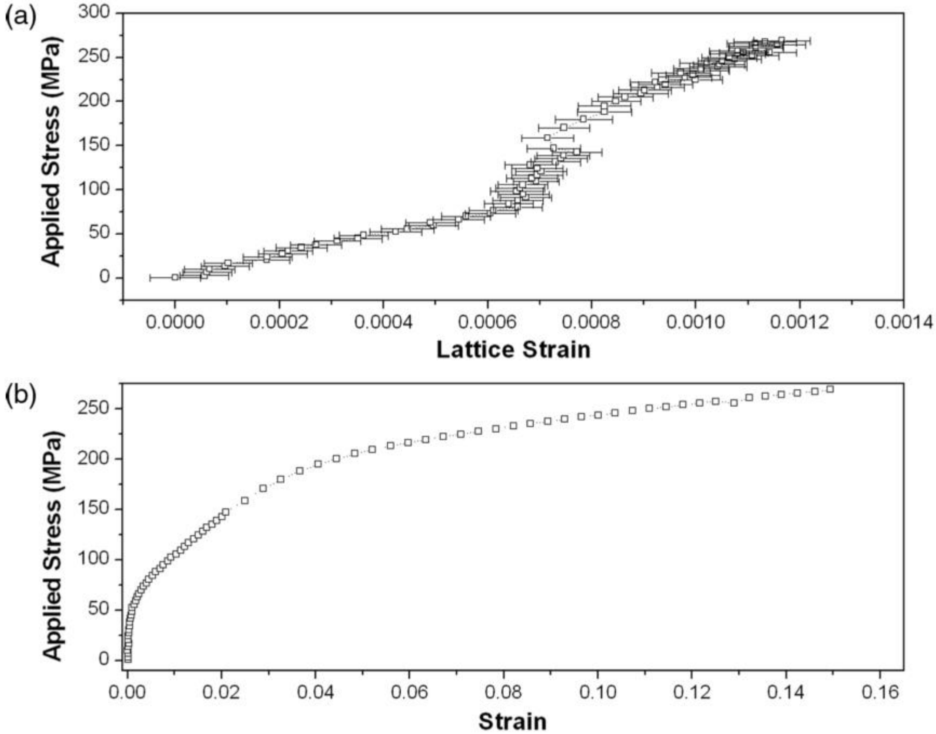

Fig. 2.3: Results of in-situ tensile test using neutron diffraction, performed on a Cu-Cr alloy [11]. *(a) Cu <220> lattice strain parallel to the loading direction and the long axis of the Cu-rods, as a function of applied stress. (b) Macroscopic stress-strain response.*

The transition from stage 1 (elastic-elastic) to stage 2 (elastic-plastic) is very sharp in the above discussed Cu-Cr eutectic. In contrast, the Cu-Nb nano-composite wires, studied by Thilly and Vidal et al. [14–16], exhibit a much more gradual transition and a deflection point cannot be observed. The fine microstructure of these wires is obtained by bundling Nb wires in a Cu mantle and cold drawing them, followed by a process of rebundling and redrawing. As a result, the Cu matrix is a heterogeneous mixture of different length scales. The first Cu mantles become very fine Cu-channels, whereas the later mantles remain relatively broad Cu-channels. The yield strengths of these mantles are also different, resulting in early yielding of the broad Cu-channels and later yielding of the fine Cu-channels. Additionally, the large Cu-channels exhibit an extended micro plastic regime. The load transfer from Cu to Nb therefore occurs much more gradual.

2.2.2 Intergranular stresses and strains

Not only the various phases in a material have different elastic and plastic properties, also differently oriented grains will respond differently to an applied load. The latter differences will give rise to the development of intergranular internal and residual strains and stresses, i.e. differences in local lattice strain because of the different elasto-plastic response of each grain. Because an Fe-C alloy is used in this work, the intergranular strain development in two other iron based alloys will be shortly discussed here.

Dakhlaoui et al. [12] investigated the internal lattice strain development during in-situ tension and compression tests on a duplex stainless steel. The material was hot rolled and consists of elongated austenite grains in a ferrite matrix (50-50 vol%). The lattice strain response during an in-situ tensile test can be seen in Fig. 2.4. The line indicated by Γ corresponds to plastic yielding of the austenite, while Ω corresponds to the onset of ferrite plasticity. Before Γ both phases are elastic and the difference in response between the various grain families can be attributed to elastic anisotropy. After Γ the austenite lattice strains can be seen to level off, indicating load transfer to the stronger ferrite phase. Yielding in the <200> austenite grains happens significantly later. The same trend is observed for the <200> ferrite grains. Oliver et al. [17] suggested that this effect can also be attributed to elastic anisotropy. As the <200> grains are the most compliant ones, they bear a smaller internal stress and yield at a higher macroscopic load. Beyond the Ω point, all grain family responses diverge further, indicating the presence of significant plastic anisotropy. Only for the <110> and <211> ferrite grain families this is not the case, illustrating that they behave very similarly from both an elastic and plastic point of view.

Perpendicular to the loading direction, plastic anisotropy in the ferrite phase is much more pronounced. Especially the remarkable cross-over of the <200> lattice strain should be noted. This is a feature often observed for bcc materials which has been explained in detail by Oliver et al. [17] and to which more attention is paid in section 2.3.2.

Similar results were obtained by Daymond et al. [13] on Cu-Fe alloys (Fig. 2.5), with varying volume fractions of the Cu-rich phase (17, 50, 67 and 83 vol%). They also observed two distinct yield points. From their data it can be seen that the intergranular strain development becomes somewhat more pronounced after yielding of the second phase. A remarkable difference with

Dakhlaoui's data is the lack of a clear <200> cross-over in the ferrite phase. Daymond et al. attribute this to the fact that the lattice strains remain small during their experiments.

However, the current author would like to suggest a second possible explanation. The data presented might indicate that intergranular strain development is in general smaller if the volume fraction of that phase is low (Fig. 2.5, left). It is unclear whether this is related purely to volume fraction, or whether it is an effect of the phase's particle sizes. Also, it should be remarked that the experimental data shows quite some scatter for the low volume fraction phases, making intergranular strain development more difficult to observe. Additionally, the 50-50 alloy does hint at the onset of <200> cross-over in the transverse direction (Fig. 2.5, right). It is thus plausible that the interphase strains simply dominate over the intergranular strains, or even suppress intergranular strain development to some extent.

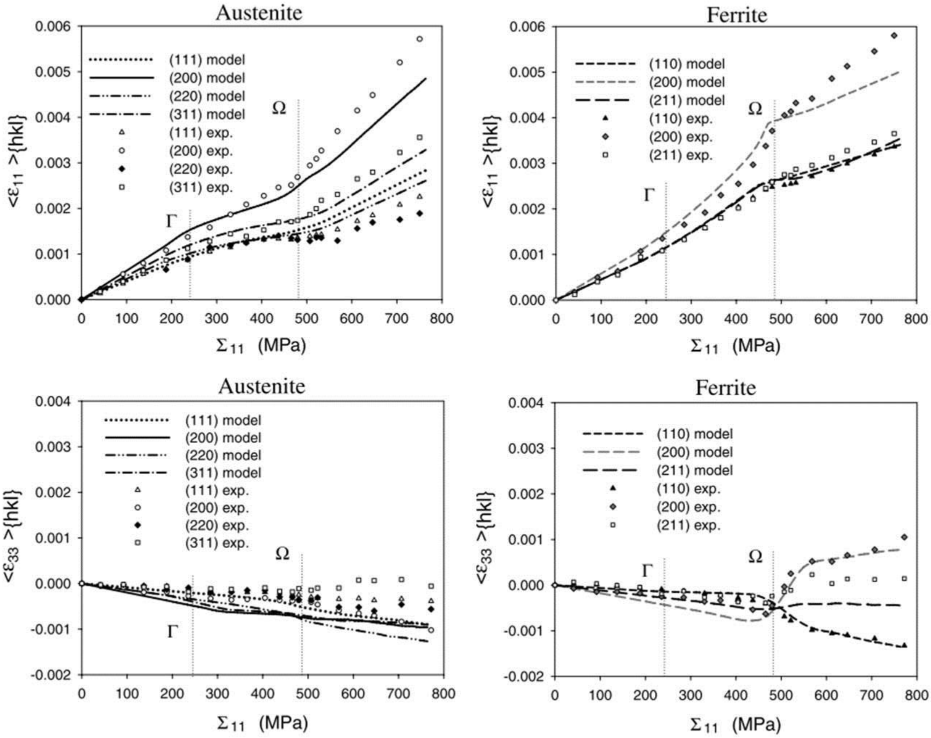

Fig. 2.4: Lattice strains parallel $\langle\varepsilon_{11}\rangle_{(hkl)}$ and perpendicular $\langle\varepsilon_{33}\rangle_{(hkl)}$ to the load direction, versus applied stress Σ_{11} along the TD. Results obtained on a austenite-ferrite, duplex stainless steel. Points belong to experimental measurements, lines belong to modelling results. [12]

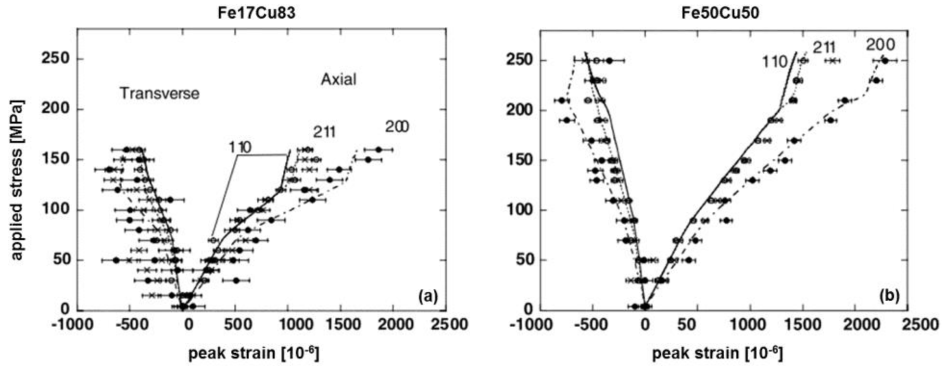

Fig. 2.5: Fe lattice strain responses during an in-situ tensile test performed on Fe17Cu83 and Fe50Cu50 alloys. Both the transverse and axial responses are shown. [13]

2.3 Fe-C systems

In this section, the internal and residual stresses in carbon steels will be discussed based on the available literature. A distinction is made between micro-phase stresses and intergranular stresses. The former result from the different behaviour of the ferrite and cementite phases, while the latter result from the elastic and plastic anisotropy of both phases. Steel with a globular cementite morphology (spheroidite) and a lamellar microstructure (pearlite) are distinguished, as well as one study on a bainitic steel. For an introduction to pearlitic steels and their deformation behaviour, the reader is referred to Chapter 3.

2.3.1 Micro-phase stresses and strains

One of the first attempts to measure the internal stress in spheroidite was, to the authors knowledge, published by Wilson and Konnan in 1964 [18]. Using laboratory X-ray diffraction and a relatively high carbon steel (1.14wt%) they obtained estimates of the internal stress during a tensile test and the remaining residual stress after unloading. These back stresses are believed to originate from dislocation loops accumulating around non-yielding cementite particles. They found that, as is now generally accepted, the residual stress that develops as a result of plastic deformation in a high carbon steel involves large tensile cementite stresses in the loading direction (up to 600-780 MPa), which are balanced by opposing stresses of smaller average magnitude in the ferrite phase.

Wilson and Konnan also concluded that the micro-phase stresses reach a limiting value at 7-8% extension due to increased slip-processes in the matrix. Very similar experiments were performed by Hanabusa et al. [9]. The results are comparable, but differ as far as the limiting value or saturation is concerned. Hanabusa et al. observed a maximum at around 6% tensile strain, after which the cementite residual stress decreases somewhat (Fig. 2.6). This decrease and subsequent saturation is attributed to the climbing or cross-slip of dislocation loops. On the other hand, saturation of the residual stress was also observed on a lamellar pearlite by Bonner et al. [19], where the explanation by climbing and/or cross-slip of dislocation loops does not hold.

Later work by Oliver et al. and Young et al. on spheroidite steels shows a fast saturation of the residual micro-phase stresses after unloading, at a plastic strain as small as 4% [17,20]. Oliver et al. attribute the saturation to reverse yielding of the ferrite phase upon unloading, rather than cementite plasticity, particle fracture or interface damage. Reverse yielding of the ferrite phase occurs if the ferrite is plastically compressed during unloading. It is then the elastic strain and thus stress in the cementite phase which supplies the force necessary to achieve this compression. Attributing the saturation to reverse yielding has experimentally been supported by comparing the observed residual stress to the residual stress value found by linear extrapolation from the measured stress before unloading (see Fig. 2.8). It could be seen that the measured residual stress was 10% lower than the extrapolated value, indeed suggesting reverse ferrite yielding.

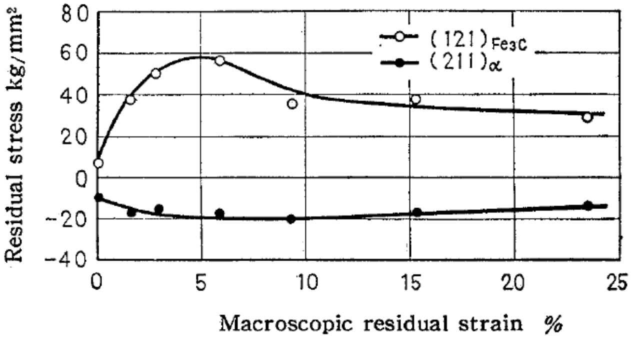

Fig. 2.6: Cementite and ferrite residual stress after tensile loading of a spheroidised high carbon tool steel (SK1). The residual stress is given as a function of the macroscopic strain after elastic relaxation. [9]

The work by Oliver et al. [17] on spheroidite steels, shows a strong shift in the lattice strains upon macroscopic yielding, as can be seen from Fig. 2.8. (c, d). A similar large 'jump' was also observed by Young et al. [20] on a spheroidite steel. At larger macro strains, the ferrite lattice strain continues to increase considerably, except for the <200> transverse lattice strain. Daymond and Priesmeyer [21] investigated a hypereutectoid steel, having lamellar pearlite colonies with single phase ferrite at the colony boundaries. Here, a sudden lattice strain shift at the yield point was not observed, and the increase in lattice strain after yielding was somewhat less strong. Finally, Tomota et al. [22,23] investigated an as-patented steel with a fully pearlitic microstructure and observed a constant ferrite lattice strain in the axial direction after yielding. These observations indicate that, when the microstructure evolves towards a more lamellar morphology, load transfer from cementite to ferrite in the plastic regime becomes more pronounced, as is also supported by fatigue experiments [8]. The disappearance of the lattice strain shift upon yielding, additionally indicates that the load transfer is more gradual in a lamellar material.

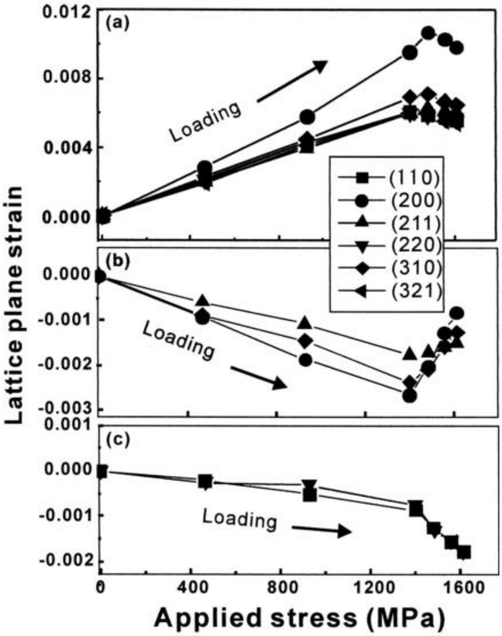

Fig. 2.7: Lattice plane strains in the ferrite matrix of a swaged sample during an in-situ tensile test: (a) the axial and (b), (c) the transverse directions. The sample consist of a lamellar pearlite with lamellae aligned along the loading direction and exhibits a <110> fibre texture [24].

In deformed, swaged [23,24] or cold drawn [22], and subsequently stress relieved lamellar pearlite, the average axial ferrite micro-phase strain after yielding decreases instead of increasing or saturating as was observed for undeformed samples with various microstructures. In the transverse direction, the same seems to be true for all but the <110> grain families. The result as obtained by Kanie et al. on a swaged and stress relieved sample can be seen in Fig. 2.7. Very similar results were obtained on as-cold rolled sheet by Seefeldt et al. [25]. The deviatory behaviour of the <110> grain families will be treated in section 2.3.2. The decreasing lattice strain after loading has been attributed to increased load transfer to the cementite phase [22–24], due to the strong alignment of the lamellae.

The above already illustrates the importance of the morphology in the development of *internal* micro-phase stresses, going from globular over randomly oriented lamellae, to well aligned lamellae. Under the assumption that the intergranular stress development in the axial direction is small (see section 2.3.2), the loading-unloading tests performed by Tomota et al. [22] also show the influence of the cementite morphology on the *residual* micro-phase strain development after tensile loading. A globular morphology results in a saturation of the residual micro-phase strain at a macroscopic tensile strain of only 2%. On the contrary, a lamellar microstructure results in a much slower saturation starting from 8-10% macroscopic strain, and a higher residual strain magnitude after saturation.

Reports on residual stress values at high strains, which cannot be reached by a tensile test, are scarce. One such report has been given by Van Acker et al. [26] for cold drawn wires. Micro-phase residual stresses of the order of 2 GPa were reported for the cementite phase and -150 MPa for the ferrite phase at an accumulated true drawing strain of 1.92. After further drawing to a strain of 2.59, the micro-phase residual stresses decreased somewhat. Van Acker et al. attribute this to fragmentation of the cementite phase. The work by Tomota et al. [22] further indicates that the residual stress present in an as-cold drawn wire with aligned lamellae does not change significantly anymore if it is subsequently subjected to a tensile test, providing additional evidence for residual stress saturation, even at high strains.

Another interesting feature is the influence of the interlamellar spacing (ILS) on the internal and residual stress development in lamellar pearlite. H. Yahyaoui et al. [27] show that the *internal* stresses during an in-situ tensile test are larger for a sample with a smaller ILS. This is attributed to the larger in-situ ferrite yield stress associated to a smaller ILS. On the other hand, the *residual* stress after unloading is larger for a sample with a larger ILS and thus a smaller in-situ ferrite yield stress. This would indicate that it is the difference in yield stress between the ferrite and cementite phases which is the main factor determining the absolute value of the residual stress. These observations are however contradicted by T. Shinozaki et al. [28], who report that the absolute value of the *residual* stress is increased with decreasing ILS, indicating that the ferrite yield stress controls the magnitude of the residual stress. A very similar material was used in both studies, but Yahyaoui et al. used X-ray diffraction to measure the total ferrite residual stress at the surface, while T. Shinozaki et al.

used neutron diffraction getting a volume average micro-phase residual stress. It is thus possible that the mechanism by which the ILS influences the residual stress is different at the surface as compared to the centre of the sample.

2.3.2 Intergranular stresses and strains in ferrite

An in depth and instructive analysis of the intergranular stresses in the ferrite phase has been performed by Oliver et al. [17]. To get more insight in the interplay between the micro-phase stresses and the intergranular stresses they compared the internal and residual stress evolution in a low carbon steel (LC) and a globular high carbon steel (HC, 1wt% C). The main experimental results, obtained using in-situ neutron diffraction, are reproduced here. In Fig. 2.8, the lattice strain response as a function of the applied stress in an axisymmetric tensile test can be seen.

It is interesting to note that, for the LC steel and in the axial direction, the <200> lattice strain response remains approximately linear through the macroscopic yield point, indicating that the <200> axial grain family yields later, although it can be shown that it has the lowest Taylor factor. This is attributed to the fact that the <200> grain family is also the most compliant one and therefore carries a smaller load when the macroscopic yield point is reached. Elastic and plastic anisotropy thus always have to be considered together and tend to influence intergranular strain development in opposite ways, thereby reducing the magnitude of axial intergranular strains in ferrite.

A further analysis of the lattice strain responses in the transverse direction, based on an Elasto-plastic Self Consistent (EPSC) model and crystal plasticity arguments, shows that although large axial residual stresses do not develop in the LC steel, this does not imply that the transverse residual stresses are also small. Oliver et al. illustrate that the distribution of slip directions does not allow differently oriented grains to transversely contract to the same extent, causing large transverse incompatibilities to develop. In fact, their reasoning is very similar to the one developed by Hosford [29] to explain the observed curling behaviour in wire drawn bcc material. The transverse strain is therefore also particularly sensitive to the exact grain orientation, pointing to the importance of crystallographic texture in analysing internal and residual stress development.

During deformation of the HC steel, micro-phase stresses also develop. By analysing the residual lattice strains after unloading and after subtraction of the average micro-phase stress response, Oliver et al. conclude that the axial intergranular trends in the LC steel are almost completely reversed in the HC steel, while in the transverse direction this is not true. An explanation is provided by the fact that in the axial direction the ferrite micro-phase stresses, which are compressive in the axial direction, counteract the intergranular stresses. In the transverse direction however, the micro-phase stresses reinforce the intergranular stresses.

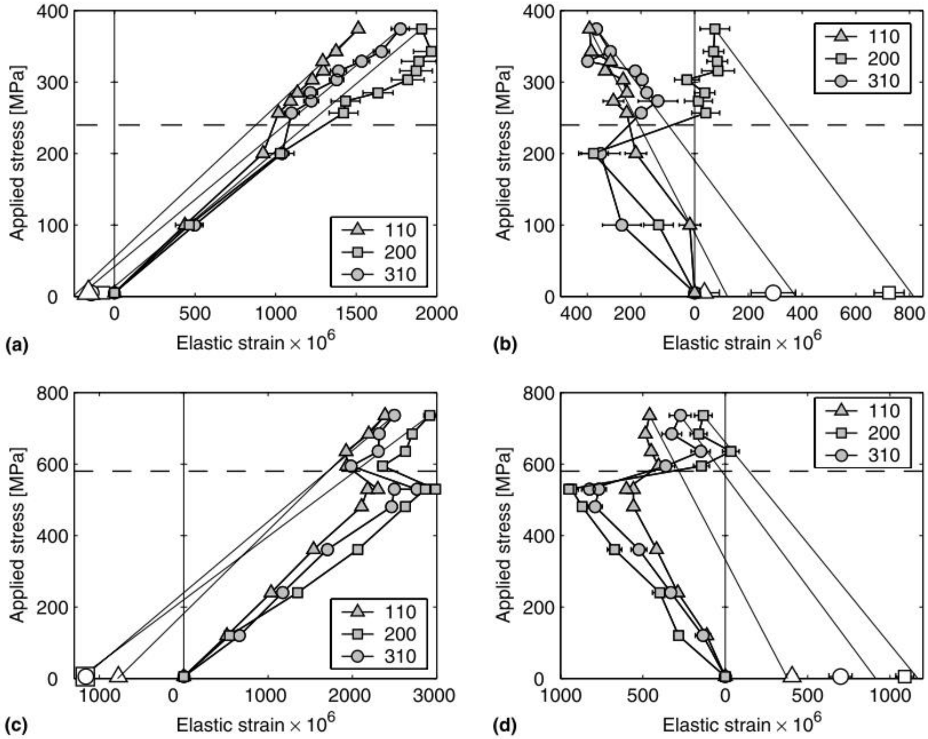

Fig. 2.8: Average ferrite grain family elastic strains plotted against applied stress (filled data points), for a low carbon (LC) steel and a spheroidised high carbon (HC) steel. Unloading responses expected for purely elastic unloading are shown by the straight lines extrapolating the data points at highest applied stress to zero stress. The actual strains measured after load removal are shown by unfilled data points. (a) LC, axial. (b) LC, transverse. (c) HC, axial. (d) HC, transverse. [17]

Comparing Fig. 2.8 (a) and (b) to (c) and (d) the current author also observes that the intergranular divergence is somewhat larger for the LC steel than for the HC steel, particularly if the transverse direction is considered. This might indicate that the dominance of the micro-phase stresses can to some extent suppress the development of intergranular stresses.

The high carbon steel investigated by Oliver et al. has a globular morphology. Remarkably, Daymond and Priesmeyer [21] obtained very similar results on a hypereutectoid steel (0.35-0.4 wt% C, 1.3-1.6 wt% Mn) consisting largely of lamellar pearlite colonies, surrounded by single phase ferrite. The undeformed material exhibits no crystallographic or morphological texture.

The lattice strain was measured during an in-situ tensile test up to a tensile strain of 3.5%. All ferrite grain families behaved very similar to the observations made by Oliver et al.. Daymond and Priesmeyer also conclude that the load is transferred to cementite very rapidly after initial yielding of the ferrite phase, although the large lattice strain shifts observed by Oliver et al. upon yielding were not observed here. Additionally, it was shown that the <110> and <211> ferrite grain families behave qualitatively similar. Results nearly identical to those presented by Daymond and Priesmeyer were obtained on a fully pearlitic steel by Morooka et al. [23]. These observations suggest that, at least for an in-situ tensile test without observation of cementite plasticity and on an undeformed sample, the cementite morphology has little influence on the intergranular stress development in ferrite.

Cold deformed, swaged samples have been investigated by Kanie and Morooka et al. [23,24], showing a different behaviour for the <110> transverse grain family. The transverse behaviour is still similar as far as the <200> and <310> peak shifts after yielding are concerned. However, the <110> residual lattice strain after unloading becomes compressive, while it is expected to be tensile due to the large micro-phase stresses, indicating the presence of significant intergranular residual stresses in the transverse direction. In the axial direction the intergranular residual stress evolution is quite limited. An explanation for the transverse intergranular stresses can be found in Gil Sevillano’s work on Nb wires [30,31] and is actually similar to the explanation given by Oliver et al. [17] for the observed smaller, while still tensile, residual stress in the <110> grain family of their investigated steels. Due to the development of a <110> fibre texture and the inhomogeneous distribution of <111> slip directions that accompany it (Fig. 2.9), 110 oriented grains will undergo plane-strain deformation. Contraction will be realised in the transverse <200> direction, but not in the transverse <110> direction. Due to the constraint of the global axisymmetric deformation in the grain’s environment, a compressive intergranular residual stress will develop along the <110> direction, while a tensile residual stress will develop along the <200> direction, thereby also explaining why a considerably higher tensile residual stress was observed in the <200> direction.

T. Shinozaki et al. [28] further report that the interlamellar spacing influences the intergranular stress development. Their in-situ tensile tests on a lamellar pearlitic steel show that the intergranular stresses, while being small, are more pronounced in a sample with a smaller interlamellar spacing. Except for the interlamellar spacing, no other differences are reported between the two samples that might explain this observed behaviour.

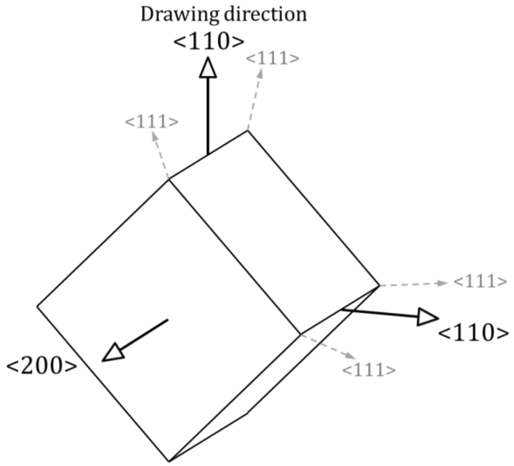

Fig. 2.9: Illustration of a crystal oriented with a <110> direction parallel to the wire drawing axis. The <111> slip direction are indicated by the dashed arrows. It can be seen that only the upper two slip direction can be activated, realizing a contraction in the <200>, but not the <110> direction. (After Oliver et al. [17]*)*

2.3.3 Intergranular stresses and strains in cementite

The early work by Wilson and Konnan, and Hanabusa et al. was mainly focussed on the micro-phase stresses that develop in a globular pearlite. However, an important contribution by Hanabusa et al., which is only a foot note in their paper, is the observation of different d-$\sin^2\psi$ slopes for various cementite reflections measured on a high carbon cast steel (4.3wt% C, 65.7 vol% Fe_3C). This must be one of the first, if not the first, experimental observation of the presence of intergranular stresses in the cementite phase. An observation which was later confirmed by Weisser et al. [32] for a bainitic steel, and by Kanie et al. [24] and Young et al. [20] for a pearlitic steel.

Measuring the internal and residual lattice strains in the cementite phase of a carbon steel is often very difficult. This can be attributed to the cementite's low crystal symmetry and its often low volume fraction (<13vol%). Upon deformation, the situation is aggravated by the strong peak broadening and resulting peak overlap which is observed for the cementite phase. As a result, only a limited amount of data is available on the cementite phase, especially regarding the intergranular stresses.

To this date and to the authors knowledge, the best reports on cementite intergranular stresses have been given by Kanie et al. [24], Young et al. [20] and Weisser et al. [32]. While the results of Kanie et al. and Young et al. compare well, they differ significantly from the data presented by Weisser et al. A short discussion of their observations and particularly the differences between them is given below.

Kanie et al. performed in-situ tensile tests on a swaged sample with a lamellar microstructure, while Young et al. used a spheroidite sample with a very high cementite volume fraction (34 vol%). The cementite remains elastic and no intergranular stress development is observed between different cementite reflections, suggesting that cementite does not exhibit significant elastic anisotropy (Fig. 2.10). This is however contradicted by the observations made by Weisser et al. on a 1% MoCrV tempered bainitic steel (Fig. 2.11). They do observe a significant elastic anisotropy as had also been reported from ab-initio calculations, by Jiang et al. [33], Nikolussi et al. [34] and Henriksson et al. [35]. It should be noted that the anisotropy observed by Weisser et al. is not as strong as that obtained from the ab-initio calculations, which might be contributed to effects from the embedding ferrite matrix.

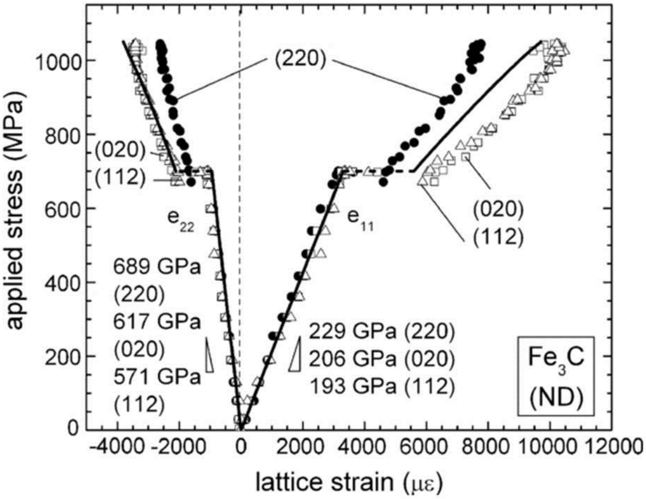

Fig. 2.10: Applied stress vs. lattice strain for the Fe_3C <020> (<200>)*, <220> (<202>)* and <112> (<121>)* reflections as measured by Young et al. [20], *parallel and transverse to the applied load. *The reflection names between brackets refer to the notation used in this work to label the cementite peaks.*

The <200> and <202> grain families measured by Young et al. would, based on ab-initio calculations have a similar elastic modulus, explaining why Young et al. did not observe a different slope in the elastic regime. However, the <112> reflection studied by Young et al. should have a significantly different slope. Weisser et al. argue that maybe the <121> reflection overlaps with the <210> reflection, altering the resulting lattice strain. Furthermore, it should be remarked that the additional alloying elements in the steel used by Weisser et al. could have an influence on the elastic properties of the carbides.

In the plastic region of the in-situ test, the cementite peak quality degraded too much in Weisser's study to be able to determine intergranular stress evolutions. Kanie et al. and Young et al. however, show that all cementite grain families behave qualitatively similar, but that absolute values of their internal and residual lattice strains differs. As Young et al. reported cementite to be elastically isotropic and to remain elastic throughout the entire tensile test, they attribute this observed anisotropy to orientation relationships between the ferrite and cementite. The anisotropy of the ferrite matrix is then reflected in the cementite phase, rather than plastic anisotropy of the cementite itself.

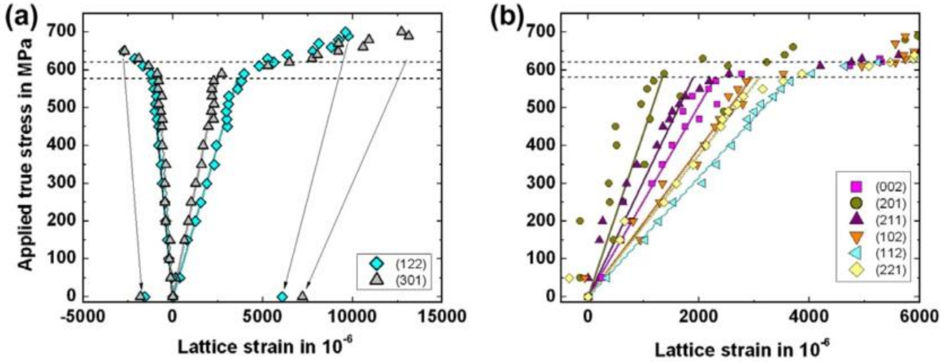

Fig. 2.11: Lattice strain with applied true stress for various cementite grain families, as measured by Weisser et al. [32]*: (a) 122 and 301 parallel and transverse to the applied load and (b) other non-overlapping reflections parallel to the applied load.*

2.4 Peak broadening and micro strain

Internal and residual lattice strains do not only result in peak shifts, as has been discussed in sections 2.2 and 2.3. Within a diffracting volume contributing to a certain reflection, both an inhomogeneous elastic and plastic strain field might exist. Possible origins are strain gradients, differently oriented grains (i.e. having a different angle of rotation around the diffraction vector) and the presence of lattice defects, such as dislocations. In such a case this inhomogeneous strain field will result in a broadening of the diffraction peak. However, one should be careful in translating the peak width to strains or dislocation densities. First of all it is very difficult to deconvolute the different strain contributions. Additionally, there can be other influences on the peak width such as the size of the coherently diffracting domain. In the following, some literature on peak broadening in pearlitic steel will be presented.

Tensile loading-unloading tests were performed by Tomota et al. [22] on pearlitic steel samples with various microstructures. The diffraction profile of the <110> ferrite peak exhibited strong broadening of the peak tails, attributed to the size effect. The peak broadening contributions of the size effect and microstrain $\langle \varepsilon^2 \rangle^{1/2}$ were separated. Tomota et al. observed that, while the microstrain increases upon applying a load, it decreases again after removal of the load. The dislocation density is assumed to be the main responsible for the microstrain development. It is therefore postulated that the dislocation density increases with forward deformation, but decreases again with unloading. Dislocations would then move forward with increasing applied stress, but move backward again with unloading. This is feasible, as long as the dislocations are not absorbed by grain boundaries and as long as they are not pinned by dislocation-dislocation interactions.

Additionally, the ‘block size’, which is related to the coherently diffracting domain, was correlated to a decrease in interlamellar spacing (ILS) as a result of the tensile deformation. Based on their data, the current author would have to conclude that the ILS of an as-patented sample decreases from 150 nm down to 60 nm, within a macroscopic tensile strain of 8%. This seems to be an unreasonably large decrease in ILS and it is likely that other factors also play a role.

Van Acker et al. [26] measured the peak width of the ferrite and cementite phases in cold drawn pearlitic steel samples and compared these to a sample recovered by a heat treatment. They saw a very strong increase in peak width as a result of cold drawing to a strain of 1.96. The cementite peaks broadened much more than the ferrite peaks. Further cold drawing to a strain of 2.59 did not increase the peak width further. Macroscopic stress gradients were excluded as a possible cause for the peak broadening. The fact that also the cementite peaks broadened strongly is therefore attributed to plastic deformation of the cementite lamellae.

The cementite diffraction peaks measured by Wilson and Konnan [18] on a globular pearlite, already broadened significantly after 3-7% tensile straining. Anodic etching to remove the ferrite matrix, left free standing cementite particles in which the residual stress was relaxed. Simultaneously, the cementite peak broadening was reversed. This leads the current author to suggest that, at least for small deformations, the peak broadening is mainly caused by strong elastic strain gradients in the cementite particles. This does not exclude that at higher strains, as suggested by Van Acker et al., plastic deformation of the cementite can contribute to its peak broadening.

Very strong cementite peak broadening was also reported by Winholtz and Cohen [36] in shot peened samples, and by Weisser et al. [32] in bainitic steel samples subjected to a tensile test. All observations made on carbon steels show that the cementite peak broadening is much more pronounced than the ferrite peak broadening. At small plastic strains just after the onset of macroscopic yielding Weisser et al. attribute the cementite peak broadening to the existence of different strains in grains having a different rotation angle around the diffraction vector. These differences could come from the complex arrangement of cementite to their neighbouring ferrite grains. However, as the lattice strain goes towards 1%, an inhomogeneous strain field within cementite particles or a reduction of the coherent scattering size cannot be excluded.

2.5 Consequences of internal and residual stress/strain

Internal and residual stresses and strains that develop during or as a result of an applied load, be it a thermal, mechanical or any other load, can significantly influence the materials response to that load or its properties after removal of the load. While this section does not give an exhaustive summary of all possible effects of internal and residual stresses and strains, it presents a number of illustrations to give the reader a feeling for the practical importance of these stresses and strains.

Wilson and Konnan [18] conclude that the back stresses in the ferrite matrix of a globular ferrite-cementite microstructure contributes to an increase in the observed tensile flow stress of the aggregate. According to their estimates, the back stress could be responsible for up to 60% of the total increase in work-hardening due to the presence of precipitates. In its simplest form this can be understood from the fact that the internal stress has to be added to the externally applied stress to obtain the total stress locally present in the material. With a compressive back stress in the matrix, the total internal stress will be lower than the externally applied stress, resulting in an increase of the macroscopically observed yield stress.

Winholtz and Cohen also observe that the emergence of back stresses in the ferrite matrix of pearlitic steel results in additional strain hardening. However, they explain this in terms of dislocation movement. To be able to continue their movement, dislocation in the matrix must overcome the back stresses which are present. This results in a higher apparent critically resolved shear stress.

The development of internal stresses can lead to a softening on load reversal (Bauschinger effect) [10,11]. Compressive residual stresses, generated in the soft phase upon tensile deformation, add up to the externally applied load. If the external load is now decreased or even reversed, the softer phase will reach its yield point at a macroscopic load which is lower than that phase's yield stress. In materials that contain very large elastic strains, the internal stress can be large enough to initiate reverse, compressive flow even when the applied stress remains tensile. Reverse yielding will occur in the softest element of the material once the stress in that element has been reduced from its flow stress in tension to its flow stress in compression.

As has been stated above, the local total internal stress during loading is the sum of the residual stress locally present in the material before loading and the externally applied stress. As a result, the material will behave differently under a tensile load as compared to a compressive load, as has been observed by Dakhlaoui et al. [12] for a duplex stainless steel. T. Suzuki et al. [37] similarly show that micro-phase stresses in the ferrite matrix of a lamellar pearlitic steel wire can result in strength anisotropy. On average, the ferrite micro-phase stress in drawn wire is compressive in the drawing direction and tensile in the radial and hoop directions. As a result, the macroscopic tensile strength is increased in the drawing direction, while the compressive strength is decreased. The opposite is true for the radial direction. Because the cementite micro-phase stress is opposite in sign to the ferrite micro-phase stresses, this also means that yielding of the ferrite phase determines the macroscopic yield point. The same effect which leads to a different behaviour under compression and tension, will lead to a directional dependence, i.e. anisotropy, of the macroscopic material properties once residual stresses have been introduced in the material.

Winholtz and Cohen describe the influence of residual stresses on the low-cycle fatigue of a 1080 steel [8,36]. A compressive residual stress in the matrix is usually considered as beneficial for the fatigue properties. However, if this stress is a micro-phase stress which is accompanied by larger tensile stresses in a harder minority phase, this may not provide the desired fatigue resistance. It is therefore important to determine the residual stress in all phases of a multiphase material.

Residual stresses can also cause longitudinal splitting of bcc materials during wire drawing or during the wire's service life. A bcc material develops a <110>-fibre texture during wire drawing, resulting in plane-strain deformation conditions for the individual grains [29] and a particular microstructure of flat grains curled around the wire axis. Because of this, intergranular tensile residual stresses develop in the transverse direction. These act perpendicular to the axially aligned grain boundaries which are also parallel to {001} crystal planes. These planes are cleavage planes for bcc crystals and the tensile stress acting on them can result in longitudinal splitting. [30,31]

2.6 Conclusions and open questions

Micro-phase stresses develop during the deformation of multiphase alloys. In-situ experiments reveal that a load transfer from the soft phase to the hard phase occurs upon yielding of the softer phase. This can be seen from a first deflection point in the macroscopic stress-strain curve and from the lattice strain response. A second deflection point is observed as the second phase yields. It should be remarked however that these sharp deflections points cannot be observed in materials where yielding is a gradual phenomenon.

A lamellar morphology of the hard phase results in a more pronounced load transfer as compared to a globular morphology. Tomota et al. [22] propose that aligning the lamellae with the loading direction strengthens this load transfer further, illustrated by a decreasing lattice strain in the soft phase after yielding. However, Cu-Nb nano-wires in which alignment is perfect and complete co-deformation is assumed does not exhibit this decreasing lattice strain after yielding of the soft phase. This illustrates that good alignment alone is not sufficient to explain the decreasing lattice strain observed in aligned pearlite and that the exact mechanism behind this very large load transfer should be studied further.

After removal of the external load, residual stresses remain. In particular, tensile residual stresses develop in the hard phase and compressive ones in the soft phase, parallel to the loading. With increasing strain these residual stresses reach a limiting value. For spheroidite this saturation has been explained by reverse yielding of the matrix phase, however for a lamellar microstructure other mechanisms such as fragmentation of the reinforcing phase are also possible. Further research is required to uncover what mechanisms could lead to saturation, especially in lamellar pearlite.

Furthermore, most information on the residual stresses come from in-situ deformation tests to relatively small strains. The work by Tomota et al. [22] and Van Acker et al. [26] does suggest that saturation or even a decreasing trend is also observed at larger strains, but more extensive work on cold drawn or rolled material is required to irrefutably proof residual stress saturation at large deformations.

Intergranular residual stresses are superposed on the micro-phase stresses. The morphology of the material does not seem to qualitatively change the intergranular stresses. However, going from a globular to a lamellar microstructure does seem to reduce the magnitude of the intergranular stresses. This might be due to the presence of larger micro-phase stresses which reduce the intergranular stress tendencies. Additionally, intergranular stresses become more pronounced once both phases are deforming plastically.

In pearlitic steels, there seems to be an influence of the interlamellar spacing (ILS) on the magnitude of the residual micro-phase stress. Unfortunately literature results contradict each other making it unclear whether a smaller ILS results in larger or smaller residual micro-phase stresses. One report by Shinozaki et al. [28] also shows that a smaller ILS results in more pronounced intergranular stresses in ferrite.

During deformation of a carbon steel, the ferrite and cementite peak width increase significantly. All reports also show that cementite peak broadening is more severe than ferrite peak broadening. Additionally, it is clear that after removal of the load, the peak width again decrease. Several mechanisms behind this peak broadening have been proposed such as (1) an increase in the dislocation density, (2) macroscopic strain gradients in the case of neutron diffraction measurements, (3) a decrease of the coherently scattering domain, (4) intergranular stresses between grains that are part of the same grain family and (5) elastic strain gradients within one grain. However, it remains unclear what mechanisms are responsible for the largest contribution to peak broadening. Furthermore, the much stronger broadening of the cementite peaks has never been discussed before.

As a case study, the current work will focus on the micro-phase and intergranular stress evolution in pearlitic steels. It is therefore essential to also have some understanding off the plastic deformation and strain hardening behaviour of pearlite and the difference in behaviour between the ferrite and cementite phase. In chapter 3 an introduction is given to this topic and special attention is paid to cementite phase whose mechanical properties are to this date largely unknown.

2.7 The goals of this work

Based on the open questions identified in the previous section, the goals of this work can be stated. They are given in Table 2.1, together with the chapters or sections of this text where these goals are addressed. Table 2.1 can thus be used as a guide to help the reader process this text.

Goals	**Sections**
1. Investigate and try to explain the residual strain development in pearlitic steel sheet over a broad strain interval.	6.2; 7.2; 8.1; 8.2
2. Investigate whether residual strain saturation occurs up to large strains and try to understand the origins of such saturation.	6.2; 7.2; 8.1.3
3. Investigate and try to understand the occurrence of intergranular residual strain development.	6.2; 8.1.4; 8.2
4. Investigate the influence of the interlamellar spacing on the residual strain development in pearlite.	6.2.2.1
5. Investigate and try to understand the very large load transfer observed during in-situ tensile testing of pearlite.	6.3; 7.3; 8.3.1
6. Investigate and try to understand peak broadening as a result of deformation as well as the reversal of such broadening.	6.2.3; 6.3.3; 8.3
7. Come to a better understanding of the in-situ deformation behaviour of ferrite and cementite within the pearlite composite.	8.3; 8.4

Table 2.1: The goals set forth in this work, along with the chapters or sections where these problems are tackled.

3 Pearlite and its deformation

Pearlitic steel is a carbon steel used in many applications. The material can be wire drawn to very high strains, resulting in exceptionally high strengths up to 6.3 GPa [38]. These wires are primarily used as a reinforcement in tires, for the cutting of Si wafers and as filaments in steel cords and cables used for example in the construction of suspension bridges. Pearlitic steel is also used as the main railroad steel.

Pearlite owns its exceptional properties to its microstructure. The undeformed microstructure consists of randomly oriented stacks of ferrite and cementite plates, called lamellae (see section 6.1.1). Each differently oriented stack is termed a colony. The ferrite phase has a relatively soft body centred cubic (b.c.c.) crystal structure, while cementite is a hard, carbon rich phase with an orthorhombic crystal structure (see section 3.2). This microstructure is typical for carbon steels with a composition near the eutectoid point (0.77 wt% C).

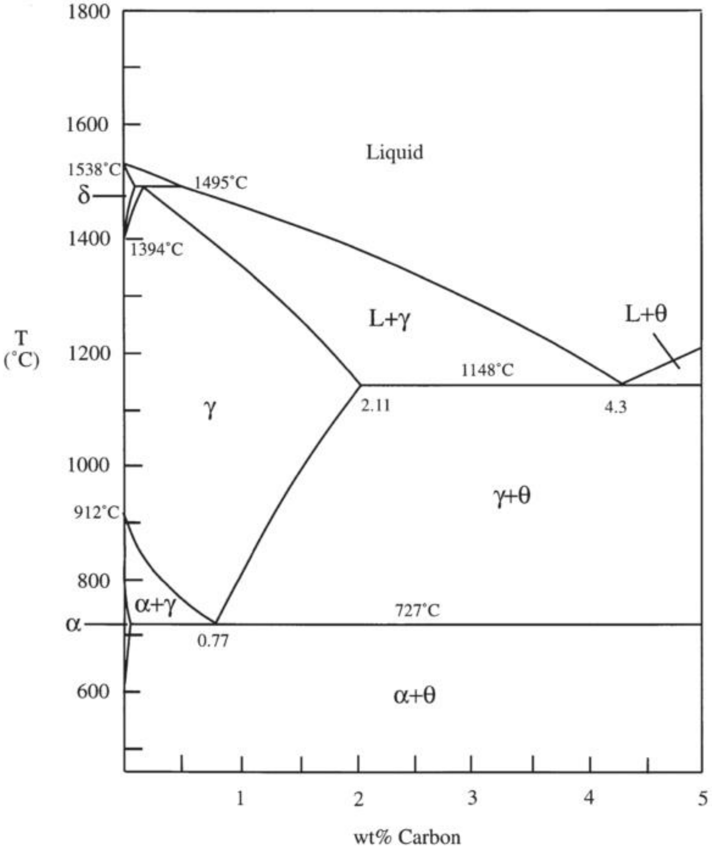

Fig. 3.1: Fe-C phase diagram. [39]

Upon cooling from the high temperature single-phase austenite γ-region, through the eutectoid point (0.77wt% C, 727°C), a two-phase region is reached, as can be seen from the Fe-C phase diagram in Fig. 3.1. As the material wants to form a carbon depleted ferrite (α) and carbon enriched cementite (θ) phase, diffusion of carbon atoms is required. It is this diffusion process which causes lamellae to form in order to reduce the diffusion distance. [39,40] This process of heating the material in the one phase region followed by subsequent cooling is called patenting. The obtained undeformed microstructure will here be referred to as *'as-patented' pearlite*.

During deformation, such as drawing or rolling, the as-patented material undergoes a number of important changes. These will be discussed in the next section, based on literature reports, followed by a closer look at the poorly understood cementite phase. Finally, the strength and strain hardening behaviour of pearlitic steel will be discussed.

3.1 Deformation microstructure

Pearlitic steel can be deformed to very high strains through processes such as wire drawing, cold rolling or swaging. During these processes, the material's microstructure will change significantly. Both the crystallographic texture and the phase morphology (i.e. the shape and orientation of the lamellae) will change. Additionally the dislocation content will increase and result in the emergence of a deformation substructure. These changes will be addressed in this section.

3.1.1 Crystallographic texture

As is the case for all crystalline materials, plastic deformation will cause a rotation of the crystal lattices of the individual grains. It is well known that bcc materials develop a <110>-fibre texture during wire drawing and a rolling texture characterized by the α and γ fibres in orientation space. The same textures will develop in the ferrite phase of a pearlitic steel, although the texture development might be somewhat delayed or altered due to the presence of a second phase [41–44]. Unfortunately, virtually nothing is known about the texture development in the cementite phase. There is one report by Van Acker et al. [26] which seems to suggest that some texture development does take place. However, this has never been confirmed and other authors claim that the cementite phase breaks-up at high strains in very fine, randomly oriented crystallites [45–48], destroying any crystallographic cementite texture which might have developed at smaller strains. This is only possible if the cementite had a random crystallographic texture prior to the breakup or if all the crystallites undergo a random rotation after breakup. In the latter case, an explanation should be found as to why the rotation could be random. [49]

3.1.2 Changing pearlite morphology

Large plastic strains result in the elongation of individual pearlite colonies and force the cementite lamellae to align themselves according to the imposed deformation. In the ideal case, cold rolling will force the lamellae to rotate and position themselves parallel to the rolling plane, while the lamellae themselves remain planar. However, in reality, bending, buckling and fracture of the lamellae will occur. In wire drawing, the lamellae align with the drawing direction, while at the same time curling around this direction [29]. This results in a significant difference between a cold rolled and a cold drawn microstructure.

Zelin [50] suggests that most lamellae will be aligned at a strain of 2 for axi-symmetric deformation and at a strain of 1.5 for plane-strain deformation. This is supported by experimental observations made by Zhang et al. [51], showing that at a drawing strain of 1.5, 97% of the cementite lamellae make an angle of 30° or less with the drawing direction.

The alignment is accompanied by thinning of the lamellae [52]. The distance between the centres of two cementite lamellae, called the interlamellar spacing (ILS), is expected to decrease proportionally with the thickness of the sheet or the diameter of the wire [50]. This would result in an exponentially decreasing ILS with increasing longitudinal strain ε: $ILS\ wire \sim \exp(\varepsilon/2)$ and $ILS\ sheet \sim \exp(\varepsilon)$. However, Langford [53] showed that for sheet material, the ILS reduces at a slower rate than expected: $ILS\ sheet \sim \exp(\varepsilon/2)$. This difference is attributed to inhomogeneous deformation during sheet drawing or rolling (see section 3.1.3).

As the lamellae thin down, they necessarily lengthen in the drawing or rolling direction. In drawn wire, the cementite additionally shortens in sections perpendicular to the wire axis, as a result of fragmentation due to the curling of the lamellae [51]. Also in the longitudinal direction fragmentation of cementite lamellae can occur [52,53]. At this point, it should be remarked that 2-D SEM images have to be treated with care. What looks as break-up in a 2-D section might just be a perforation in the 3-D plane of the lamella, as has been experimentally illustrated by Wang et al. [54].

At even higher strains, the cementite phase starts to dissolve. The amount of carbon in cementite drops below 25 at% and the carbon content in the ferrite phase is increased [45,47,55–57]. Two main mechanisms have been proposed by which this dissolution takes place: a thermodynamic destabilization of the cementite phase through an increase of the surface to volume ratio [47,56], and the mechanical dragging of carbon atoms from cementite to ferrite by the movement of dislocations [58–60]. Which mechanism is most important and whether the C-atoms are homogeneously distributed in ferrite or gather at lattice defects, is yet a matter of debate. Also the strain at which cementite dissolution starts varies considerably amongst reports.

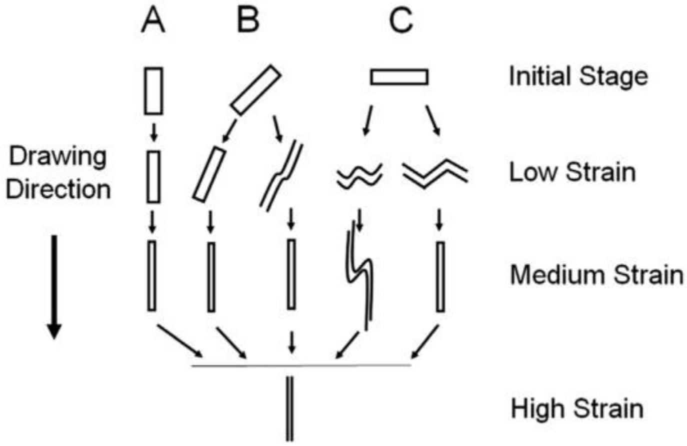

Fig. 3.2: Schematic illustration of six routes for changes in the alignment, morphology and thickness of cementite lamellae, as observed in a section parallel to the wire axis of a cold drawn wire. [64]

The changes in morphology discussed above (thinning, elongation and alignment of the lamellae) occur by a combination of uniform lengthening and localised deformation in the form of shearing or twisting [51]. The exact method of lamellae thinning and alignment depends on the initial lamellae orientation and is best described by the sketch in Fig. 3.2. The fact that the cementite lamellae first have to orient themselves with the macroscopic deformation direction, tends to delay the thinning of the lamellae somewhat, deviating from a pure exponential decrease of the cementite lamellae thickness. This is confirmed by Langford's experiments on oriented pearlite, prepared using a method of forced velocity transformation [61–63]. The observed decrease of the ILS with increasing drawing strain agreed very well with the expected exponential decrease. Additionally, although the spread on the data is significant, Zhang et al. show that the ILS of A type colonies decreases somewhat faster than that of B and C type colonies [64]. At higher strains, thinning of the cementite can be enhanced by the onset of cementite dissolution [65].

Langford's experiments show that not only the initial orientation of the cementite plane with respect to the wire axis is important. Also the orientation of the ferrite slip systems with respect of the cementite plane will influence the amount of thinning a certain lamella can undergo in a given macroscopic strain interval. Soft colonies, with favourably oriented ferrite slip systems will accommodate themselves to neighbouring, hard colonies with short slip distances. The above considerations indicate that pearlite will be a very inhomogeneous material, from the point of view of the local material properties.

As is suggested by Fig. 3.2, while the microstructure at intermediate strains looks very inhomogeneous, it becomes more uniform at high strains, with straight, elongated lamellae throughout the entire material. The same trend has been observed for rolled sheet [66], although literature results do suggest that the microstructure of rolled sheet appears much more inhomogeneous and the cementite more fragmented because of the emergence of shear bands [67]. While the microstructure of heavily drawn wire may look homogeneous, Zhang et al. [64] show that the origin (A, B or C) of the lamellae can still be recognized from the crystallographic misorientations along and across ferrite lamellae. These are negligible for type A regions while high angle grain boundaries (up to 40°) exist between adjacent lamellae for type B and C regions. Also along the length of ferrite lamella, point-to-point misorientation up to 7° can develop in B and C regions.

3.1.3 Emergence of shear bands

The work done by Langford [53] illustrates that shear bands readily develop in sheet material, while they are much less pronounced in drawn wire. The emergence of these shear bands in sheet is coupled to the observation that the ILS reduces at a slower rate than the sheet thickness. Inhomogeneous deformation through shear banding allows the sheet to elongate without proportional reduction of the ILS, as is confirmed by the work of Tagashira et al. [66], showing that the ILS remains larger in colonies that contain shear bands. There are two sets of shear bands, inclined 30-45° to the wire axis [50,53,68]. These shear bands persist with increasing deformation. More may form, but the ones that have formed remain active.

Through a combination of EBSD and SEM work, Zhang et al. [51,69] illustrate that the shear bands observed in cold drawn wire are parallel to {110} and {112} ferrite slip plane traces. This indicates that slip starts in the ferrite phase and is then transferred to cementite lamellae. Tagashira et al. suggest that those colonies which have a higher deformation stress with respect to cold rolling will be the ones that form shear bands, while the softer colonies will deform more uniformly. On the other hand, it has been shown that, during a tensile test, more shear bands develop in colonies with a larger ILS [68]. Zhang et al. [51] also show that shearing becomes more uniform (i.e. more finely spaced bands) as the cementite thickness is reduced. The latter could be linked to the difficulty of forming large dislocation pile-ups in thin lamellae, from which shear bands seem to initiate [70].

3.1.4 Development of a deformation substructure

Gil Sevillano [67] shows that the ILS in pearlite is smaller than the expected cell size of the cellular substructure that would form in single phase ferrite. It is therefore impossible for such a cellular structure to form in the fine ferrite lamellae. Only walls transverse to the interfaces are likely to develop. This is confirmed in an experimental study by Zhang et al. [65].

Zhang et al. investigated a cold drawn pearlite where the ILS decreases from 90 nm ($\varepsilon = 0$) to 20 nm ($\varepsilon = 3.68$) and found that the dislocation density increases from $7.5 \times 10^{13} m^{-2}$ to $2 \times 10^{16} m^{-2}$. A high dislocation density was also observed by Goto et al. [46]. In contrast, Languillaume et al. [47] did not observe a significant dislocation density in wires cold drawn to a strain of 3.5.

A TEM study of Zhang's wires, deformed up to a strain of 2.67, showed that dislocations are evenly distributed along the length of the ferrite lamellae with a spacing of 10-20 nm between the dislocations. The two ends of each dislocation line are located at steps in the ferrite/cementite interface. A similar, homogeneous distribution of dislocations was also observed on a tensile test specimen by Dollar et al. [68]. In a follow-up study, Zhang et al. [64] found low angle boundaries (misorientations of 2-7°) along the length of ferrite lamellae, but only for type B and C lamellae (see Fig. 3.2), although local misorientation of 1-2° are also reported for type A lamellae. Additionally, all studies also found a high density of dislocations at the interfaces, resulting in apparent high angle boundaries (>40°) when travelling across ferrite lamellae. The word 'apparent' is introduced here, because in fact there is also a cementite lamellae in this 'boundary'.

Based on these results, Zhang et al. argue that the formation and storage of dislocations in the ferrite lamellae may be directly related to the amount of reorientation each single pearlite colony has undergone. This will give rise to local difference in the material properties and strengthening mechanisms.

3.2 Cementite

3.2.1 Crystallography

Cementite is a stoichiometric phase containing 75 at% Fe and 25 at% C. The atoms are arranged in a orthorhombic crystal structure of which the details are described in [71]. Because of this crystal structure and its lower symmetry, the choice of the a, b and c lattice parameters has to be clearly indicated! The (122) lattice plane for example is not equivalent to the (212) lattice plane, as is the case for cubic materials. In literature, two conventions can generally be found for cementite: a < b < c or c < a < b. The latter convention seems to be used more often and will be adopted in this work. Many slightly different values for the lattice parameters can be found in literature, see Table 3.1. Unless otherwise mentioned, the values reported by Van Acker et al. will be used here.

Table 3.1: Cementite lattice parameters. In this work the lattice parameters reported by Van Acker et al. will be used.

a [Å]	**b [Å]**	**c [Å]**	**Reference**
5.0816	*6.7446*	*4.5206*	*Van Acker et al.* [26]
5.092	6.741	4.527	Fruchart et al. [72]
5.0896	6.7443	4.5248	Fasiska and Jeffrey [71]
5.0787	6.7297	4.5144	Martinez-Perez et al. [5]

3.2.2 Deformation of cementite

Very little is known about the mechanical properties of cementite. This stems from the fact that cementite is a metastable phase, making it very difficult to produce bulk samples for mechanical testing. Some data on cementite strength and other properties is available from for example the group of Umemoto et al. [73–75], who produced and characterised bulk cementite through powder metallurgical processing. Another route, is to (electro)chemically extract cementite from steel as has been done by for example Webb and Forgeng [76]. However, it has been suggested [32,66] that the embedding ferrite matrix might considerably influence the mechanical behaviour of cementite. And, if we want to come to a better understanding of the deformation behaviour of pearlite, it is exactly this in-situ behaviour of cementite which is of importance.

Hanabusa et al. [9] estimate the yield stress of cementite to be 10 times larger than that of ferrite, which leads them to a value of 2.2 GPa for the cementite yield stress. This agrees with the value of 2.60 GPa, obtained by Umemoto et al. [73] from compression tests on powder-metallurgical bulk cementite. However, Tomota et al. estimated the residual cementite stress in a pearlitic steel wire, based on measurements of the internal ferrite stress and found a stress of 5 GPa, indicating a flow stress of at least 5 GPa. Although it cannot be excluded that defects in the produced bulk cementite reduce its strength, the discrepancy between embedded cementite and bulk cementite might also illustrate the importance of the embedding ferrite matrix.

Many authors have presented indisputable evidence that lamellar cementite can and must deform plastically during wire drawing. Zhang et al. [51,64] determined cementite lamella thickness using TEM and showed that the cementite lamellae in a cold drawn pearlite reduce in thickness from 19 nm to 2 nm at a strain of 3.7. They additionally observed slip steps on cementite and bending to S-shapes without fracture. Tagashira et al. [66] observed bending of cementite lamellae in a cold rolled sheet without fracture, along with extreme thinning without fragmentation in shear bands. Porter et al. [70] observed strong ductility leading to necking of cementite and their TEM study seems to indicate the storage of dislocations in cementite, thus requiring the activation of multiple slip systems. A. Inoue et al. [77,78] also observed some dislocations in thick pearlitic cementite (300-500nm), deformed at room temperature. At higher temperature (400-700°C), pile-ups and the formation of dislocation networks were even observed, along with extreme necking of the cementite phase. This illustrates that at high temperatures cementite can easily deform plastically and exhibits multiple slip.

Langford [53] investigated the literature, up to 1977, for evidence that there is an effect of the cementite lamellae thickness on its tendency to deform plastically. He found that some authors present proof for brittle fracture of coarse cementite while others observed dislocations in equally coarse lamellae. Langford does state that no evidence could be found for extended plastic deformation of cementite lamellae thicker than 100 nm, nor for extensive, brittle fragmentation of cementite lamellae thinner than 10 nm. Additionally, plasticity is mainly observed on drawn or swaged wires, while brittle fracture is mainly observed for tension or compression tests. This indicates the importance of the deformation mode. A large hydrostatic compression component possibly prevents brittle cementite fracture. Furthermore, the current author is not aware of any evidence for room temperature plasticity in a globular microstructure, illustrating the influence of cementite morphology on its plasticity.

Porter et al. [70] illustrate that thinner cementite lamellae and a finer ILS will lead to a more homogeneous deformation in the ferrite phase. In contrary, if the ILS is wide, large pile-ups will develop in the ferrite phase, leading to local stress concentrations which cause shearing of the cementite lamellae (see

Fig. 3.3). Together with the observation of widely spaced (100 nm) slip steps in coarse cementite with corresponding slip lines in ferrite, Porter et al. attribute this shearing to the massive movement of dislocations in the cementite, on a single slip plane, initiated by stresses at the tip of dislocation pile-ups in ferrite. Coarse cementite then undergoes plastic deformation by rigid blocks sliding past each other. However, it is unclear whether this is indeed a plastic phenomenon or brittle shearing of the lamellae. In any case, such shearing will be transferred to the neighbouring lamellae and an avalanche of broken lamellae will be created. On the other hand, a more homogeneous deformation in the ferrite will result in a more homogeneous stress transfer to the cementite phase. A higher homogeneous stress will therefore be reached along the entire length of the cementite lamellae, allowing for homogeneous plastic deformation, resulting in thinning and elongation of the cementite lamellae. The deformation behaviour of cementite thus seems to be linked to dislocation glide in the ferrite phase which has to be transferred to cementite through the interface, an idea which is supported by many other authors [48,51,53,66,68]. Langford [53] then argues that the strength of cementite must come from the high stress required to initiate slip, close to the theoretical stress for nucleating dislocations in a dislocation free solid.

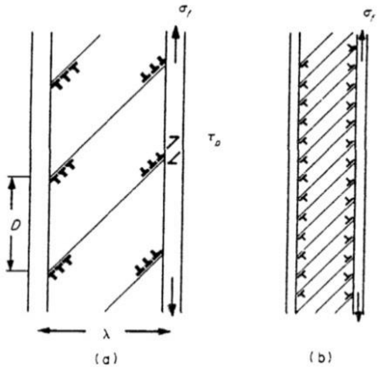

Fig. 3.3: Illustration of the generation of pile-ups in wide ferrite lamellae vs. a more homogeneous deformation in fine lamellae. The former leads to local shearing of the cementite, while the latter results in a homogeneous thinning and elongation of the cementite.[70]

Recent results by Fang et al. [48], provide a completely different view on cementite plasticity. They show that in undeformed pearlite dislocations can fairly easily be transferred from ferrite to cementite because of the coherent structure at the interface. However, because of the difference in crystal structure between ferrite and cementite, it does seem difficult to imagine a completely coherent interface. At strains of around 1.6 cementite develops subgrains, separated by high angle boundaries. As deformation proceeds, the structure of the interface is altered and dislocations can no longer pass into cementite. Deformation of the cementite would then occur through rotation and/or sliding of nano-scale cementite crystallites. Although other authors have also observed the fragmentation of cementite in small crystallites [45–47], more experimental evidence is required before this view on cementite plasticity can unambiguously be adopted.

The dislocation nucleation in cementite can be compared to the case of Cr rods in Cu-Cr structures investigated by Sinclair et al. [10]. They find that the introduction of dislocation in the Cr fibres is limited by the ability of the interfaces to supply/nucleate them. Dislocations can be seen to bow out from one interface, travel across the fibre and be absorbed by the opposite interface. As a result the dislocation density in the Cr fibres remains small. Cr-fibres tested ex-situ exhibit a load drop upon yielding, related to plastic strain localization. This is not the case for in-situ Cr fibres. The constraint imposed by the Cu matrix inhibits large local non-uniform deformation. The embedded Cr-fibres can therefore not propagate a plastic front. Similar mechanisms could also be at work in embedded cementite.

To conclude, a short word on cementite slip systems. As discussed above, many authors observed dislocations in cementite, and efforts have also been undertaken to quantify their slip planes and Burgers vectors [70,77–80]. In summary of that work, the overview given by Gil Sevillano [81] is repeated here in Table 3.2. For the last three Burgers vectors, one of the 1's must have a minus sign in order to have the Burgers vector in the slip plane: D.A. Porter et al. [70], referring to both Gil Sevillano's and older work, suggest the activation of $\langle 1\bar{1}1 \rangle$ Burgers vectors. Furthermore, it has been shown that cementite dislocations can split into partial dislocations [79,80].

Table 3.2: Possible slip systems in cementite [81].

Cementite slip systems			
(010)	[001]	(110)	[001]
	[100]	(011)	[100]
(100)	[001]	(101)	[010]
	[010]	(110)	[111]
(001)	[100]	(011)	[111]
	[010]	(101)	[111]

3.3 Deformation, strength and strain hardening of pearlite

In the ideal case, drawn or rolled pearlite can be considered as a composite with two phases infinitely elongated along the loading direction. The strength of pearlite is then given by a law of mixtures [82]:

$$\sigma_y^{pearl} = (1 - V_\theta)\sigma_y^\alpha + V_\theta\sigma_y^\theta \tag{3.1}$$

α and θ refer to the ferrite and cementite phases, respectively. V_i is the volume fraction of the i^th^ phase and σ_y^i is the yield stress of the i^th^ phase.

However, as stated by Embury and Fisher [52], the rule of mixtures should not be applied here, because of the imperfect and inhomogeneous microstructure of deformed pearlite. Additionally, the strength of multiphase, in-situ composites is heavily underestimated by the rule of mixtures when the strengths of the bulk components are used as input [67]. It is thus clear that other strengthening mechanisms are at work in fine-scale metallic composites as compared to the individual bulk materials.

In bcc and hcp materials, subject to wire drawing, a particular curled microstructure develops as a result of the crystallographic texture, as mentioned in section 3.1.2. The curling of flattened grains along the wire axis requires the storage of an excess of equal sign edge dislocations which are difficult to annihilate through processes of dynamic recovery [67]. This results in a very long stage of linear strain hardening, even in single phase materials [83]. It does not, however, explain why cold rolled pearlite also exhibits significant strain hardening.

Embury and Fisher [52] and Langford [53] attributed the strength of pearlite mainly to the small ILS, assuming that the cementite acts as a barrier to dislocation movement. Langford therefore suggested that the strength of pearlite is primarily controlled by dislocation motion within the ferrite and is proportional to the square root of the ILS. The proportionality constant depends on the strength of the cementite, as pile-ups in ferrite must generate sufficient stress to propagate slip through the cementite.

The result is a Hall-Petch type of hardening relationship in which the strength is proportional to $\mathrm{ILS}^{-1/2}$. However, it has also been proposed that a proportionality with ILS^{-1} should be adopted [68]. The ILS is in turn proportional to the wire diameter d:

$$d = d_0 \exp(-\varepsilon/2) \tag{3.2}$$

Combining this with the $\mathrm{ILS}^{-1/2}$ proportionality leads to an exponential strain hardening of cold drawn wire:

$$\sigma_y = \sigma_0 + k_1 \exp(\varepsilon/4) \tag{3.3}$$

Although the thickness of sheet reduces proportionally to exp(-ε), a similar strain dependence of the strength of cold rolled sheet can be expected, as shown by Langford [53]. The reason is, that the ILS in sheet reduces at a slower rate than the thickness, as has been discussed in section 3.1.2.

While the exponential strain hardening rule captures experimental data quite well, it is not entirely clear what the microstructural mechanisms are behind the increase of strength with a decrease of the ILS. Furthermore, plotting the tensile strength as a function of exp(ε/4) shows a deviation from this rule, especially at high strains [65]. Therefore, other strengthening mechanisms, next to a simple Hall-Petch like barrier effect of cementite must be considered.

Application of a Hall-Petch type relationship for boundary strengthening (such as eq. 3.3) is based on the assumption that dislocation pile-ups can exist within a single ferrite lamella. Such pile-ups were indeed observed in samples with a relatively large ILS [68] and Zhang et al. [65] illustrate that pile-ups of about 10 dislocations can exist even in lamellae with a spacing of around 20 nm. Only when the ILS drops below 10-15 nm it would be impossible for pile-ups to exist. Embury [84] likewise suggests that, as the ILS drops below a certain threshold, the existence of pile-ups becomes questionable: "Fine scale plasticity may not occur by groups of dislocations moving on slip planes separated by distances of the order of a micro meter, but instead by single dislocations moving on closely spaced glide planes from one boundary to the next." This would also explain the reduced amount of sheared-off cementite in samples with a small ILS, as has been discussed in section 3.2.2, Fig. 3.3.

As the ILS becomes small enough, the strength is instead governed by the shear stress necessary to push a dislocation loop through the confined space between the two interfaces or by the stress required to activate dislocation sources [67,82]. In the former scenario, the strengthening would be of an Orowan type. In combination with the reduction of the ILS this also results in an exponential hardening. Gil Sevillano further predicts that dislocation storage will be limited within the confines of a single lamella [67]. Bowing out of dislocations could then be considered as the main mechanism for dislocation movement. However, Gil Sevillano's mathematical model for strain hardening, in the same paper, shows that it is not the movement of dislocations which is responsible for the strain hardening, but the difficult multiplication of dislocations through dislocation mills (in the absence of interfacial dislocation sources). This is in contrast to an earlier paper by Dollar et al. [68] in which they suggest that strain hardening is controlled by the movement of dislocations through the ferrite channels, while dislocations are easily generated at the interfaces due to misfit stresses. It is then rather the increased dislocation density in the ferrite lamellae which results in strain hardening.

In another paper, Gil Sevillano [85] suggested that, at small strains, strain hardening is controlled by the movement of dislocation loops which are easily nucleated at soft interface-sources. Strain hardening then results from the larger Orowan stress needed to move the dislocation as the ILS decreases. Once the soft interface-sources are depleted, it is the generation of dislocations in the 'bulk' of the lamellae that controls the hardening. The mechanism of pure Orowan-strengthening in the first stage suggested by Gil Sevillano is however contradicted by the observation of high stored dislocation densities in heavily deformed pearlite [46,65]. These dislocations will constitute a barrier to the movement of the dislocation loops, suggesting that hardening due to an increased dislocation density will be non-negligible at medium to high strains.

The observation by Zhang et al. [65] of homogeneously distributed dislocations throughout the length of ferrite lamellae, further does not agree well with the mechanisms of moving dislocation loops suggested by other authors. In the latter case, dislocations are mainly stored at the interfaces, and do not explain the relatively straight dislocation sections with one end on each opposing interface. The observation of the latter kind of dislocation segments, raises the question as to whether these segments could also move, parallel to the interface. Such a mechanism has indeed been proposed by Janecek et al. [86].

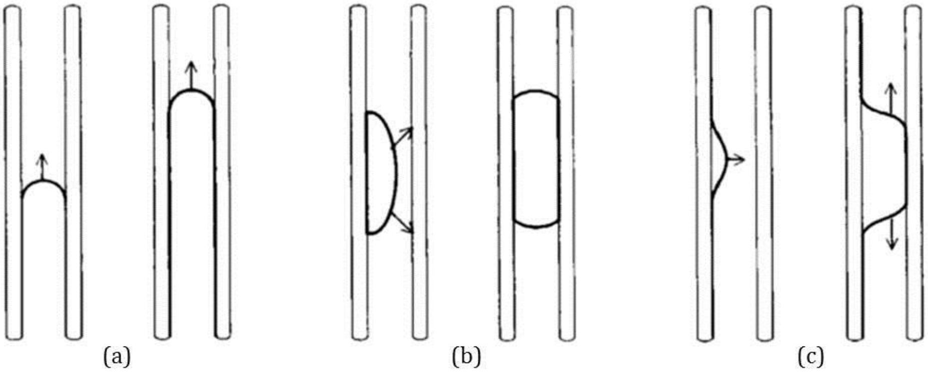

Fig. 3.4: (a) Movement of a hairpin dislocation through a fine ferrite channel. The shear stress required for movement is determined by the radius of the leading dislocation section according to the Orowan equation. (b) Generation of a dislocation loop by bulging from the interface. (c) Generation of a Z-shaped dislocation by bulging from the interface. [86]

Janecek et al. observed dislocation nucleation in a pearlitic steel TEM foil deformed at 350°C and found that dislocations can be generated by bulging from the interface. This can then either result in a dislocation loop which can expand based on the previously proposed Orowan mechanism, or in the generation of two z-shaped dislocation segments which can more easily move along the length of the ferrite channel without increasing of the dislocation line length. (Fig. 3.4) However, according to Janecek et al., these bulging sources are only expected to become active at ferrite channels thinner than 10 nm. Their calculation further illustrates that hairpin-shaped 'Orowan' dislocations can no longer move at very small ILS. In that case, strain can only result from the generation of new dislocations, traversing the lamella and moving into the opposite interface.

Using atomistic simulations, Zhang et al. [87] show that dislocations can indeed be nucleated from interfaces (in this case fcc-bcc). However, the structure of the interface is crucial in determining which dislocations are nucleated and how much energy is required. This illustrates the importance of the interface structure, which will change as a result of increasing strain. Fang et al. [48] indeed showed that the interface between cementite and ferrite loses its coherency with increasing strain. The change of the interface structure can be a result of individual rotations of the ferrite and cementite crystal lattices, or be caused by processes of dislocation nucleation and annihilation at the interfaces. Even if dislocations pass from ferrite into cementite, misfit dislocations will remain at the interface because of the different Burgers vectors in ferrite and cementite, thereby changing the interface structure. This evolution of the interface structure will then also have an influence on strain hardening, through an influence on nucleation processes at the interface.

In summary of the above, the following qualitative view on the development of plasticity and strain hardening in a lamellar material such as pearlite is proposed: *At small deformations and large ILS*, ferrite still behaves more or less as a bulk material. Pile-ups can develop and a 'normal' Hall-Petch type of hardening can develop, with the cementite lamellae providing the barriers to dislocation movement. Dislocations might at this stage be produced by intra-lamellar sources such as the dislocation-mill proposed by Gil Sevillano. *At intermediate ILS*, dislocations start to move as hairpins in the ferrite channels. Dislocation nucleation through dislocation-mills becomes more difficult and is being replaced by interfacial dislocation generation. Up to this point, strain hardening is probably controlled by the stress required to move dislocations, under the assumption that there are still enough 'soft dislocation sources' active. *At small ILS*, the movement of hairpin dislocations becomes impossible and is replaced by the Z-shaped dislocations as described by Janecek. The dislocation configurations observed by Zhang et al., consisting of dislocation segments with one end on each of two opposing interfaces, can then be explained as the two 'ends' of hairpins that were trapped or the transverse sections of the Z-shaped dislocations. As the ILS is reduced further, movement of dislocations is further impeded. Deformation will now mainly be achieved by the nucleation of new dislocations, which traverse the lamella and are deposited at or absorbed in the opposing interface. At this point, strain hardening is controlled by the stress required to nucleate dislocations from interfaces and thus, by the structure of the interfaces.

The above discussion dealt with dislocation nucleation, dislocation glide and boundary strengthening due to the presence of the cementite phase, as well as their effect on strain hardening. Hereafter, a few other possible strain hardening mechanisms will be introduced. Additional hardening can result due to an increase of the carbon content in ferrite caused by cementite dissolution (solid solution strengthening) [46,50,65]. Dynamic strain ageing can be facilitated by the adiabatic heating up to 150-250°C during wire drawing [50]. Zhang et al. [65] found that solid solution strengthening only becomes important at strains above 3, suggesting that at smaller strains carbon enrichment in the ferrite phase is limited.

The development of a system of internal stresses can also result in additional strain hardening. If it is assumed that, during a tensile test, cementite does not deform plastically, then the pearlite flow stress is determined by the flow stress of the ferrite phase. The internal stress in the ferrite phase counteracts the applied load and a higher external load will be required to sustain plastic flow in the ferrite phase.

The effect of internal stress is akin to a load transfer to the cementite phase, resulting in what has also been termed fibre loading of the cementite lamellae. As a portion of the external load is carried by the cementite phase, less load is imposed on the ferrite phase and a higher external load will be required to initiate ferrite yielding and thus yielding of the composite. The load transfer will be more pronounced for well aligned, continuous lamellae. Rotation of the lamellae towards the loading direction will therefore also constitute a contribution to the strain hardening.

On the other hand, any processes that result in a reduction of the cementite load bearing capacity will cause a strain softening of the pearlite. Examples are fragmentation of the cementite along the loading direction, but also cementite decomposition. The latter process can however also result in a global strengthening due to solid solution hardening as has been stated above.

Finally, it should be mentioned that Dollar et al. [68] illustrated that the work hardening rate is independent of the ILS.

To come to one single strain hardening rate, the contributions from all possible mechanisms need to be combined. Zhang et al. [65] illustrate that a linear addition can give good results. However, it is not unreasonable to suggest that not all contributions will be independent. A complete, realistic description of strain hardening will thus require very sophisticated models.

So far, this text has focused almost solely on the strain hardening of the ferrite phase. However, also the cementite should be considered. If the cementite strain hardens, its load bearing capacity and the development of the internal stresses will be influenced, as will be shown in this work. Unfortunately, very little is known about the cementite phase. It has been suggested [53,67] that, due to the cementite lamellae being very thin, a dislocation density based strain hardening is very unlikely. A lattice-friction controlled strength or Whisker type strengthening, in which dislocations aren't stored, but pass through the lamellae to disappear in the opposing boundary, is thus more appropriate. However, Porter et al. [70] did observe possible signs of dislocation storage in cementite. Cementite strain hardening can also be compared to that proposed for Cr-whiskers in the work by Sinclair et al. [11]. Because of the lack of dislocation storage, the Cr-fibres will not strain harden due to an increased dislocation density, but due to the continued accumulation of plastic misfit. As dislocations are either transmitted across the interface or absorbed and re-emitted, there will be a residual Burgers vector, giving rise to an unbalanced plastic strain in the two phases. This has to be accommodated by an additional elastic strain, which will increase linearly with applied strain as long as the misfit per arriving Cu Burgers vector remains constant. The result is a constant work hardening rate of the fibre. It is clear that future experimental and/or modelling work will be required to provide an answer to the question of cementite strain hardening.

To conclude, a word on the failure of pearlite: Based on internal stress measurement in a spheroidite steel (34 vol% Fe_3C), Young et al. [20] state that, because the ferrite lattice strains only slightly increase up to sample failure, once the ferrite phase becomes plastic, failure depends on the maximum load the cementite phase can bear. The initiation of macroscopic failure as a result of shearing and fracture of cementite lamellae is supported by several other authors [68,70]: Samples with a smaller ILS exhibit less shear bands and less cementite fractures during a tensile test, which results in a higher observed ductility. Porter et al. [70] suggest that a smaller ILS would also lead to more crack branching and more extensive plastic deformation ahead of the crack. Porter et al. further indicate that colony boundaries act as barriers to shear band propagation. This is supported by experimental evidence for increased ductility as a result of smaller colony sizes [88].

3.4 Conclusions

Literature results show that with increasing strain, the dislocation density in the ferrite phase increases. All authors agree that a large amount of dislocations is stored at the interfaces, but there is less agreement on the dislocation substructure itself. The deformation of the cementite phase has been discussed and it has been shown that cementite can deform plastically. Plasticity is facilitated in thin lamellae subjected to a deformation that has a hydrostatic compression component. Most authors agree that slip is initiated in the ferrite phase and subsequently transferred to the cementite. This illustrates the important role of the interfaces and suggests that ferrite controls the pearlite strain hardening. It is the dislocation movement in ferrite that, through the interface, controls dislocation nucleation and plasticity of the cementite phase.

It is important to realise that the strain hardening of pearlite and thus the emergence of its magnificent properties is a very complex issue. There are many parameters and microstructural features that play a role. And, although the heavily deformed microstructure seems relatively homogeneous on the micrometre length scale, the local material properties can still vary considerably. These local variations may, at least partly, find their origin in the inhomogeneity of the initially randomly oriented pearlite.

Pearlite strain hardening is mainly controlled by the ferrite phase. Many possible mechanisms have been proposed: solid solution hardening, boundary strengthening, dislocation strengthening, cementite fibre loading, kinematic hardening due to internal stresses and increased difficulty of dislocation nucleation. Which of these are more important and how to combine the different contributions into one theory is the subject of ongoing and future research.

Although there are many similarities between drawn wire and rolled sheet, it has been shown that they develop a different crystallographic texture and phase morphology. Only the wire develops the typical curled lamellae, while shear banding is more pronounced in sheet. This leads to a more heterogeneous microstructure after rolling. Reducing the ILS can counteract this to some extend by resulting in a more homogeneous dislocation motion and less shear banding.

4 Material choice and sample preparation

In this chapter, the various samples used throughout this research project will be introduced. Before doing so, it should be remarked that the experiments performed by the current author mainly involved laboratory rolled pearlitic steel sheet. However, reference will also be made to experiments performed on cold drawn wire which were part of the Ph.D. work of M. Kriška, but to which the current author contributed significantly. The most important information on the wire material can be found in section 4.5.1, while more comprehensive information can be found in M. Kriška's thesis or in the published experimental reports. In the current chapter, unless otherwise mentioned, the cold rolled sheet and its preparation will be described.

4.1 Material choice: shape and chemical composition

As has been mentioned before, internal and residual stresses develop in all multiphase materials subject to plastic deformation. As a case study the current work focusses on pearlitic steel because of its industrial relevance and the scientific challenge that it represents. The latter is especially true when considering the hard cementite phase, of which even the elastic constants have not yet been determined unambiguously.

Secondly, although most applications of pearlitic steel are based on cold drawn wire, here cold rolling will be applied. This has a number of practical benefits: The rolling can be performed within university, and the samples are larger, making them easier to handle and measure. There is also a scientific argument involved in the choice for sheet material: Good residual stress data on cold drawn wire are already available through the work of M. Kriška. The comparison of results obtained for wire and sheet could yield additional information as to which extent residual lattice strain and stress development depend on the deformation mode.

As for chemical composition, a material was chosen that is readily available from industrial suppliers. The material had to be of eutectoid composition with as little additions as possible to avoid the formation of carbides other than cementite or any other inclusions. The plain carbon steel, specified as AISI 1075/C75, was eventually used. The chemical composition is specified in Table 4.1. This material contains ~12vol% cementite.

Table 4.1: Chemical composition for the AISI1075/C75 steel used in this investigation.

C	**Mn**	**Si**	**P**	**S**
0.76 wt%	0.65 wt%	0.21 wt%	≤ 0.04 wt%	0.016 wt%

4.2 Phase transformation and interlamellar spacing

The as-received material is hot-rolled and has a globular cementite morphology. In order to obtain the required lamellar morphology, the material has to be reheated in the austenite single phase region, followed by cooling through the eutectoid point. The resulting interlamellar spacing (ILS) mainly depends on the velocity of the transformation front [39,40] and thus on the cooling rate. However, the work by Elwazri et al. [88] also indicates that a larger prior austenite grain size results in a larger ILS. In this work the prior austenite grain size has been fixed by fixing the austenitization temperature and time. The ILS can then be changed by changing the transformation velocity.

Two methods of transformation could be applied: continuous cooling and isothermal transformation. While the former method is easy to perform, the cooling and thus transformation speed was impossible to control. Additionally, it resulted in severe oxidation due to high temperature contact with the atmosphere. Isothermal transformation in a bath with molten salt was therefore used for sample preparation.

Durferrit® GS430 and GS540 salts were used to be able to cover a range of temperatures from 500°C up to the transformation temperature. Inerter (R2) was added to prevent decarburization and oxidation. During austenitization decarburization and oxidation were prevented by heating in a tubular furnace under argon atmosphere. The furnace was suspended on rails and could be positioned above the salt bath, allowing a quick transfer of the sample by opening the bottom of the furnace and dropping the sample in the bath below.

Austenitization was performed by heating the samples to 825°C for two hours. Three transformation temperatures were chosen within the interval allowed by the available salts: 500°C, 600°C and 680°C. It should be remarked that these temperatures are approximate, as local variations in the salt bath temperature up to 20 degrees were measured. The samples were kept in the salt bath for 15 min to allow complete transformation, before water quenching to room temperature. The measured ILS as a function of transformation temperature can be found in Table 4.2, along with the name used to designate the samples series obtained after cold rolling. Any thermal stresses that remained in the sample were removed by a short heat treatment of 10-15min. at 450°C. Finally, any oxides that did form were removed prior to rolling, by applying a 25 vol% phosphoric acid solution followed by thorough rinsing.

Table 4.2: Used transformation temperatures and resulting interlamellar spacings (ILS). In the last column, the name used to designate the three samples series is given.

Trans. temp.	ILS [nm]	Sample series
500°C	140	P500
600°C	220	P600
680°C	350	P680

4.3 Cold rolling

Cold rolling has been performed on a laboratory mill at UGent. Obtaining straight, flat samples with a good surface finish is, as the operator liked to put it, ‘more of an art than exact science’. Lubrication is applied by dipping the samples in oil. The roll spacing is adapted manually, but could be controlled relatively well to within a range of ~10µm. Still, it was not possible to a priori specify the thickness reduction required on each rolling pass. This is caused by spring back of the sample, strain hardening, compliance of the rolling mill, slight vertical movements of the rolls and in general a lack of experience as is only available in the case of industrial scale processes. Instead, it was decided to simply reduce the roll spacing by 100µm after each rolling pass.

The starting material had a thickness of 3mm and a width of 20mm. It was possible to reduce the thickness down to ~1mm by reducing the roll spacing in steps of 100µm. After that smaller steps were used, based on the experience of the operator. To obtain the final thicknesses of 0.4 and 0.3mm, the rolls were brought within touching distance and the samples passed two or three times through the rolls.

The strips were always passed to the rolls with the same end first in order to not change the strain path. However, the samples were turned upside-down between every pass, i.e. top surface became bottom surface. This was required in order to minimize bending of the strips. During rolling, the strips heated up to some extent. The temperature was not measured, but was likely between 50-80°C: It was possible to lightly touch the samples in order to move them, but it was not possible to firmly grasp them.

At various strains, samples were retained for later analysis. An overview of the rolled samples, their designations, thicknesses and strains, will be given in section 4.5.2.

4.4 Final sample preparation

After cold rolling, the samples were investigated by means of scanning electron microscopy and X-ray and neutron diffraction techniques. Standard specimen preparation was used for all microscopy investigations. The samples were cut, imbedded in resin, ground and polished. Grinding paper with the following grit sizes were used: 320, 800, 1200 and 4000. Special care was taken to remove enough material so that there could be no effect from the sample cutting. The final polishing steps were performed with 3 μm diamond paste and 0.25μm silicon oxide particles (OPS). No electro polishing was applied. The microstructure was revealed through light etching in a 2% Nital solution (2 vol% HNO_3 in ethanol).

It has been pointed out by Wilson and Konnan [18] and by V.M. Hauk et al. [89] that grinding introduces additional residual stresses into the material's surface layer. Therefore, no grinding and/or polishing operations were performed before measuring the residual strains or stresses. For laboratory X-ray diffraction measurements, this could result in a slight decrease in intensity due to a thin oxide layer. Additionally, due to the low penetration depth of these X-rays, a thin, heavily deformed surface layer might significantly influence the results. In the case of neutron diffraction measurements no significant influence is expected because of the small volume fraction of the surface layer.

Finally, it should be mentioned that the rolled strips were too long to fit into the laboratory diffractometer. It was therefore required to cut the samples in shorter sections (~4-7cm). Stress and strain measurements were always performed well away from the cutting edges. Additionally, a number of samples were measured before and after cutting and it was shown that due to the still large length over thickness ratio, the residual stresses and strains were not altered.

4.5 Sample overview

4.5.1 Cold drawn wire

The cold drawn pearlitic steel wire investigated in the work of M. Kriška, and re-evaluated in the framework of the current research project, have the chemical composition shown in Table 4.3. The ILS of the undeformed sample is about 180nm. The cementite phase takes up about 16vol% of the material. The as-patented wire had a thickness of 890μm and a thin brass coating of about 1.1μm thickness. The steel wire has been cold drawn to various strains, up to a true drawing strain of 4 (D = 120μm). The true drawing strain is defined as:

$$\varepsilon = \ln\left(\frac{{D_0}^2}{{D_1}^2}\right) \tag{4.1}$$

in which D_0 is the wire diameter before drawing and D_1 after drawing.

Table 4.3: Chemical composition of the cold drawn wire (wt%).

C *equivalent*	**Mn**	**Si**	**P**	**S**
0.815-0.94	0.30-0.42	0.18-0.25	≤ 0.012	≤ 0.010

4.5.2 Cold rolled sheet

The cold rolled strips have a starting thickness of 3mm and were cold rolled to thicknesses on the order of 0.3-0.4mm. The true rolling strain is defined as:

$$\varepsilon = \ln\left(\frac{t_0}{t_1}\right) \tag{4.2}$$

in which t_0 is the strip thickness before rolling and t_1 after rolling. The thicknesses, strains and reductions for all cold rolled samples can be found in Table 4.4. The sample names, used to designate the various samples are also given. It should be noted that the number following the 'S' has nothing to do with the amount of rolling passes. It is just the number of the sample.

In order to facilitate interpretation of the in-situ neutron diffraction results which are described in section 6.3, and to compare the experimental results with the model developed in chapter 7, a sample with a sandwich microstructure is desired. Such a sample should, in the ideal case, have perfect, planar lamellae which are all aligned with the rolling plane. Additionally, the sample should still be sufficiently thick to have enough diffraction volume and thus diffracted neutron intensity. The first criterion can of course never be achieved with a 'real' material. However, based on microstructural investigations, it seems that a good compromise between the first and second criterion is achieved at a rolling strain of about 1. This sample, from the P500 series, will therefore be used for in-situ testing and is highlighted in the table below.

Table 4.4: Overview of all the cold rolled samples. The highlighted P500S12 sample is the cold rolled sample used for in-situ neutron diffraction measurements.

Sample name	**Thickness [mm]**	**Reduction [%]**	**True strain [-]**
P500 sample series			
P500S0	3.000	-	-
P500S1	2.903	3.22	0.03
P500S2	2.821	5.96	0.06
P500S3	2.705	9.82	0.10
P500S4	2.589	13.69	0.15
P500S5	2.518	16.06	0.18

Sample name	Thickness [mm]	Reduction [%]	True strain [-]
P500S6	2.389	20.38	0.23
P500S7	2.279	24.02	0.27
P500S8	2.061	31.30	0.38
P500S9	1.729	42.36	0.55
P500S10	1.392	53.61	0.77
P500S11	1.196	60.13	0.92
P500S12	***1.026***	***65.80***	***1.07***
P500S13	0.711	76.29	1.44
P500S14	0.589	80.38	1.63
P500S15	0.519	82.71	1.75
P500S16	0.429	85.71	1.95
P500S17	0.379	87.37	2.07
P600 sample series			
P600S0	3.000	-	-
P600S1	2.877	4.11	0.04
P600S2	2.808	6.40	0.07
P600S3	2.690	10.32	0.11
P600S4	2.593	13.57	0.15
P600S5	2.491	16.97	0.19
P600S6	2.401	19.97	0.22
P600S7	2.330	22.32	0.25
P600S8	2.197	26.78	0.31
P600S9	2.076	30.81	0.37
P600S10	1.733	42.22	0.55
P600S11	1.381	53.98	0.78
P600S12	1.225	59.16	0.90
P600S13	0.981	67.31	1.12
P600S14	0.710	76.34	1.44
P600S15	0.600	80.00	1.61
P600S16	0.513	82.90	1.77
P600S17	0.413	86.24	1.98
P600S18	0.363	87.91	2.11
P680 sample series			
P680S0	3.000	-	-
P680S1	2.910	3.01	0.03
P680S2	2.819	6.02	0.06

Sample name	Thickness [mm]	Reduction [%]	True strain [-]
P680S3	2.669	11.02	0.12
P680S4	2.364	21.20	0.24
P680S5	2.080	30.66	0.37
P680S6	1.757	41.44	0.54
P680S7	1.337	55.44	0.81
P680S8	1.190	60.33	0.92
P680S9	1.002	66.60	1.10
P680S10	0.711	76.29	1.44
P680S11	0.608	79.73	1.60
P680S12	0.493	83.56	1.81
P680S13	0.414	86.19	1.98
P680S14	0.344	88.53	2.17

5 Experimental techniques

5.1 Microstructural observations

All microstructural observations were performed using standard techniques. Because of the scale of the microstructure, scanning electron microscopy was required. Next to a study of the cementite morphology, the interlamellar spacing was also determined. In this study, all interlamellar spacings (ILS) are apparent interlamellar spacings [90]. A line is drawn perpendicular to the cementite lamellae observed in the micrograph. The spacing is determined by dividing the length of the line by the number of lamellae crossing it. The spacing is called 'apparent' because it is determined on a random polishing plane intersecting the lamellae. The spacing is therefore not truly perpendicular to the plane of the lamellae.

The ILS was always determined on a sample cross-section perpendicular to the rolling direction. With increasing rolling strain the lamellae align themselves towards the rolling plane. The measured interlamellar spacing should therefore approach the true ILS at high rolling strains.

Observations of the local orientation distributions were also performed using electron backscatter diffraction (EBSD). This was done using step sizes varying from 100 to 10nm, depending on the scale of the microstructure. The best results were obtained under low vacuum conditions, at 20kV and relatively small spot sizes (spot 5). The aperture opening had a 30 μm diameter. Under these conditions, reasonable results were obtained even on deformed samples. Only the ferrite phase has been indexed.

5.2 Residual and internal stress and strain determination

5.2.1 Diffraction techniques

There are various techniques available for the determination of residual stresses. Mechanical techniques such as hole-drilling only provide information on the macroscopic residual stresses. To obtain phase specific information, diffraction techniques should be applied. Diffraction techniques based on X-ray or neutron diffraction return the lattice spacing of a certain <hkl>-grain family.

The term 'grain family' is defined by Oliver et al. as: 'The subset of grains which contribute to a particular diffraction reflection along a certain scattering direction." The <hkl>-RD grain family comprises all grains in which an <hkl> plane normal lies parallel or within a few degrees of the rolling direction. Similarly, the TD and ND grain families are defined as all grains in which an <hkl> plane normal lies parallel to the transverse and normal directions, respectively. These different <hkl>-grain families all comprise a different subset of grains.

From the obtained lattice plane spacing, the lattice strain can be calculated using the following equation:

$$\varepsilon^{hkl} = ln\left(\frac{d_{hkl}}{d_0}\right) \tag{5.1}$$

The above definition of a grain family shows that the lattice spacing, and therefore also the calculated strain, will be an average value. The stress can then be calculated from the strain based on a number of simplifying assumptions, as described in section 5.2.2. It follows that diffraction techniques are an indirect way to measure residual stresses, based on the experimental observation of lattice plane spacing.

The measured value for d_{hkl} can be the result of a combination of different types of stresses (section 2.1). Which types of stresses contribute depends on the diffracting volume and thus penetration depth of the used radiation. If the entire sample is penetrated, the contribution of the macroscopic stress profile will average out to zero and only the micro-phase stresses will influence the value of d_{hkl}. This is the case for neutrons, which have a penetration depth of several centimetres in steel. It should be mentioned that the macroscopic stress profile will only average out if the material under consideration is homogeneous throughout its cross section, or if inhomogeneities such as texture or microstructure gradients are symmetric with respect to the material cross section. In the case of both cold rolling and drawing the latter criterion is likely to be fulfilled. Therefore, in the following it is assumed that the macroscopic stress profile does indeed average out.

Laboratory X-rays on the other hand only penetrate a few micrometres into the sample. The value of d_{hkl} will thus be the result of a superposition of both macro and micro stresses. Synchrotron X-rays have a penetration depth somewhere between that of neutrons and laboratory X-rays. Which types of stresses contribute to d_{hkl} will then depend on the size of the sample.

For that reason, neutron diffraction was utilized to measure the residual lattice strains in the cold rolled sheets. As the main focus here is on the micro-phase strains, full penetration of the sample is required, which was for the sheets only possible using neutron diffraction. The pearlitic steel wires previously measured in the framework of M. Kriška's Ph.D. were much thinner and the use of synchrotron X-rays resulted in complete wire penetration for those wires thinner than 600 μm.

The total stress, i.e. sum of macro and micro stresses, can be obtained at the sample surface by applying laboratory X-ray diffraction. Combining this with the micro-phase stress obtained with neutron or synchrotron radiation allows to separate the two contributions to the total surface stress based on the following set of equations [36]:

$$\sigma_{ij}^{t,\alpha} = \sigma_{ij}^{M} + \sigma_{ij}^{\mu,\alpha} \tag{5.2}$$

$$\sigma_{ij}^{t,\beta} = \sigma_{ij}^{M} + \sigma_{ij}^{\mu,\beta} \tag{5.3}$$

The superscripts t, M and μ indicate the total, macro and micro stresses, respectively. The superscripts α and β refer to two different phases. It should be noted that this procedure can only be applied for an average micro-phase stress, i.e. after averaging out intergranular stress differences. It is also worth mentioning that, in this approach, the macro residual stresses are assumed to be the same in all phases.

5.2.2 Calculating stress from measured strain

5.2.2.1 d-$\sin^2\psi$ method

The d-$\sin^2\psi$ method is a well-established techniques to obtain residual or internal stresses. The technique has the advantage that the unstrained lattice plane spacing d_0 is not required a-priori and that it allows for the calculation of the full stress tensor.

The general idea behind the method is to measure lattice plane spacings for a number of directions L_3. These directions can be described relative to the sample reference frame using the angles ψ and ϕ as defined in Fig. 5.1. In order to be able to calculate the full stress tensor, three angles of ϕ are chosen (ex. 0°, 45° and 90°) and for each of these angles, the lattice plane spacing d is measured at a series of ψ angles. In the absence of shear stresses and texture, plotting d as a function of $\sin^2\psi$ for a certain ϕ angle yields a straight line from which the residual stress in the in plane direction defined by ϕ can be obtained.

This technique has been described in great detail numerous times. For a comprehensive description of the technique and the accompanying mathematics, the reader is referred to the book by Noyan and Cohen [91]. The presence of a strong texture can greatly complicate the application of the d-$\sin^2\psi$ method. More information regarding this issue can be found in the paper by Van Houtte and De Buyser [92].

In the current work, the d-$\sin^2\psi$ method has been used to obtain the residual stresses at the surface of a series of cold rolled pearlitic steel plates, using laboratory X-ray diffraction available at MTM. The residual stresses reported for pearlitic steel wire, which were measured using synchrotron radiation at HZB, Berlin, were also calculated using this method.

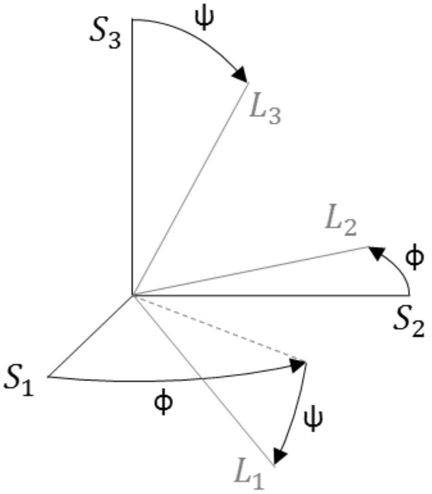

Fig. 5.1: Illustration of the sample (S_i) and lattice (L_i) reference frames. Definition of the ψ and ϕ angles used in the description of the d-sin²ψ method [91].

5.2.2.2 Principal directions method

The above mentioned d-$\sin^2\psi$ method requires the measurement of a large number of diffraction profiles. When long measuring times are needed, or a large number of samples have to be measured, it is not always feasible to measure a multitude of diffraction profiles for each sample. In that case, the lattice strain can be measured in the three principal sample directions. For cold rolled steel plate the principal direction are assumed to be the rolling direction (RD), the transverse direction (TD) and the normal direction (ND). This is a simplification, and means that shear strains are neglected or assumed to average out over the diffracting volume. However, upon full penetration of the sample, as is obtained by neutron diffraction, it is reasonable to assume that the volume averaged strain, calculated from the diffraction peak positions, indeed has its principal axes aligned with RD, TD and ND. From the measured principal strains, the stresses can be calculated using Hooke's law in which diffraction elastic constants are used.

In the following, the calculation of the diffraction elastic constants will be elaborated, after which the procedure to calculate the stresses from the measured strains will be explained.

As has been mentioned above, the measured lattice strains are average values obtained from all grains belonging to a certain grain family. However, all these grains have a different crystal orientation and their stiffness and compliance tensors expressed in the sample reference frame will all be different. To calculate the average stress from the average strain, average elastic constants have to be calculated. These will be called diffraction elastic constants (DEC's).

In the following, the matrix notation for stresses, strains and elastic constants will be adopted. The 3x3 stress and strain tensors are thus converted into a vector with 6 elements and the compliance and stiffness tensors into 6x6 matrices. The indices p and q used in the matrix notation therefore range from 1 to 6. The correspondence to the tensor indices is as follows: 1-11; 2-22; 3-33; 4-23,32; 5-13,31; 6-12,21.

To greatly simplify the calculation of these DEC's, the stress can be assumed to be equal in all crystals belonging to one grain family (Reuss assumption), or the strain can be assumed to be equal (Voigt assumption). The average stress in a certain grain family can be written as

$$\overline{\sigma_p} = \sum_i \sigma_p^i V^i \tag{5.4}$$

in which V^i is the volume fraction of grains with a certain orientation, and σ_p^i describes the stress in these grains. Under the assumption of a constant strain (Voigt) this can be rewritten as

$$\overline{\sigma_p} = \left(\sum_i C_{pq}^i V^i\right) \varepsilon_q \tag{5.5}$$

The average stiffness tensor according to Voigt can now be seen to be

$$\overline{C_{pq}^V} = \sum_i C_{pq}^i V^i \tag{5.6}$$

The volume fraction of grains dV that lie in an interval dg around an orientation g is described by the orientation distribution function f(g). Equation (5.6) can now be written in integral form as

$$\overline{C_{pq}^V} = \int C_{pq}(g) f(g) dg \tag{5.7}$$

This corresponds to equation (22) in the paper by P. Van Houtte and L. De Buyser [92]. Here we are only interested in the average stiffness tensor for a given <hkl>-grain family. Because all grains in this family have their {hkl}-plane normal parallel to the diffraction vector, equation (5.7) can be written as an integration over all grains which are obtained by rotating around this normal direction.

$$\overline{C_{pq}^{hkl,V}} = \frac{\int_0^{2\pi} C_{pq}^{hkl}(\lambda) f[g_{hkl}(\lambda)] d\lambda}{\int_0^{2\pi} f[g_{hkl}(\lambda)] d\lambda} \tag{5.8}$$

λ represents the rotation angle around the {hkl}-plane normal. C_{pq}^{hkl} is the stiffness tensor for a specific grain, expressed in the sample reference system and g_{hkl} describes an orientation belonging to the <hkl>-grain family. The compliance tensor can then be obtained by inverting the stiffness tensor.

$$\overline{S_{pq}^{hkl,V}} = \left(\overline{C_{pq}^{hkl,V}}\right)^{-1} \tag{5.9}$$

A similar derivation can be made for the Reuss assumption. Starting from the average strain which can be written as

$$\bar{\varepsilon_p} = \sum_i \varepsilon_p^i \, V^i \tag{5.10}$$

an expression for the average compliance tensor can be found analogously to the above derivation.

$$\overline{S_{pq}^{hkl,R}} = \frac{\int_0^{2\pi} S_{pq}^{hkl}(\lambda) f[g_{hkl}(\lambda)] d\lambda}{\int_0^{2\pi} f[g_{hkl}(\lambda)] d\lambda} \tag{5.11}$$

The stiffness tensor can then be obtained by inverting the compliance tensor.

$$\overline{C_{pq}^{hkl,R}} = \left(\overline{S_{pq}^{hkl,R}}\right)^{-1} \tag{5.12}$$

It is important to remark that the average elastic constants obtained using the Voigt and Reuss assumptions are not equal. The DEC's obtained using equations (5.8) and (5.11) can now be used to calculate the stresses from the measured strains.

Daymond [93] describes a method to calculate a continuum mechanics equivalent strain from the measured <hkl>-strains, in order to allow comparison to finite element models. This equivalent strain is determined from a physically realistic weighing of strains obtained from multiple single peak diffraction measurements. The macroscopic stress can then be obtained from the strain by multiplication with the bulk modulus. However, this means that the intergranular stress information is lost. Therefore, in the current work a different method will be used.

In general, the average stress in a grain family can be calculated from the measured average <hkl> lattice strain by the generalized Hooke's law

$$\overline{\sigma_p^{hkl}} = \overline{C_{pq}^{hkl}} \, \overline{\varepsilon_q^{hkl}} \tag{5.13}$$

The strain has been measured in three directions (RD, TD and ND). However, the diffraction signal for each direction comes from a different set of grains. Equation (5.13) therefore has to be written three times, once for each direction, and each time with different DEC's. If it is assumed that the stress averaged over all the grains contained in the three grain families (<hkl>-RD, TD and ND) is equal to σ_p^{hkl}, a set of three equations is obtained from which the three principal stresses can be calculated.

$$\begin{aligned}\varepsilon_1^{RD,hkl} &= \overline{S_{1p}^{hkl,RD}}\ \sigma_p^{hkl}\\ \varepsilon_2^{TD,hkl} &= \overline{S_{2p}^{hkl,TD}}\ \sigma_p^{hkl}\\ \varepsilon_3^{ND,hkl} &= \overline{S_{3p}^{hkl,ND}}\ \sigma_p^{hkl}\end{aligned} \tag{5.14}$$

The summation over p goes from 1 to 3, as there are no shear stresses in the principle axes reference frame. The superscripts RD, TD and ND refer to the direction in which the strain was measured and the grain family used to calculated the DEC's.

5.2.3 Overview of the performed diffraction experiments

5.2.3.1 Ex-situ Synchrotron diffraction at HZB, Berlin

Energy dispersive synchrotron diffraction experiments were performed on cold drawn steel wires because of (1) the higher penetration depth in steel as compared to laboratory X-rays and (2) the ability to record the complete diffraction spectrum at once. This is necessary in order (1) to average out over the entire macroscopic stress profile, thereby only obtaining the micro-phase stresses, and (2) to obtain lattice strain information for various grain families. From that point of view, time-of-flight neutron diffraction could also be used. However, previous neutron diffraction measurements by M. Kriška et al. have shown that at high drawing strains (>3), only the 110-ferrite peak remains strong enough to be analysed [94]. The excellent brilliance of the synchrotron X-rays allows to overcome this problem.

Additionally, the cementite diffraction peak positions and thus residual and internal lattice strains and stresses are very difficult to measure. This difficulty stems from:

- the low volume fraction (~12-16 vol%),
- the orthorhombic crystal structure which causes the total reflected intensity to be spread amongst many small diffraction peaks,
- the small dimensions of the cementite lamellae (thickness < 20 nm),
- the large strains achieved through cold deformation processes.

The high radiation intensity obtained using synchrotron X-rays should make the cementite diffraction peaks visible even after the accumulation of strain.

Diffraction patterns were collected from wires drawn to different strains using energy dispersive synchrotron radiation. The measurements were carried out at the Helmholtz Zentrum Berlin (HZB) using the EDDI beam line [95]. They were performed using a diffraction angle 2θ of 8°. For each strain, patterns were recorded at two angles of φ (0° and 90°) and 21 angles of ψ, resulting in a total of 42 patterns. The diffracting volume of one wire is very small. To remedy this, a number of wires was placed next to each other. This is illustrated in Fig. 5.2, together with the definition of the angles. The residual stress in both the axial (φ = 0°) and transverse (φ = 90°) directions could be determined from the slopes of d-$\sin^2\psi$ curves.

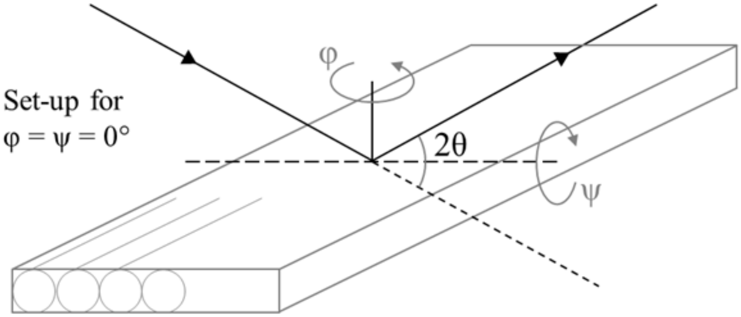

Fig. 5.2: Illustration of the experimental set-up used to measure residual stresses on cold drawn wire. $\sin^2\psi$ measurements were performed for φ = 0° and φ = 90°. The figure illustrates the 0° case as well as the lay-up of the multiple wires used to increase the diffracting volume.

The beam current and thus intensity of the synchrotron radiation varied with time. At regular intervals a bunch of electrons was injected into the beam causing the beam current to increase. After each injection the beam current dropped exponentially until the next injection. Measured intensities thus had to be corrected for the beam current. Despite this correction, small peaks were more difficult to resolve at low beam current.

The used set-up could also be used to get an indication of texture. Consider the horizontal axis of the pole figure to be parallel to the wire axis. The intensity along the horizontal axis of the pole figure can then be measured by varying ψ from 0° to 90°, for φ equal to 0°. Varying ψ for φ equal to 90° yields the intensity distribution along the vertical axis of the pole figure.

5.2.3.2 Ex-situ Neutron diffraction at PSI, Villigen

Residual lattice strains as a function of cold rolling strain were determined using the strain scanner POLDI at the neutron diffraction facility SINQ in the Paul Scherrer Insitut (PSI). The equipment and data analysis procedure have been described in detail by Stuhr et al. [96,97]. A pulsed time-of-flight (TOF) neutron source is utilised. This means that pulses of neutron with a continuous range of velocities (and therefore wavelengths) are directed at the specimen. The incident spectra are polychromatic, each measurement at a pulsed neutron source therefore implicitly captures the entire diffraction pattern. The scattering vectors for all reflections recorded lie in the same direction, and thus indicate the strain in that direction.

The TOF-POLDI strain scanner was chosen to measure the residual stresses in the ferrite phase specifically because of its ability to record the entire diffraction spectrum in one measurement. That way, the intergranular strain development can easily be determined. Additionally, the use of neutrons makes it possible to penetrate the entire sample cross-section, even for the undeformed sample with a thickness of 3mm. This was necessary because we are interested in measuring the micro-phase strains only. Although the applied pulse-overlap technique results in an enhanced intensity, it was not possible to observe cementite diffraction peaks.

The strains were measured in the three principle sample directions (RD, TD and ND) and for rolling strains varying from 0 up to ~2. The RD and TD strains were measured in a transmission geometry, while the ND strain was measured in a reflection geometry. At higher strains, the strips become very thin. To increase the diffraction volume, a number of strips with equal rolling strain were stacked on top of one another. The slits and radial collimator result in a cubic gauge volume of 3.8mm^3. The gauge volume was centred on the specimen, allowing the full sample cross section to be irradiated. Alignment of the samples was performed by scanning with the neutron beam.

The peak positions were obtained from a full 2D fit of intensity as a function of scattering angle and neutron arrival time. The origin of these plots from a time-of-flight diffractometer with multiple pulse overlap, as well as their interpretation is explained in [96]. The fitting has been performed by T. Panzner and colleagues, using the Mantid program [98,99].

5.2.3.3 Ex-situ Neutron diffraction at MLZ, Garching

The cementite micro-phase stresses in the steel strips could not be measured at the PSI neutron facility. However, the reactor at the Heinz Maier-Leibnitz Zentrum (MLZ) in Garching has a higher brilliancy of neutrons, making the detection of the cementite reflections possible. The strains were determined at the Stress-Spec beam line. The beam line has been described previously by M. Hofmann et al. [100] and was operated at a wavelength of about 2.1Å. In comparison to the previously measured wires, using synchrotron radiation was no option because of the larger thickness of the strips (up to 3 mm). Neutrons on the other hand, do allow a full penetration of the sample and therefore the measurement of the micro-phase strains. Despite the higher neutron brilliance, long measuring times were still required to obtain reasonable cementite diffraction peaks.

Mono-chromatic neutrons are used, which makes that the technique is very similar to normal laboratory X-ray diffraction. To obtain the full diffraction spectrum, the diffraction angle 2θ needs to be varied. This is facilitated to some extend because of the availability of a 2D detector. Because of the relatively long measuring times and limited beam time, only one detector position and therefore range of 2θ angles could be measured. The strain was measured in the three principle sample directions (RD, TD and ND) for as many samples as possible.

At higher strains, the strips become very thin. To increase the diffraction volume, a number of strips with equal rolling strain were stacked on top of one another. The incoming beam had a width of 3mm and a height of 10mm. The radial collimator cut-off the out-going beam on 2mm. The resulting 3x10x2mm gauge volume allowed to capture the entire sample cross section. Alignment of the samples was performed by scanning with neutron beam.

5.2.3.4 In-situ Neutron diffraction at NPI, Řež

In-situ neutron diffraction measurements were carried out on the TKSN-400 (HK9) strain diffractometer at the Nuclear Physics Institute (NPI) in Řež near Prague. Neutrons are required to be able to fully penetrate the 1mm thick steel samples. As such, the internal micro-phase strain evolution with increasing tensile strain could be determined. The internal lattice strains could only be measured in the loading direction because of time considerations and the availability of only one detector.

All the samples used had a dog bone shape. The gauge section had a width of 8mm and a thickness of 1mm. The samples were cut from the cold rolled strips in such a way that the tensile direction is parallel to the rolling direction. The tensile strain was measured using an extensometer attached to the sample, outside of the neutron beam.

In the elastic region, the tensile test were performed in stress control. Once macroscopic yielding occurred, the test was continued in strain control. Unloading and re-loading cycles were also performed in stress-control mode. At each measurement point, the tensile test was stopped and the stress or strain held constant throughout the entire measurement period (1 hour). In strain control, this led to some relaxation of the load.

Four ferrite diffraction peaks were measured (200, 211, 220 and 310). A 2-D detector with an angular range of about 15° was available for these measurements. For each peak a different detector position was used so as to position the peak in the centre of the detector. The measurement time was 15 min per peak.

The neutron radiation consisted of two different wavelengths: λ_1 = 2.394Å and λ_2 = 1.197Å. The ratio of the intensities corresponding to each wavelength was $I(\lambda_1)/I(\lambda_2) = 0.15$. The incoming slit was 14.6mm high and 7.4mm wide, the outgoing slit was 8mm high and 3mm wide. Care was taken to position the samples so that they were completely enclosed in the diffraction gauge volume. This is required in order to prevent any artificial peak shifts.

6 Experimental results and interpretation

The results obtained with the various experimental techniques described in Chapter 5 will be discussed here. To guide the read through this chapter, a short summary of the used techniques is presented in Table 6.1. The techniques are ordered according to their order of occurrence in this chapter. Each technique is linked to the goals outlined in Table 2.1 (see section 2.7). The main benefits of the techniques, in achieving the goals linked to them, are also summarised.

Section	Applied Technique	Linked Goal(s)	Main Benefit(s)
6.1.1	SEM	General characterisation, not linked to specific goal.	Visualisation of nano-scale structure.
6.1.2	EBSD	General characterisation, not linked to specific goal.	Local crystal orientation linked to microstructure.
6.2.1	Ex-situ *synchrotron* diffraction on cold drawn *wire* (HZB)	1. RS over broad strain range 2. RS saturation? + origin 3. Intergranular RS	High intensity radiation to get signal from small sample volumes.
6.2.2.1	Ex-situ *neutron* diffraction on cold rolled *sheet* (PSI)	1. + 2. + 3. 4. Influence of ILS on RS Make comparison between sheet and wire possible	Can penetrate full sample cross section to cancel out macro RS. + TOF to get full diffraction spectrum.
6.2.2.2	Ex-situ *synchrotron* diffraction on cold rolled *sheet* (MLZ)	Same as 6.2.2.1, but make measurement of cementite possible	Higher brilliancy of neutrons to be able to observe cementite peaks.
6.2.3; 6.2.4	Closer investigation of results from 6.2.2.1 and 6.2.2.2	6. Origins of peak broadening 7. Understanding pearlite	-
6.3	*In-situ* neutron diffr. on sheets with various microstructures	5. Load transfer during tensile loading 6. Origins of peak broadening	Previous experience with similar experiments.

Table 6.1: Overview of the experimental techniques applied in Chapter 6. The techniques are linked to the goals given in Table 2.1 and their main benefits are summarized.

6.1 Microstructural characterization of cold rolled pearlite

6.1.1 Evolution of morphology (SEM)

6.1.1.1 Alignment of the lamellae

An undeformed pearlitic steel sample consists of colonies in which the lamellae can more or less be considered as a stack of parallel ferrite and cementite lamellae. The orientation of the lamellae differs from one colony to another, i.e. the orientation of the lamellae is uniformly distributed. This is illustrated for a sample isothermally transformed at 500°C by the micrograph in Fig. 6.1.

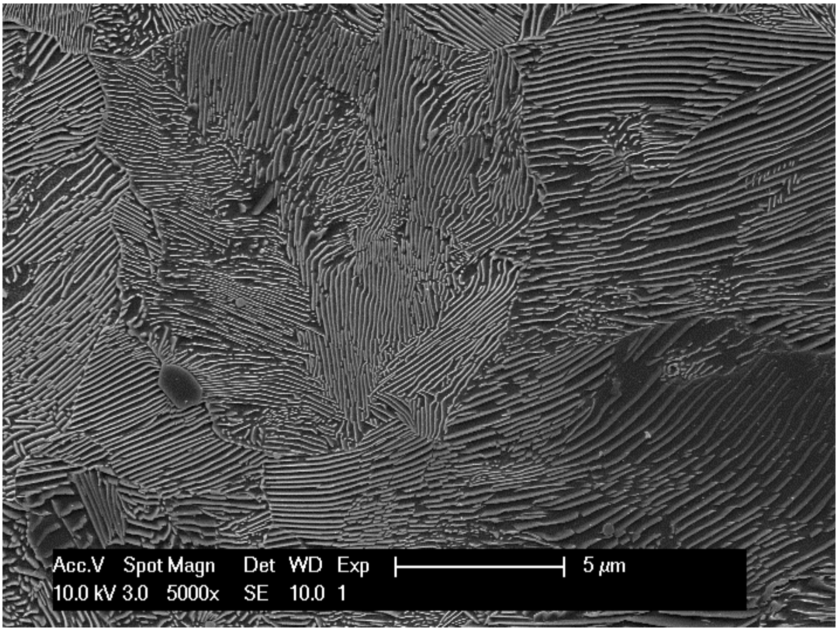

Fig. 6.1: Microstructure of undeformed pearlitic steel, isothermally transformed at 500°C.

With increasing rolling strain the lamellae will align with the rolling plane. This is illustrated by the micrograph in Fig. 6.2. The sample was isothermally transformed at 500°C and subsequently rolled to a strain of 1.1. Some residual dirt can be seen, which are small grains of silica that stuck to the sample after polishing. The rolling direction is the vertical direction, the normal direction is horizontal. The shown micrograph is representative for the majority of the sample volume.

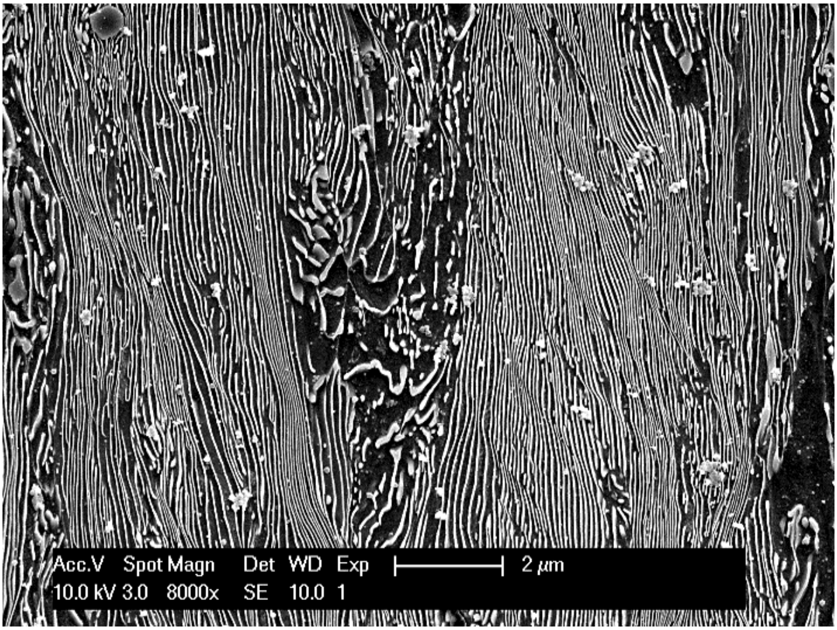

Fig. 6.2: Microstructure of cold rolled pearlitic steel, isothermally transformed at 500 °C and rolled to a strain of 1.1. The rolling direction is vertical, the normal direction horizontal. Representative for majority of the sample.

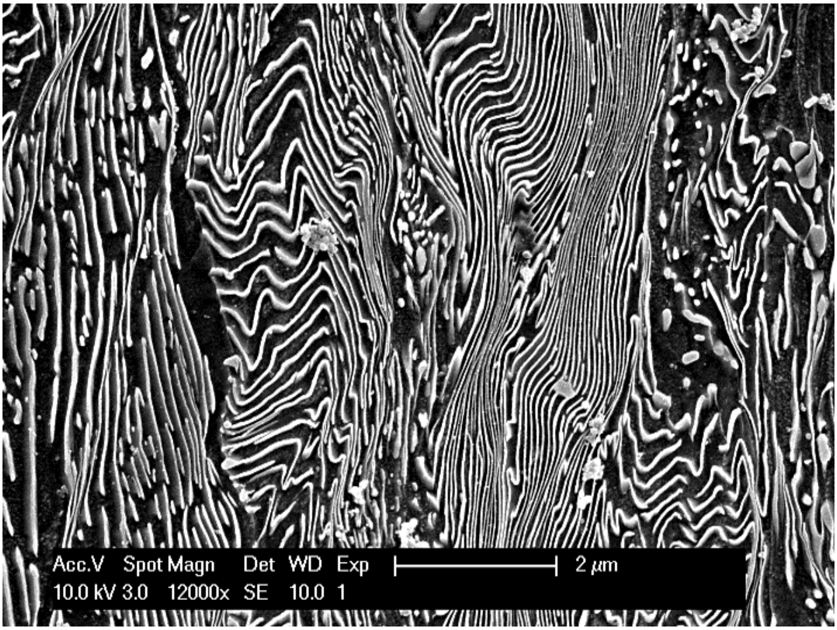

Fig. 6.3: Microstructure of cold rolled pearlitic steel, isothermally transformed at 500 °C and rolled to a strain of 1.1. The rolling direction is vertical, the normal direction horizontal. Illustration of imperfect lamellae alignment.

By the time a strain of about 1 is reached, the alignment has almost saturated. At higher strains, the lamellae alignment only improves slowly. It should be pointed out that the aligned microstructure remains far from the ideal scenario of perfectly flat and parallel lamellae. The lamellae do not align completely with the rolling plane and large portions of the microstructure show wavy or bend lamellae. Other sections even seem to lose their lamellar microstructure all together. An example of such a defected area in the same sample as previously mentioned is shown in Fig. 6.3.

6.1.1.2 Reduction of the interlamellar spacing

With increasing rolling strain, the thickness of the sample is reduced according to the following relationship:

$$t = \frac{t_0}{\exp(\varepsilon)}$$

t_0 is the initial thickness of the sample, ε the imposed rolling strain. The interlamellar spacing (ILS) has often been assumed to decrease proportional to the sample thickness.

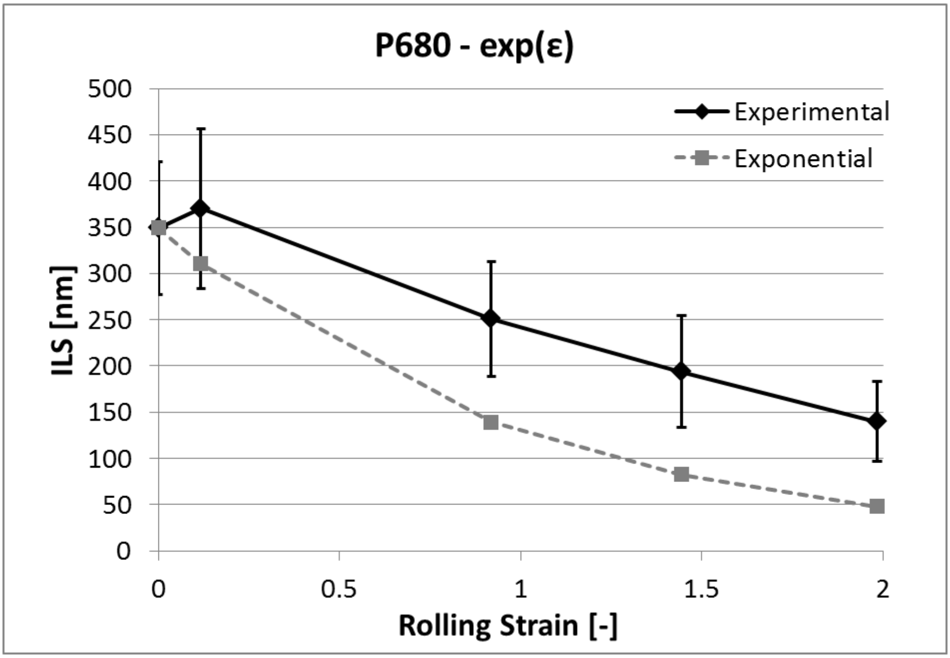

Fig. 6.4: Evolution of the apparent ILS with increasing rolling strain, determined for a sample isothermally transformed at 680°C. In black: experimentally determined apparent ILS. Dashed lines: expected exponentially decreasing ILS ~exp(ε).

The apparent ILS has been determined by drawing straight lines perpendicular to the direction of the lamellae and dividing the length of the line by the number of lamellae crossing it. The evolution of the ILS with rolling strain for a sample isothermally transformed at 680°C is shown in Fig. 6.4. The black solid line represents the experimentally determined ILS, which can indeed be seen to decreases. However, the decrease does not follow the exponential relationship illustrated by the dark grey squares.

The slower decrease of the ILS can be understood by realizing that the lamellae thickness will only follow the exponentially decreasing sheet thickness if the lamellae are aligned parallel to the rolling plane. The ILS decreases more slowly because the lamellae are still rotating towards the rolling plane. Additionally, it was shown by Langford [53] that a significant amount of the strain is concentrated in shear bands that do not contribute to lamellae thinning. Langford found that the ILS decreases proportional to exp(ε/2) instead of exp(ε). From Fig. 6.5 it can be seen that this indeed gives a much better fit. After additionally correcting for the initially observed increase of the ILS, an almost perfect fit with the experiment is obtained.

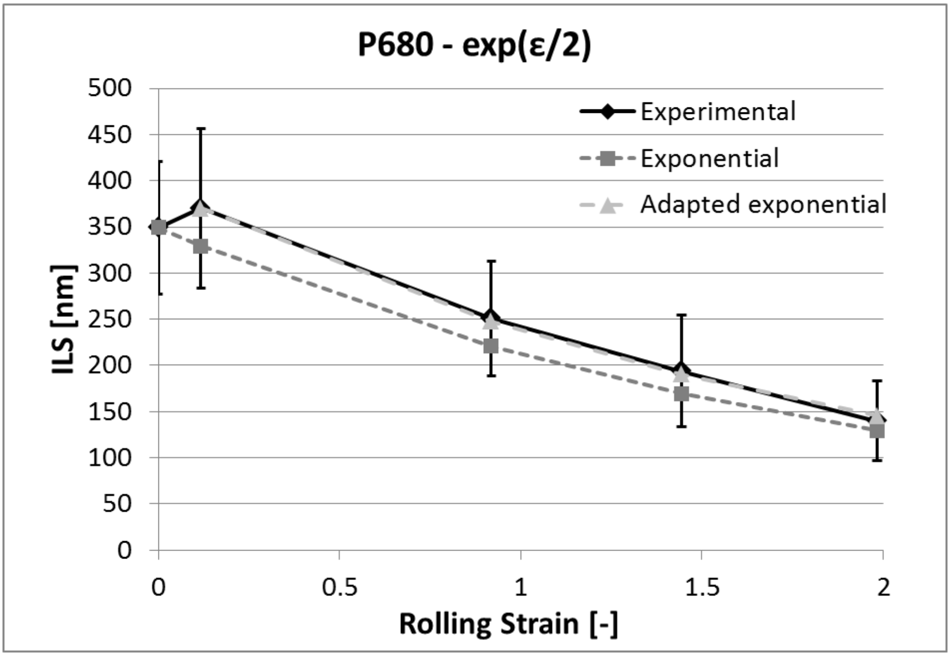

Fig. 6.5: Evolution of the apparent ILS with increasing rolling strain, determined for a sample isothermally transformed at 680°C. In black: experimentally determined apparent ILS. Dashed lines: (squares) expected exponentially decreasing ILS ~exp(ε/2) and (triangles) expected exponential decrease after correcting for initial increase.

6.1.1.3 Plastic deformation of cementite lamellae

The deformed microstructure of samples isothermally transformed at temperatures between 500 and 680°C have been closely investigated using electron microscopy. Samples deformed to strains of around 0.1, 1, 1.5 and 2 were studied. Evidence for the plastic deformation of cementite lamellae is clearly observed starting from samples deformed to a strain of 0.92. The evidence consists of the following observations:

1. Thinning of the cementite lamellae
2. Shear bands containing cementite lamellae
3. Necking of the cementite lamellae
4. Slip steps on the cementite lamellae

An overview of the evolution of the microstructure with increasing cold rolling strain can be found in Appendix 0. In the following, the existence of the above mentioned features will be shown in more detail. It should be emphasized that, although only a limited number of micrographs can be shown, the mentioned features are observed throughout the microstructure of the samples deformed to strains of 0.92 and higher.

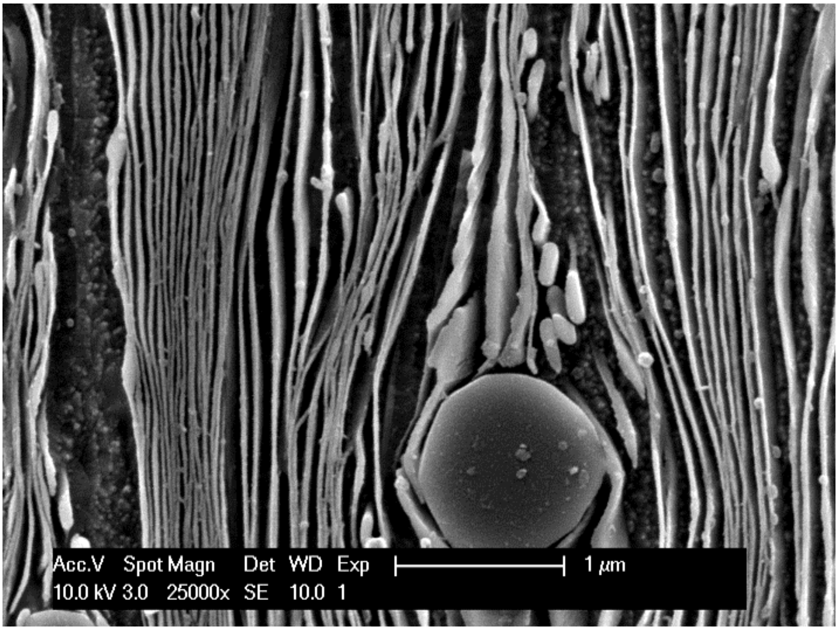

Fig. 6.6: SEM micrograph of a pearlitic steel, isothermally transformed at 600°C and cold rolled to a strain of 1.98. Stacks of very thin cementite sheets can be seen. The material flows around a spherical carbide particle.

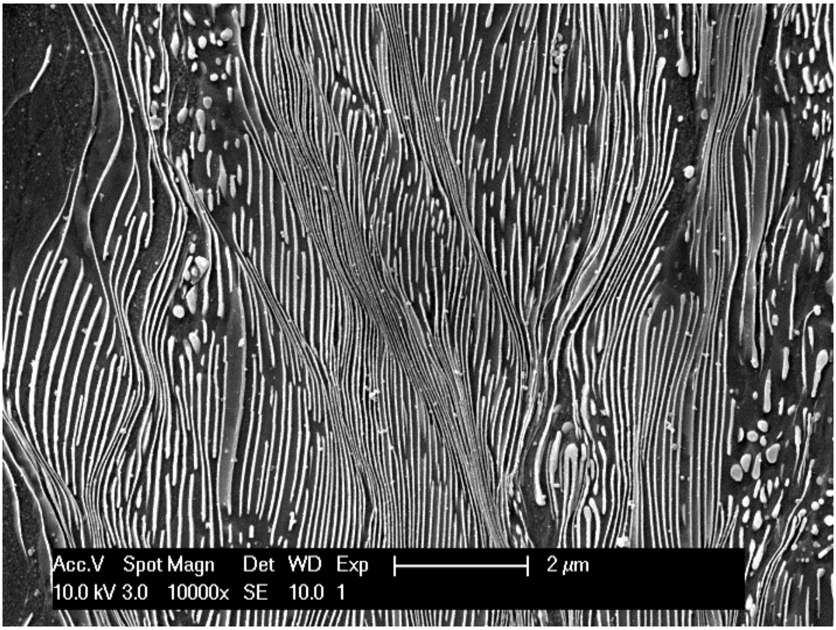

Fig. 6.7: SEM micrograph of a pearlitic steel, isothermally transformed at 650°C and cold rolled to a strain of 1.1. The presence of multiple shear bands can be observed, along with thinning of the cementite lamellae in these bands.

Thinning of the cementite lamellae

Although thinning of the cementite lamellae is obvious from the overview given in Appendix 0, it is illustrative to look at an example. On the left hand side of Fig. 6.6, a band with many cementite lamellae close to one another can be seen. This band has a width of about 525 nm and contains 14 lamellae, yielding a local ILS of 37.5 nm. The actual thickness of the cementite lamellae cannot be measured directly. An upper bound for the thickness can be estimated by considering that the local volume fraction of cementite is quite high. If a volume fraction of 50% is assumed, the cementite thickness is roughly 19 nm. The undeformed sample has an average apparent ILS of 230 nm, with a cementite volume fraction of 12%, giving an average cementite thickness of 27.6 nm. This proofs that, even for a very conservative estimate, the cementite thickness indeed reduces. Such a reduction can only be obtained if the cementite phase is deforming plastically.

Shear bands containing cementite lamellae

Throughout the deformed microstructures, shear bands containing cementite lamellae can be observed. This can be seen from the figures in Appendix 0 and is illustrated in more detail in Fig. 6.7. Within the shear bands themselves, the cementite lamellae are quite straight. They are also significantly thinner as compared to part of the lamellae outside of the shear band. Closer inspection shows that the cementite lamellae are not broken at the edge of the shear band. The change in the direction of the cementite lamellae thus causes severe local bending of the cementite. This local bending, together with the extensive thinning of cementite in the shear bands, constitutes an additional proof for the plasticity of the cementite phase.

Necking of the cementite

The thickness of cementite lamellae varies along their length, suggesting inhomogeneous plastic deformation. This often results in a cementite lamellae that look like a 'pearl necklace', as shown in Fig. 6.8. A possible explanation for this appearance is multiple necking of the cementite lamellae. As these necks become unstable, the lamellae can break up in separate, elongated ellipsoids. Multiple necking and subsequent break-up of the cementite lamellae can result in regions containing fragmented cementite with rounded edges, as illustrated in Fig. 6.9. The observed necking does not necessarily result from a plastic instability of the cementite phase itself, in the classical sense of the word. It might also be related to local variations of for example the dislocation structure at the interface, in the ferrite. Such local variations in the ferrite phase may result in local variations in the plastic behaviour of cementite. For more information regarding the possible influence of the ferrite phase on cementite plasticity, the reader is referred to the discussion in section 8.4.

Slip steps on the cementite lamellae

Slip steps can be seen on the cementite lamellae. The occurrence of slip steps seems to be limited to thick lamellae. Whether this is because there are no steps on the thinner lamellae, or that they could simply not be resolved by the microscope is unclear. An example of such steps can be seen on the lamella above the spherical particle in Fig. 6.6. Another example is shown in Fig. 6.10, where the steps can be observed at the bottom of the thick lamella in the centre. These slip steps can be formed by the movement of dislocations on parallel slip systems in the cementite. The close spacing of the steps and the lack of any contrast on the top surface of the lamellae suggests that the lamellae are not broken on these locations. In that case, the movement of dislocations is indeed involved and the steps are not caused by a shearing of the cementite 'particle'. As such, these slip steps constitute an additional proof for the plastic deformation of cementite.

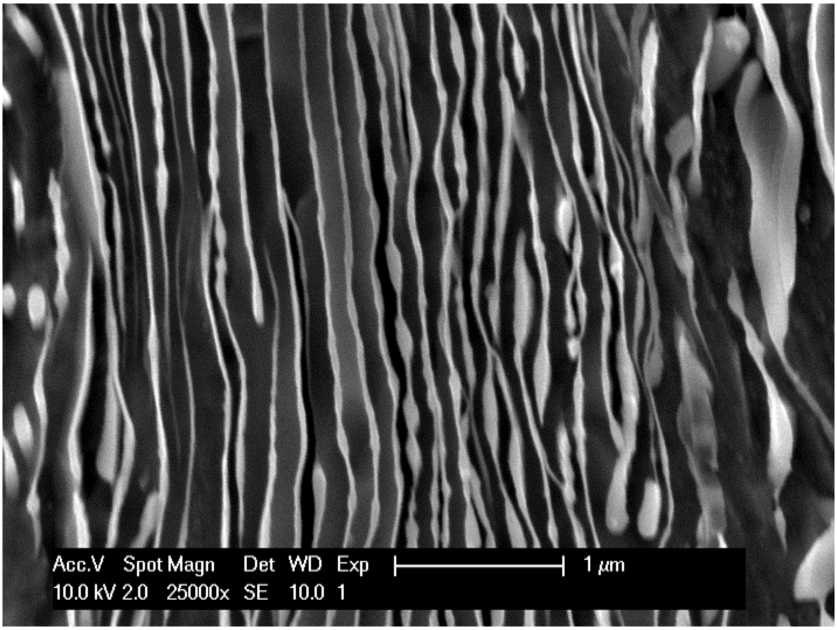

Fig. 6.8: SEM micrograph of a pearlitic steel, isothermally transformed at 680°C and cold rolled to a strain of 1.44. Necking of the cementite lamellae can be observed in multiple locations.

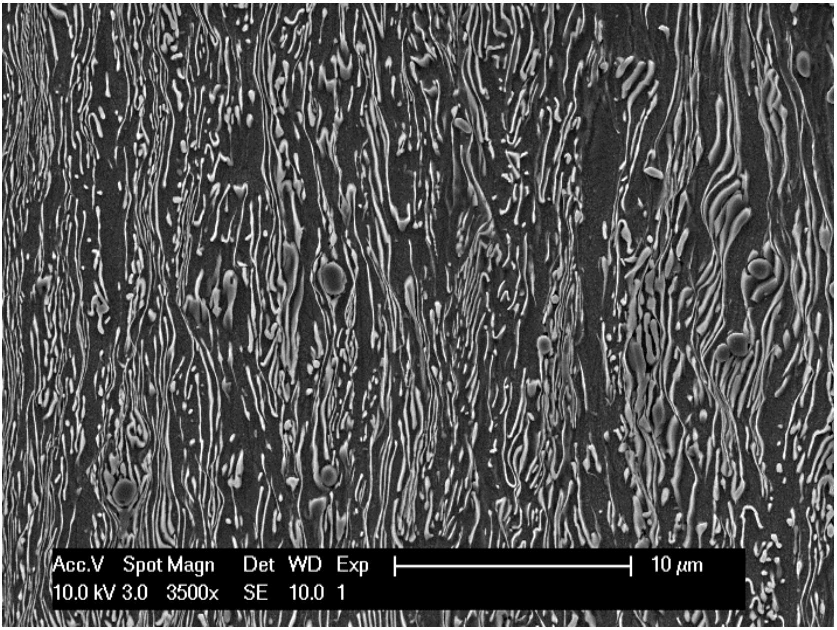

Fig. 6.9: SEM micrograph of a pearlitic steel, isothermally transformed at 680°C and cold rolled to a strain of 1.44. Location in the material with strongly fragmented cementite lamellae, possibly caused by extensive multiple necking.

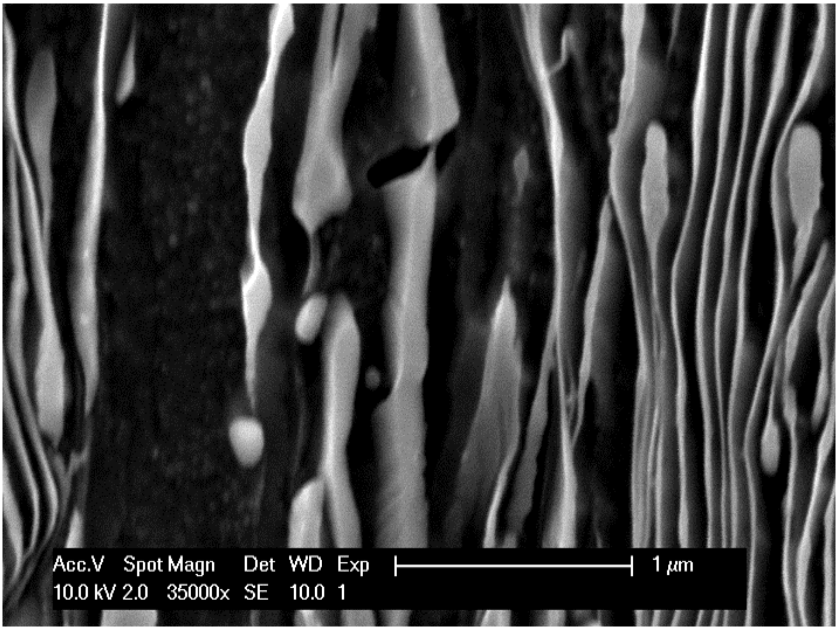

Fig. 6.10: SEM micrograph of a pearlitic steel, isothermally transformed at 680°C and cold rolled to a strain of 1.98. Small slip steps can be observed on the thick lamella in the middle of the micrograph.

6.1.1.4 Break-up of cementite lamellae

As has been discussed above, plastic deformation of the cementite can lead to necking and subsequent break-up of the lamellae. The frequent observation of elongated ellipsoidal cementite particles and needle-tipped cementite lamellae suggests that this is the mean mode of fragmentation. However, in some locations brittle fracture of the cementite lamellae can be observed, see Fig. 6.11. This observation has only been made on samples rolled to small strains (< 0.12). While this agrees with the idea that plastic deformation is facilitated in thinner lamellae [53], it must be pointed out that at higher strains the microstructure is in general more fragmented, making it more difficult to distinguish evidence of brittle fracture. The observation of brittle fracture in some locations, as compared to plastic deformation in the bulk of the samples, might indicate that the deformation state is significantly different in these locations. In the next section, this will be illustrated further by comparing cold rolled samples to a tensile test sample.

Another micrograph which can be taken as evidence for non-plastic deformation of cementite is shown in Fig. 6.12. Thick lamellae, initially oriented parallel to the normal direction, are being compressed along their

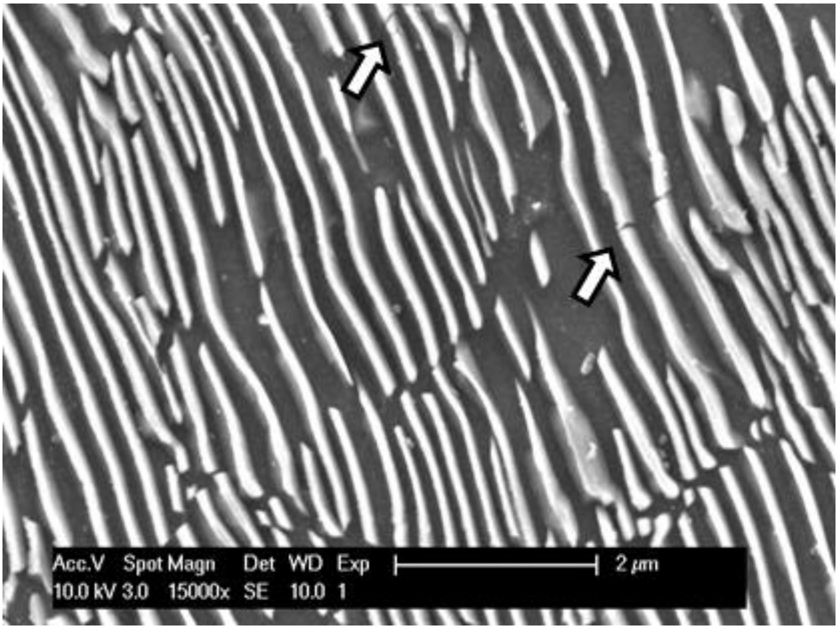

Fig. 6.11: SEM micrograph of a pearlitic steel, isothermally transformed at 680°C and cold rolled to a strain of 0.12. Evidence of brittle fracture can be observed in the locations indicated by the arrows.

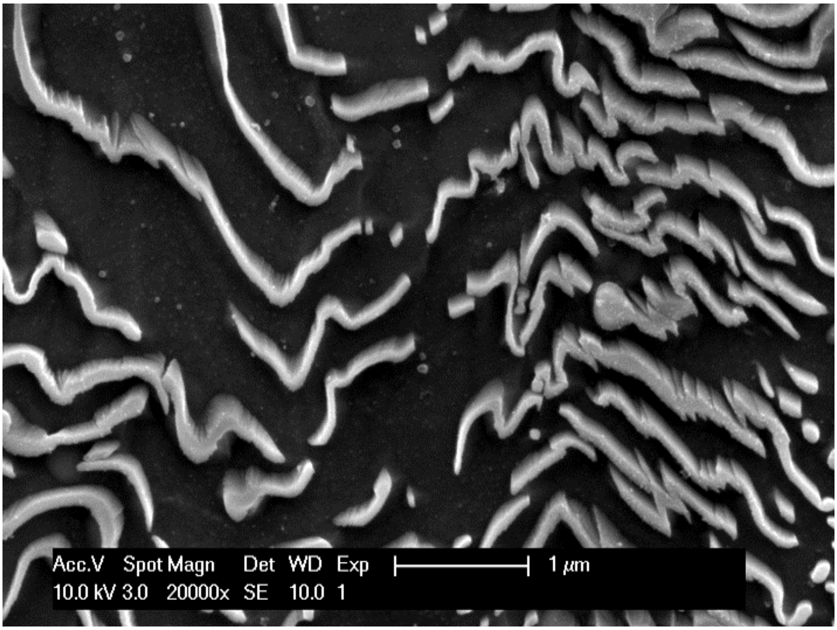

Fig. 6.12: SEM micrograph of a pearlitic steel, isothermally transformed at 680°C and cold rolled to a strain of 0.96.

long axis. They react to this compression in a brittle way by breaking into smaller sections that can slide across each other like a deck of cards. This mechanism seems to be more exotic and has only been observed twice, on two different samples (isothermally transformed at 680°C; ε = 0.96, 1.44).

6.1.1.5 Brittle fracture of cementite during a tensile test

A pearlitic steel sample has been subjected to a tensile test and its microstructure investigated. The sample has been transformed during furnace cooling from the austenite into the pearlite region. It can therefore best be compared to the samples isothermally transformed at 680°C. The sample was deformed at a strain rate of 0.013%/sec up to a fracture strain of 12%.

No evidence of plastic deformation of the cementite lamellae was found. Although at such small strains the microstructure of the cold rolled samples also does not exhibit any evidence for cementite plasticity, the tensile test sample shows a remarkably high amount of brittle fracture in the cementite lamellae. As can be seen from Fig. 6.13, an individual cementite lamellae is broken in multiple fragments.

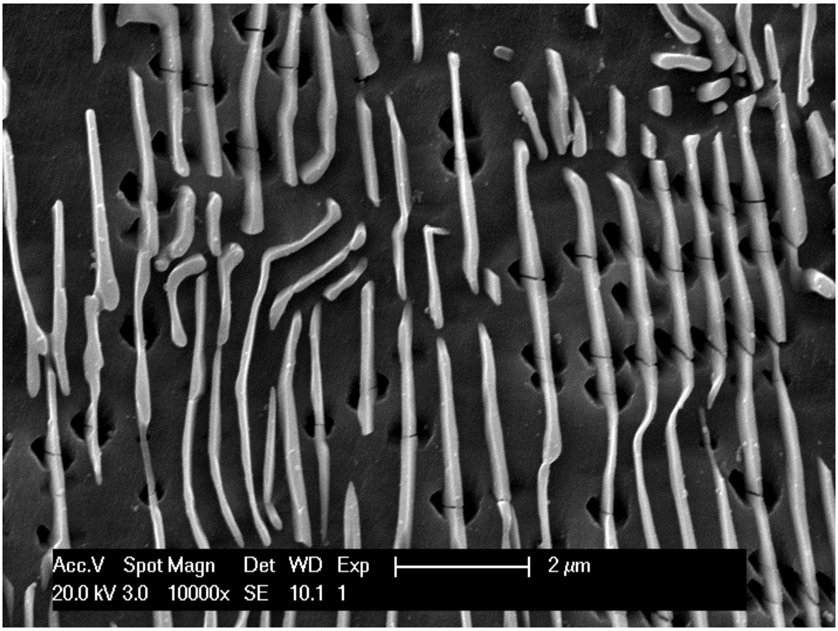

Fig. 6.13: SEM micrograph of a pearlitic steel sample, transformed during furnace cooling and deformed to a fracture strain of 12% in a tensile test. Evidence for brittle fracture of cementite can be observed.

Pits can be observed around the fracture points. It is unclear whether these pits are the results of voids created by two cementite fragments moving away from one another during the tensile test or of sample preparation. Etchant might gather in the cracks and have trouble etching away the surrounding cementite, dissolving the neighbouring ferrite instead. Therefore, no statement can be made regarding the significance of these pits.

The remarkable difference between cold rolled sheet and a tensile test sample can be understood from the difference in deformation state. While the tensile test sample is subject to uniaxial elongation, the sheet is elongated as a result of compression along the normal direction. The presence of compressive stresses inhibits brittle fracture, leading to plastic deformation instead.

6.1.2 Evolution of local ferrite crystal orientation (EBSD)

The microstructural observation made using SEM have been complemented with a limited EBSD study. Inverse pole figure (IPF) and image quality (IQ) maps recorded on the undeformed sample (P680S0) are shown in Fig. 6.14. The EBSD map was cleaned using Neighbour Confidence Index Correlation (NCIC, min. CI = 0.1), but only a very limited number of points was changed, resulting in no visible change to the map. The IQ-map reveals the positions of cementite lamellae and colony boundaries. It can be seen that the crystal orientation is continuous across lamellae, within a large section of material. Still, there are significant variations in crystal orientation within a single pearlite colony. In this and following maps, high angle boundaries (HAB's) with misorientation angles between 5° and 15° are drawn in black. Low angle boundaries (LAB's) with misorientation angles between 2° and 5° are drawn in white.

Maps for a sample cold rolled to a strain of 0.12 can be seen in Fig. 6.15. The EBSD map was cleaned using NCIC, followed by Grain dilatation (DIL, min. grain size = 5, grain-tolerance angle = 2). NCIC resulted in the adaptation of a large number of badly indexed peaks, located at the cementite lamellae. These have been added to the ferrite lamellae. As a result it seems as if the individual ferrite lamellae are separated by a ferrite grain boundary, while in fact there is a cementite lamella in between. DIL did not result in a further significant change of the EBSD map's appearance. By looking at both the IQ and IPF maps, it can be concluded that the ferrite lamellae have been fragmented in small sections, along the length of the lamellae. Two misorientation profiles are shown in Fig. 6.16. Line 1 is parallel to the lamellae and illustrates that there are both LAB's and HAB's along the length of the lamellae, while between those boundaries there is very little variation in crystal orientation. Line 2 is perpendicular to the lamellae and illustrates that the crystal orientation differs significantly from one ferrite lamellae to the next. These boundaries are however not HAB's in the strict sense of the word, as there is also a cementite lamellae included in this boundary.

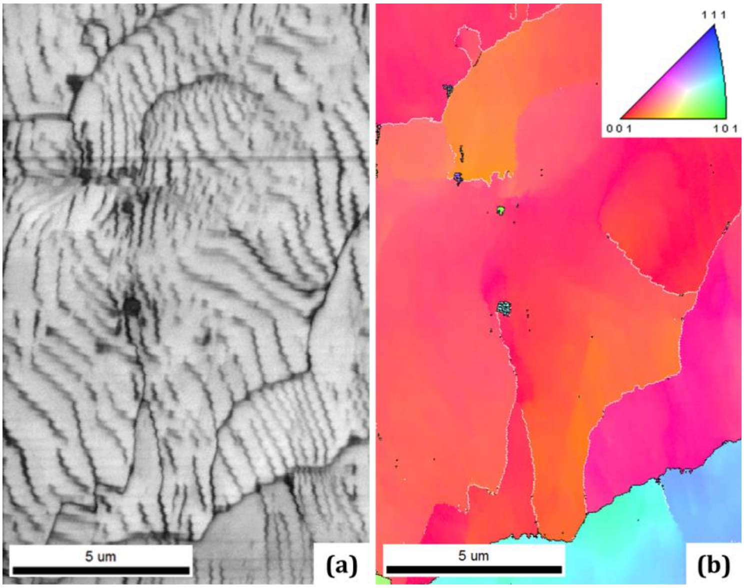

Fig. 6.14: (a) IQ map and (b) IPF for sample P680S0 (ε = 0). The crystallographic directions parallel to the TD are shown, along with the HAB's (black) and LAB's (white).

Unfortunately, the result shown in Fig. 6.15 could not be repeated. Additional measurements on samples cut from the same region of the sheet as for the previous measurement all resulted in maps similar to those illustrated in Fig. 6.17 (only NCIC clean-up, no significant changes). While the variations in grain orientation are much more significant than for the undeformed sample, fragmentation is far less pronounced as compared to Fig. 6.15. Still, the position of the cementite lamellae can clearly be observed. This indicates that a single colony does not deform as one block, but that the individual ferrite lamellae follow slightly different strain paths. At higher strains the microstructure gradually evolves towards more fragmentation as can be seen from Fig. 6.18 (only NCIC clean-up, no significant changes), but a sharp fragmentation has not been observed even at strains as high as 1.1.

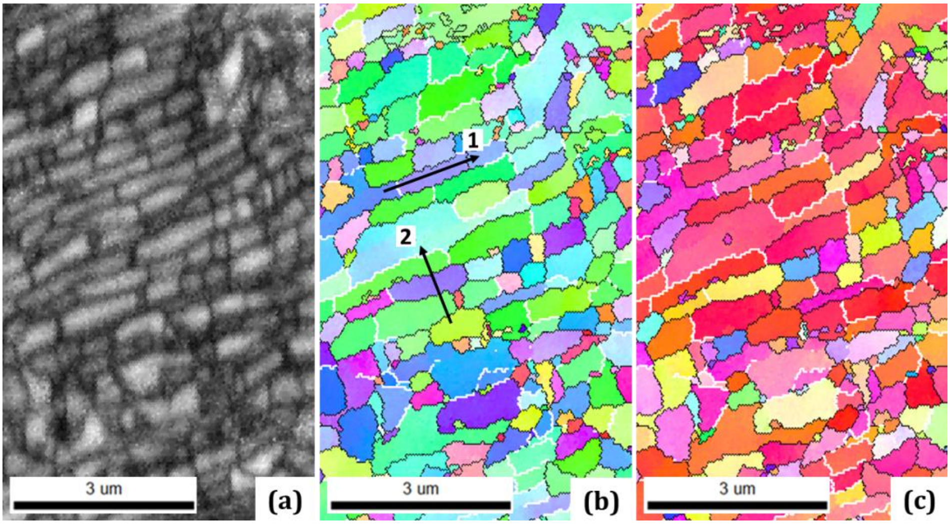

Fig. 6.15: (a) IQ map, (b) and (c) IPF for sample P680S3 (ε = 0.12). The crystallographic directions parallel to the TD and ND are shown in figure (b) and (c), respectively. HAB's (black) and LAB's (white) are also shown. The misorientation angles along two directions are shown in Fig. 6.16.

It remains unclear why the result in Fig. 6.15 could not be repeated. There are no indications for sources of error, either during sample preparation or the measurement itself, that allow to dismiss this result. The fragmentation is real, but is apparently very localized. Unfortunately, the position of the maps on the sample has not been recorded. At best, it can be said that this again confirms the inhomogeneous nature of the pearlitic steel.

No EBSD measurements were performed on samples with a strain higher than 1.1, due to the greatly reduced Kikuchi-pattern quality with increasing deformation. A significant number of studies have been performed on undeformed pearlite, among which [101–103], that agree with the observations in Fig. 6.14. However, to the current authors knowledge, only a very limited amount of EBSD work has been done on deformed pearlite. One report by Zhang et al. [64] shows an IPF-map recorded on wire cold drawn to a strain of 2.67. It does not exhibit the significant variations in ferrite crystal orientation illustrated in Fig. 6.17 and Fig. 6.18. This could indicate that orientation fragmentation occurs at small and intermediate strains. And that at larger strains the crystallographic orientations of all these fragments again have to evolve in the same direction, in agreement with the evolution of a strong macroscopic crystallographic texture.

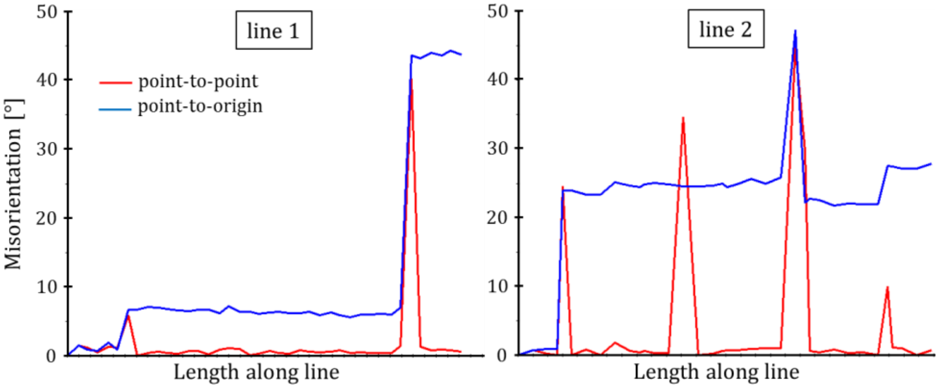

Fig. 6.16: Misorientation in degrees along the two lines indicated in Fig. 6.15(b).

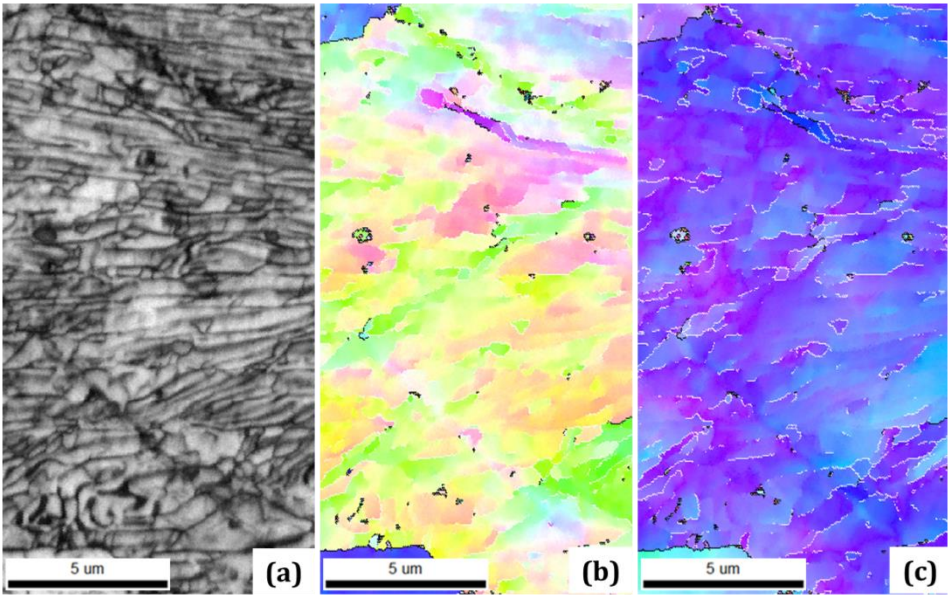

Fig. 6.17: (a) IQ map, (b) and (c) IPF for sample P680S3 (ε = 0.12). The crystallographic directions parallel to the TD and ND are shown in figure (b) and (c), respectively. HAB's (black) and LAB's (white) are also shown.

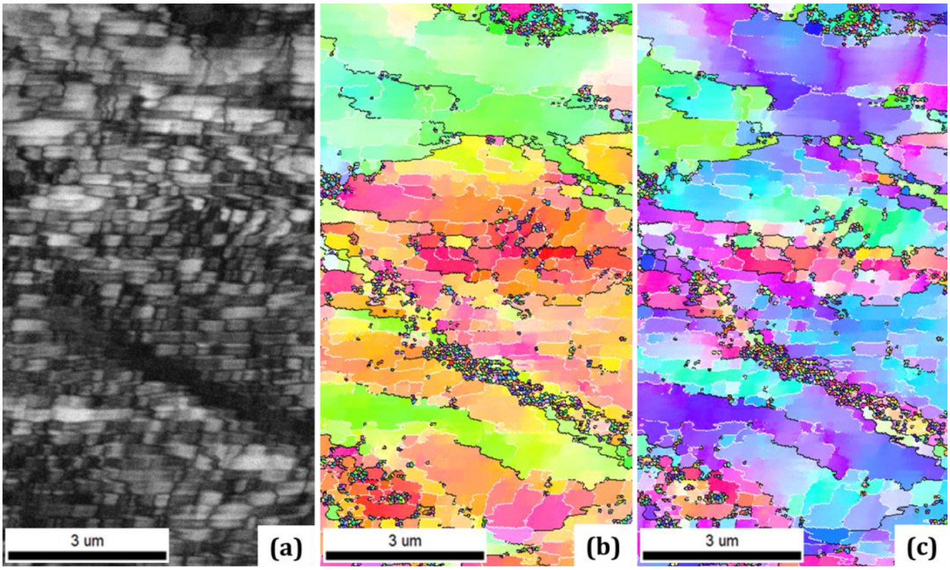

Fig. 6.18: (a) IQ map, (b) and (c) IPF for sample P680S6 (ε = 0.54). The crystallographic directions parallel to the TD and ND are shown in figure (b) and (c), respectively. HAB's (black) and LAB's (white) are also shown.

6.2 Residual stress and strain characterization

The residual lattice strains present in the pearlitic steel wire and sheet after cold drawing and rolling, respectively, were measured using neutron diffraction and will be presented here. By the application of neutron diffraction, a volume averaged strain is obtained. This means that the macroscopic stress profile is averaged out and that the strains and stresses presented here are micro-phase residual strains and stresses. The total stress at the surface of the rolled sheets has also been measured, using laboratory X-ray diffraction. However, these results did not lead to new insights and are not required in the analysis of the neutron diffraction data. The results for the total stress in the sheet are therefore presented in Appendix B. The current section will conclude with a more detailed analysis of shapes of the recorded diffraction profiles.

6.2.1 Residual micro-phase stresses in cold drawn wire

6.2.1.1 Ferrite micro-phase stress

The micro-phase stresses in cold drawn *wire* were measured as a function of cold drawing strain. The results presented here were obtained as part of the Ph.D. of Martin Kriška and have previously been reported [104,105]. For more information on the performed experiments and the conclusions drawn by

Kriška et al., the reader is referred to the published papers. Because of the authors own contribution to the experiments and as a reference with which to compare the residual stresses in cold rolled pearlitic steel *sheet*, the results of the experiments performed on wire are also reported here. Additionally, a source of error will be reported that affects the final conclusions.

The cold drawn pearlitic steel wire was supplied by NV Bekaert and had a starting diameter of 890 μm. Through one directional cold drawing, the diameter was reduced over multiple passes to a final diameter of 120 μm. Micro-phase stresses were determined using synchrotron diffraction at the EDDI beam line of the Helmholtz Zentrum Berlin (HZB). For the first few drawing passes the synchrotron beam does not completely penetrate the wire. As a result, the measured micro-phase stress contains a small contribution from the macroscopic stress profile, up to a strain of 0.6.

A diffraction profile recorded on the as-patented wire is shown in Fig. 6.19. The strongest peaks are, in order of decreasing energy, the ferrite <110>, <200> and <211> reflections. The ferrite <110> peak maximum intensity is around 5500 counts, but has been cut off at 1000 counts to make the smaller peaks visible. The peaks at 87.55 and 97.86 keV are the ferrite <220> and <310> reflections respectively. The larger peak at 34 keV (90 counts) and the smaller peak at 32.8 keV (30 counts) are escape peaks related to the <110> ferrite peak. The small peaks at energies below 10 keV are not caused by diffraction but by X-ray fluorescence and are of no interest to the current investigation. The other small peaks are related to the cementite phase and will be discussed in the next section.

Residual stresses were determined based on the traditional $\sin^2\psi$ method. The diffraction elastic constants were calculated using a Kröner/Eshelby type model for a random texture. It has been shown by M. Kriška et al. [105] that, for the surface stresses as measured using laboratory X-rays, including texture effects has rather little influence on the residual stress values for this material (of the order of a few tens of MPa). The micro-phase stresses have been determined for various ferrite grain families. The stresses in the axial direction are shown in Fig. 6.20, together with the total ferrite phase stress as measured using laboratory X-ray diffraction on the <211> ferrite reflection.

Three separate regions can be discerned in the micro-phase stress evolution. First there is a region of monotonously increasing compressive stresses for all ferrite grain families ($\varepsilon = 0\text{-}0.5$), after which the residual stress value seems to saturate ($\varepsilon = 0.5\text{-}2.3$), with little variation among the grain families At larger strains, the residual stress response of the different grain families diverges.

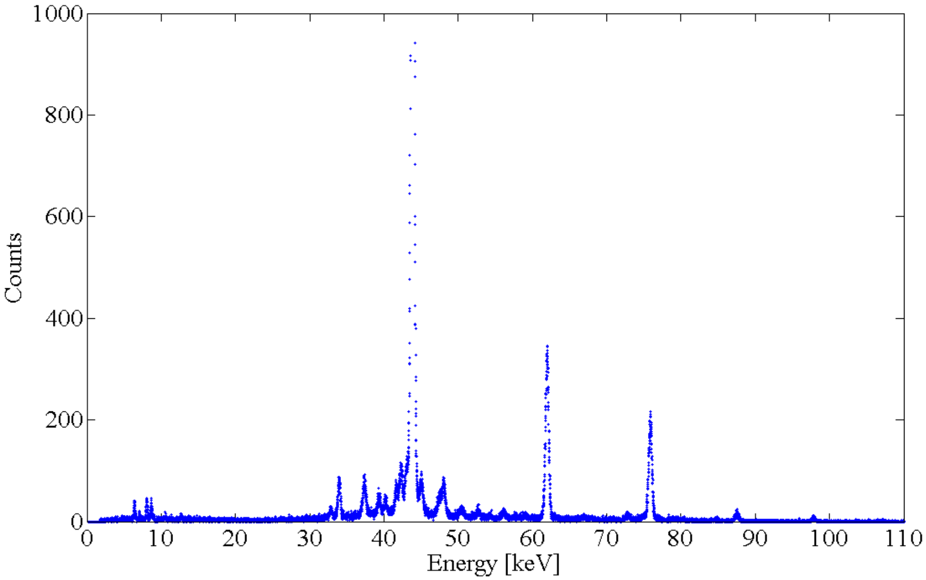

Fig. 6.19: Energy dispersive synchrotron diffraction spectrum obtained from the as-patented pearlitic steel wire ($\phi = \psi = 0°$).

Initial increase of the micro-phase RS (ε = 0-0.5): The development of micro-phase RS in this region is attributed to the different elastic and plastic properties of the cementite and ferrite lamellae. The continued increase of RS indicates that a significant portion of cementite has not yet yielded, or that it strain hardens more than ferrite. The total phase stress in this region is dominated by the micro-phase residual stress.

Slow increase and saturation of the micro-phase RS (ε = 0.5-2.3): In this region, the micro-phase stress is still a result of the load partitioning between the two phases. It has been suggested that the observed saturation could indicate the onset of massive cementite plasticity. On the other hand, a reduced load bearing capacity by fragmentation of the cementite lamellae could also be occurring. The total phase stress in this region doesn't saturate and is therefore dominated by the macro RS development.

Divergence of the grain family responses (ε > 2.3): In this region, the load partitioning between ferrite grain families dominates over the load partitioning between the two phases, resulting in the observed divergent micro-phase stresses.

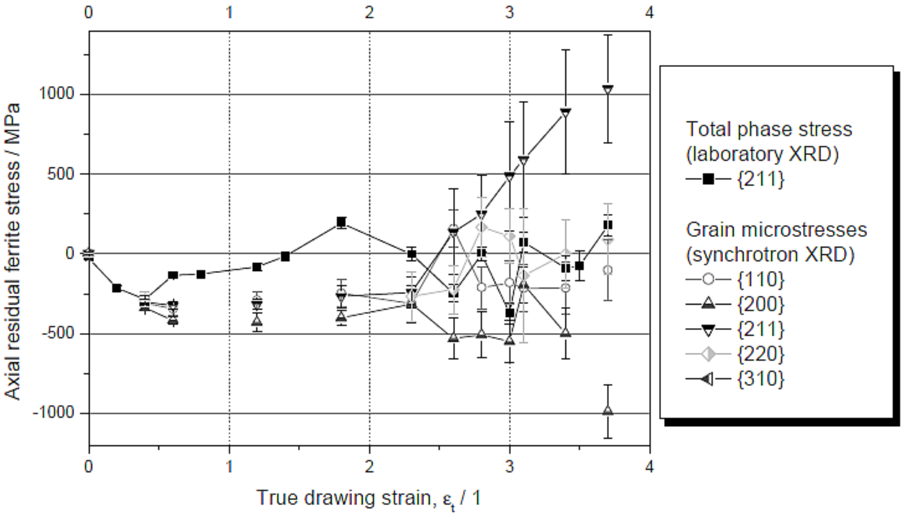

Fig. 6.20: Residual stresses in the ferrite phase of cold drawn pearlitic steel wire as a function of true drawing strain. The <hkl> micro-phase stresses measured using synchrotron diffraction is shown, together with the <211> total phase stress measured at the surface of the wire using laboratory X-ray diffraction. [105]

There are two indications that led us to re-investigate the residual stress evolution of the <211> diffraction peak. Firstly, literature shows that the <211> peak always behaves very similar to the <110> peak, at least for smaller strains. Secondly, such a divergence of the <211> peak response has not been observed on cold rolled sheets (see section 6.2.2.1).

In Fig. 6.22 a number of diffraction profiles recorded at increasing ψ angles on a wire cold drawn to a strain of 3.34 is shown. The <211> diffraction peak is situated at around 1.17Å. However, there is also an unidentified peak around 1.185Å. The peak positions as obtained using the software available at HZB are indicated with dashes. These same peak positions were used to find the stress from a d-sin^{2}ψ plot, as shown in Fig. 6.21, and are influenced by the unidentified peak. It can be seen that especially for the profiles 10-14 and 20, the found peak position is far from the actual <211> peak position, which is situated at lower d-values. If one were to neglect or correct these peak positions, the d-sin^{2}ψ plot would look completely different and a negative residual stress would be obtained.

By investigating the d-sin^{2}ψ plots and diffraction profiles of samples at a lower drawing strain, it could be seen that the problem starts to manifest itself at a strain between 2.3 and 2.6. This corresponds exactly to the point where the deviatory behaviour of the <211> peak starts. While at these middle range strains only the profiles at very large ψ angles are problematic (#19-21), at higher strains more profiles become problematic, increasing the shift towards higher d-values.

In light of Fig. 6.22 it is clear that the poor quality of the peaks results in a large error. In fact, it would have been prudent not to have used the data for this peak in the first place. In conclusion, it can be stated that the stress values obtained for the <211> ferrite peak as shown in Fig. 6.20 are erroneous. To understand what is truly happening, the origin of the unidentified peak should first be elucidated. It has already been ascertained that the unidentified peak cannot be ascribed to carbides other than cementite, fluorescence peaks, escape peaks, residual austenite, aluminium from the sample holder or other materials that may have entered the beam path.

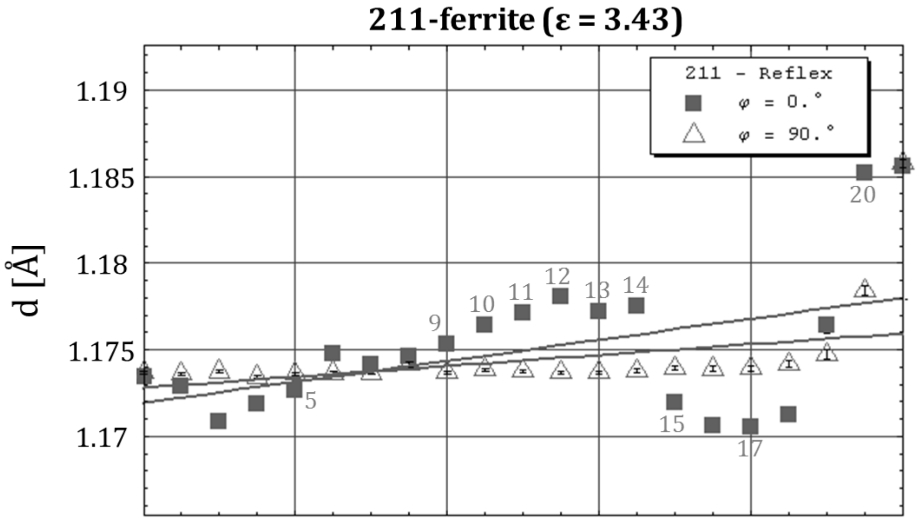

Fig. 6.21: d-sin$^2\psi$ plot for the <211> ferrite reflection as measured on a wire cold drawn to a strain ε = 3.34. The numbers indicated in the figure refer to the profiles depicted in Fig. 6.22.

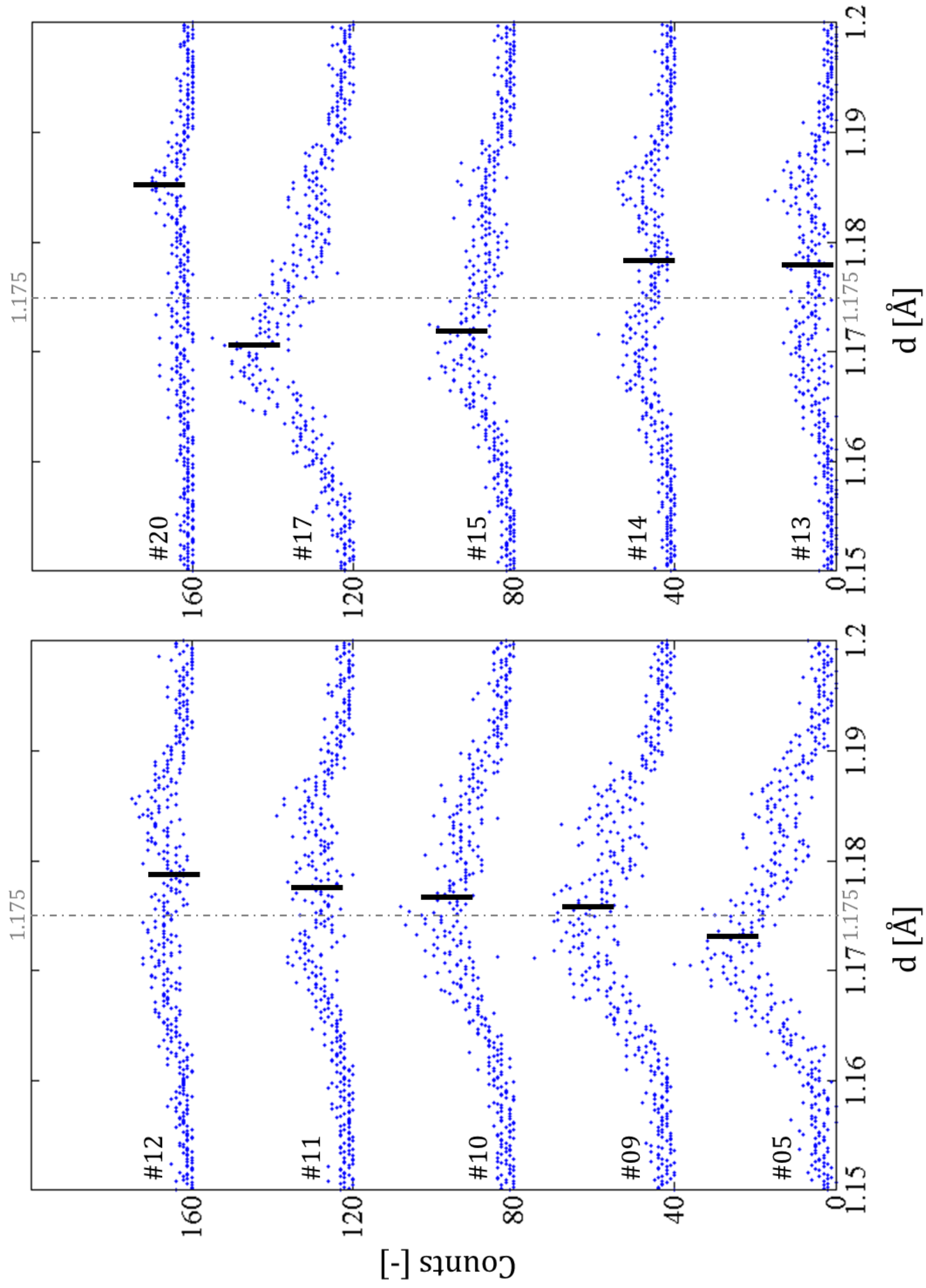

Fig. 6.22: Diffraction profiles around the <211> peak position, for a wire with a cold drawing strain ε = 3.34. The profiles were obtained at increasing ψ angles. The numbers refer to data points in the d-sin²ψ curve in Fig. 6.21. The thick lines correspond to the d-spacing obtained using the available program at HZB. The dot-dash line at d = 1.175 Å is drawn to help guide the eye.

6.2.1.2 Cementite micro-phase stress

Synchrotron radiation diffraction experiments were performed on cold drawn steel wires at the Helmholtz Zentrum in Berlin (HZB) using the EDDI beam line. The prime goal and result of these measurements was to obtain the ferrite micro-phase stresses, as already discussed in section 6.2.1.1. However, the obtained cementite reflection were analysed by the current author in order to extract as much information from them as possible. The text in this section is based on the proceedings paper by Tacq et al. [106].

The full diffraction pattern obtained on a patented wire has been shown in Fig. 6.19. A detail of the same pattern around the <110> ferrite reflection is shown in Fig. 6.23, indicating the presence of cementite diffraction peaks. Weisser et al. [32] measured a much sharper diffraction pattern of cementite in bainite. Some of the peak positions found by Weisser are indicated with lines in Fig. 6.23. Where peaks overlap too much, no separate lines have been drawn. A comparison of the profile with the indicated cementite peak positions shows that most of the peaks can be identified as cementite. However there is one peak with a d-spacing of 2.133 Å that could not be attributed to any of the allowed cementite reflections.

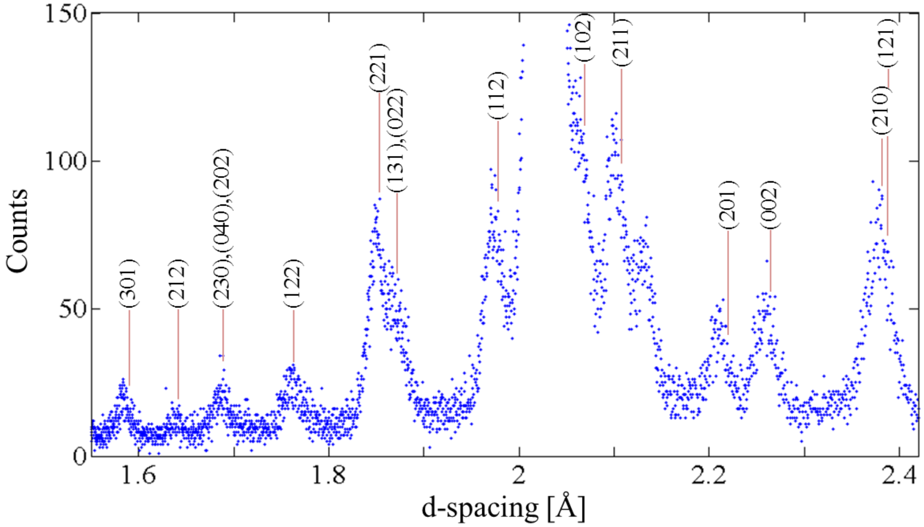

Fig. 6.23: Detail of the diffraction spectrum of the as-patented pearlitic steel wire around the <110> ferrite peak. Energy values have been converted into d-spacings.

This extra peak can be attributed to the thin brass coating covering the wire. The observed d-spacing corresponds to the <111> reflection of fcc α-brass with lattice parameter a = 3.694 Å. If the stress in the coating is considered to be negligible for the as-patented wire, the measured lattice parameter corresponds to a zinc content of about 36 wt% [107]. This peak is discussed in some more detail further on in this section.

A close-up of the diffraction patterns (φ,ψ = 0°) for wires cold drawn to true strains of 0 up to 1.2 is shown in Fig. 6.24. At a true strain of 0.4 the peaks on the high-d-side of the <110> ferrite peak become much broader and begin to overlap. The patterns for a true strain of 0 and 0.4 were measured at comparable beam currents. The beam currents during measurement of the patterns for wires with true strains of 0.6 and 1.2 were only half as high due to the exponentially decreasing beam current after electron injection (see section 5.2.3.1). The peaks on the high d side now almost seem to disappear completely. The patterns at a higher ψ angle (for ε = 0.6 and 1.2) were again measured at a higher beam current. Even then the peaks could still not be discerned unambiguously. Only the brass peak remains visible. It strongly overlaps with the <110> ferrite peak so that it manifests itself as a strong asymmetry of the ferrite peak towards the high-d-side.

On the low-d-side the maximum intensity of the peak around 1.85 Å also strongly decreases. This peak seems to stabilise at a true strain of 0.6 and remains more or less visible, depending on the beam current. The software provided at HZB was able to fit this peak and determine the peak position. It should be held in mind, however, that this peak is a combination of three cementite reflections (<221>, <131> and <022>).

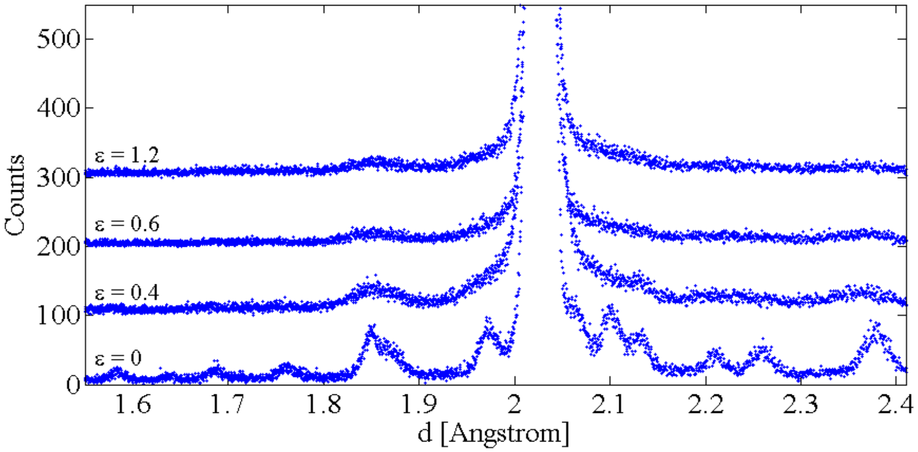

Fig. 6.24: Diffraction spectra (ϕ = ψ = 0°) measured on pearlitic steel wires cold drawn to different strains (0, 0.4, 0.6 and 1.2). Each subsequent pattern has been shifted up by 100 counts to allow comparison.

At still higher strains, accurately determining the peak position of the peak around 1.85 Å becomes more difficult. Patterns were collected for many ψ angles and the peak positions determined. After a selection of the reliable peak positions, which coincides with high beam currents, enough points were left in the d-$\sin^2\psi$ curves to determine the cementite residual micro-phase stresses in the axial direction up to a true train of 2.8, as shown in Fig. 6.25. The stress in the transverse direction is always a mixture of hoop and radial stresses and remained zero, within the accuracy of the current experiment. The transverse stresses will therefore not be discussed further.

The fact that the cementite micro-phase stress is calculated from a peak consisting of several reflections requires some consideration. The d_0 spacing is not required because d-$\sin^2\psi$ curves are used to calculate the residual stresses. However, the diffraction elastic constants (DEC's) to be used in the calculation should be known. This is not straightforward because the DEC's of the three contributing reflections are different. The DEC of the <221> reflection is used because, based on the pattern of the as-patented wire, it gives the largest contribution to the observed peak. The DEC's were calculated according to Kröner and a homogeneous texture was assumed. The single crystal elastic constants according to Nikolussi et al. [34] were used as input. The choice of elastic constants will be elaborated on with respect to the stress calculation in cold rolled sheet in section 6.2.2.2.

One problem that might occur is a fake peak shift being recorded as a consequence of one of the three reflections preferentially increasing in intensity due to texture. However, no significant cementite texture was observed as is shown further on in this section. Therefore, the problem of a fake peak shift doesn't arise here. As long as the stress on the different lattice planes doesn't vary too much as a result of grain-grain interactions, the calculated value for the stress is considered to be a reasonable approximation for the stress in the cementite phase.

It should be remarked that, as a result of the decreasing wire diameter, the sample is only fully penetrated by X-rays starting from $\varepsilon = 0.6$. The measured stress therefore evolves from a mixture of macro stress and micro phase stress at $\varepsilon = 0$ to only micro phase stress at $\varepsilon = 0.8$ because the macro stresses cancel out when averaged over the entire cross-section.

The cementite residual micro-phase stress (Fig. 6.25) in the axial direction can be seen to increase sharply after the first drawing pass. It then seems to increase somewhat more slowly up to 3.3 GPa at a true drawing strain of 1.6 and subsequently drops again. It should however be noted that the quality of the peaks for the wire drawn to a strain of 1.6 was very bad due to low beam current at the time of the measurement. It is therefore not clear whether a maximum truly occurs at a strain of 1.6 or that saturation is reached at lower strain values, which would correspond more closely to the point where the ferrite residual micro-phase stress starts to saturate (ε = 0.5). Oliver et al. [17] and Hanabusa et al. [9] reported saturation of residual stress for spheroidised cementite. Oliver attributed the saturation to reverse ferrite yielding upon unloading. Another possible mechanism for saturation of the cementite stress is fragmentation of the cementite lamellae. However, even if the point at a strain of 1.6 is not taken into account, Fig. 6.25 might also suggest a slow continues decrease of the residual stress after a strain of 1.2, rather than a true saturation. This will be discussed further based on the model presented in section 7.2.

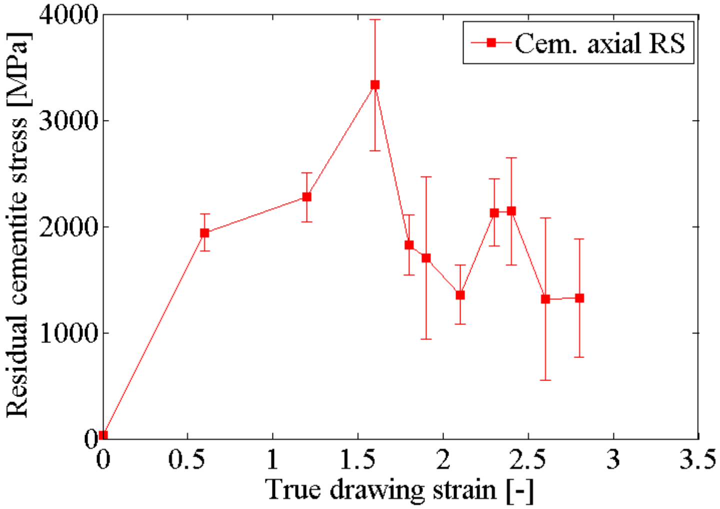

Fig. 6.25: Axial micro-phase residual stress in the cementite phase of cold drawn pearlitic steel wire, as a function of cold drawing strain.

The intensity evolution of the cementite peak at 1.85 Å and the brass peak was investigated. To eliminate intensity evolutions related to peak broadening and draw some conclusions on the texture development, the integrated intensity should preferable be used. Here the maximum intensity is used because the peak that overlaps with the <110> ferrite reflection could not be fitted and the fit of the other peak was often unreliable. However, the observed peak width doesn't change for either peak. Using the maximum intensity should therefore give a good approximation. The point where strong asymmetry begins is chosen as the maximum intensity for the <111> brass peak overlapping with the <110> ferrite reflection. The observed maximum intensity is corrected for changes in beam current.

The intensity distribution for two different drawing strains is shown in Fig. 6.26 for φ = 0° and 90° on the left and right hand side, respectively. Both investigated peaks have a higher intensity in all patterns where φ = 90°, as a result of the alignment of the wire and the incoming synchrotron beam. At higher strains the intensities also drops visibly, as a result of the peak broadening caused by deformation of the microstructure.

The cementite peak only shows a decreasing intensity towards higher ψ tilts, which is a geometrical effect. It can thus be concluded that the cementite shows no significant indication of texture development. The <111> brass peak, at a d-spacing of around 2.13 Å, on the other hand does show traces of a texture evolution. Along the φ = 90° direction there is no intensity evolution except for a geometrical effect. However, along the φ = 0° direction at a drawing strain of 1.9 there is a clear intensity evolution. At higher strains the same evolution becomes even more pronounced. The observed intensity agrees well with a double fibre texture <111> + <001> as can be expected for a fcc material subjected to axially symmetric elongation.

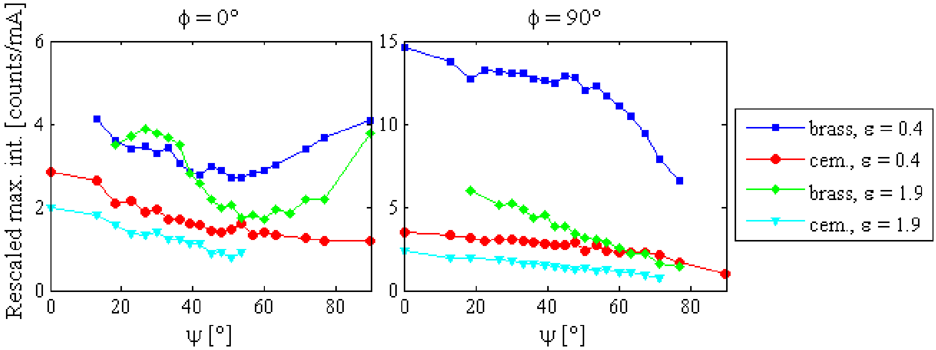

Fig. 6.26: Rescaled maximum intensity for both ϕ = 0° and ϕ = 90°, as a function of ψ, for the <111> brass peak and the <221>-<131>-<022> cementite peak. This corresponds to the intensity evolution along two lines of a pole figure with the wire axis parallel to the horizontal axis. For ϕ = 0°, the horizontal line of the pole figure from the centre to the edge and, for ϕ = 90°, the vertical line.

At high strains the <110> ferrite peak exhibits a strong asymmetry towards the high-d-side for patterns collected where φ is 0°. For φ equal to 90° this asymmetry is not present, while the <111> brass peak is again more clearly visible. The patterns for a true drawing strain of 2.1 and ψ = 30° are shown in Fig. 6.27. The fcc α-brass is softer and more ductile then the bulk wire. The difference between the two patterns can thus be explained as the brass peak being under compression in the axial direction while bearing almost no stress in the transverse direction, shifting the peak to a higher d-spacing and away from the <110> ferrite peak in the transverse direction. This effect will be reinforced by the lower <110> ferrite peak intensity in the transverse direction, which is linked to the strong <110>-fibre texture in cold drawn bcc materials.

All the above observation form a consistent picture, making it safe to assume that the peak at 2.13 Å is indeed α-brass. Moreover the <111> reflection is the strongest reflection for fcc materials, which explains why only the <111> reflection is observed. The fact that the peak persists to high strains makes it very unlikely that this is a cementite peak. Heavy deformation of the cementite and its decomposition at high strains should strongly decrease the intensity of the observed reflections.

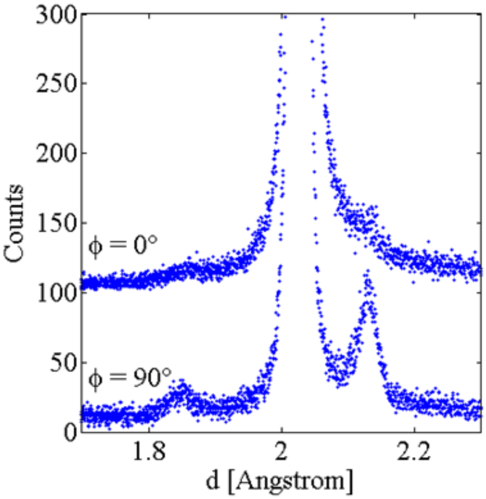

Fig. 6.27: Detail of diffraction spectra measured on wire with $\varepsilon = 2.1$ ($\psi = 30°$).

The main conclusions from the analysis of the cementite diffraction peaks can be summed up as follows:

- No indications have been found for the evolution of a cementite deformation texture.
- The cementite residual micro-phase stress increases sharply at the onset of cold drawing, in correspondence to the observed ferrite micro-phase stress, after which the residual stress saturates or even slightly decreases.

6.2.2 Residual micro-phase strains/stresses in cold rolled sheet

6.2.2.1 Ferrite micro-phase strain/stress

The POLDI beamline at the Paul Scherrer Institute (PSI) in Villigen, Switzerland, used for the micro-phase residual strain measurements, is a time-of-flight (TOF) neutron diffractometer. This allows to measure the entire diffraction spectrum at once. The neutron diffraction measurements at PSI were thus focussed on obtaining the ferrite lattice strains for various grain families and over a large interval of rolling strains. Two sample sets with a different starting interlamellar spacing were measured: P500 (ILS_0 = 140nm) and P680 (ILS_0 = 350nm). The ferrite peak positions were determined in the rolling (RD), transverse (TD) and normal (ND) directions.

Based on the peak positions, the lattice plane spacing and finally strains could be calculated. To get good reference peak positions, a stress free reference sample was measured. This sample was first isothermally transformed at 600°C, after which it was annealed at 670°C for 42 hours and furnace cooled to room temperature. The peak positions in the three measurement directions were nearly identical, with differences on the order of 10^{-4} Å being well within the experimental error, illustrating that the sample is indeed stress free. The average of the peak positions measured in the three directions is taken as the reference peak position from which the strains in the deformed samples were calculated.

The lattice strains for the P500 sample set are shown in Fig. 6.28, Fig. 6.29 and Fig. 6.30 for the RD, TD and ND directions, respectively. The lattice strain for the <220> reflection is not shown because, as expected, the results are identical to those of the <110> reflection. This correspondence does however indicate the good quality of the measurements.

The lattice strains in the TD remain close to zero for all grain families. Although it is not shown here, the same is true for the P680 sample set. The TD lattice strains will therefore not be discussed further. The lattice strain evolution in the ND is also similar for both sample sets, although the lattice strain is on average $0.5E^{-3}$ lower for the P680 samples. However, the P680 RD lattice strains are significantly different from the P500 RD ones, and are shown in Fig. 6.31.

It can be seen that the strain in the undeformed sample is slightly tensile, especially in the RD. This can be explained by the thermal strain misfit after cooling from the transformation temperature. The ferrite phase has a larger thermal expansion coefficient and will therefore want to shrink more than the cementite, leaving the ferrite in a state of tension.

The residual lattice strain in the RD and ND of the P500 sample increases very quickly at small rolling strain. Subsequently, a stage of nearly constant lattice strain in the RD follows, up to a strain of around 1.2. In this saturation stage, there is no intergranular residual lattice strain development in the RD. At strains larger than 1.5, intergranular strains suddenly start to develop in the RD. The <211> and <110> lattice strains can be seen to behave similarly and

(continues on page 96)

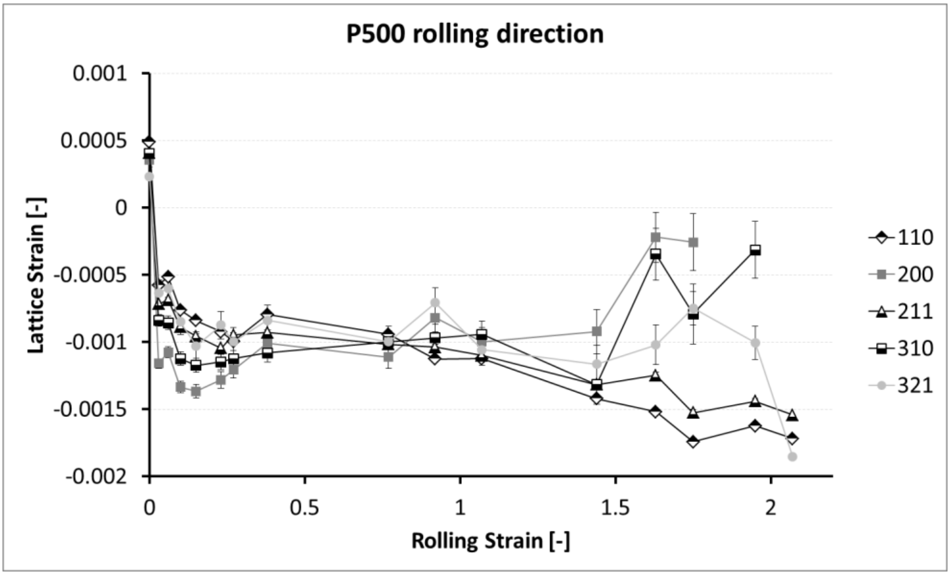

Fig. 6.28: Lattice strain for various ferrite grain families as a function of cold rolling strain. The lattice strains were obtained from peak positions measured in the rolling direction, on the P500 samples (ILS_0 = 140nm). When the error bars are not visible, they are of the same size as the data symbols.

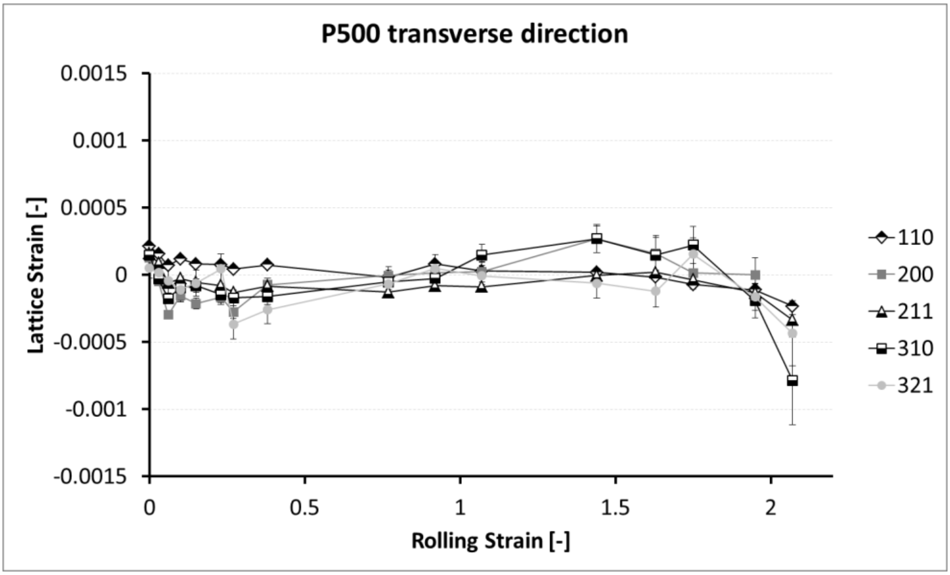

Fig. 6.29: Lattice strain for various ferrite grain families as a function of cold rolling strain. The lattice strains were obtained from peak positions measured in the transverse direction, on the P500 samples (ILS_0 = 140nm). When the error bars are not visible, they are of the same size as the data symbols.

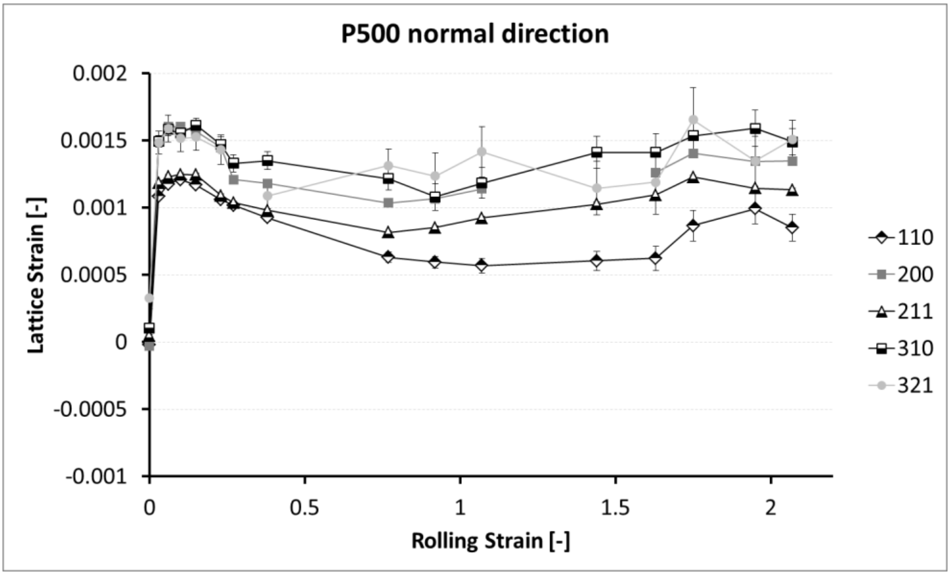

Fig. 6.30: Lattice strain for various ferrite grain families as a function of cold rolling strain. The lattice strains were obtained from peak positions measured in the normal direction, on the P500 samples (ILS_0 = 140nm). When the error bars are not visible, they are of the same size as the data symbols.

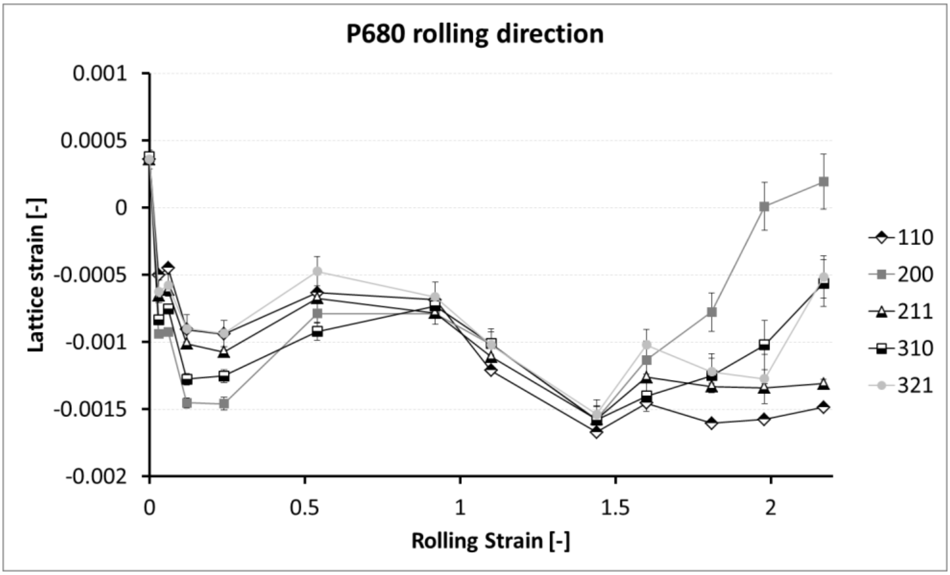

Fig. 6.31: Lattice strain for various ferrite grain families as a function of cold rolling strain. The lattice strains were obtained from peak positions measured in the rolling direction, on the P680 samples (ILS_0 = 350nm). When the error bars are not visible, they are of the same size as the data symbols.

continue to increase in absolute value with increasing rolling strains. On the other hand, the <200> and <310> lattice strains decrease in absolute value.

In the ND, a slight decrease of the lattice strain can be observed after the initial strong increase. In the RD, only the <200> lattice strain exhibits this drop. Some intergranular residual strain development can be observed in the ND. But with increasing rolling strain, there is very little variation.

The decrease of the lattice strain in the ND might be attributed to the increasing alignment of the lamellae parallel to the rolling plane. In the case of a perfect sandwich microstructure (i.e. a stack of flat and perfectly aligned ferrite and cementite sheets), no residual lattice strains can develop in the ND because the phases do not constrain each other in this direction and are not required to co-deform. The fact that the residual lattice strain remains well above zero indicates that, while the microstructure evolves in the direction of a sandwich, a perfect sandwich microstructure is never reached. This is confirmed by the microstructural observations in section 6.1.1.

As the rolling strain increases, the ferrite lattice strain in the rolling direction becomes compressive, as a result of the co-deformation with the harder cementite phase. The ferrite undergoes more plastic deformation than the cementite. This plastic misfit is countered by the introduction of a compressive strain in the ferrite phase and an expected tensile strain in the cementite phase. In the normal direction the material is compressed instead of extended and the opposite reasoning leads to the observed tensile residual ferrite lattice strain.

The RD residual lattice strains of the P680 sample set are different from the P500 samples. The decrease in absolute value of the lattice strains after the initial increase is much more pronounced. As a result there is no stage of nearly constant lattice strain. At these mid-range rolling strains, the intergranular strain development, although small in both sample sets, is as good as non-existent for the P680 samples. Additionally, the onset of strong intergranular strain development is shifted to slightly higher strains. From that point on, the absolute values of the <110> and <211> lattice strains don’t increase anymore, while those of the other grain families start to decrease. This difference in behaviour is discussed in section 8.1.3.

From the strains, the stresses were calculated according to the method described in section 5.2.2.2. The ferrite single crystal elastic constants were taken from J. Rayne and B. Chandrasekhar [108] and are shown in Table 6.2. Reuss type DEC’s were used in the calculation. In the following, only the results for the P500 sample series will be discussed. The results for the P680 sample series are shown in Appendix C, but they did not allow to draw any new or different conclusions. The P500 residual stresses are shown in Fig. 6.32, Fig. 6.33 and Fig. 6.34 for the three principle axes of the macroscopic sample. For three samples, the calculation has also been done taking into account the crystallographic texture. From Table 6.3, it can be seen that the differences are small compared to the range of stresses considered.

Table 6.2: Ferrite single crystal elastic constants used to calculate the DEC's. [108]

Ferrite elastic constants [GPa]	
C_{11}	233
C_{12}	135
C_{44}	118

Table 6.3: Residual stresses [MPa] in the rolling direction, calculated for different ferrite grain families, with and without crystallographic texture.

	No Tex.	With Tex.	No Tex.	With Tex.	No Tex.	With Tex.
Rolling strain	0.77		1.07		1.63	
σ^{110}	-200	-196	-254	-251	-365	-346
σ^{200}	-120	-120	-75	-76	140	140
σ^{211}	-213	-225	-221	-235	-232	-251
σ^{310}	-95	-90	-59	-53	115	124
σ^{321}	-147	-163	-146	-164	-173	-203

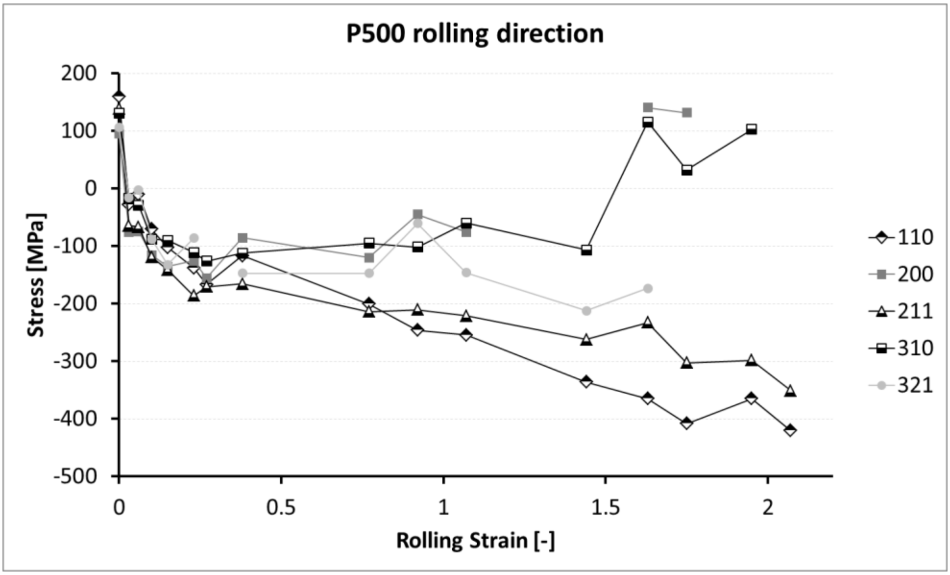

Fig. 6.32: Residual stress for various ferrite grain families as a function of cold rolling strain. The lattice strains were obtained from peak positions measured in the rolling direction, on the P500 samples.

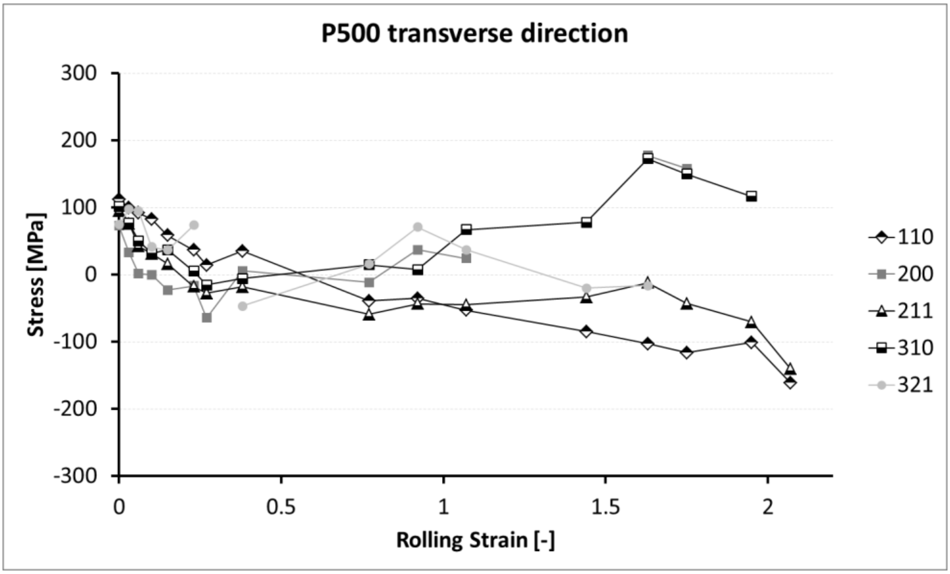

Fig. 6.33: Residual stress for various ferrite grain families as a function of cold rolling strain. The lattice strains were obtained from peak positions measured in the transverse direction, on the P500 samples.

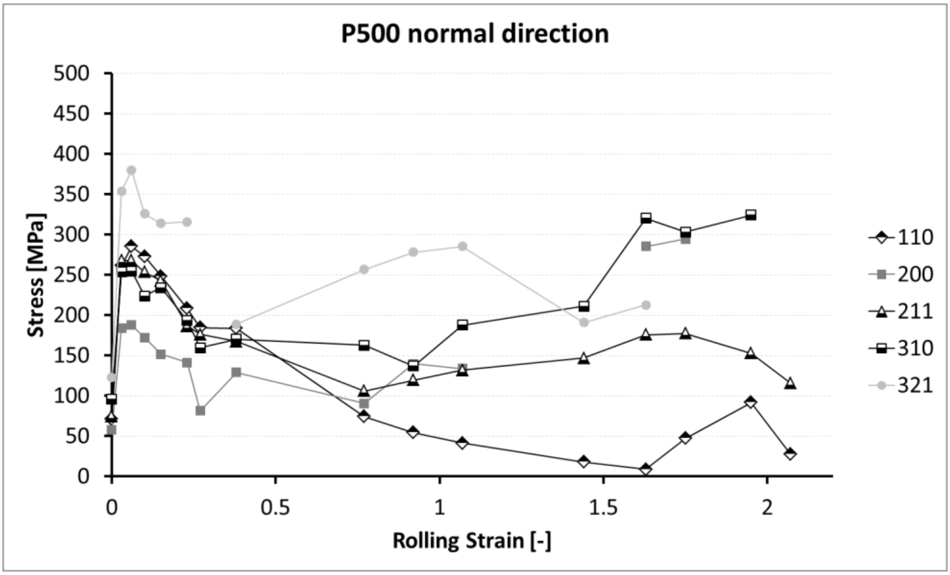

Fig. 6.34: Residual stress for various ferrite grain families as a function of cold rolling strain. The lattice strains were obtained from peak positions measured in the normal direction, on the P500 samples.

Neutron diffraction measurements were also carried out at the Heinz Maier-Leibnitz Zentrum (MLZ) in Garching. These where focussed on obtaining as much information as possible from the cementite phase. Nevertheless, the <110>-ferrite peak position was also determined because it only took a short time (2min.) to get a good diffraction peak. The same stress free reference sample was measured as used at POLDI. Although the sample is stress free, as was proven by the PSI measurements, the peak positions in the three measurement directions show deviations of ~0.01°. According to M. Hoffman, the responsible beam line scientist, this corresponds to the expected experimental error. The average of the peak positions measured in the three directions was taken as the reference peak position from which the strains in the deformed samples were calculated.

Only the P500 sample set was measured due to time considerations. From the strains, the stresses were calculated according to the method described in section 5.2.2.2. The same elastic constants were used as for the PSI measurements. Both the stress and strain evolution are almost identical to the PSI measurements and are given in Appendix D. This confirms the good quality of the measurements and indicates that the cementite strains measured at MLZ (see next section) can be safely compared to the ferrite strains measured at PSI.

6.2.2.2 Cementite micro-phase strain/stress

The cementite strains reported here were obtained on the P500 sample series at the MLZ in Garching. The measurements were done using a 2D-detector with an angular range of about 14°. In order to be able to measure for a long time, a single detector position had to be chosen. Based on the results for the first few deformation passes, it was decided to position the detector in such a way that the <131>, <221>, <122>, <230> and <040> cementite reflections could be observed. The <230> and <040> cementite lattice planes have virtually the same lattice plane spacing and their individual peaks cannot be distinguished. Additionally, the cementite <022> reflection overlaps with the <131> reflection and the <202> with the <230>-<040> reflection. However, based on the structure factors reported in [71], the intensity of the <022> and <202> peaks is too small to noticeably influence the diffraction profile.

The cementite reflections are clearly visible in both the stress-free reference sample and the undeformed starting material. The diffraction profile measured on the stress-free reference sample is shown in Fig. 6.35. The Miller indices of the observed cementite reflections have been indicated. Two peaks could not be attributed to either the ferrite or the cementite peak. They could also not be attributed to any other carbides known to occur in carbon steels, nor to escape peaks, fluorescence peaks, residual austenite, the sample holder material or any other material that could have entered the beam path. The two peaks thus remain unidentified.

The full profile is a combination of three separate profiles, obtained at three detector positions (62.5°, 72.5° and 82.5°). Already after the first rolling step (ε=0.03), the cementite peaks broaden significantly, making it difficult to separate them from the background. This is illustrated in Fig. 6.36, where the reference peak positions are indicated for comparison. At higher strains, the diffraction profile degrades even more, making peak fitting increasingly difficult and inaccurate. As a consequence the absolute values of calculated stresses and strains might be subject to significant errors, and it is rather their evolution with increasing rolling strain which is of interest.

In the same way as for the ferrite peak (see section 6.2.2.1), a reference peak position is obtained by averaging the peak positions as determined in three directions (RD, TD and ND) on the stress-free reference sample. After the first deformation step, the <131> and <221> cementite reflections completely overlap and could only be fitted as a single peak. The average of the <131> and <221> peak positions before deformation is taken as the reference position for this peak. The <230>-<040> cementite reflection was the only other cementite

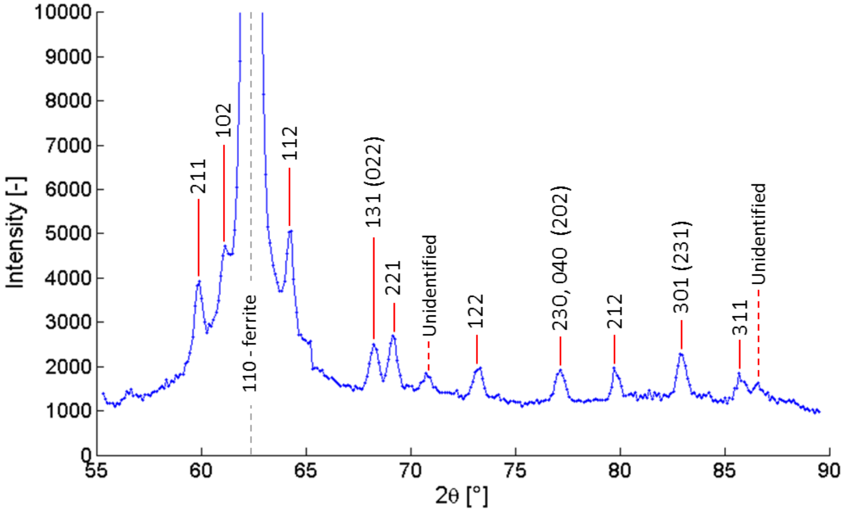

Fig. 6.35: Diffraction profile for the stress free reference sample, as measured at MLZ, Munich. The various diffraction peaks have been labelled with their Miller indices. The indices between brackets indicate cementite planes which do not reflect enough intensity to notably influence the measured profile. Two peaks cannot be attributed to either phase and remain unidentified.

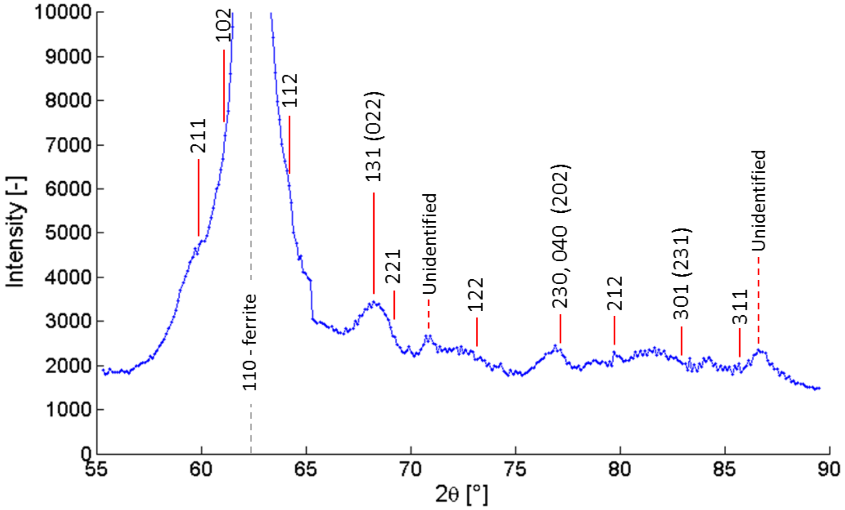

Fig. 6.36: Diffraction profile for a sample isothermally transformed at 500°C and cold rolled to a strain of 0.03. The stress-free reference positions of the cementite peaks are shown as a comparison.

reflection for which the peak position could be determined with agreeable accuracy. In analogue to the cold drawn wire, where it was shown in section 6.2.1.2 that cementite does not exhibit a strong deformation texture, any peak shift is assumed to be attributable to the existence of lattice strains and not to changes of the relative intensities of the two reflections contributing to one peak. The obtained lattice strains are shown in Fig. 6.37 and Fig. 6.38. Due to time considerations, the lattice strains in the TD could not be measured for all samples.

It can be seen that the sign of the calculated lattice strains for both cementite reflections is opposite to that of the ferrite reflections in the rolling and normal directions. This corresponds to the expectations, and the explanation for the observed behaviour is therefore analogous to the one given in section 6.2.2.1. The same cannot be said for the strain in the TD. There are ample reasons why this deviation could occur, as will be discussed further on in combination with the results of the stress calculation.

The residual stresses can be calculated from the measured lattice strains, under the assumption that the RD, TD and ND directions are the principal directions of the stress and strain state. This was done in the same way as for the ferrite stresses, according to the method described in section 5.2.2.2. For those samples for which the strain in the TD direction could not be measured, the average value of the TD strain in the previous rolling passes was adopted. This is believed to be a reasonable assumption as it could be seen from the PSI measurements that the lattice strain in the TD remains nearly constant.

Two major complications present themselves when calculating the cementite stress. Firstly, both studied peaks are a combination of two individual reflections. It is therefore unclear which DEC's should be used. Secondly, literature presents multiple sets of single crystal elastic constants which are not always similar. In the following, both issues will be addressed.

The importance of the first issue was assessed by comparing the stress values obtained when using the DEC's for each of the two grain families contributing to a single peak. It could be seen that the stress calculated for the <131>-<221> reflection did not differ qualitatively when using the DEC's for either the <131> or <221> grain family. The same holds for the <230>-<040> reflection. The difference in calculated stress is around 200 MPa, but is independent of the rolling strain. The evolution of the residual stress therefore doesn't depend on the choice of the DEC's, only its magnitude. In light of the uncertainty on the peak position and the single crystal elastic constants (see below), it was decided to use the average of the DEC's of the two grain families contribution to one peak for the stress calculation.

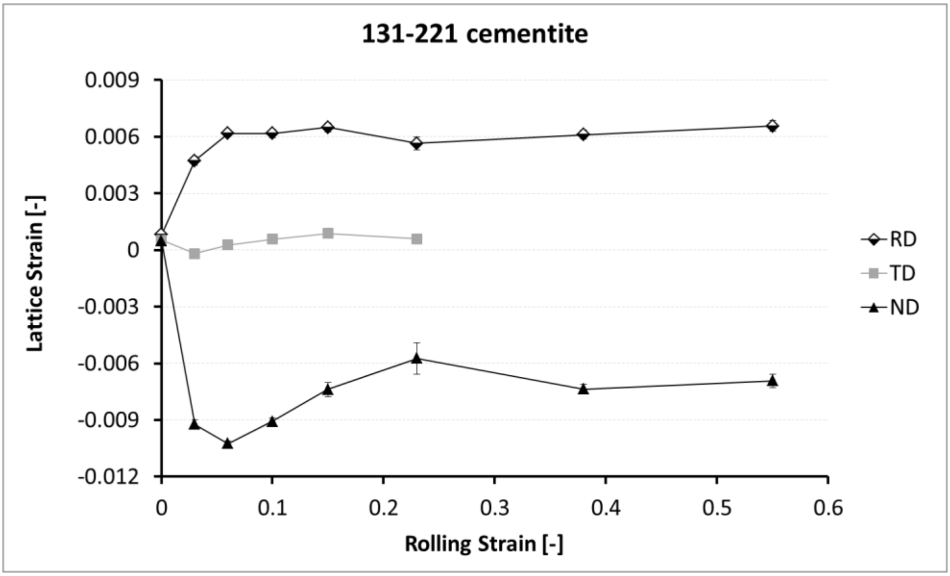

Fig. 6.37: Cementite lattice strain as a function of cold rolling strain, as obtained for the <131>-<221> overlapping reflections. The lattice strains are shown for the three principle directions of the rolled sheet.

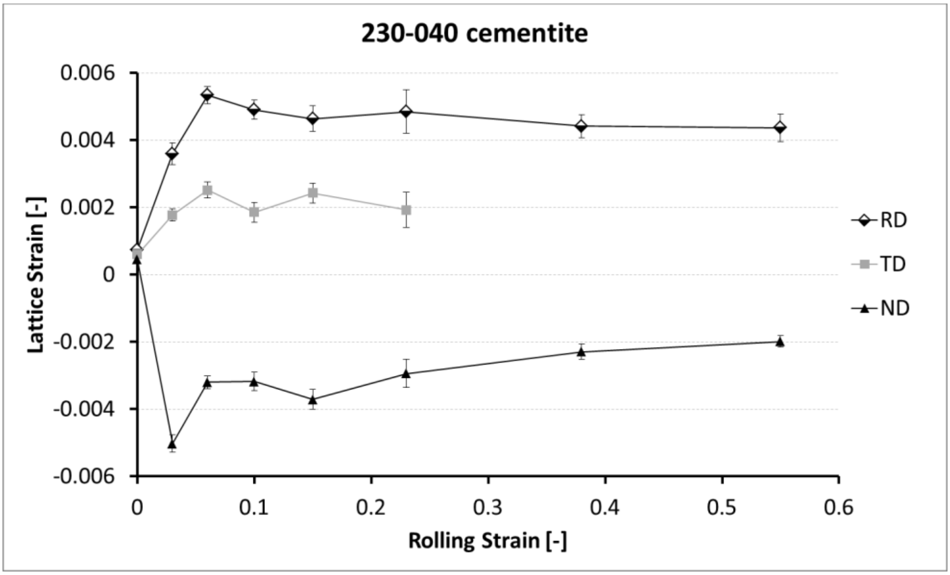

Fig. 6.38: Cementite lattice strain as a function of cold rolling strain, as obtained for the <230>-<040> reflection. The lattice strains are shown for the three principle directions of the rolled sheet.

The second issue requires a somewhat more in depth analysis. Previously, DEC's for the d-sin$^2\psi$ method used for the stress measurements on wire were calculated based on the single crystal elastic constants proposed by Jiang et al. [33] and Nikolussi et al. [34] (see section 6.2.1.2), which were obtained from ab-initio calculations. The same single crystal elastic constants were adopted to calculate the DEC's for use with the principle directions method. The residual stresses thus calculated for the <131>-<221> reflection are shown in Fig. 6.39. It is immediately obvious that this gives a completely different picture as compared to the lattice strain evolution (Fig. 6.37). The stress values are strongly influenced by the lattice strains in the ND. The residual stresses in the RD direction even becomes negative, which contradicts the expectations. As no significant ferrite intergranular stresses develop at small and moderate deformations, it is expected that the different cementite grain families also behave similarly. A negative cementite residual stress in the rolling direction thus violates the stress equilibrium equation.

A remarkable feature of the elastic constants proposed by Jiang et al. and Nikolussi et al. is the extreme elastic anisotropy caused by the very low c_{44} component of the stiffness matrix. Although there is experimental validation available for the elastic anisotropy of cementite from the data obtained by Weisser et al. [32], their values differ considerably from the data published by Nikolussi et al. This difference is attributed to the effect of the embedding matrix. Moreover, ab-initio calculations by Henriksson and Nordlund [35] did not result in a very low c_{44} component. Jiang et al. also illustrate the possibility of a higher c_{44} component, if during the calculation internal atomic relaxations are not allowed. In that case, elastic constants are obtained which are very similar to those calculated by Henriksson and Nordlund. The aforementioned single crystal elastic constants are summarised in Table 6.4.

Table 6.4: Cementite single crystal elastic constants. All values are expressed in GPa. The values according to Henriksson and Nordlund were used in all subsequent stress calculations. ^{a} with and ^{b} without internal atomic relaxation.

	c_{11}	c_{22}	c_{33}	c_{44}	c_{55}	c_{66}	c_{12}	c_{13}	c_{23}
Jiang et al. [33]^a	388	345	322	15	134	134	156	164	162
Jiang et al. [33]^b	413	412	378	82	136	140	154	167	170
Nikolussi et al. [34]	385	341	316	13	131	131	157	162	167
Henriksson and Nordlund [35]	*394*	*412*	*360*	*83*	*133*	*136*	*157*	*146*	*166*

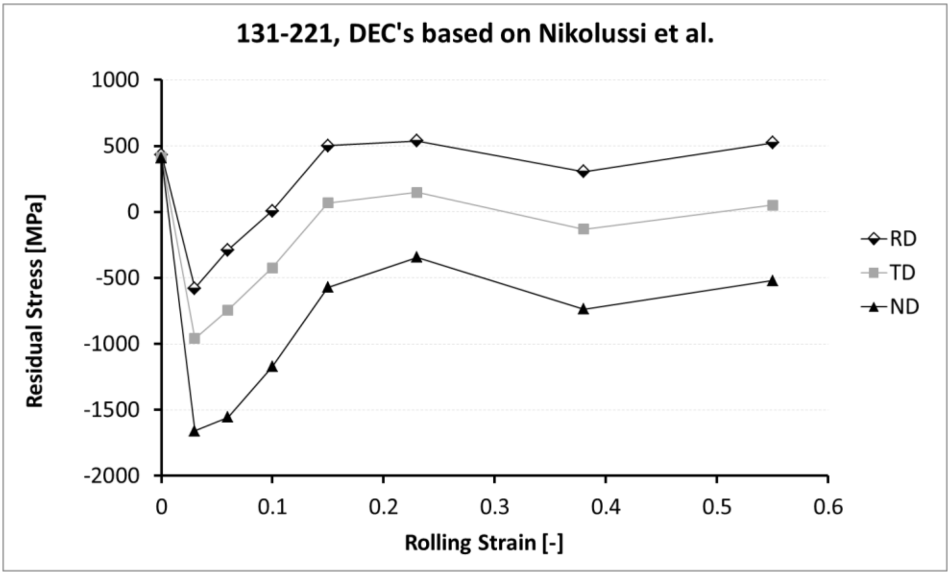

Fig. 6.39: Residual cementite stress for the <131>-<221> reflection as a function of cold rolling strain. The DEC's used for the calculation were obtained based on the single crystal elastic constants proposed by Nikolussi et al. [34]*.*

The residual stresses for the <131>-<221> cementite reflection, calculated with DEC's based on the elastic constants proposed by Henriksson and Nordlund, are shown in Fig. 6.40. A nearly identical result can be obtained by using the Nikolussi elastic constants, if the c_{44} component is set to 80 GPa, proving that the difference between Fig. 6.39 and Fig. 6.40 can be attributed to the different c_{44} component. A positive residual stress is now obtained in the rolling direction, thereby more closely respecting the stress equilibrium equation. It is therefore believed that the cementite elastic behaviour in the current study and material is better described by the more isotropic constants proposed by Henriksson and Nordlund.

The correct values for the cementite elastic constants are still a matter of debate. It is at this point not possible to give a decisive argument as to why and under what circumstances which elastic constants should be chosen. To complicate this matter further, Jiang and Srinivasan [109] recently reported a calculation indicating that the elastic behaviour of cementite can change under deformation. Furthermore, experimental results obtained by Ledbetter [110] suggest that embedded cementite might behave different from free 'bulk' cementite, as was also suggested by Weisser et al. [32]. The embedding matrix might cause a structural change of the cementite crystal lattice and change the elastic constants through a mechanism similar to the one described by Jiang and Srinivasan. Or, alternatively, the deviation from ab-initio calculations might be caused by a ‘component stiffness effect’, where the shape of the cementite lamellae influences the stiffness in the same way as the structural shape of a beam determines its elastic behaviour. Finally, one can imagine that the electronic structure of cementite is influenced by the electrons in the neighbouring ferrite, if the cementite lamellae become thin enough (nanometre scale, 10nm = 15-22 cementite unit cells). As the electronic structure changes, so will the elastic constants. It might then even become possible for the elastic constants to change with increasing deformation and thinning of the lamellae.

To the authors knowledge, the effects of the embedding ferrite matrix on the cementite elastic constants have not yet been taken into account in ab-initio calculations. Unless mentioned otherwise, the single crystal elastic constants according to Henriksson and Nordlund will be adopted for all stress calculations based on the principal directions method. However, all calculated cementite residual stresses should be viewed in light of the above discussion.

The residual stresses for the <230>-<040> cementite reflection have also been calculated and are shown in Fig. 6.41. Surprisingly, for these grain families the difference between the stresses obtained using the elastic constants proposed by Nikolussi et al. and those proposed by Henriksson and Nordlund is very small.

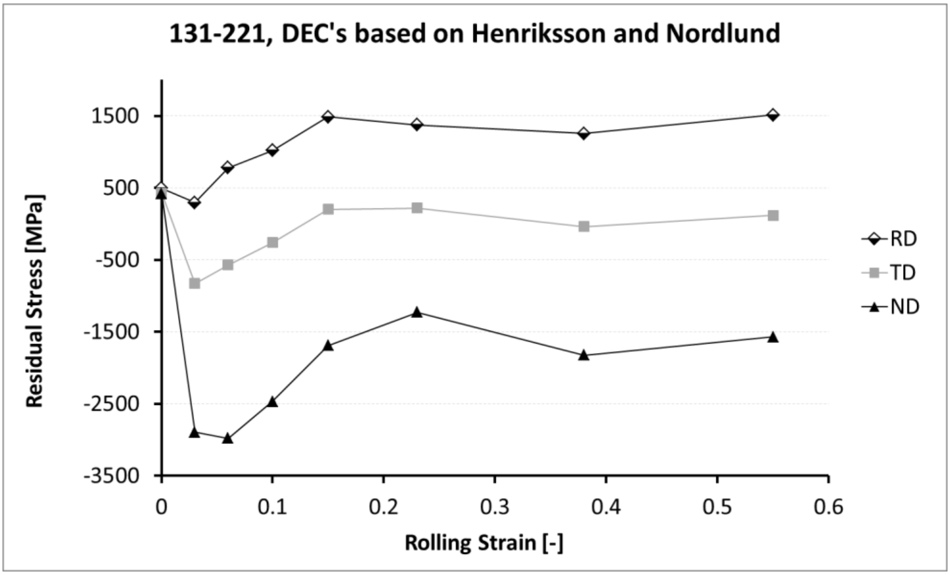

Fig. 6.40: Residual cementite stress for the <131>-<221> reflection as a function of cold rolling strain. The DEC’s used for the calculation were obtained based on the single crystal elastic constants proposed by Henriksson and Nordlund [35].

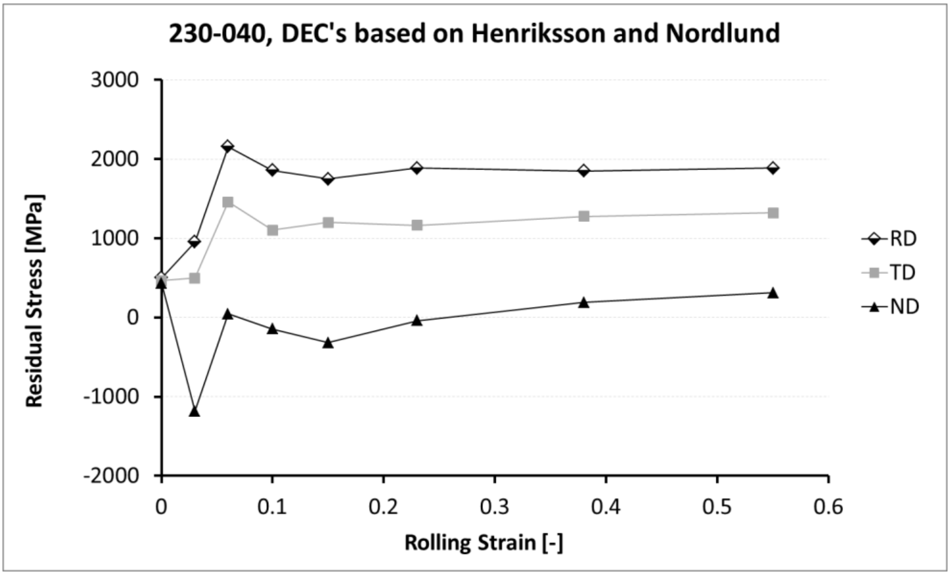

Fig. 6.41: Residual cementite stress for the <230>-<040> reflection as a function of cold rolling strain. The DEC's used for the calculation were obtained based on the single crystal elastic constants proposed by Henriksson and Nordlund [35].

Two problems present themselves when the ferrite and cementite residual stresses and strains are compared. Firstly, the stresses and strains in the undeformed (S0) sample are positive in both phases. Secondly, the stresses and strains in the transverse direction are positive for both the ferrite phase and the <230>-<040> cementite reflection. These two observations violate the stress equilibrium equation and can only be explained as an error in the strain and/or stress calculation.

A physical source of error could be introduced if the reference material is not actually stress free, but contains thermal residual stresses. Because the thermal stresses/strains are tensile in the ferrite phase and compressive in the cementite phase, correcting for the already present thermal stresses would shift the found ferrite stresses/strains more towards tension and the cementite stresses/strains more towards compression. Although this would make the current data more coherent, it would lead to thermal ferrite stresses which are much higher then what has previously been reported (50-100 MPa) from experiments and calculations [22,111,112]. Additionally, the thermal stress as calculated assuming the used reference as stress free, already results in a value which is slightly higher than the expected value of around 100 MPa.

Different reference peak positions have been used in an attempt to obtain 'better' results. 'Better' means that the experimental cementite residual stress differs less from the cementite stress as calculated from the experimental ferrite stress. It has been tried to take the undeformed sample S0 as a reference or to take a separate reference position for the three measurement directions, instead of averaging over the three directions, but neither option gave better results. Nor is there any physical basis as to why the undeformed sample would be a better reference than the annealed sample. Finally, it should be mentioned that it was not possible to use theoretical lattice constants as a reference, because the neutron wavelength at MLZ was not exactly known.

Considering the unsatisfying quality of the cementite peaks, the strong overlap with the background and <110> ferrite peak tails, the uncertainty in the reference peak position and the ambiguity of the cementite elastic constants, it is best to focus on the evolution of the lattice strain and residual stress with rolling strain. The evolution is less dependent on the reference peak position, the quality of a single peak or value of the elastic constants and can safely be discussed based on the obtained data.

Finally, it should remarked that, for the <131>-<221> cementite reflection, the stress and strain evolution give a different view on what is happening. Whether this is an real, physical phenomenon, or an effect caused by a possible deviation between calculated and real single crystal elastic constants is unclear. However, the discrepancy has been observed, and should be held in mind during the subsequent discussion of the results.

In light of the above, and as has also been pointed out in the previous section, the obtained stress values are to be considered as indicative values instead of the actual stress in present in the material. Further discussion and analysis of the results will therefore mainly be based on the lattice strain measurements, which do give a physically correct value for the strains actually present in each phase.

In conclusion to this section, it is useful to repeat what can unambiguously be inferred from the cementite results:

- The lattice strains show a smooth evolution that quickly reaches a saturation value in the RD and decreases in the ND after an initial strong increase. They are opposite in sign to the ferrite lattice strains and the strain evolutions in both phases are in close agreement.
- The residual micro-phase stress calculated for the <230>-<040> cementite reflection also saturate quickly and follow the lattice strain evolution fairly well. They qualitatively correspond to what would be expected from the ferrite micro-phase stress, albeit with a shift towards tension.

6.2.3 Diffraction line broadening

The various ex-situ diffraction experiments described in the previous sections were all aimed at determining lattice strains. However, not only the peak position is obtained, the fitting procedure also yields the peak shape. The peak width is characterized by the Full Width at Half Maximum (FWHM). Alternatively, the Integral breadth could be used. However, the used fitting routines only yielded the FWHM. In this section, the observations which can be made based on the peak width and shape for the measurements made on cold rolled sheet will be reported.

Two types of peak fit functions were used. The peaks measured at MLZ were fitted using Pseudo-Voigt profiles, while the peaks measured at PSI were fitted using a routine (Mantid) specially designed to handle the 2D TOF measurements. The former functions is a simplification of the Voigt profile, which is a convolution of a Gaussian profile and a Lorentzian profile. Instead of convoluting the two profiles, the Pseudo-Voigt profile is obtained by summing the Gaussian and Lorentzian profile. The η-parameter determines the relative contributions of the two profiles. For $\eta = 1$, the Pseudo-Voigt profile becomes Lorentzian. For $\eta = 0$, the Pseudo-Voigt profile becomes Gaussian.

Using the Pseudo-Voigt function allows a separation of size and strain broadening. Size-broadening results from a reduction of the coherently diffracting domain size, which is linked to grain size, dislocation cell size or in this case also the ILS. Strain-broadening results from variations in local strain state between regions contributing to the same diffraction peak. The Lorentzian contribution to the Pseudo-Voigt profile is believed to represent the contribution of size-broadening to the peak width, while the Gaussian contribution represents strain-broadening [113].

The evolution of the relative FWHM of various ferrite reflections measured at PSI, is shown in Fig. 6.42 for the RD. Relative FWHM meaning FWHM divided by peak position, in Q-space ($2\pi/d$). A sharp initial increase of the peak width is observed. At intermediate strains the peak width continues to increase, albeit at a significantly slower rate. Starting from a strain of 1.2, which is also the point where intergranular strains start to develop, the various ferrite grain families start to behave somewhat different. This is the only difference when comparing to the P680 samples, where the divergence is much less pronounced. In the transverse and normal directions, the evolution is very similar, except for the fact that at larger strains the divergence of FWHM is not observed (see Fig. 6.43). The observed peak widths are largest for the ND and smallest for the TD, but the difference is not significant. These observations were confirmed for the 110 reflection by the MLZ measurements.

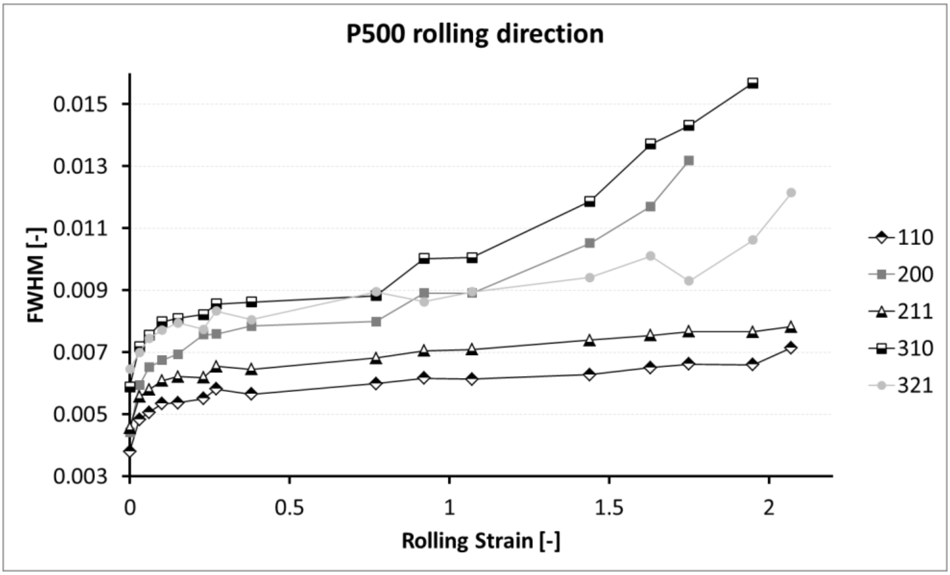

Fig. 6.42: Relative FWHM of various the ferrite reflection as a function of cold rolling strain. The FWHM is given for peak profiles measured in the rolling direction and for the P500 sample.

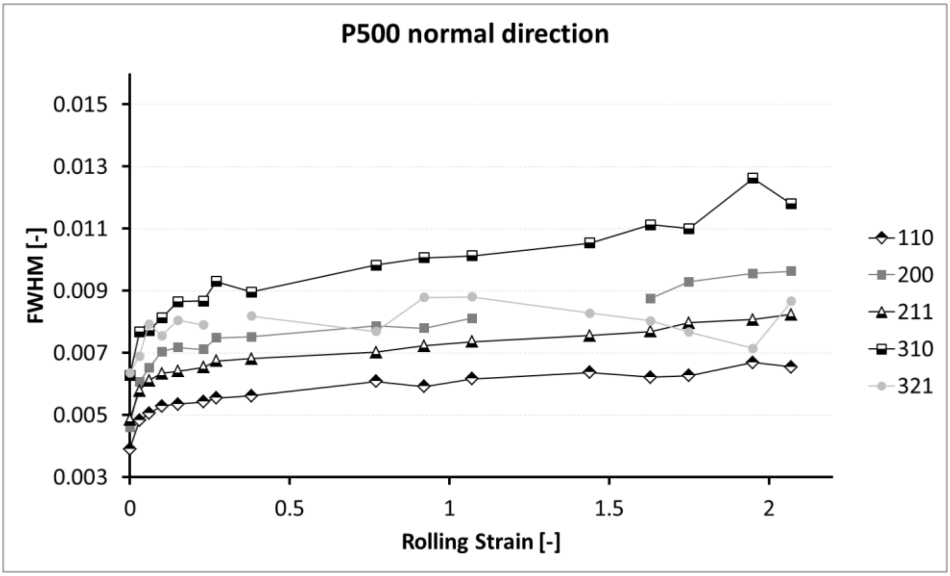

Fig. 6.43: Relative FWHM of various the ferrite reflection as a function of cold rolling strain. The FWHM is given for peak profiles measured in the normal direction and for the P500 sample.

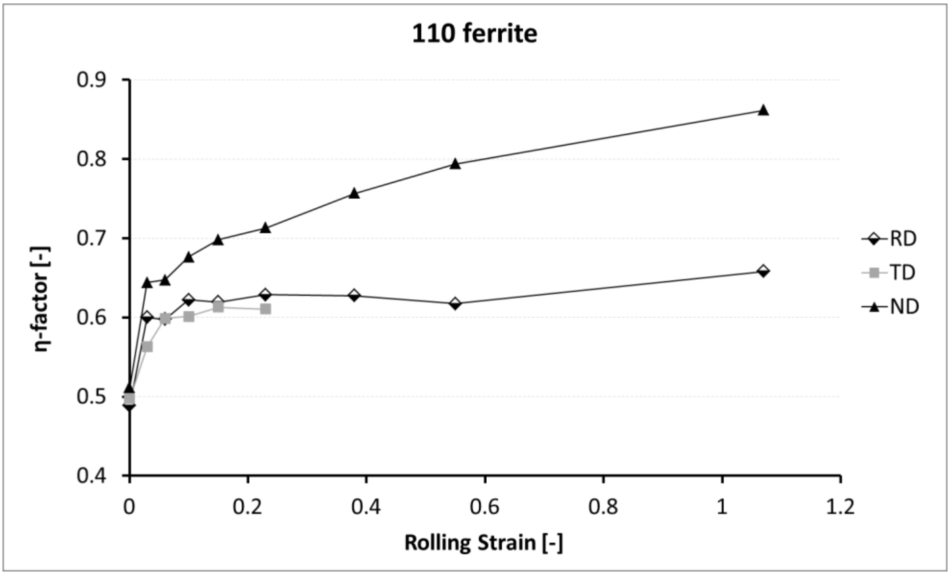

Fig. 6.44: Value of the eta-factor, obtained after fitting of the profiles with a Pseudo-Voigt function. This factor is a measure for the Lorentzian contribution to the peak profile.

As stated above, the <110> ferrite peak measured at MLZ was fitted using a Pseudo-Voigt function. The Lorentzian contribution to the Pseudo-Voigt function can be characterized by the η-factor. The value of the η-factor as a function of cold rolling strain is shown in Fig. 6.44. It can be seen that the η-factor increases a lot after the first deformation pass. Subsequently, the increase is almost stopped in the RD and TD directions, while it continues in the ND.

The origin of the different Lorentzian contribution to RD and TD peaks as compared to ND peaks can be understood from the lamellar microstructure of the material. Bragg's law in theory only holds for an infinite stack of lattice planes. Because all crystals are finite, a certain amount of diffraction peak broadening will occur. For equiaxed grains, this peak broadening is the same in all directions. However, in a perfect, lamellar sandwich as illustrated in Fig. 6.45 the normal direction is not equivalent to the other two, and will exhibit a different amount of size broadening. In the RD and TD directions, diffraction can in principle occur from an infinite stack of lattice planes, resulting in minimal size broadening. In Fig. 6.45 these lattice planes are drawn in dark and medium grey. The diffraction peaks recorded in the ND direction come from planes perpendicular to ND. As can be seen from the sketch, the amount of ferrite lattice planes which can be stacked uninterrupted is limited by the presence of cementite lamellae, resulting in significant size broadening. As the microstructure evolves towards a sandwich due to the alignment of the lamellae, the difference between ND and the other directions will increase and the size broadening in the ND will become more and more important. This is further reinforced by the reduction of the interlamellar spacing with increasing rolling strain.

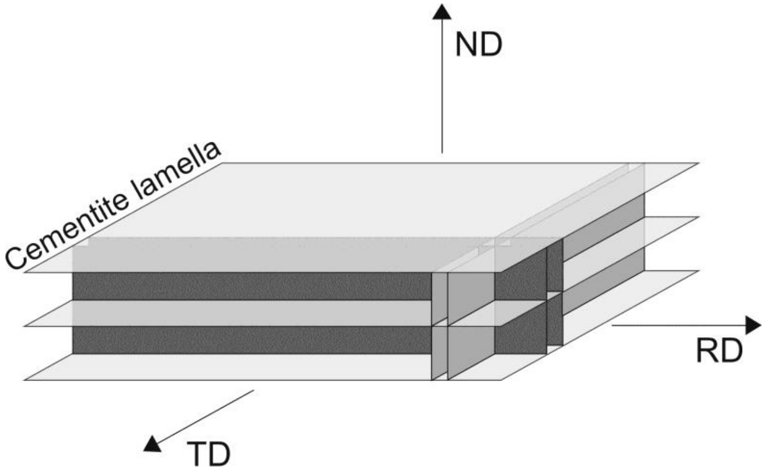

Fig. 6.45: Illustration of the diffracting planes perpendicular to the TD (dark grey) and the RD (medium grey) in a stack of parallel cementite lamellae (light grey) aligned with the rolling plane.

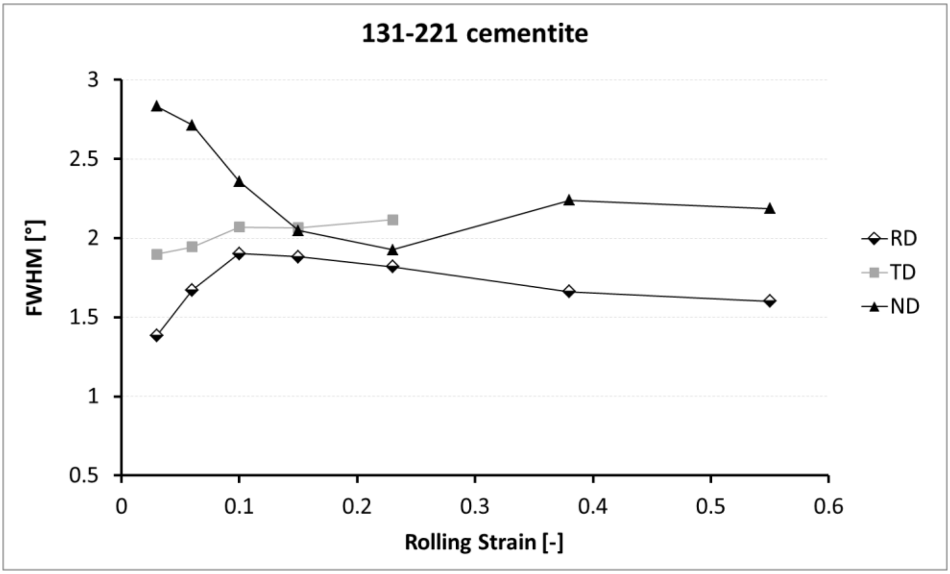

Fig. 6.46: FWHM of the <131>-<221> cementite reflection as a function of cold rolling strain. The FWHM is given for peak profiles measured in the three principle sample directions. In the RD, strong overlap with the <110> ferrite tail occurs, thereby artificially reducing the peak width.

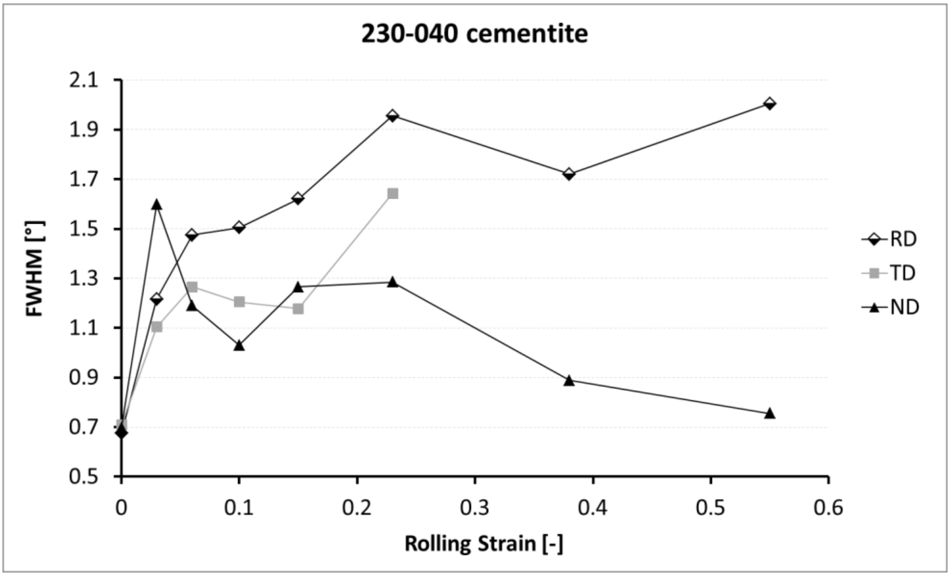

Fig. 6.47: FWHM of the <230>-<040> cementite reflection as a function of cold rolling strain. The FWHM is given for peak profiles measured in the three principle sample directions. The curves are less smooth as a result of the somewhat lower quality of the <230>-<040> cementite peak.

The peak widths could also be determined for the <131>-<221> and <230>-<040> cementite reflections and are shown in Fig. 6.46 and Fig. 6.47, respectively. It should be remarked that the peak width at zero strain is not given for the <131>-<221> reflection because, at that point, the two peaks were not yet overlapping. Only after the first rolling pass does strong peak broadening result in the overlapping of the <131> and the <221> cementite reflection. A comparison of the double peak's width to the single peaks' peak width does not have any physical meaning. At larger strains, following the evolution of the width of the double peak is meaningful, as long as both profiles have the same shape and don't become asymmetric. All other cementite reflections were so broad and small that they overlapped too much with other peaks or their tails were overshadowed too much by the background to be able to reliably determine the peak shape and thus width.

For the <230>-<040> peak a comparison to the undeformed material is possible. It follows that the peak width nearly doubles after the first rolling step with a strain of 0.03. Although it cannot be expressed quantitatively, this very strong broadening after the first rolling step can also be observed when comparing the diffraction profiles in Fig. 6.35 and Fig. 6.36. It is this strong broadening that results in the overlapping of the <131> and <221> diffraction peaks.

The peak width of the <131>-<221> reflection in the rolling direction became very unreliable at rolling strains larger than 0.1. The <131>-<221> reflection is superimposed on the tail of the very intense <110> ferrite reflection. As the rolling strain increases, the <110>-tail becomes increasingly more intense because of texture development. This results in the tail of the <131>-<221> reflection being swallowed by its ‘background’. It therefore seems as if the peak width is decreasing, while in reality the peak is likely broadened continuously. This trend can indeed be observed for the <230>-<040> reflection.

The problem described above does not occur for the peak measured in the normal direction. The strong crystallographic texture of the ferrite phase results in a much lower intensity of the <110>-peak in the normal direction. Consequently, the tails of the <110>-peak do not reach all the way to the <131>-<221> cementite reflection. The observed decrease in peak width in the normal direction is thus a real phenomenon as is also confirmed by the observation of the same trend for the <230>-<040> reflection.

At the small strain where this phenomenon is occurring (rolling strain <0.2), size broadening is not believed to effect the evolution of the peak width, nor can it explain a reversal of the peak broadening in the ND. The observed changes in peak width thus have to be linked to strain broadening. This will be discussed in-depth in section 8.3.

The above discussion is entirely focussed on the peak profiles as obtained from cold rolled pearlitic steel sheet. However, also the synchrotron measurements on cold drawn wire indicate importance of significant peak broadening. The results for the ferrite phase have previously been reported by Kriška et al. [105]. The cementite peaks undergo a strong broadening and a decrease of their intensities after the first drawing pass. However, at higher strains no continued broadening of the cementite peaks could be observed. This is in disagreement with the observations made in [32] and the current observations on cold rolled sheet. However, the lack of broadening during the synchrotron diffraction study is probably due to the instrumental broadening being too large to accurately measure the cementite peak profiles. An observed reduction in peak intensity without a broadening of the peaks indicates that when the peaks broaden, the tails are lost in the background.

6.2.4 Diffraction profiles

The diffraction information obtained at PSI is a 2D spectrum, which, as has been discussed in section 5.2.3.2, can be fitted with specialized software. In order to visualize and interpret the peak shapes, this data can be translated in a 1D spectrum and fitted with standard fitting tools. From these 1D spectra, it could be seen that the ferrite diffraction peaks develop a marked asymmetry with increasing rolling strain. The tail on one side of the ferrite peaks is lifted to higher intensity values. In Fig. 6.48 this is illustrated for the <110> ferrite peak in the rolling direction, measured at a rolling strain of 1.75. The intensity is given as a function of $Q = 2\pi/d$. A perfect fit could be obtained using an asymmetric Pearson VII function, which was available in the software present at PSI, as is shown by the dotted line. The asymmetry is captured by allowing different fitting parameter on the left and right hand side of the maximum intensity position. As a reference, a symmetric single peak Gaussian fit is drawn with a solid line. This kind of asymmetry starts to become visible from a rolling strain of ~0.9 on. The higher the strain, the more pronounced the asymmetry.

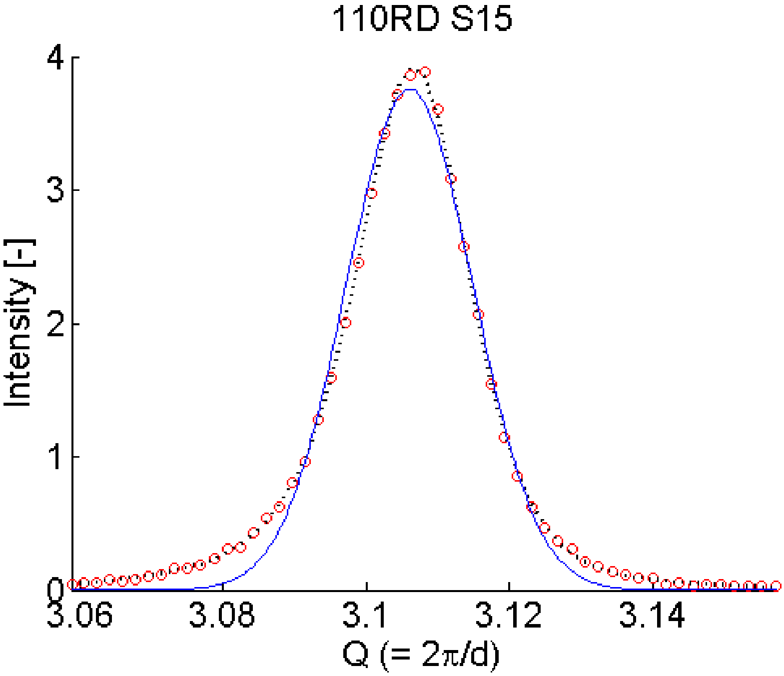

Fig. 6.48: <110> ferrite diffraction peak measured at POLDI, PSI in the rolling direction of a sheet cold rolled to a strain of 1.75. The dotted line illustrates the fit obtained using an asymmetric Pearson VII function. The solid line gives the fit using a Gaussian function. Q has units of Å^{-1}.

The asymmetry is also visible for all other diffraction peaks. However, for low intensity peaks the asymmetry is much more difficult to observe. All diffraction peaks measured in the rolling direction have their low-Q-side tail lifted, while all diffraction peaks measured in the normal direction have their high-Q-side tail lifted. In the transverse direction, the asymmetry is much less pronounced even though the peak intensities are reasonably high. Still, a slight lifting of the low-Q-side tail is also observed.

It should be mentioned that, while Fig. 6.48 shows a diffraction profile measured at PSI, the asymmetry was also observed for the <110> peaks measured at MLZ. Additionally, the diffraction profiles measured on cold drawn steel wires using synchrotron diffraction at BESSY also exhibit the same asymmetry. The asymmetry of the peaks is therefore clearly a material related effect, which might be independent of the imposed deformation mode.

Further analysis of the peak profiles showed that very good fits can be obtained by summing two symmetric Gaussian profiles:

$$f(x) = a_1 \exp\left(-\left(\frac{x-b_1}{c_1}\right)^2\right) + a_2 \exp\left(-\left(\frac{x-b_2}{c_2}\right)^2\right)$$

Two examples of such fits are shown in Fig. 6.49. The sum of the two Gaussian profiles as well as the individual Gaussians are depicted. The goodness of the fit is obvious from the graphs. The intensity and position of the total peak is mainly determined by the highest of the two Gaussians, while the low intensity, broad Gaussian is responsible for the peak asymmetry.

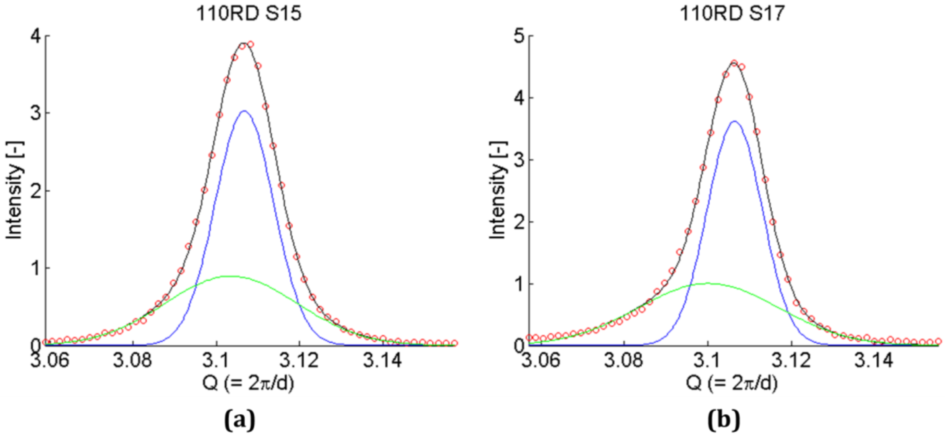

Fig. 6.49: 110 ferrite diffraction peaks as measured in the rolling direction of two samples from the P500 sample set: (a) ε = 1.75; (b) ε = 2.07. The evolution of the peak asymmetry can clearly be observed.

A qualitative analysis of the peak shape based on a sum of two Gaussians has only been performed for the highest intensity peaks, i.e. the <110> peak in the rolling direction and the <211> peak in the normal direction. For the <110> peak, the low intensity, broad Gaussian is shifted towards lower Q values, or thus higher d values. This means that the smaller peak moves towards less compressive strains. For the <211> peak, it is shifted towards higher Q values, or thus lower d values. It therefore moves towards less tensile strains. The small peak then behaves as if it would belong to a material, with a flow strength in between that of ferrite and cementite. As will be discussed in more detail further on, this could be explained by a region with a much higher dislocation density at the interface between ferrite and cementite.

Based on the individual peak positions of the two Gaussian profiles, the strains were calculated and compared to the strain obtained from the full 2D Mantid fitting (see section 6.2.2.1). In Fig. 6.50 the result as obtained for the <110> peak measured in the rolling direction is shown. The slim, high intensity Gaussian is referred to as 'bulk' ferrite. The broad, low intensity Gaussian is referred to as 'interface' ferrite. It can be seen that the bulk ferrite behaves nearly identical to the result obtained from the 2D Mantid fitting. The interface ferrite behaves radically different. Although it is not as pronounced, a same trend can be observed in Fig. 6.51 for the <211> peak, measured in the normal direction, albeit only at higher rolling strain values.

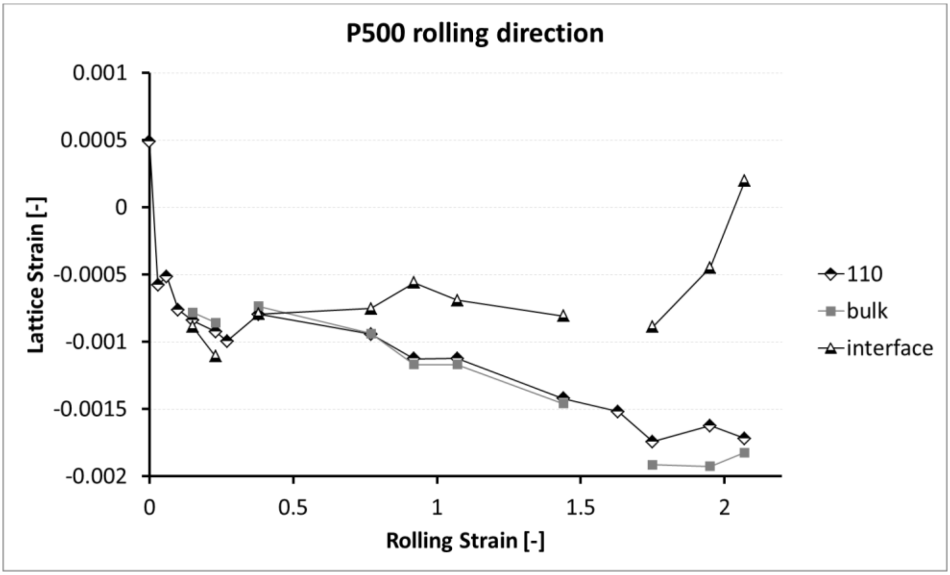

Fig. 6.50: Lattice strain in the rolling direction, as a function of cold rolling strain, for the P500 sample set. The lattice strain as obtained from the Mantid peak positions (110) is compared to the lattice strain obtained from the high intensity (bulk) and low intensity Gaussians as illustrated in Fig. 6.49.

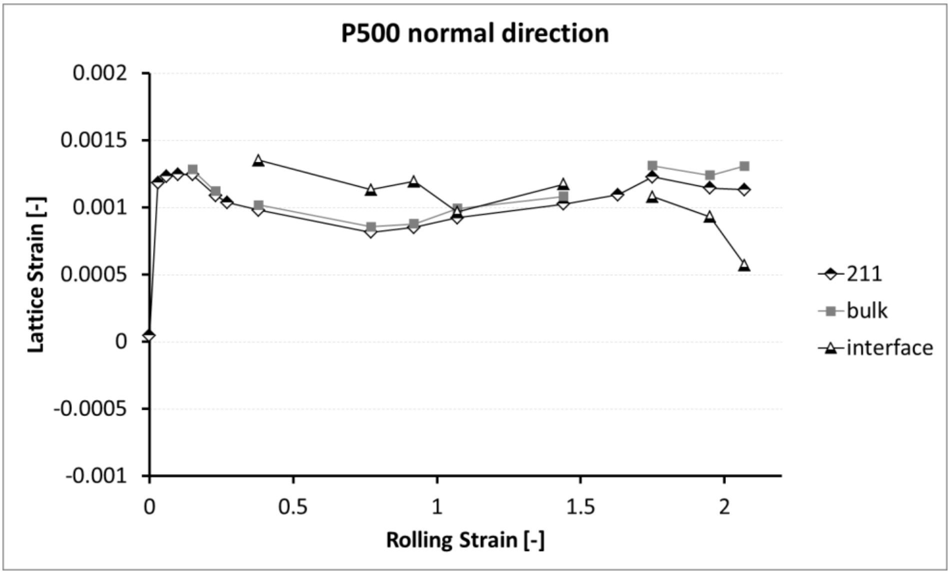

Fig. 6.51: Lattice strain in the normal direction, as a function of cold rolling strain, for the P500 sample set. The lattice strain as obtained from the Mantid peak positions (<211>) is compared to the lattice strain obtained from the high intensity (bulk) and low intensity Gaussians as illustrated in Fig. 6.49.

Taking into account these observations, it is reasonable to postulate the existence of ferrite with a locally higher flow stress at the interface between ferrite and cementite. This interface-ferrite could result from the accumulation of dislocations at the ferrite-cementite interfaces. Because of the strongly increasing dislocation density, this interface phase would exhibit a very high strain hardening rate and reach a flow stress much higher than that of the 'bulk' ferrite, i.e. in the centre of the lamellae or in non-lamellar regions, but lower than that of cementite.

By comparing the integrated intensity of the two individual Gaussian peaks to that of the total peak, the volume fractions of interface and bulk ferrite can be estimated. The result is shown in Fig. 6.52. A clear trend can be observed. The volume fraction of bulk ferrite decreases, while the volume fraction of interface ferrite increases. This could indicate that the dislocation rich interface layer becomes thicker with increasing strain.

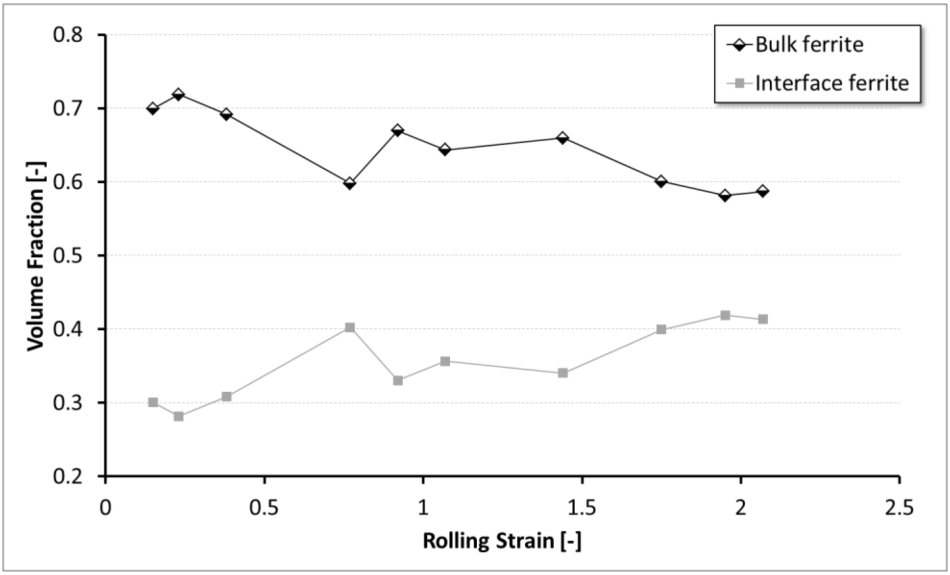

Fig. 6.52: Volume fractions of bulk and interface ferrite. Estimated from the integrated intensity of the individual Gaussians, obtained from fitting the experimental profile with a sum of two symmetric Gaussian profiles.

A similar two-peak analysis of an asymmetric diffraction profile was, to the authors knowledge first proposed by Ungár and Mughrabi et al. [114,115], for the analysis of deformed copper single crystals. During deformation a cell substructure developed and two symmetric profiles, one for the cell walls and one for the cell interior, were shown to be combined in the experimentally observed asymmetric diffraction peaks. More recently, Thilly et al. [16] performed a similar analysis for multi-scale Cu-Nb wires. The above interpretation based on the presence of interface-ferrite is also supported by SEM and TEM investigations that indeed illustrate the accumulation of dislocations at the interfaces (see Chapter 3).

As an additional remark, it should be mentioned that the onset of peak asymmetry might be responsible for the larger increase in peak width of the <310>, <200> and <321> ferrite peaks at strains larger than 1. These peaks have a much smaller intensity than the <110>, <211> and <220> peaks. The asymmetry which is mainly limited to the tails of the peaks therefore has a larger influence on the FWHM as compared to the high intensity peaks. For the latter peaks, the asymmetry is situated well below the half intensity point.

6.3 Internal lattice strain characterization

In this section, the results obtained during in-situ tensile tests on a number of samples will be presented. The experiments were performed at the Nuclear Physics Institute (NPI) in Řež. Four kinds of samples were produced and tested:

1. *As-patented:* Austenitized and isothermally transformed at 500°C.
2. *As-rolled:* Isothermally transformed at 500°C and cold rolled to a strain of 1.1.
3. *RS-relieved:* Cold rolled to a strain of 1.1, followed by a heat treatment for 15min at 470°C in order to remove the residual stresses present after rolling.
4. *Spheroidised:* Cold rolled to a strain of 1.1, subsequently heat treated for 8.5hours at 670°C and followed by overnight furnace cooling to room temperature.

From all samples dog-bone shapes were machined, which were subjected to a uniaxial tensile test. A few unloading-loading cycles were also performed. In the following, first the macroscopic stress-strain response will be presented, followed by the ferrite lattice strain as measured using neutron diffraction. The section will be concluded with an analysis of the ferrite peak broadening during the tensile test.

6.3.1 Macroscopic stress-strain response

The engineering stress-strain curves of all four samples are shown in Fig. 6.53. These were recorded ex-situ. The as-patented sample can be used as reference with which to compare the other samples. It has a sharp yield point followed by a short Lüdersbanding region, after which a significant amount of strain hardening takes place up to an engineering strain of about 5.

The as-rolled sample reaches a much higher flow stress, but exhibits an extended micro-yield domain instead of a sharp yield point. This can be explained by the significant microstructural inhomogeneity which was also observed from the SEM study. Another possible explanation is the development of intergranular residual stresses during the prior cold rolling. The differences in residual stress among the differently oriented grains will result in different hardening contributions from local back stresses and therefore in a broad band of yield limits. However, in light of the results presented in section 6.2.2.1, this effect will be rather limited.

The remarkable decrease of the flow stress and apparent high ductility result from the necking region being positioned inside the extensometer. This is confirmed by the in-situ stress-strain curves shown in Appendix E. There the extensometer strain only reaches a strain of 2.14% while the actuator strain reaches a strain of 6.7%, illustrating that the necking region was situated outside the extensometer.

The RS-relieved sample yields at a smaller stress, but has a much sharper yield transition as compared to the as-rolled sample. On the other hand, it is not as sharp as for the as-patented sample. This indicates that the annealing treatment decreased the inhomogeneity to some extent, as well as the residual stresses. However, the inhomogeneity of the cementite morphology still results in a micro-plastic regime. A significant amount of strain hardening is also observed, albeit not as much as for the as-patented sample.

Finally, a completely different behaviour can be seen for the spheroidised sample. This sample exhibits a sharp yield point, followed by some yield softening. After that, a small amount of strain hardening occurs up to a strain of 10%. In the last stage of deformation, no strain hardening can be observed and the flow stress remains constant up to final ductile failure. A last remarkable difference between the spheroidised sample and the other samples is the much thinner hysteresis loop during the unloading-loading cycles. The width of the loop also doesn’t increase at higher tensile strains.

6.3.2 Ferrite lattice strain

The ferrite lattice strains in the tensile direction, which is also the rolling direction of the deformed samples, were measured for the <200>, <211>, <220> and <310> grain families. During the neutron diffraction measurement, the engineering strain was held constant. In this measurement period, some stress relaxation occurs, as can be seen from the in-situ stress-strain curves presented in Appendix E.

In Fig. 6.54 the ferrite lattice strain evolution for the as-patented sample is plotted as a function of the tensile strain. The lattice plane spacing before the start of the tensile test was taken as a reference to calculate the strains. This means that any residual strains initially present in the material are neglected. Similar plots can be found in Appendix E for the other samples. However, as can be seen from Fig. 6.54 and the figures in Appendix E, all ferrite grain families behave qualitatively the same after the yield point. The various samples can therefore more easily be compared by focussing on only one grain family. This is done in Fig. 6.55 for the <220> grain family.

From the linear part of the applied stress vs. lattice strain plots, the diffraction elastic constants (DEC’s) of the various grain families can be determined. The obtained DEC’s are given in Table 6.5. In combination with Fig. 6.54 for the as-patented sample, it can be concluded that the different DEC’s result in the development of intergranular strains in the elastic region.

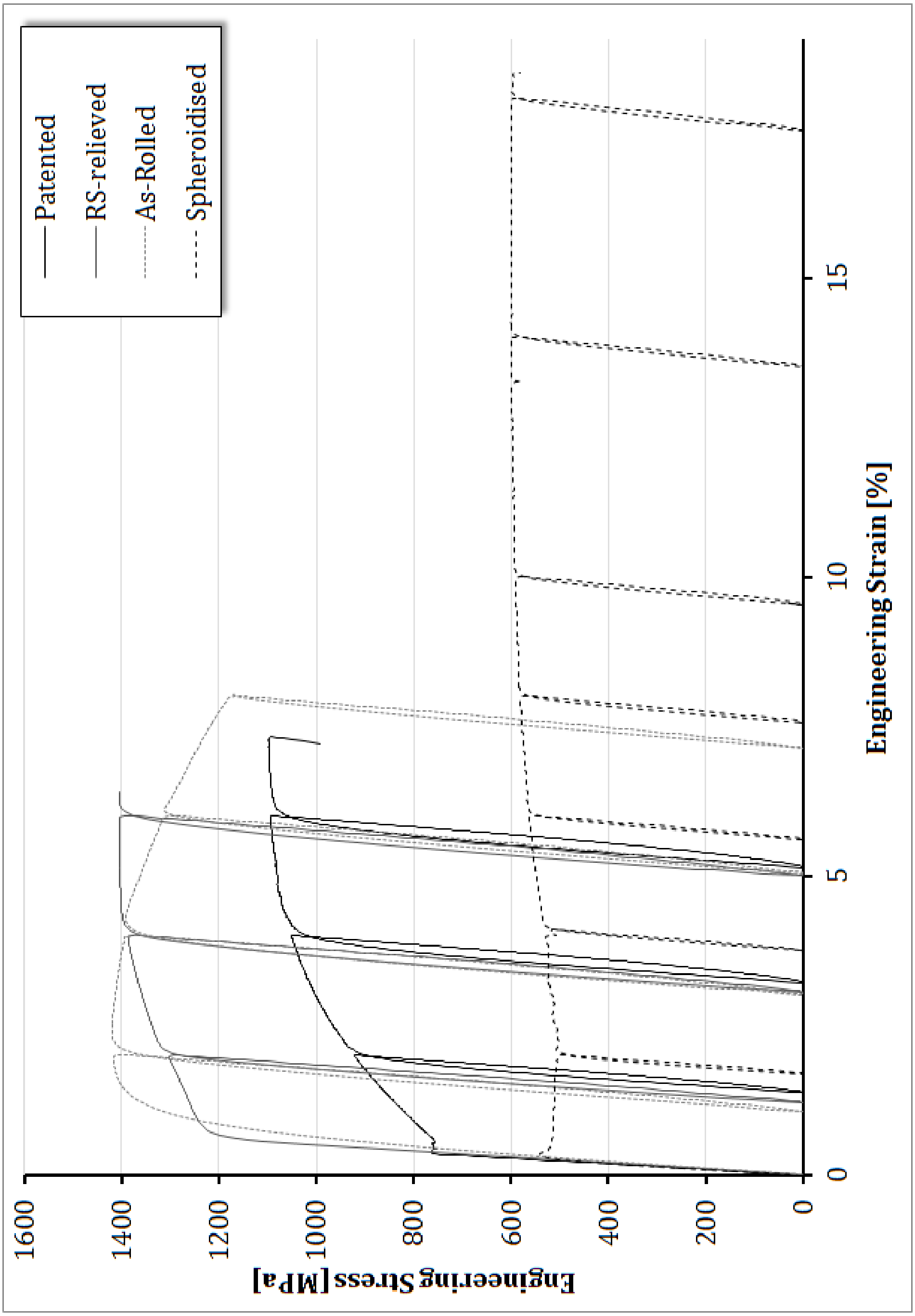

Fig. 6.53: Engineering stress-strain curves obtained on four different samples, as described in the accompanying text.

After yielding, all grain families behave qualitatively the same and the ratios of the lattice strains do not change much anymore. Further intergranular strain development in the plastic region is therefore rather limited. The same observation can be made for the as-rolled and RS-relieved samples, where the lattice strains also scale with the DEC's. One exception is the <211> grain family of the RS-relieved sample.

The spheroidised sample behaves somewhat different. In the elastic region the difference in DEC's also leads to the development of intergranular strains, except that now the <310>-DEC is smaller than the <200>-DEC. This results in the <310> grain family exhibiting the largest lattice strain as opposed to the <200> grain family. After yielding, the ratios of the lattice strains also undergo a large change, suggesting that intergranular strain development is more significant during plastic deformation, as compared to the other samples.

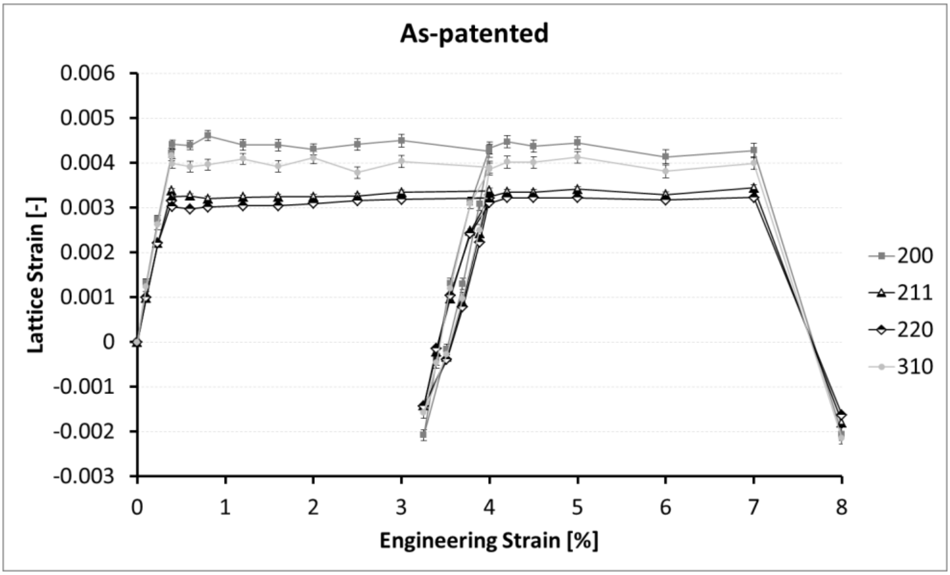

Fig. 6.54: Ferrite lattice strain in the loading direction as a function of macroscopic tensile strain, for the as-patented sample. The lattice strain for all four measured ferrite grain families is shown. Error bars are shown, but are of the same size as the data symbols.

DEC's [GPa]	*As-patented*	*As-rolled*	*RS-relieved*	*Spheroidised*
<220>	221	223	215	217
<211>	207	207	215	213
<310>	170	189	199	173
<200>	167	173	172	184

Table 6.5: Diffraction elastic constants (DEC's) as obtained from the linear portion of the engineering stress vs. lattice strain plots.

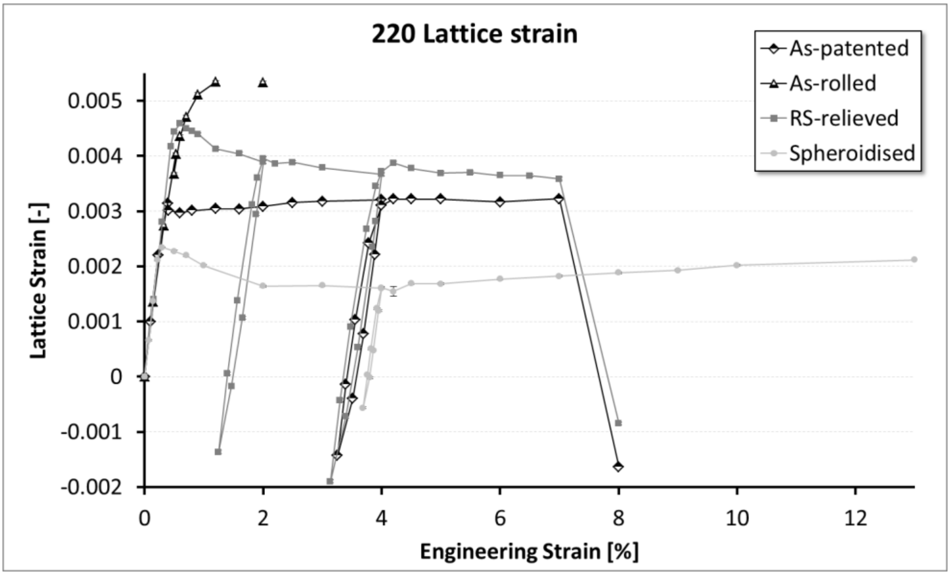

Fig. 6.55: Ferrite <220> lattice strain in the loading direction, as a function of macroscopic tensile strain for all measured samples. Error bars are shown, but are of the same size as the data symbols.

The overall lattice strain in all four samples is well described by the strong <220>-ferrite reflection, shown in Fig. 6.55. It should be remarked, that while the figure only shows the tensile strain up to 13%, the spheroidised sample has a fracture strain of 24%. Additionally, not much can be said about the as-rolled sample because of its small fracture strain. It does however exhibits the largest ferrite lattice strain, which can be attributed to the higher in-situ ferrite flow stress.

The ferrite lattice strain in the spheroidised sample drops significantly after yielding up to a strain of about 2. After that point, the lattice strain continuously increases again up to the point where the ultimate tensile strength is reached. At that point, the lattice strain has again attained the same level as at the yield point. This behaviour compares very well to the results presented by for example Oliver et al. [17], except for the fact that the lattice strain in Oliver et al.'s study drops much faster after yielding. This can likely be attributed to the scale of the microstructure, which will be much finer and more inhomogeneous in the sample used for the current study. As a result, stress transfer to the cementite phase does not happen at the same macroscopic strain level everywhere throughout the material. The region in which the ferrite lattice strain is again increasing, coincides with a region of negligible macroscopic strain hardening. This suggests that, while the ferrite phase is strain hardening with increasing strain, some of the load borne by the cementite phase is again distributed to the ferrite. This illustrates that the spheroidised microstructure makes load transfer to the stronger cementite phase inefficient.

The as-patented material, with a randomly oriented, lamellar microstructure behaves quite differently. A very small drop in the lattice strain can be observed upon yielding, after which the ferrite lattice strain remains virtually constant. Because the as-patented material strain hardens considerably, this means that increase in strength of the composite material has to originate from the harder cementite phase carrying an increasingly large portion of the load. This indicates that a lamellar microstructure results in a much more efficient load transfer to the stronger phase.

The RS-relieved sample has been cold rolled and has its lamellae approximately aligned with the loading direction. Because of the applied heat treatment, any residual strains which were initially present have been removed and the deformation substructure has been relaxed to some extent. It can be seen that after yielding, the ferrite lattice strain continuously decreases, while the sample does exhibit significant macroscopic strain hardening. This leads to the conclusion that a lamellar microstructure is not only more efficient to transfer load to the stronger phase, but that aligning these lamellae with the loading direction also increases the load transfer to the stronger phase. This confirms the conclusions drawn from the literature in section 2.3.1. Lamellae alignment therefore also provides a significant contribution to the large strain work hardening of lamellar materials. A more detailed discussion of the observed decrease ferrite lattice strain is given in section 8.3.1.

Finally, a number of unloading-reloading cycles were also performed. For the spheroidised sample, both the unloading and reloading are almost completely linear as far as the lattice strains are concerned. This is not true for the as-patented and RS-relieved samples. They both exhibit a significant hysteresis which is of the same order of magnitude in both samples. The difference between the latter two samples can be found in the point where non-linearity starts. In the as-patented sample, the non-linearity starts at the point where the ferrite lattice strain has become zero. In the RS-relieved sample, the non-linearity starts virtually at the very beginning of the unloading cycle.

6.3.3 Ferrite peak width

Together with the peak position, the peak width has also been determined during the tensile tests and the unloading-reloading cycles. The line widths of the <220> ferrite diffraction peak for all but the as-rolled sample are shown in

Fig. 6.56. The latter sample is not included because no extra information is obtained from the few data points that are available. The line widths are given as a function of measurement number in order to emphasize the evolution. Arrows indicate the end of the elastic regime. The start and end of the unloading-reloading cycles are highlighted using circles. The point where the macroscopic stress becomes zero is highlighted using a square.

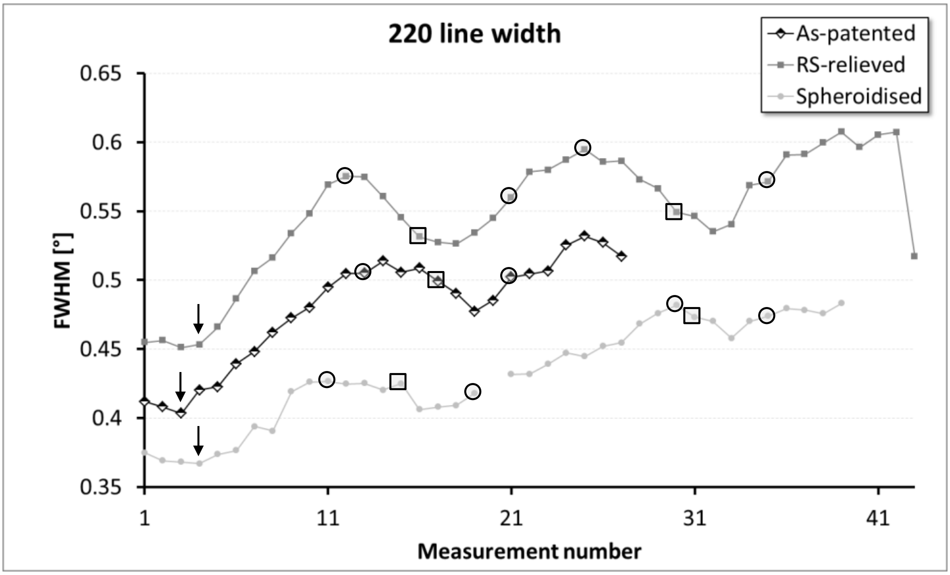

Fig. 6.56: <220> ferrite diffraction line width as a function of measurement number. Arrows indicate the end of the elastic region. Start and end of the unloading-reloading cycles are indicated using circles. The point where the macroscopic stress becomes zero is indicated using a square.

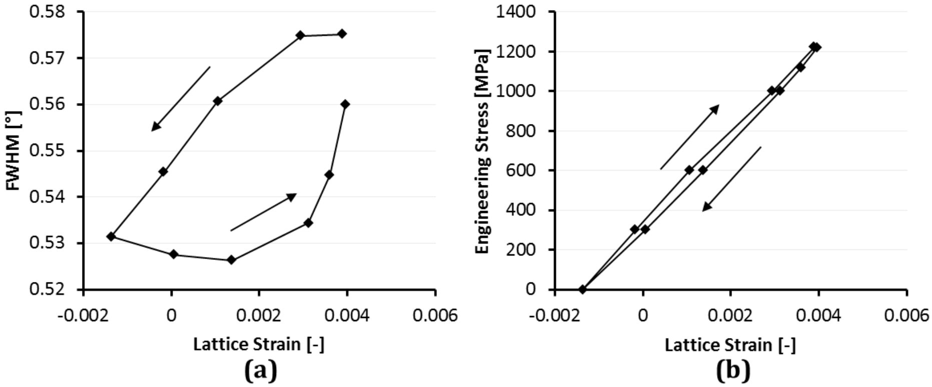

Fig. 6.57: (a) <220> line width as a function of lattice strain and (b) engineering stress as a function of lattice strain, both for the RS-relieved sample.

The figure shows that in the elastic region the peak width doesn't change. After the onset of yielding, there is a significant amount of line broadening for all samples. In the regions where the unloading-reloading cycles take place, a remarkable decrease and again increase of the line width is observed for the patented and RS-relieved samples, but not for the spheroidised sample. Detailed plots of the first unloading cycle for the RS-relieved sample are shown in Fig. 6.57. With unloading, the strain broadening decreases significantly in the RS-relieved sample. This trend even continues somewhat after zero applied stress is reached, and into the reloading section of the cycle. However, by the time the same stress level is reached as before the unloading, the peak width has almost fully 'recovered'. A similar evolution is seen for the as-patented sample, although there the decreasing peak width is strangely concentrated in the reloading section of the cycle.

Peak broadening can have a wide variety of origins. However, because there should be no large macroscopic strain gradient associated with a tensile test, there is no additional broadening associated with the averaging of the lattice strains through the cross-section of the sample. Additionally, the deformation reached in a tensile test is rather small as compared with cold rolling, it is therefore safe to assume that also size broadening will not play a major role. The evolution of the peak width can therefore be interpreted as a change in the amount of broadening resulting from deformation, i.e. strain broadening. This will be discussed in more detail, in correlation with other experimental results in section 8.3.

6.4 Summary

SEM investigations have shown that the microstructure changes drastically upon cold rolling. The initially randomly oriented lamellae gradually align themselves with the rolling plane while at the same time becoming thinner. The alignment is largely completed at a strain of 1. However, the microstructure is not a perfect stack of ferrite and cementite lamellae. Many of the lamellae are bent, wavy or are broken up in smaller pieces. Additionally, significant variations in local cementite volume fraction were observed. Indications for plastic deformation of cementite have also been presented.

Spatial maps of the crystallographic orientation of ferrite have been made using EBSD. The crystallographic orientation in as-patented pearlite remains constant across many lamellae and colony boundaries. After less than 10% rolling strain, these large regions break up and variations of ferrite crystal orientation can be observed both along and perpendicular to the ferrite lamellae. Some literature seems to suggest that at very large strains there is again an evolution towards less variation in the crystallographic orientation.

The residual stresses at the surface of cold rolled sheets were measured using X-ray diffraction. These stresses were seen to depend on the surface finish of the samples and are likely strongly influenced by the exact, local rolling conditions. Nevertheless, it was clearly shown that the residual stress increases in magnitude with decreasing ILS.

Micro-phase residual stresses were measured in both the ferrite and cementite phase of cold drawn wire and cold rolled sheet. While in both materials the residual stress in the deformation direction was seen to increase quickly at small deformations and then apparently saturate, the saturation occurs faster in cold rolled sheet. The strong and quick increase in residual stress occurs simultaneously with a strong broadening of the diffraction peaks.

In the cold drawn wire, the initial saturation was seen to occur for all ferrite grain families. After a strain of around 1.6, the response of the different grain families again diverges. A similar observation was made on sheet, with the starting point of the diverging grain family response around a strain of 1.2.

The strains in the TD and ND directions of the cold rolled sheet were also measured. While the strain in the TD remains small, the strain in the ND direction shows the same strong increase as the strain in the RD. However, in the ND no saturation is observed, but rather a decrease in the residual stress. In the cementite phase this is mirrored by a decrease in the diffraction peak width, while no reduction in peak width is observed for the ferrite phase.

From the measured residual lattice strains, residual stresses were calculated. In the region where the residual lattice strain seems to saturate, the calculated residual stresses already exhibit a significant degree of intergranular stress development. This is attributed to the elastic anisotropy of the ferrite phase. The calculation of the cementite stresses revealed that care has to be taken in the selection of the cementite elastic constants. More specifically, it seems that cementite deforming in-situ in pearlite is less elastically anisotropic than ab-initio calculations of the elastic constants of bulk cementite suggest.

The ferrite diffraction peaks were seen to become strongly asymmetric at large plastic deformations. This asymmetry could be accounted for by fitting the peaks with a sum of two Gaussian profiles: a broad low-intensity peak and a slim high-intensity peak. The emergence of the broad peak was attributed to the possible existence of ferrite with a higher dislocation content at the interface.

Internal micro-phase strains during tensile testing of samples with various microstructures were recorded using neutron diffraction. All grain families exhibit the same trend, but the magnitude of the lattice strains differs relative to the observed diffraction elastic constants of each grain family. The ferrite lattice strains in the as-patented sample remain virtually constant after yielding, while those in the RS-relieved sample, having aligned lamellae continue to decrease until fracture of the sample. This is attributed to a stronger load transfer to the cementite phase when the lamellae are aligned with the loading direction.

Changes in peak width were also observed and were shown to be linked to strain broadening. The amount of strain broadening increases with increasing deformation. However, upon unloading, the peak width and thus strain broadening decreases again.

7 Modelling work

7.1 Introduction

7.1.1 The use of simplified analytical models

The development of residual stresses in multiphase materials is a complex phenomenon in which a lot of parameters play a role. How do the yield strengths of the separate phases influence the residual stress? What is the importance of the in-situ strain hardening behaviour of the phases? But also the exact microstructure, phase volume fractions and the presence of reverse yielding will be important. Next to material related parameters, also variations and changes in the imposed deformation during rolling or wire drawing will influence the residual stress development. It is very hard, if not impossible to consider all these influences simultaneously while studying the obtained experimental data.

In order to investigate what mechanisms are responsible for the development of residual stresses, simplified models were created. By simplifying reality, the models remain intuitive and don't become black-boxes with an in- and outflow of data. On the other hand, because of their simplicity, the models cannot be used to predict experimental data. They should rather be considered as a tool to guide the thought while considering what happens when a multiphase material is deformed and starts to develop residual stresses.

7.1.2 Idealized microstructure: The sandwich model

The largest step towards simplifying the problem is by considering an idealized microstructure. An undeformed sample has its lamellae grouped in randomly aligned colonies. With increasing rolling strain the lamellae start to align with the rolling plane. For industrial purposes, it is the heavily deformed material that is of interest. As the lamellae are strongly aligned at large strains, the morphology of the material can be approximated by a stack of parallel plates of ferrite and cementite. The thicknesses of the plates scales with the volume fraction of the phases. Further, because the lamellae in all colonies reach the same alignment, the material can be considered to consist of only one 'colony' with the lamellae extending infinitely in the rolling and transverse directions. The microstructure idealized as such will be called a sandwich microstructure and the models based on this microstructure sandwich models. This idealization and the made assumptions are to some extent similar to the slab-model proposed in [116].

Residual and internal stress and strains can develop as a result of local variations in mechanical properties or an inhomogeneous externally applied deformation field. These variations and inhomogeneities exist on various length scales: the scale of the sample dimensions, the size of regions with homogeneous crystal orientation, the colony size and the interlamellar spacing. Idealizing the material as a sandwich microstructure implicitly implies that only the length scale of the interlamellar spacing will be considered.

When rolling a material with a sandwich microstructure, the total strain in both phases has to be equal in the RD and TD, and equal to the externally applied strain. In the ND the two phases can contract individually without external constraint. No internal or residual stresses will therefore exist in the ND. However, residual elastic strains may exist, as a result of the constraint deformation in the RD and TD.

7.2 1-D residual stress sandwich model

7.2.1 Problem description and assumptions

The goal of the 1-D residual stress sandwich model is to obtain the residual micro-phase stress in the two phases of the sandwich microstructure as a function of applied rolling strain. The model should be able to show the influence of phase volume fraction, phase yield stress and phase strain hardening behaviour on the residual micro-phase stress development. The questions this model should answer specifically are whether it is possible to obtain a saturation of the residual stress, whether this saturation can be followed by a decreasing residual stress and how possible reverse yielding of the ferrite phase plays a role. It should be stressed at this point, that the model is not meant to predict experimentally observed data. Rather, it should be viewed as a tool to study the influence of the above mentioned parameters on the residual stress evolution.

The in-situ mechanical behaviour of ferrite and cementite is required as input. The in-situ mechanical behaviour is the stress-strain response of the phase as it behaves inside the composite microstructure and is not the same as the ex-situ mechanical behaviour, which is the stress-strain response of the single phase equivalent of the phase. Unfortunately, the in-situ mechanical and specifically strain hardening behaviour of ferrite and cementite is not known and impossible to measure directly. Therefore, a number of different in-situ stress-strain curves will be constructed as input for the model. The resulting residual micro-phase stress behaviour can then be analysed and compared to the experimental results.

Under perfect plane strain deformation, used as an approximation for cold rolling, the total strain in the TD should be zero. If the situation is further simplified by assuming that zero total strain is obtained by making both the elastic and plastic strain in the TD zero, rather than their sum, there will be no misfit strains between the two phases in the TD. As could be seen from the experimental results this does not necessarily mean that there will be no residual stress development in the TD. However, to maintain the simple and intuitive nature of the calculations, any stress and/or strain development in the TD will be neglected. Additionally, because the sandwich microstructure is adopted in this model, the presences of stresses and strains in the ND will also be neglected. Under these assumptions, only the RS development in the RD will be taken into account. The model can then be limited to one dimension.

The stress equilibrium and the co-deformation of both phases can be expressed as the boundary conditions to the mathematical problem. The former condition results in the following stress balance in the RD, without externally applied load (i.e. after unloading)

$$\sigma_\alpha \cdot (1 - V_\theta) + \sigma_\theta \cdot V_\theta = 0 \tag{7.1}$$

The subscripts α and θ refer to the ferrite and cementite phases, respectively. The co-deformation of the two phases results in the condition that their total strain during loading and after unloading always has to be equal in the RD

$$\varepsilon_\alpha^{tot} = \varepsilon_\theta^{tot} \tag{7.2}$$

In section 7.2.2 a rigorous solution will be proposed by following the stress-strain response of the two phases during the loading and subsequent unloading. In section 7.2.3 a mathematically much more elegant approach based on a work criterion will be proposed. It will be shown that both approaches result in exactly the same solution.

7.2.2 Stress/Strain-based solution

This approach to the problem starts by first imposing a load to the material, specified by the deformation ε^L. During this loading step, plastic and elastic deformation can occur in both phases. The ferrite phase is softer as compared to cementite and will undergo a larger plastic strain. These strains are illustrated in Fig. 7.1. During the subsequent unloading, the elastic strain in the ferrite will first be relaxed completely along with a part of the cementite strain. This is illustrated by the arrow labelled with $-\varepsilon_\alpha^{L,el}$. The remaining elastic strain in the cementite still wants to relax further, resulting in a compression of the ferrite phase which will first be elastic. However, if the elastic strain remaining in the cementite phase is large enough, reverse yielding of the ferrite phase might occur. An equilibrium between the compressive stress in the ferrite phase and the tensile stress in the cementite phase will eventually be reached after a certain amount of unloading strain ε^{UL}. The total strain of the composite after loading and unloading will be ε^{tot}. All the strain definitions are illustrated in Fig. 7.1.

In the following, a calculation procedure to obtain the residual stresses will be proposed. The in-situ stress-strain curves of both phases are assumed to be known and representative for the real behaviour of the material. The applied loading strain ε^L is used as input for the calculation and the total elastic strain after relaxation of the load has to be calculated.

The solution described in this section is based on a strain description of all deformations. As an alternative, the deformations can also be described starting from displacements from which the strains are deduced. While the first method is more elegant and easy to understand, the second method provides a more elaborate mathematical background. The displacement based solution is presented in Appendix F. Both methods were implemented in Matlab and yield exactly the same result. However, the displacement based method converges faster and the results in section 7.2.4 are based on the displacement implementation.

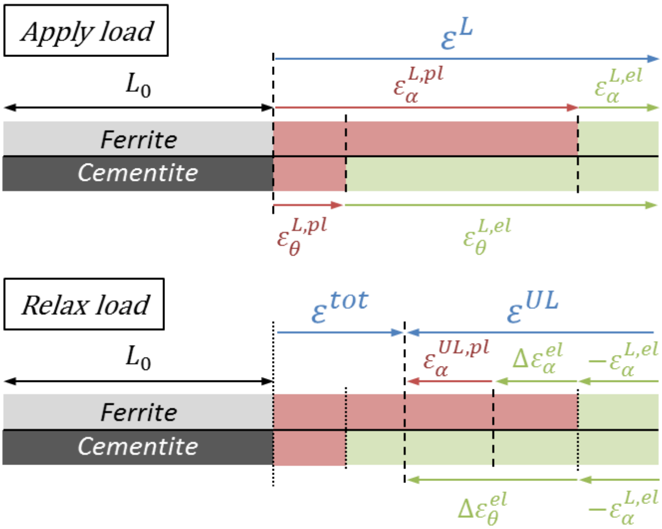

Fig. 7.1: Illustration of the strains and their definition, as used in the Stress-Strain based solution of the residual stress calculations. The superscripts L, UL, pl and el refer to the loading step, the unloading step, plastic strain and elastic strain, respectively. The subscripts α and θ refer to the ferrite and cementite phase, respectively.

Loading step

The stress in both phases can be found from their flow curves and is a function of the applied strain ε^L. The elastic and plastic parts of the strains can then easily be found as

$$\varepsilon_i^{L,el} = \frac{\sigma_i^L}{E_i} \tag{7.3}$$

$$\varepsilon_i^{L,pl} = \varepsilon^L - \varepsilon_i^{L,el} \tag{7.4}$$

E is the Young's Modulus. The subscript *i* refers to the *i*th phase.

Unloading step

After unloading, stress equilibrium (eq. 7.1) can be written as

$$E_\alpha \cdot \varepsilon_\alpha^{tot,el} \cdot (1 - V_\theta) + E_\theta \cdot \varepsilon_\theta^{tot,el} \cdot V_\theta = 0 \tag{7.5}$$

From Fig. 7.1 it can be seen that the total elastic strain in each phase can be written as

$$\varepsilon_i^{tot,el} = \varepsilon_i^{L,el} - \varepsilon_\alpha^{L,el} + \Delta\varepsilon_i^{el} \tag{7.6}$$

The total strain after unloading is the sum of the total plastic strain and the total elastic strain

$$\varepsilon_i^{tot} = \varepsilon_i^{L,pl} + \varepsilon_i^{UL,pl} + \varepsilon_i^{tot,el} \tag{7.7}$$

And has to be equal in both phases (eq. 7.2). By introducing eq. 7.6, eq. 7.2 can be written as

$$\begin{aligned} &\varepsilon_\alpha^{L,pl} + \varepsilon_\alpha^{UL,pl} + \varepsilon_\alpha^{L,el} - \varepsilon_\alpha^{L,el} + \Delta\varepsilon_\alpha^{el} \\ &\qquad = \varepsilon_\theta^{L,pl} + \varepsilon_\theta^{UL,pl} + \varepsilon_\theta^{L,el} - \varepsilon_\alpha^{L,el} + \Delta\varepsilon_\theta^{el} \end{aligned} \tag{7.8}$$

By taking into account that the loading strain in both phases was equal and that cementite will not deform plastically during unloading, eq. 7.8 reduces to

$$\varepsilon_\alpha^{UL,pl} + \Delta\varepsilon_\alpha^{el} = \Delta\varepsilon_\theta^{el} \tag{7.9}$$

The equilibrium condition (eq. 7.5) can now be elaborated by introducing eq. 7.6, which yields

$$E_\alpha \cdot \Delta\varepsilon_\alpha^{el} \cdot (1 - V_\theta) + E_\theta \cdot \varepsilon_\theta^{L,el} - \varepsilon_\alpha^{L,el} + \Delta\varepsilon_\theta^{el} \cdot V_\theta = 0 \tag{7.10}$$

The value of $\varepsilon_\alpha^{L,el}$ was already determined during the loading step. Equations 7.9 and 7.10 thus form a set of two equations in the three unknowns $\varepsilon_\alpha^{UL,pl}$, $\Delta\varepsilon_\alpha^{el}$ and $\Delta\varepsilon_\theta^{el}$. This can be solved by realizing that $\varepsilon_\alpha^{UL,pl}$ and $\Delta\varepsilon_\alpha^{el}$ are not independent, but are linked to each other through the reverse yield curve, as can be seen from Fig. 7.2.

Unless the strain hardening behaviour during unloading can be described by a linear function, the set of three relations found above cannot easily be solved analytically. Instead, an iterative solution scheme is proposed. An additional definition for $\varepsilon_\alpha^{UL,pl}$ is required before the iterative scheme can be implemented.

$$\begin{aligned} \varepsilon_\alpha^{UL,pl} &= \varepsilon^{UL} - \varepsilon_\alpha^{UL,el} \\ &= \varepsilon^{UL} - \left(-\varepsilon_\alpha^{L,el} + \Delta\varepsilon_\alpha^{el}\right) \\ &= \varepsilon^{UL} - \Delta\varepsilon_\alpha^{el} + \varepsilon_\alpha^{L,el} \end{aligned} \tag{7.11}$$

The above equations, together with Fig. 7.2, can be used to come to the iterative solution scheme presented in Fig. 7.3.

The iterative loop should be repeated until the left hand side of the equilibrium equation equals zero. In practice this means that a critical level has to be set below which the left hand side of the equilibrium equation should drop. Once that level is reached the last chosen value of ε^{UL} is assumed to be the correct one.

The model has been developed with as a purpose to evaluate the residual stress development in both phases, as well as the amount of reverse yielding in the ferrite phase. The total elastic strain in both phases, after unloading, can be calculated using eq. 7.6 and the residual stress can be obtained by applying Hooke's law. The amount of reverse yielding in the ferrite phase is expressed by eq. 7.11.

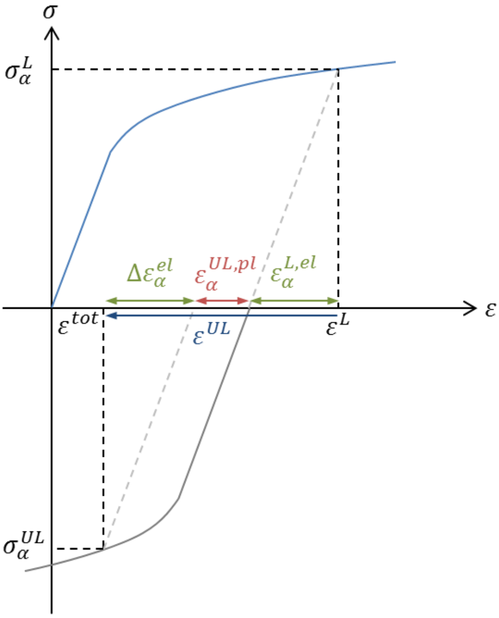

Fig. 7.2: Sketch of the unloading step of the 1-D stress/strain-based residual stress calculation. The strains occurring in the ferrite phase are illustrated with the help of the forward and reverse flow curve. Both flow curves are assumed to be known prior to the calculation.

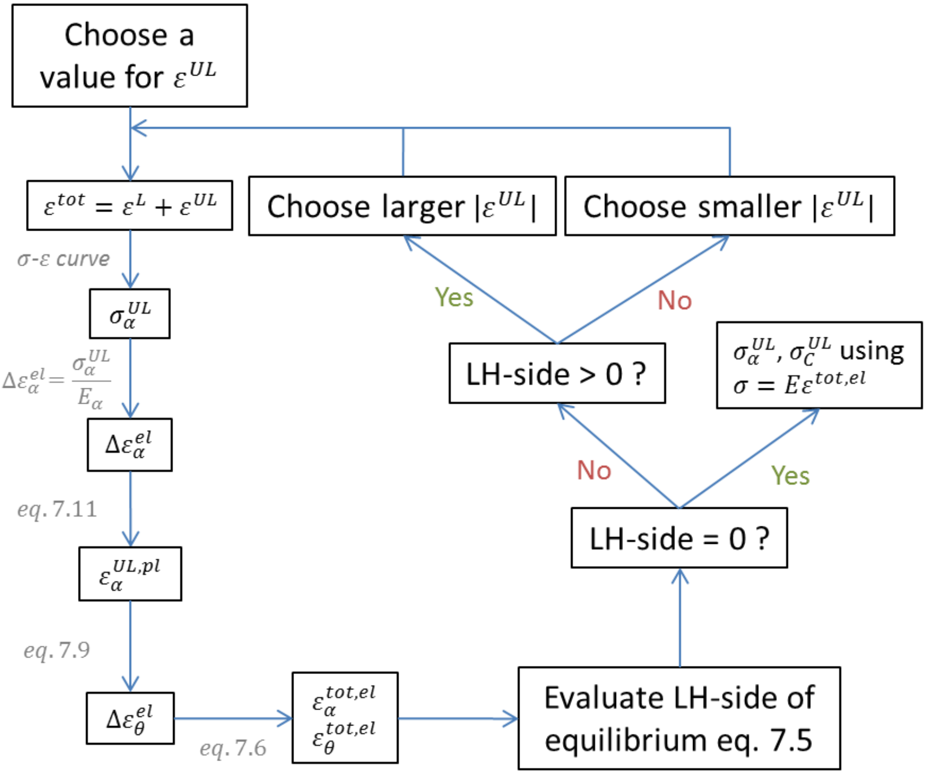

Fig. 7.3: Iterative solution scheme for the stress/strain-based solution procedure of the 1-D residual stress sandwich model. The unloading strain ε^{UL} is the parameter that needs to be optimized in order to fulfil the equilibrium equation.

7.2.3 Work-based solution

In order to come to a simpler solution to the problem described above, a three step procedure is now proposed. It will be shown that, when no reverse yielding of the ferrite phase is allowed, a simple analytical solution can be found. In the case that reverse yielding of the ferrite phase is required, a solution based on a minimal work criterion will be developed.

Instead of following the evolutions of the strains during loading and subsequent unloading, an artificial intermediate stress-free state is introduced as can be seen from Fig. 7.4. After application of the load, the two phases are allowed to relax individually to a stress free state. In doing so, the iso-strain assumption is no longer fulfilled. In the next step, iso-strain is again imposed. This is achieved by elastic elongation of the cementite phase and elastoplastic compression of the ferrite phase.

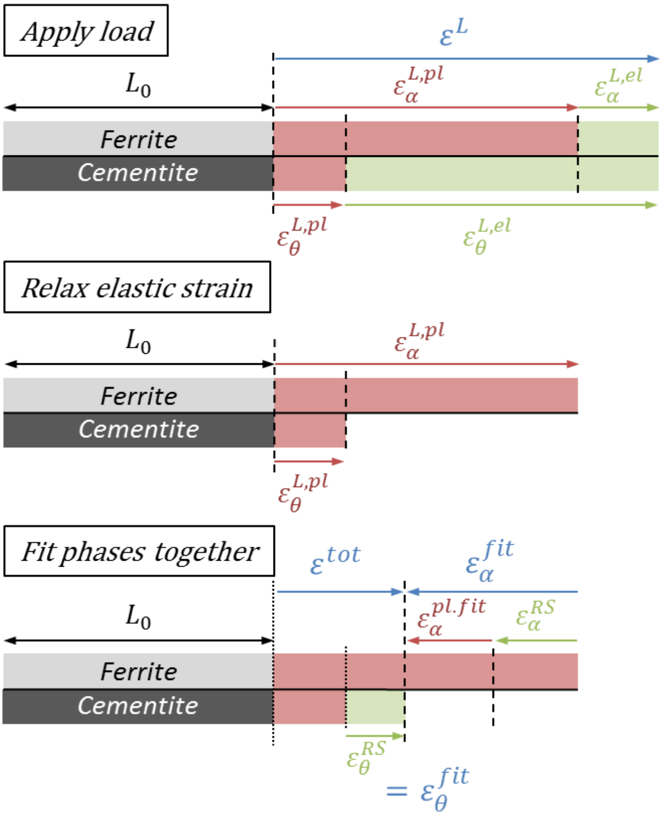

Fig. 7.4: Illustration of a three step procedure to find the residual stress developed after loading of a two-phase lamellar sandwich material.

The first step, i.e. applying the load, is evaluated in exactly the same way as in section 7.2.2. The applied load is characterized by the applied deformation ε^L. From the in-situ flow curves of both phases the amounts of elastic and plastic strain are determined. The relaxation step is also straight forward and does not require any calculation, but is there as a visualization of the solution procedure.

Finding the residual stresses present in the material after deformation requires solving the third step, i.e. the 'fitting' step. The boundary conditions to this problem are again the requirement of stress equilibrium

$$\sigma_\alpha^{RS} \cdot (1 - V_\theta) + \sigma_\theta^{RS} \cdot V_\theta = 0 \tag{7.12}$$

and the iso-strain assumption

$$\varepsilon_\alpha^{tot} = \varepsilon_\theta^{tot} \tag{7.13}$$

ε_i^{tot} is the total strain in the i^{th} phase after having gone through all three steps illustrated in Fig. 7.4.

$$\varepsilon_i^{tot} = \varepsilon^L + \varepsilon_i^{relax} + \varepsilon_i^{fit} \tag{7.14}$$

ε^L is the applied deformation strain and is known. ε_i^{relax} is assumed to be equal to

$$\frac{-\sigma_i^{flow}}{E_i}$$

This implicitly implies that unloading is assumed to be 100% linear, as was also the case in the previous section. ε_i^{relax} is therefore known. That leaves ε_i^{fit} to be determined. The fitting strain can have both an elastic and plastic component and can be expressed as

$$\varepsilon_i^{fit} = \varepsilon_i^{RS} + \varepsilon_i^{pl.fit} = \frac{\sigma_i^{RS}}{E_i} + \varepsilon_i^{pl.fit} \tag{7.15}$$

No reverse yielding

To illustrate this approach, let's first assume that no plastic deformation of the ferrite phase is required to fit both phases together. In that case

$$\varepsilon_\alpha^{pl.fit} = \varepsilon_\theta^{pl.fit} = 0$$

and the iso-strain assumption reduces to

$$\varepsilon_\alpha^{relax} + \varepsilon_\alpha^{RS} = \varepsilon_\theta^{relax} + \varepsilon_\theta^{RS}$$

$$-\frac{\sigma_\alpha^{flow}}{E_\alpha} + \frac{\sigma_\alpha^{RS}}{E_\alpha} = -\frac{\sigma_\theta^{flow}}{E_\theta} + \frac{\sigma_\theta^{RS}}{E_\theta} \tag{7.16}$$

Combining eq. 7.15 and eq. 7.12 yields the residual stresses in both phases:

$$\sigma_\alpha^{RS} = \frac{V_\theta E_\theta E_\alpha}{V_\theta E_\theta + V_\alpha E_\alpha} \cdot \left(\frac{\sigma_\alpha^{flow}}{E_\alpha} - \frac{\sigma_\theta^{flow}}{E_\theta}\right) \tag{7.17}$$

$$\sigma_\theta^{RS} = \frac{V_\alpha E_\theta E_\alpha}{V_\theta E_\theta + V_\alpha E_\alpha} \cdot \left(\frac{\sigma_\theta^{flow}}{E_\theta} - \frac{\sigma_\alpha^{flow}}{E_\alpha}\right) \tag{7.18}$$

Assuming the Young's modulus to be equal for both phases further simplifies the solution.

$$\sigma_\alpha^{RS} = V_\theta\left(\sigma_\alpha^{flow} - \sigma_\theta^{flow}\right)$$

$$\sigma_\theta^{RS} = V_\alpha\left(\sigma_\theta^{flow} - \sigma_\alpha^{flow}\right)$$

This shows that, for this simple case the residual stress only depends on the difference in flow stress between the two phases and the volume fraction of the phases. However, if the residual stress obtained for the ferrite phase is larger than the reverse flow stress, reverse yielding will need to be taken into account.

With reverse yielding – Min. work approach

By allowing reverse yielding, equation 7.13 becomes

$$\varepsilon_\alpha^{relax} + \varepsilon_\alpha^{RS} + \varepsilon_\alpha^{pl.fit} = \varepsilon_\theta^{relax} + \varepsilon_\theta^{RS} + \varepsilon_\theta^{pl.fit} \tag{7.19}$$

The presence of the plastic fitting strains greatly complicates the problem if a solution is sought in terms of the stress equilibrium equation. Therefore, an alternative criterion is proposed, namely a minimization of the amount of work spent on the material, by an imaginary set of external forces, to fit both phases together in the 'fitting' step.

The validity of this criterion is illustrated with the help of Fig. 7.5. In (a) the loading and relaxation steps are illustrated. The part of the forward cementite flow curve and reverse ferrite flow curve around the strains reached after relaxation is enlarged in Fig. 7.5(b)-(d). In (b), the energy required to bring both phases to the strain indicated by the line ABC is coloured grey. For the simplicity of illustration, it is assumed that both phases constitute 50vol% of the material. It can then be seen that by moving the line to the left, the grey area and thereby the required energy is reduced. Similarly, in (c) moving the line ABC to the right will also reduce the energy required for fitting. The fitting energy is minimized in (d). It can be seen that this point indeed corresponds to equal and opposite stresses in both phases, thereby fulfilling the stress equilibrium equation.

To solve this problem, the fitting energy needs to be expressed as a function of ε_α^{fit}. This function then needs to be minimized with ε_α^{fit} as a variable. Once the fitting strain has been determined, the residual stresses in both phases and the amount of reverse yielding in either one of the phases can be obtained from the in-situ flow curves of both phases.

In incremental form the fitting energy is

$$dW = V_c \sigma_c d\varepsilon_c^{fit} + V_\alpha \sigma_\alpha d\varepsilon_\alpha^{fit} \tag{7.20}$$

ε_α^{fit} is measured from the point $\varepsilon^L + \varepsilon_\alpha^{relax}$, while ε_θ^{fit} is measured from the point $\varepsilon^L + \varepsilon_\theta^{relax}$. After integration the total amount of energy expended on fitting is found.

$$W = V_\theta \int_0^{\varepsilon_\theta^{fit}} \sigma_\theta\left(\varepsilon_\theta^{fit}\right) d\varepsilon_\theta^{fit} + V_\alpha \int_0^{\varepsilon_\alpha^{fit}} \sigma_\alpha\left(\varepsilon_\alpha^{fit}\right) d\varepsilon_\alpha^{fit} \tag{7.21}$$

ε_θ^{fit} can now be written as a function of ε_α^{fit} and inserted in eq. 7.21 to have a single minimization parameter ε_α^{fit}.

$$\varepsilon_\theta^{fit} = \left(\varepsilon_\alpha^{relax} - \varepsilon_\theta^{relax}\right) + \varepsilon_\alpha^{fit}$$

$$W = V_\theta \int_0^{\varepsilon_\alpha^{fit}} \sigma_\theta\left(\varepsilon_\alpha^{relax} - \varepsilon_\theta^{relax} + \varepsilon_\alpha^{fit}\right) d\varepsilon_\alpha^{fit} + V_\alpha \int_0^{\varepsilon_\alpha^{fit}} \sigma_\alpha\left(\varepsilon_\alpha^{fit}\right) d\varepsilon_\alpha^{fit} \tag{7.22}$$

To implement this solution in Matlab, the integrals in eq. 7.21 have been split up in two parts. First a part where both phases still behave elastically and then a part where one phase deforms elastically and the other plastically.

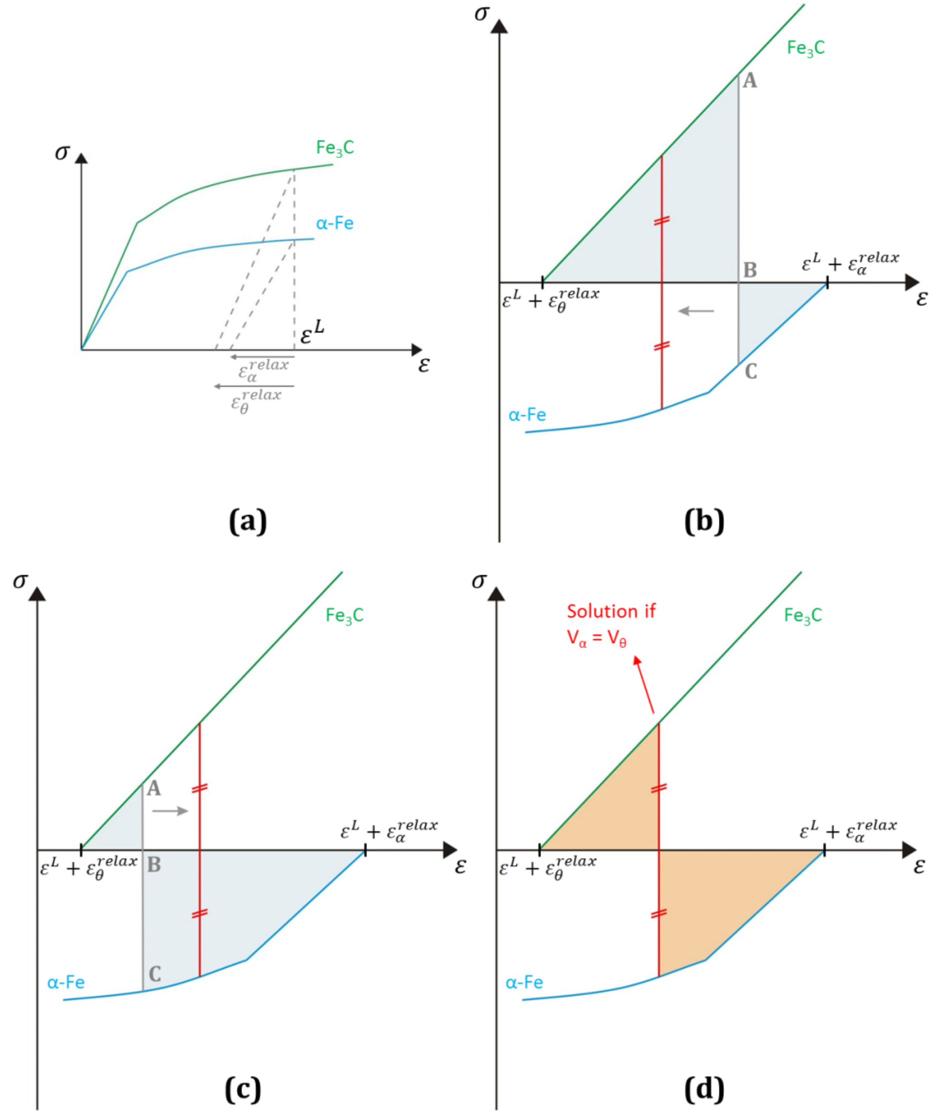

Fig. 7.5: Illustration of the principle that minimizing the work required to fit both phases together will yield a solution which fulfils the stress equilibrium equation. In the sketches, the volume fraction of both phases is assumed to be 50%. For more information, the reader is referred to the accompanying text.

Equality of stress equilibrium and energy minimization

Through Fig. 7.5 it was illustrated that the energy minimization criterion is equivalent to the stress equilibrium criterion. This can also be deduced from the expression for the work expanded on fitting. Equation 7.22 can be written as

$$W = \int_{0}^{\varepsilon_\alpha^{fit}} V_\theta \sigma_\theta\left(\varepsilon_\alpha^{relax} - \varepsilon_\theta^{relax} + \varepsilon_\alpha^{fit}\right) d\varepsilon_\alpha^{fit} + V_\alpha \sigma_\alpha\left(\varepsilon_\alpha^{fit}\right) d\varepsilon_\alpha^{fit}$$

To find the minimum in W as a function of ε_α^{fit}, we need to find the point where the derivative is equal to zero.

$$\frac{dW}{d\varepsilon_\alpha^{fit}} = 0$$

Applying this to the expression for W yields

$$\frac{dW}{d\varepsilon_\alpha^{fit}} = V_\theta \sigma_\theta\left(\varepsilon_\alpha^{relax} - \varepsilon_\theta^{relax} + \varepsilon_\alpha^{fit}\right) + V_\alpha \sigma_\alpha\left(\varepsilon_\alpha^{fit}\right) = 0$$

which is equal to

$$V_\theta \sigma_\theta\left(\varepsilon_\theta^{fit}\right) + V_\alpha \sigma_\alpha\left(\varepsilon_\alpha^{fit}\right) = 0$$

■

Advantages of this approach

The greatest advantages of this approach are (1) its mathematical simplicity and (2) its greater flexibility. The first point especially manifests itself during implementation of the model in for example Matlab. The amount of equations is reduced significantly reducing the room for programming errors. Secondly, numerical integration is a very well-conditioned problem and multiple implementation schemes are available [117].

The greater flexibility results from the mathematical simplicity and can be illustrated by a couple of examples. First of all, when implementing the work-based solution, no prior assumptions have to be made as to which is the harder phase. As a result, this approach can more easily be used for materials in which the initially softer phase strain hardens to such extend that it eventually becomes the stronger phase.

Secondly, because the fitting strain of each phase can be expressed as a function of the fitting strain of another phase, one phase can be chosen as a reference and its fitting strain used as the minimization parameter (see eq. 7.22). As a result, a large number of ‘phases’ can be incorporated in the calculation simultaneously. This could for example be used to incorporate different ferrite grain families by assigning each ‘phase’ a yield behaviour representative for one particular grain family.

A very similar approach would be not to minimize the energy required for fitting, but to maximize the energy released upon unloading. The procedure would then again be a two-step procedure, where individual relaxation of the phases is not performed. Any pre-defined unloading curves, followed by a reverse flow curves could be used along which integration is performed as the strain is reduced from the loading strain ε^L to the total strain after unloading ε^{tot}. In the first, unloading part, all phases release a certain amount of energy. When one of the phases starts to be compressed, energy is consumed. As long as the energy released by the further unloading of the phases which are still in tension is larger than the energy consumed by the phases being compressed, unloading will continue because the amount of energy released continues to increase. An equilibrium position will be reached when the energy released with an additional incremental unloading strain is the same as the energy consumed. At that point the amount of released energy will be maximal. This implementation would have the added advantage that non-linear unloading conditions could be incorporated.

7.2.4 Results

Using the 1-D sandwich model, the residual stresses as a function of rolling strain were calculated. Both proposed solutions, i.e. stress-based and work-based, have been used to calculate the residual stresses. Both solutions yield exactly the same result, with a precision better than 100 Pa. This confirms the proof given above, that within the assumptions of the model, stress equilibrium is achieved by minimizing the energy expanded on fitting both phases together or by maximizing the energy released upon unloading.

Two types of strain hardening behaviour have been used with which to characterize both phases. First, Voce strain hardening [118] was assumed for both ferrite and cementite:

$$\sigma = C \cdot [1 - m \cdot \exp(-n \cdot \varepsilon^{pl})]$$

The result obtained is shown in Fig. 7.6. The numbers in the legend indicate, in that order, the ferrite yield strength, the ferrite flow stress at $\varepsilon^{pl} = 3$, the cementite yield strength and the cementite flow stress at $\varepsilon^{pl} = 3$, in units of 10^2 MPa. The yield point corresponds to zero plastic strain. The value for ‘n’ was chosen to be 1. The remaining unknown parameters ‘C’ and ‘m’ can then be found by fitting the Voce curve through the two points described.

The in-set of Fig. 7.6 shows the cementite residual stresses at small loading strains. At very small strains, before the first deflection point, both phases deform elastically and no residual stresses build up. At higher strains, between the first and the second deflection point, the ferrite phase deforms plastically, while the cementite phase remains elastic during loading. This leads to a quick increase of the residual stresses. After the second deflection, both phases deform plastically and the build-up of residual stresses slows down. The blue curve shows a fourth deflection point, marked by a square. This is the point where reverse yielding of the ferrite phase occurs during unloading. The difference in flow stress between the ferrite and cementite has to be sufficiently large so that the generated back stress is able to initiate this reverse yielding, as can be seen by comparison to the red-dashed curve. Reverse yielding also occurs in the green curve, but here reverse yielding starts at the same point where cementite starts deforming plastically during loading. A separate deflection point is therefore not observed.

Saturation of the residual stress is not observed for either the blue or red curve. This illustrates that reverse yielding of the ferrite phase might slow down the residual stress build-up, but is not a sufficient condition to reach saturation. The green dot-dash curve exhibits a slight decline in the RS, going towards an almost constant value. This behaviour was obtained by giving both phases a very similar strain hardening behaviour, so that the difference in flow stress remains more or less constant.

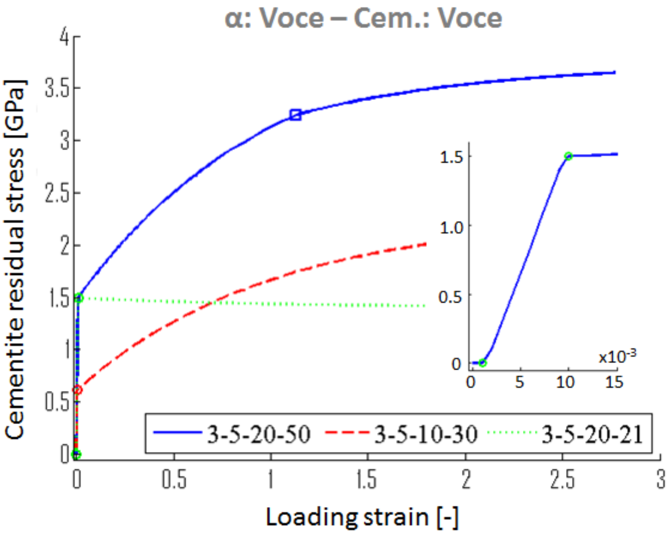

Fig. 7.6: Cementite residual stress as a function of loading strain, calculated using the 1-D residual stress sandwich model. Voce strain hardening was assumed for both phases. The numbers in the legend determine the shape of the flow curve and are described in the accompanying text. They, in that order, the ferrite yield strength, the ferrite flow stress at ε^{pl}=3, the cementite yield strength and the cementite flow stress at ε^{pl}=3, in units of 10^2MPa.

Next to the cases discussed in detail above, a range of Voce-type hardening behaviours have been input and the resulting residual stress responses classified in Fig. 7.7. Mode I and II were most prominent. An increasing amount of reverse yielding of the ferrite phase is observed because of the large difference in flow stress between ferrite and cementite and the larger relative strain hardening for cementite. In Mode I, the difference in yield stress between ferrite and cementite is larger, allowing initiation of reverse ferrite yielding before forward plasticity in cementite occurs. In Mode III and IV no reverse yielding of the ferrite phase is observed due to the smaller difference in flow stress between ferrite and cementite. In Mode IV, the ferrite phase is additionally allowed to strain harden more than the cementite phase, resulting in a decreasing amount of residual stress with increasing macroscopic strain. Mode V is obtained by making the difference in yield stress between ferrite and cementite large enough to initially result in reverse yielding of ferrite. However, because ferrite strain hardens more, relative to its initial yield point, the amount of reverse yielding decreases and eventually becomes zero. By decreasing the cementite strain hardening, Mode IV and V can be combined.

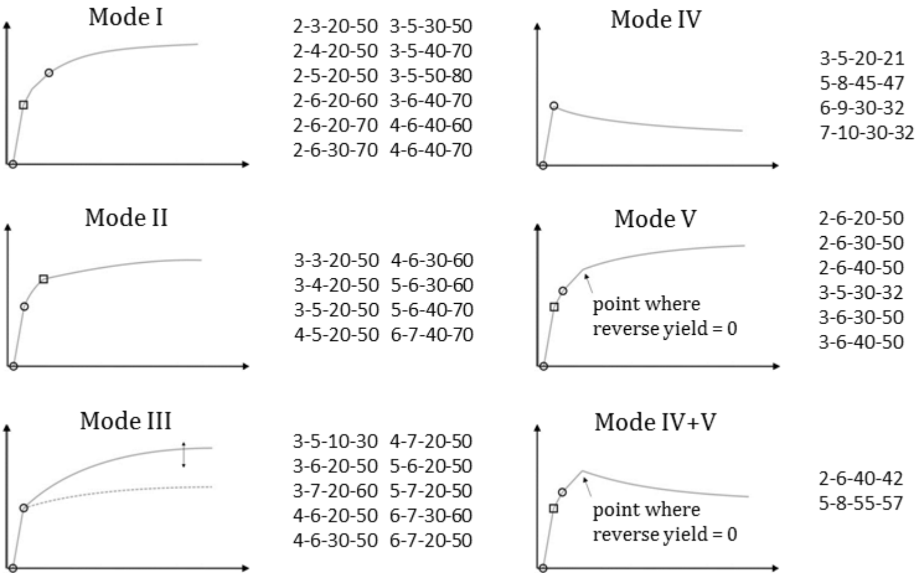

Fig. 7.7: Classification of the various residual stress behaviours obtained using Voce hardening for both phases in the 1-D residual stress model. The numbers describing the hardening behaviour are explained in the accompanying text. They are, in that order, the ferrite yield strength, the ferrite flow stress at $\varepsilon^{pl}=3$, the cementite yield strength and the cementite flow stress at $\varepsilon^{pl}=3$, in units of 10^2MPa. A circle refers to the onset of ferrite or cementite plasticity. A square refers to the onset of reverse yielding of the ferrite phase.

Alternatively, the ferrite phase was allowed to strain harden exponentially, while the cementite phase keeps it Voce strain hardening behaviour. The following expression was used for the exponential strain hardening [52,53]:

$$\sigma = A + B \cdot \exp\left(\frac{\varepsilon}{4}\right)$$

Similarly as for the Voce strain hardening, the exponential strain hardening curve was fitted through two points: the yield strength and the flow stress at $\varepsilon^{pl} = 3$. The solution for three combinations of ferrite and cementite flow curves are shown in Fig. 7.8. In the blue curve, the last deflection point again corresponds to reverse yielding of the ferrite phase and is marked with a small square. Because of the exponential strain hardening of the ferrite phase, and the even stronger increase in flow stress of the cementite phase, reverse yielding now results in a exponentially increasing RS, confirming the observation that reverse yielding of ferrite does not necessarily lead to a saturation of the RS. It is rather the combination of the strain hardening behaviours of both phases that determines whether saturation occurs.

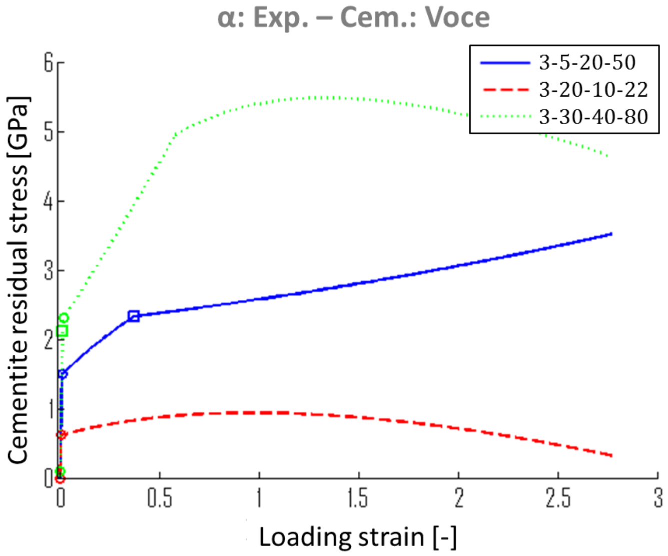

Fig. 7.8: Cementite residual stress as a function of loading strain, calculated using the 1-D residual stress sandwich model. Voce strain hardening was assumed for the cementite phase and exponential strain hardening for the ferrite. The numbers in the legend determine the shape of the flow curve and are described in the accompanying text. They, in that order, the ferrite yield strength, the ferrite flow stress at ε^{pl}=3, the cementite yield strength and the cementite flow stress at ε^{pl}=3, in units of 10^2MPa.

The red-dashed curve was obtained by allowing the ferrite phase to strain harden more than the cementite phase. At strains below 1, the strain hardening rate of the exponential function is smaller than that of the Voce function. The RS thus increases because the difference in flow stress is increased. However, at larger strains, the exponential strain hardening rate becomes larger than the Voce strain hardening rate and the RS starts to decrease. If the calculation were to be continued to larger strains, the sign of the RS would eventually switch. This shows that, under these specific conditions, not only can saturation of the RS be obtained, but even a decrease of the RS.

A last kind of behaviour is illustrated with the green, dotted curve. The difference in initial yield stress between both phases is large, resulting in the onset of reverse ferrite yielding even before cementite becomes plastic. In the strain range between cementite yielding and the deflection point at a strain of around 0.6, the residual stress is determined by the ferrite flow stress. This can be understood from the fact that in this range, reverse yielding of the ferrite phase is active. The load bearing capacity of ferrite thus determines the residual stress, as is also discussed below in relation to Fig. 7.9. Because of the strong exponential strain hardening of ferrite, the residual stress also increases. At larger strains, the ferrite phase is no longer subject to reverse yielding. It is now the difference in flow stress between ferrite and cementite that determines the residual stress, similar as for the red, dashed curve.

The model can also be used to simulate the influence of the interlamellar spacing on the residual stress evolution. It is reasonable to assume that a smaller interlamellar spacing will lead to a higher yield strength of the ferrite phase. To simulate the effect of the ILS, different ferrite yield strengths have been used in the model, while keeping the ferrite strain hardening behaviour constant. Voce strain hardening was again used for the ferrite and cementite phases.

In Fig. 7.9, a square indicates the point where reverse plastic yielding of the ferrite starts. One can observe that, before reverse plastic yielding occurs, a smaller yield strength (smaller ILS) leads to a higher RS. This is caused by the larger difference in flow stress between the two phases. However, once reverse yielding kicks in, the opposite is true: a smaller yield strength leads to a smaller RS. The reason for this is that now the ability of ferrite to carry a load determines the residual stresses which can exist. Any residual stress higher than the reverse yield strength of ferrite will simply lead to plastic relaxation instead of further build-up of the RS.

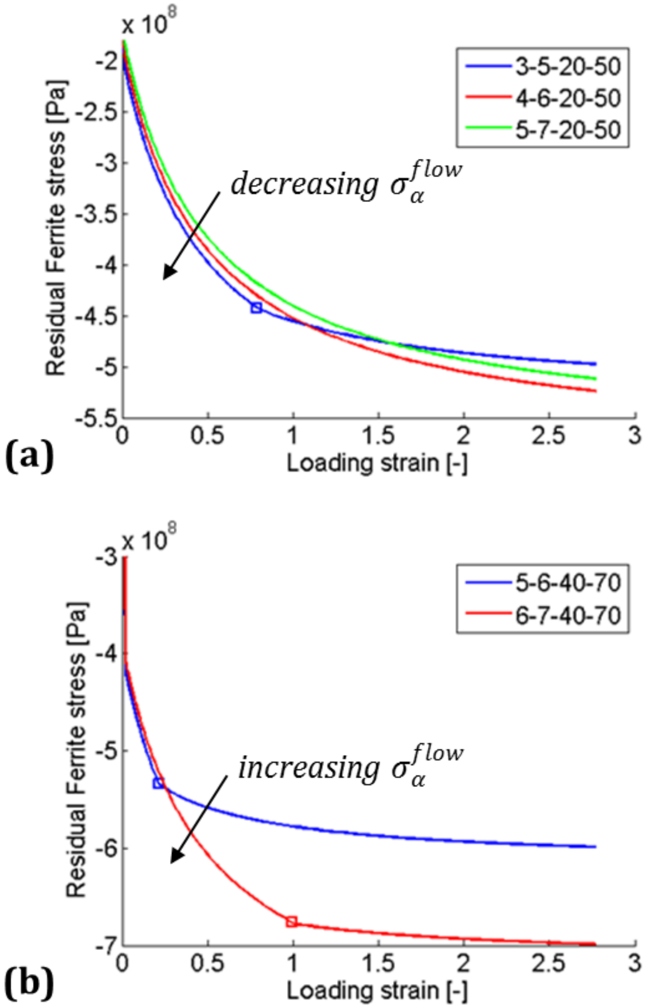

Fig. 7.9: Influence of the ferrite flow stress on the residual stress. A square indicates the onset of reverse ferrite yielding. (a) Low cementite flow stress in order to limit reverse yielding. (b) High cementite flow stress in order to promote reverse yielding.

In conclusion to the figures discussed, it is obvious that the actual in-situ strain hardening behaviour of both phases has to be considered to understand the residual stress evolution. If reverse ferrite yielding occurs, the ferrite flow stress controls the residual stress magnitude. If there is no reverse yielding, the difference in flow stress between the two phases controls the residual stress magnitude.

7.3 2-D internal stress sandwich model

7.3.1 Problem description and assumptions

Another way of understanding how and why residual stresses develop is by looking at the internal stresses and strains in the material during loading. It is these strains which, after unloading result in the remaining residual stresses. Experimentally, this can be done by executing a tensile test while following the lattice strains using neutron diffraction. While rolling is a plane strain deformation mode, a tensile test results in a 3-D strain state. With the current model, the evolution of the internal stresses during a tensile test on a thin plate will be calculated. The tensile direction is taken parallel to the RD of the sandwich model. The ND is perpendicular to the plane of the lamellae. The primary goal is to see whether, under the made assumptions, the observations from in-situ neutron diffraction experiment, presented in section 6.3, can be explained.

The sandwich microstructure is adopted again. In the RD the total strain in both phases has to be equal to the imposed strain. The arguments given under section 5.2.1 for the ND still hold and both phases can contract freely in the ND. However, there will now also be a macroscopic strain in the TD. Both phases will also constrain each other in the TD, leading to the condition that the total strain in the TD has to be equal in both phases.

If both phases contract at a different rate, for example if ferrite deforms plastically while cementite does not, an additional stress component is introduced in the material. It is therefore not possible to limit the calculation to only one direction. The stress and strain in the TD direction also have to be considered. The stress in the ND is zero, as argued above, and the strain in the ND direction can directly be computed from the strains and stresses in the other two directions. Because the actual calculation can therefore be limited to two directions, the current model is called a 2-D model.

7.3.2 Ferrite elastic – Cementite elastic

In the following, the axis x_1 is the tensile direction (RD). The axis x_2 and x_3 are the TD and ND, respectively. The strains in both the RD (i.e. tensile direction) and TD have to be equal in both phases:

$$\varepsilon_{11}^{\alpha} = \varepsilon_{11}^{\theta} \tag{7.23}$$

$$\varepsilon_{22}^{\alpha} = \varepsilon_{22}^{\theta} \tag{7.24}$$

The engineering rules for elastically isotropic materials can be used to write these iso-strain assumptions as a function of stresses.

$$\varepsilon_{11} = \frac{1+\nu}{E}\sigma_{11} - \frac{\nu}{E}(\sigma_{11} + \sigma_{22}) \tag{7.25}$$

$$\varepsilon_{22} = \frac{1+\nu}{E}\sigma_{22} - \frac{\nu}{E}(\sigma_{11} + \sigma_{22}) \tag{7.26}$$

This leads to the following expressions:

$$\frac{1}{E_\alpha}\sigma_{11}^{\alpha} - \frac{\nu_\alpha}{E_\alpha}\sigma_{22}^{\alpha} = \frac{1}{E_\theta}\sigma_{11}^{\theta} - \frac{\nu_\theta}{E_\theta}\sigma_{22}^{\theta} \tag{7.27}$$

$$\frac{1}{E_\alpha}\sigma_{22}^{\alpha} - \frac{\nu_\alpha}{E_\alpha}\sigma_{11}^{\alpha} = \frac{1}{E_\theta}\sigma_{22}^{\theta} - \frac{\nu_\theta}{E_\theta}\sigma_{11}^{\theta} \tag{7.28}$$

Additionally, the volume averaged phase stress has to be equal to the externally applied stress:

$$V_\alpha\sigma_{11}^{\alpha} + V_\theta\sigma_{11}^{\theta} = \sigma_{11}^{app} \tag{7.29}$$

$$V_\alpha\sigma_{22}^{\alpha} + V_\theta\sigma_{22}^{\theta} = 0 \tag{7.30}$$

If, for now, the applied stress is assumed to be known, this yields a set of four equations in the four unknown stress components. This set of equations can be solved to obtain expressions for the stresses in both phases:

$$\begin{aligned}
\sigma_{11}^{\alpha} &= \left(\frac{CE^{\alpha} - D\nu_\theta E_\alpha}{C^2 - D^2}\right)\sigma_{11}^{app}\\
\sigma_{22}^{\alpha} &= \left(\frac{DE^{\alpha} - C\nu_\theta E_\alpha}{C^2 - D^2}\right)\sigma_{11}^{app}\\
\sigma_{11}^{\theta} &= \left(\frac{CE^{c} - D\nu_\alpha E_\theta}{C^2 - D^2}\right)\sigma_{11}^{app}\\
\sigma_{22}^{\theta} &= \left(\frac{DE^{c} - C\nu_\alpha E_\theta}{C^2 - D^2}\right)\sigma_{11}^{app}
\end{aligned} \tag{7.31}$$

with

$$C = E_\alpha V_\alpha + E_\theta V_\theta \tag{7.32}$$

$$D = \nu_\theta E_\alpha V_\alpha + \nu_\alpha E_\theta V_\theta \tag{7.33}$$

If for example $\nu_\alpha > \nu_\theta$, ferrite will contract more than cementite in the TD. Therefore, ferrite should be in a state of transverse tension and cementite in a state of transverse compression. Because $C^2 - D^2$ is always positive and $D - C\nu_\alpha$ is in this case negative, σ_{22}^{θ} is indeed a compressive stress. From analysis of the above equations, it follows that the sign of the stresses is determined by the ratio of the Poisson ratio's, while the magnitude of the stresses is mainly determined by the ratio of the E-moduli.

The strains in both phases in the tensile direction have to be equal to each other and equal to the externally applied strain.

$$\varepsilon_{11}^{app} = \varepsilon_{11}^{\alpha} = \varepsilon_{11}^{\theta} = \left(\frac{C - D\nu_\alpha - D\nu_\theta + C\nu_\alpha\nu_\theta}{C^2 - D^2}\right)\sigma_{11}^{app} \tag{7.34}$$

From this result it follows that the composite Young's Modulus is

$$E_{11}^{comp} = \left(\frac{C - D\nu_\alpha - D\nu_\theta + C\nu_\alpha\nu_\theta}{C^2 - D^2}\right)^{-1} \tag{7.35}$$

By applying eq. 7.34, the applied stress can now be obtained from the applied strain. It is thus possible to obtain the evolution of the internal stresses and strains as a function of applied strain by executing the following steps:

1. Calculate the applied stress from the applied strain (eq. 7.34).
2. Calculate the internal stresses (eq. 7.31).
3. Calculate the internal elastic strains using the engineering rules or Hooke's law.

This procedure was followed to implement the calculation into a Matlab code.

7.3.3 Ferrite plastic – Cementite elastic

Allowing ferrite to deform plastically means that an additional plastic strain component has to be added to equations 7.27-7.28. Further introducing the applied strain as input parameters instead of the applied stress yields the following equations:

$$V_\alpha\sigma_{22}^{\alpha} + V_\theta\sigma_{22}^{\theta} = 0 \tag{7.36}$$

$$\varepsilon_{11}^{app} = \frac{1}{E_\alpha}\sigma_{11}^{\alpha} - \frac{\nu_\alpha}{E_\alpha}\sigma_{22}^{\alpha} + \varepsilon_{11}^{pl,\alpha} \tag{7.37}$$

$$\varepsilon_{11}^{app} = \frac{1}{E_\theta}\sigma_{11}^{\theta} - \frac{\nu_\theta}{E_\theta}\sigma_{22}^{\theta} \tag{7.38}$$

$$\frac{1}{E_\alpha}\sigma_{22}^{\alpha} - \frac{\nu_\alpha}{E_\alpha}\sigma_{11}^{\alpha} + \varepsilon_{22}^{pl,\alpha} = \frac{1}{E_\theta}\sigma_{22}^{\theta} - \frac{\nu_\theta}{E_\theta}\sigma_{11}^{\theta} \tag{7.39}$$

Equation 7.36 expresses the stress equilibrium in the transverse direction. Equations 7.37-7.38 express the iso-strain assumption in the loading direction and equation 7.39 expresses the iso-strain assumption in the transverse direction. The stress equilibrium equation in the loading direction is no long explicitly required to solve the problem. However, it could be seen that the solution does satisfy the stress equilibrium.

In order to be able to solve this set of equations, a link between the plastic strain state to the stress state of the material has to be made. This link is illustrated in Fig. 7.10. A Von Mises yield locus is presented of which the size depends on the equivalent plastic strain. As such, each possible plastic deformation state corresponds to a point on a certain yield locus. It is therefore possible to find the equivalent strain for this deformation state. From the normality rule, the ratios of the strain components can be obtained.

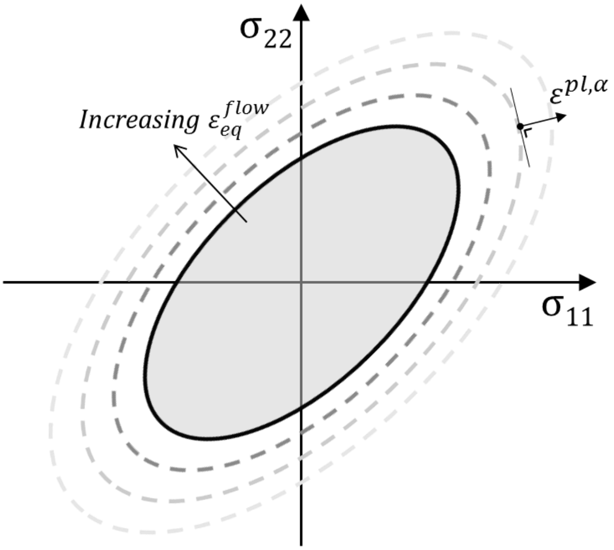

Fig. 7.10: Illustration of the concept used to link the plastic strain state to the stress state, through the use of a yield locus of which the size depends on the equivalent plastic strain.

The above idea is now going to be expressed mathematically. Assuming the material to be isotropic, a Von Mises yield locus can be used. For a planar stress state and neglecting shear stresses, i.e. assuming that the loading and transverse directions are the principle directions, this reduces to:

$$\sigma_{11}^{\alpha\,2} - \sigma_{11}^{\alpha}\sigma_{22}^{\alpha} + \sigma_{22}^{\alpha\,2} = \left[\sigma_{eq}^{flow,\alpha}\left(\varepsilon_{eq}^{pl,\alpha}\right)\right]^2 \tag{7.40}$$

with $\sigma_{eq}^{flow,\alpha}\left(\varepsilon_{eq}^{pl,\alpha}\right)$ an expression for the strain hardening behaviour of ferrite. This evolution of the equivalent flow stress with the equivalent plastic strain is assumed to be known.

The equivalent Von Mises strain can be expressed as:

$$\varepsilon_{eq}^{pl,\alpha} = \sqrt{\frac{2}{3}\left(\varepsilon_{11}^{pl,\alpha\,2} + \varepsilon_{22}^{pl,\alpha\,2} + \varepsilon_{33}^{pl,\alpha\,2}\right)} \tag{7.41}$$

The two components of plastic strain are also linked to each other by the normality rule. The Levy-Mises flow law says that

$$\dot{\varepsilon}_{kl}^{pl} = \lambda \frac{\partial F\left(\sigma_{ij}\right)}{\partial \sigma_{kl}} \tag{7.42}$$

which, for the case of the Von Mises yield locus, this results in

$$\frac{\varepsilon_{22}^{pl,\alpha}}{\varepsilon_{11}^{pl,\alpha}} = \frac{2\sigma_{22}^{\alpha} - \sigma_{11}^{\alpha}}{2\sigma_{11}^{\alpha} - \sigma_{22}^{\alpha}} \tag{7.43}$$

Finally, the conservation of volume criterion will also be needed to come to a solution.

$$\varepsilon_{11}^{pl,\alpha} + \varepsilon_{22}^{pl,\alpha} + \varepsilon_{33}^{pl,\alpha} = 0 \tag{7.44}$$

The above analysis of the problem can now be translated into a minimization problem. The goal is to find the internal stresses σ_{11}^{α}, σ_{22}^{α}, σ_{11}^{θ} and σ_{22}^{θ} resulting from a certain input loading strain ε_{11}^{app}. The following solution procedure was implemented in Matlab:

1. Choose values for σ_{11}^{α} and σ_{22}^{α}.
2. Obtain the value of $\sigma_{eq}^{flow,\alpha}$ from the yield locus on which the chosen point is located (eq. 7.40).
3. From the known strain hardening behaviour obtain $\varepsilon_{eq}^{pl,\alpha}$.
4. Using the normality rule (eq. 7.43) and the conservation of volume (eq. 7.44), the three components of the plastic deformation state can be calculated (see appendix G).
5. Calculate σ_{11}^{θ} and σ_{22}^{θ} from equations 7.36 and 7.39.
6. Define a residual for the system, based on the remaining two equations which haven't been used yet (eq. 7.37-7.38):

$$R_1(\sigma_{11}^{\alpha}, \sigma_{22}^{\alpha}) = \varepsilon_{11}^{app} - \frac{1}{E_\alpha}\sigma_{11}^{\alpha} + \frac{\nu_\alpha}{E_\alpha}\sigma_{22}^{\alpha} - \varepsilon_{11}^{pl,\alpha}$$

$$R_2(\sigma_{11}^{\alpha}, \sigma_{22}^{\alpha}) = \varepsilon_{11}^{app} - \frac{1}{E_\theta}\sigma_{11}^{\theta} + \frac{\nu_\theta}{E_\theta}\sigma_{22}^{\theta} \tag{7.45}$$

$$R(\sigma_{11}^{\alpha}, \sigma_{22}^{\alpha}) = {R_1}^2 + {R_2}^2$$

7. Find the values of σ_{11}^{α} and σ_{22}^{α} for which the residual is minimal (i.e. approaches zero).

As an illustration, the surface of residuals as calculated for a specific example is shown in Fig. 7.11. It can be seen that the surface of residuals indeed exhibits a minimum at *R = 0*. The blank area on the left side of Fig. 7.11(b) corresponds to a region inside the initial yield locus. This shows that a solution can indeed be found. However, the shallow and elongated shape of the valley makes the problem is somewhat ill-conditioned.

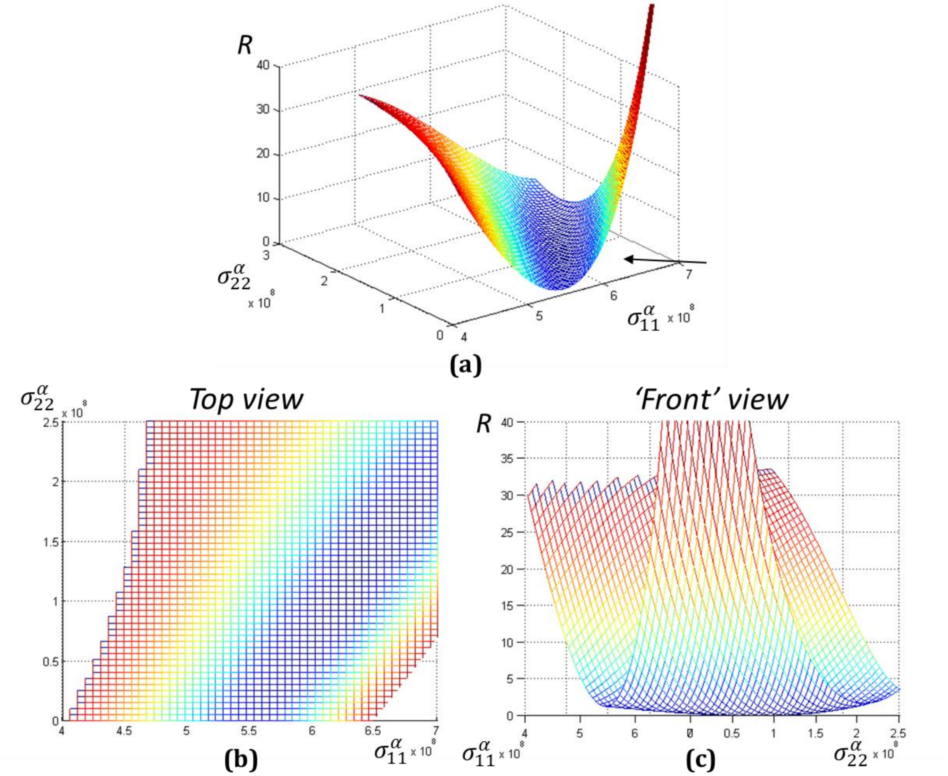

Fig. 7.11: Example of the surface of residuals as calculated from eq. 7.45, within the range $400MPa < \sigma_{11}^{\alpha} < 700MPa$; $0MPa < \sigma_{22}^{\alpha} < 250MPa$. *(a) 3-D view (b) viewed along the R-axis (c) viewed along the arrow indicated in (a).*

7.3.4 Results

7.3.4.1 1-D reference

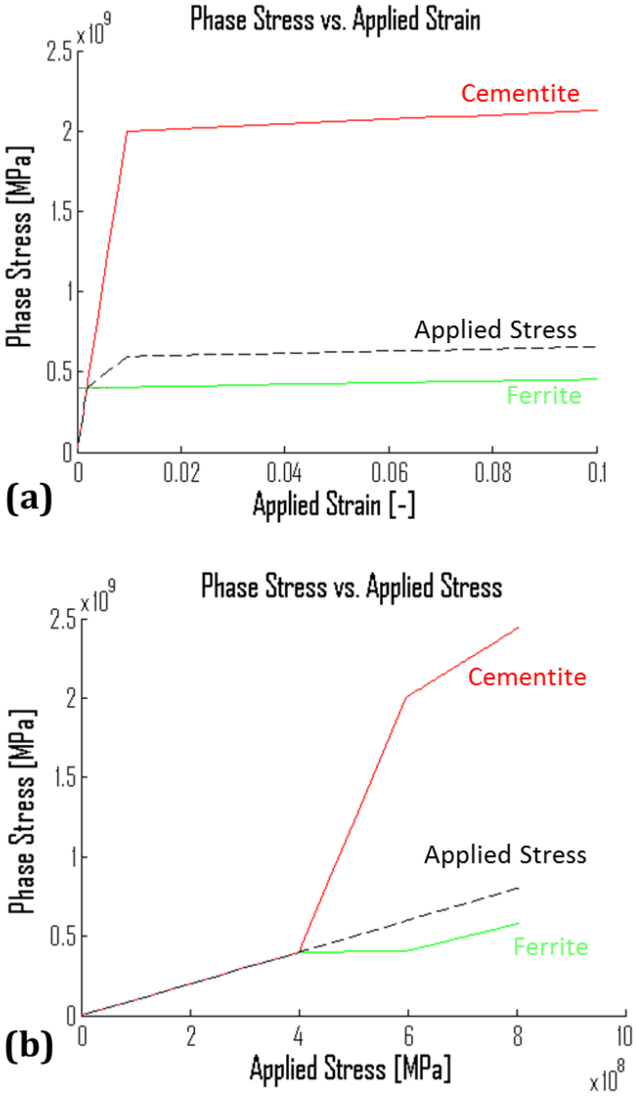

Fig. 7.12: (a) Phase stress as a function of applied strain in a two-phase lamellar sandwich microstructure, 1-D reference. (b) Phase stress as a function of applied stress.

Prior to giving the results of the 2-D internal stress sandwich model, the case where the transverse direction is not considered will be described as a reference. Under the assumption of a sandwich microstructure, both phases are subjected to a strain equal to the externally applied strain. The stress existing in a phase at a certain applied strain can then simply be obtained from its in-situ flow-curve, as shown in Fig. 7.12(a). Both phases have been assigned the same Young's Modulus. Due to the idealized microstructure, the applied stress can simply be calculated as the volume average of the phases stresses and is depicted with the dashed curve. In Fig. 7.12 (b), the phase stress vs. applied stress is shown. Two deflection points can be seen. The first one at the stress level where the ferrite phase becomes plastic, the second one where the cementite phase becomes plastic.

7.3.4.2 2-D model results

Ferrite elastic – Cementite elastic

The calculation for the case where both phases are elastic led to the following expression for the stiffness of the composite material in the loading direction (eq. 7.35):

$$E_{11}^{comp} = \left(\frac{C - D\nu_\alpha - D\nu_\theta + C\nu_\alpha\nu_\theta}{C^2 - D^2}\right)^{-1}$$

with

$$C = E_\alpha V_\alpha + E_\theta V_\theta$$
$$D = \nu_\theta E_\alpha V_\alpha + \nu_\alpha E_\theta V_\theta$$

If both phases are assumed to have the same Young's Modulus, this simplifies to

$$E_{11}^{comp} = \frac{E(1 - B^2)}{1 - B\nu_\alpha - B\nu_\theta + \nu_\alpha\nu_\theta}$$

with

$$B = \nu_\theta V_\alpha + \nu_\alpha V_\theta$$

It can then be shown that E_{11}^{comp} is always larger than or equal to E, by proving that

$$B^2 \leq B\nu_\alpha + B\nu_\theta - \nu_\alpha\nu_\theta$$

The right hand side of this inequality can be rewritten as

$$B^2 \cdot \left(\frac{\nu_\alpha + \nu_\theta}{B} - \frac{\nu_\alpha\nu_\theta}{B^2}\right)$$

Proving the inequality then comes down to proving that

$$\frac{\nu_\alpha + \nu_\theta}{B} - \frac{\nu_\alpha\nu_\theta}{B^2} \geq 1$$

or thus

$$\nu_\alpha\nu_\theta \leq B(\nu_\alpha + \nu_\theta - B)$$

Expanding B and taking into account that $V_\alpha + V_\theta = 1$ leads to the requirement

$$\nu_\alpha\nu_\theta \leq \nu_\alpha\nu_\theta + (\nu_\theta - \nu_\alpha)^2[V_\alpha - (V_\alpha)^2]$$

Because all terms are positive and smaller than 1, the above inequality is always true, which proofs that E_{11}^{comp} indeed is always larger than or equal to E.

This can be understood as follows. In the 2-D model the composite is always stiffer than the 1-D reference because of the build-up of additional stresses in the transverse direction. As the material elongates in the tensile direction, both phases want to contract according to their Poisson ratios. However, geometrical compatibility between both phases has to be maintained in the TD. If the Poisson ratios are not identical, additional stresses will be introduced in the material to enforce this geometrical compatibility. The tensile force required to reach a certain elongation now has an additional component related to the stresses in the TD. In the limiting case that ν_α and ν_θ are equal, the 2-D elastic behaviour reverts back to the 1-D reference where E_{11}^{comp} is equal to E.

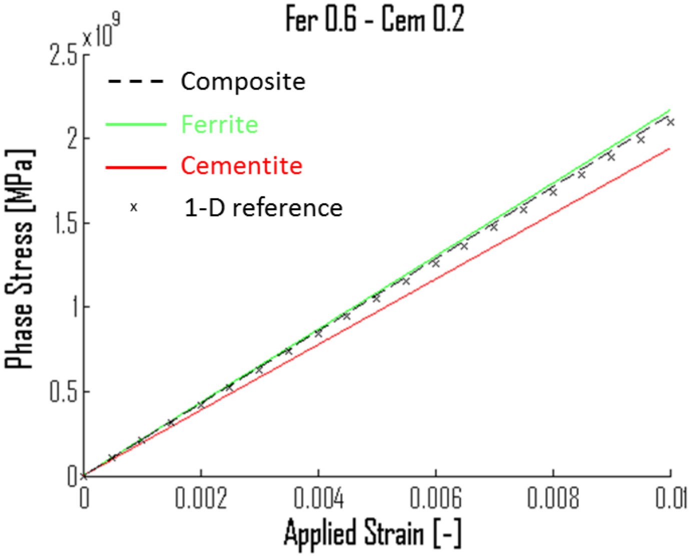

Fig. 7.13: Phase stress as a function of applied strain as calculated using the 2-D internal stress sandwich model. For illustration purposes, ν_α and ν_θ were chosen to be 0.6 and 0.2 respectively. Only the region where both phases deform elastically is shown.

Fig. 7.13 illustrates the above discussion. The crosses display the expected phase and composite stress if the TD would not be considered. To enhance the result, extreme values for the Poisson ratios were chosen: 0.6 for ferrite and 0.2 for cementite. With these Poisson ratios, the ferrite phase wants to contract much more than the cementite phase. To maintain geometrical compatibility, this results in a tensile transverse stress in the ferrite phase and a compressive transverse stress in the cementite phase. The former stress impedes further elongation of the ferrite, resulting in the observed higher stress in the tensile direction. The opposite is true for the cementite phase, where the compressive stress in the TD facilitates further elongation, leading to the observed lower stress in the tensile direction. Finally, one can also observe that stress applied in the composite is higher than the stress required in the 1-D case.

Ferrite plastic – Cementite elastic

The 2-D model was developed to gain some insight as to whether or not the assumption of a sandwich microstructure can explain the results obtained with in-situ neutron diffraction (see section 6.3). During the in-situ tensile test, there was no experimental evidence for plastic deformation of cementite. In the calculation, the cementite phase is therefore also assumed to remain elastic. The ferrite phase has been attributed a yield strength of 400 MPa and a Voce strain hardening behaviour with a UTS of 800 MPa (see description in section 7.2.4). A Von Mises yield locus was adopted for the ferrite phase. The Poisson ratio for ferrite was taken to be 0.28 as is often reported in literature. Cementite was considered to be elastically isotropic with Poisson ratio 0.33. The result of a calculation with these parameters can be seen in Fig. 7.14(a).

In the elastic-elastic case discussed above, the ferrite phase contracted more than cementite in the TD because of the chosen large Poisson ratio. Here, the ferrite phase contracts more because it is deforming plastically, which essentially means a contraction ratio of 0.5. A similar line of reasoning as in the discussion above leads to a tensile transverse stress in the ferrite phase, which impedes further elongation. As compared to the 1-D reference, this leads to a higher stress in the ferrite phase in the tensile direction. If one were to magnify the figure below, the opposite would be seen to be true for the cementite phase.

The stress applied to the composite as a whole is slightly increased, but does not change perceptibly as a result of including the transverse direction in the calculation. As illustrated in Fig. 7.14(b), repeating the calculation with the (unrealistic) Poisson ratios used for Fig. 7.13 shows the same trends for the stresses, but leads to a larger difference with the 1-D reference. This could indicate that the difference in elastic properties can result in a significant strengthening contribution for two-phase composites.

Plotting the lattice strain in the tensile direction instead of the phase stress gives exactly the same trend as for the phase stress. The lattice strain continues to increase at a rate which is slightly higher than that for the 1-D scenario. Comparing this to the experimental observation of a decreasing lattice strain, made on a ‘imperfect’ sandwich microstructure, shows that the 2-

D sandwich model does not adequately capture reality. The composite response can be compared to the experimentally recorded stress-strain curves, indicating that the strain hardening rate of the composite is much too high. This discrepancy will be discussed in more detail in the next Chapter.

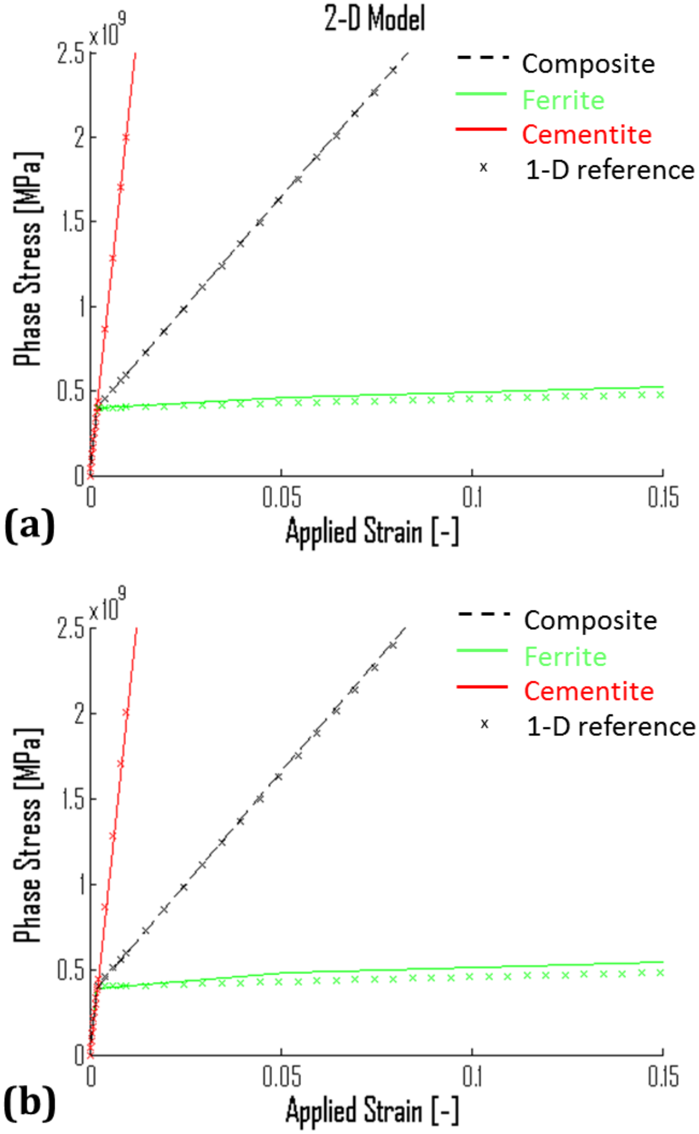

Fig. 7.14: Results obtained using the 2-D internal stress sandwich model. The phase stress is given as a function of applied strain. In (a) ν_α *and* ν_θ *are equal to 0.28 and 0.33, respectively. In (b)* ν_α *and* ν_θ *are equal to 0.6 and 0.2, respectively.*

7.4 Summary

An idealization of the real microstructure of cold rolled pearlitic steel sheet to a perfect sandwich microstructure has been proposed. This simplification has allowed to setup intuitive models to calculate the internal and residual stress evolution. It has been reasoned that a 1-D model is sufficient to come to an understanding of the residual stress development during cold rolling, while a 2-D model has been developed to study the internal stress evolution during a tensile test.

The 1-D residual stress sandwich model showed that the interplay between the in-situ strain hardening behaviours of the individual phases is paramount to understanding the residual stress evolution. Independent of the chosen strain hardening, a very strong increase of the residual stress was observed in the cementite-elastic, ferrite-plastic region. Additionally, contrary to what has been suggested in literature, reverse plastic yielding of the ferrite phase is not a sufficient condition to obtain saturation of the residual stress. On the other hand, whether or not reverse yielding occurs is important to understand the influence of the ferrite flow stress on the residual stress. If reverse yielding occurs, a higher ferrite flow stress will yield higher residual stresses. Contrary, without reverse yielding, a larger difference in flow stress between ferrite and cementite results in a larger residual stress. This also means that the ILS, which essentially influences the ferrite flow stress, can influence the residual stress in two ways.

The calculation results lead to three possible scenarios in which the residual stress saturates. The first possibility is to have reverse yielding of the ferrite phase combined with a saturating ferrite flow stress. Secondly, saturation can be obtained if both phases exhibit approximately the same strain hardening rate. Lastly, the ferrite phase can be allowed to strain harden exponentially. This then has to be combined with a relatively strong cementite phase that is allowed to strain harden significantly. At larger strains, when the ferrite flow stress starts to approach the cementite flow stress, this scenario will inevitably lead to a decrease of the residual stress.

The 2-D internal stress sandwich model shows that a composite material of which the phases have different Poisson ratio's has a higher Young's modulus. Although the effect is always present as soon as the two phases have a different Poisson ratio, it is not apparent unless the difference is fairly large. In the region where ferrite is deforming plastically, while the cementite is elastic, a similar effect results in a higher internal stress in the ferrite phase, which continues to increase with increasing tensile strain.

8 Discussion and synthesis of gained insight

Some of the results have already been discussed and explained in Chapter 6. The main results will be compared here, in order to come to a more complete view on the residual stress and strain development in pearlite, as well as on its deformation behaviour. In the first part, the results of the residual lattice strain analysis and the sandwich model will be compared and linked to one another. This will allow to come to a possible explanation for the three stages observed in the residual lattice strain development. In the second part, the existence of strain gradients in pearlite will be discussed. A couple of additional points regarding the plastic deformation of pearlite will be discussed in the third part of this chapter. The chapter will conclude by shortly re-evaluating the applicability and importance of the used sandwich model.

8.1 An explanation for the residual strain evolution in pearlite

8.1.1 Three stages in the residual lattice strain evolution: sheet vs. wire

Three stages can be recognized in the residual lattice strain evolution for cold rolled pearlitic steel sheet. The first stage is characterized by a quick increase of the residual lattice strain in the rolling direction. In the second stage the residual lattice strain evolution stagnates and is almost constant with increasing rolling strain. The intergranular strain evolution in this second stage is very limited. In the third and final stage, significant intergranular strain development is observed. Unfortunately it is difficult to estimate the evolution of the average micro-phase strain.

These three stages in the residual lattice *strain* evolution compare remarkably well with those found in the residual *stress* evolution in drawn pearlitic steel wires as measured by Kriška et al. and presented here in section 6.2.1.1. It is not straightforward to compare strain and stress measurements. The residual stress in sheet was also calculated, however, the assumptions made in the residual stress calculation for the sheet are very different as compared to those made in the $\sin^2\psi$ method used for the stress measured in wire. Additionally, because of all the assumptions involved, the stress values obtained for the sheet should rather be considered to be indicative. Therefore, the wire stress vs. sheet stress comparison would not be straightforward to make in this case. On top of that, because the d-$\sin^2\psi$ curves are strongly non-linear, as is illustrated in [105], their linearization also introduces an error on the stress value. The evolution of the lattice spacing as measured parallel to the wire axis was seen to approximately follow the evolution of the slope of the linearized d-$\sin^2\psi$ curve, from which the stresses are calculated. In figure Fig. 8.1, the slope from which the stress is calculated and the point giving the lattice spacing along the drawing direction, are illustrated for a sample cold drawn to a strain of 2.638, and for the 110 reflection. From these graphs, the lattice plane spacing in the drawing direction was estimated for a number of samples. The numeric data was unfortunately not available to the present author. From these d-values, the lattice strains were calculated and are shown in Fig. 8.2. By comparison to the residual stresses in Fig. 6.20, it can indeed be seen that the lattice strain follows the same evolution as the calculated residual stress.

In light of the above discussion, and together with the remarkable comparison between the residual strain in sheet and the residual stress in wire, it is proposed that in this special case, a comparison between the residual strain in sheet and the residual stress in wire is of interest nevertheless.

The first and last stages are slightly different for the wire. In the first stage the build-up of the residual stress is slower as compared to the sheet material. In the last stage the average micro-phase stress seemingly exhibits more of a decreasing trend in the wire. In general, the start of the three stages is also shifted towards higher strains. This shift is too large to be explained by the difference in effective strain ($\varepsilon_{\mathrm{eff,sheet}} \approx 1.1547\ \varepsilon_{\mathrm{eff,wire}}$, for a given elongation). The reason for this shift is likely related to the mechanisms at work in each separate stage and will be discussed further in the following sections.

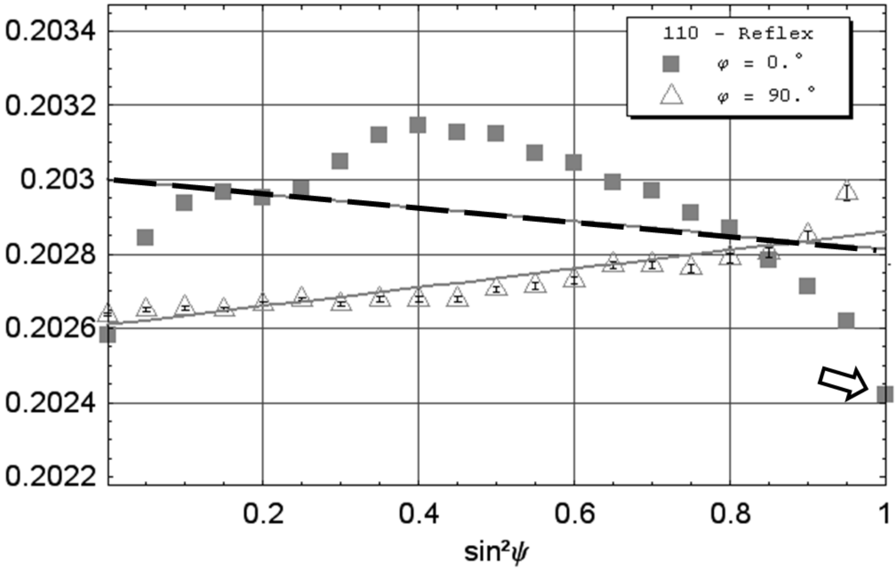

Fig. 8.1: Illustration of a d-sin^{2}ψ curve measured on a wire cold drawn to a strain of 2.638. The point where φ=0° and sin^{2}ψ=1 corresponds to the drawing direction (indicated by the arrow). The slope yielding the residual stress in the drawing direction is indicated with the thick, dashed lined.

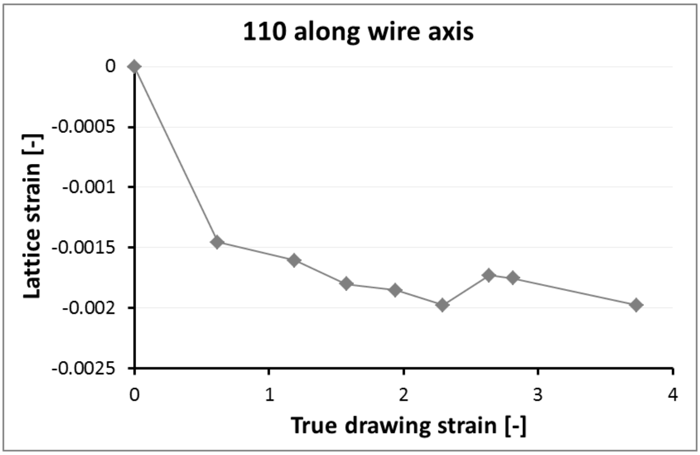

Fig. 8.2: Lattice strain along the drawing direction for the 110 reflection of the cold drawn wire. Calculated from d-values, estimated from graphical representations of the d-$\sin^2\psi$ curves.

In general, it can be said that wire and sheet behave very similarly. The reasons for the three stages are likely also similar in wire and sheet. In the following, the three stages will be discussed in a general sense. Where necessary the differences between sheet and wire will be pointed out.

8.1.2 Stage 1: Sharply increasing residual stress/strain

The first stage, of sharply increasing residual lattice strain, can for the sheet material be split in two regions. First there is a very strong increase in the residual strain after the first rolling pass (3% strain). This jump is followed by a region of a somewhat slower increase in residual strain up to the transition to stage 2. The wire material does not exhibit the initial jump in residual stress.

The initial jump compares well with the results of the sandwich model. In the model, this corresponds to the region before the point where cementite starts deforming plastically. Stage 1 could therefore be thought of as the stage in which cementite is plastifying. The slower increase in wire and the second region of stage 1 for sheet can then be caused by the inhomogeneity of the microstructure (lamellae orientation, lamellae thickness, local cementite volume fraction, local crystal orientation), leading to variations in the onset of cementite plasticity in different parts of the material.

Another possibility for the slower increase is illustrated in Fig. 7.8 by the green, dotted curve. The initial jump is followed by a region of more slowly increasing residual stress, in which the residual stress magnitude is controlled by the ferrite flow stress through reverse yielding combined with extensive strain hardening. This might indeed explain stage 1 for the sheet.

The extension of stage 1 to larger strains in wire and the more gradual increase is likely the result of a superposition of the two mechanisms proposed above. The jump might not be observed because of a more inhomogeneous microstructure, spreading the strain region in which cementite is plastifying. At the same time, the residual stress magnitude in wire may be controlled by reverse ferrite yielding up to larger strains, if the in-situ ferrite flow stress is lower in the undeformed wire as compared to sheet. Except for a slightly larger ILS (180nm in wire vs. 140nm in sheet), there is no direct evidence for the latter possibility.

8.1.3 Stage 2: Stagnating residual stress/strain

Based on the results of the sandwich model there are three possibilities to get a stagnating residual stress. The first possibility is to have a residual stress magnitude controlled by reverse yielding of the ferrite phase, combined with a saturation of the in-situ ferrite flow stress. The latter condition cannot be justified based on the reported exponential strain hardening of pearlite as a whole. Yielding of pearlite, i.e. a deviation from linearity in the macroscopic stress-strain curve, is controlled by yielding of the softer ferrite phase. The ferrite in-situ yield stress can thus be estimated by adding the residual ferrite stress to the pearlite yield stress. Because the residual stress is almost constant, the ferrite phase also has to strain harden exponentially. As a result, the proposed explanation for residual stress saturation, through reverse ferrite yielding, cannot be correct.

The second option to explain a stagnating residual stress would be to have comparable strain hardening in both phases. However, the small thickness of the cementite lamellae and lack of dislocation storage, make it unreasonable to attribute exponential strain hardening to the cementite phase. The second explanation for residual stress stagnation is therefore also not correct.

That leaves one last possibility for saturation or stagnation of the residual stress as is illustrated by the green, dotted curve in Fig. 7.8. Stagnation is obtained by allowing the ferrite phase to strain harden exponentially, while also allowing a significant, non-exponential strain hardening of the cementite phase. Eventually the residual stress magnitude would then have to start decreasing. However, it is likely that the by the time this point is reached, other mechanisms such as cementite decomposition and development of a third interface-phase will start controlling the residual stress development. In any case, the above discussion illustrates, assuming exponential strain hardening for ferrite, stagnation of the residual stress is only possible if cementite also strain hardens to some extent.

The relatively low value of the residual ferrite stress in this region (~-300MPa) constitutes an additional proof that reverse yielding of the ferrite phase cannot play an important role in stage 2. The pearlite yield stress at a rolling strain of 1 is approximately 1200MPa. The in-situ ferrite yield stress can thus be estimated to be on the order of 900MPa, which is much higher than the residual stress magnitude. The magnitude of the residual stress in stage 2 is thus controlled by the difference in flow stress $\Delta\sigma_{flow}$ between the two phases, and not by the maximum load ferrite can carry. The large difference in residual stress magnitude and ferrite yield stress also indicates that $\Delta\sigma_{flow}$ cannot be too large.

A slight increase of the residual lattice strain for the major 110 reflection can be observed for the rolled sheet. A similar slight increase in residual stress has also been observed on the cold drawn wire. In his Ph.D. thesis, this lead Kriška to suggest that in this region cementite has a slightly higher strain hardening rate as compared to ferrite. Otherwise, the drop in $\Delta\sigma_{flow}$ would cause a decrease of the residual strain magnitude. However, as mentioned above, in section 8.4.3 it will be shown that cementite is not likely to strain harden more than ferrite. The observed slight increase of the residual stress/strain magnitude can rather be explained based on the asymmetry of the ferrite peaks (section 6.2.4). From the very onset of stage 2, a dislocation rich interface-phase starts to develop. The residual stress in this stronger phase evolves towards less compression and eventually tension (see Fig. 6.50). The volume fraction of 'bulk' ferrite is also decreasing (see Fig. 6.52). Therefore, the 'bulk' ferrite will have to carry a higher compressive load.

It should also be remarked that, contrary to what has sometimes been suggested in literature, fragmentation of the cementite phase cannot explain a saturation of the residual stress. Cementite fragmentation would lead to a reduced load bearing capacity of the cementite, which could also be viewed as a form of strain softening. The resulting drop in $\Delta\sigma_{flow}$ would then rather lead to a reduction of the residual stress magnitude.

To conclude this section, the significantly different residual lattice strain evolution in the P500 and P680 sample sets should be addressed. Microstructural observations indicate that the as-patented P680 sample has a larger ILS. A literature review performed by Langford [53] showed that thicker cementite lamellae are more brittle. It is then possible that after an initial stage of elastic deformation the thickest lamellae start fragmenting, while only the thinner lamellae can deform plastically. Because of this, the average load bearing capacity of cementite is decreased, resulting in a decrease of the residual stress magnitude. Once all those lamellae unable to deform plastically have fragmented, the residual stress can again start to increase due to simultaneous strain hardening in both phases.

8.1.4 Stage 3: Development of strong intergranular stresses/strains

In the third stage intergranular strains develop. It is was unfortunately not possible to unambiguously determine the evolution of the average micro-phase stresses and strains, within the timeframe of this work. Only taking into account peak intensity and multiplicity did not provide satisfactory results. Also evolutions of diffracted intensity with for example wavelength or scattering angle and other, possibly instrument specific, elements should be considered. The discussion of stage three will therefore mainly be focussed on explaining the emergence of significant intergranular residual stress and strain development.

To understand where the intergranular stress development in stage 3 comes from, it is instructive to first consider why it does not develop in stage 2. In the LC steel investigated by Oliver et al. [17], for example, the intergranular stress development is also limited in the loading direction. In the transverse direction however, there is a more important intergranular stress development. Our experiments indicate that virtually no intergranular residual stresses develop in the cold rolled sheet, in any direction. This can be attributed to the presence of the cementite lamellae based on two different mechanisms.

Intergranular stresses result from differently oriented grains behaving differently. In pearlite, the areas that have different ferrite crystal orientations are not grains, but nodules, which may contain multiple colonies [101,119]. It is the interaction between colonies with different ferrite crystal orientations that should lead to the development of intergranular stresses. However, it is likely that the behaviour of the colonies is not in the first place governed by the ferrite crystal orientation, but by the lamellae alignment with respect to the loading axis. If the lamellae orientation is not strongly coupled to the ferrite crystal orientation, colonies with the same ferrite crystal orientation will behave differently. Any intergranular stresses which might develop between the ferrite grain families will therefore be inhibited because of differing lamellae orientations.

At larger deformations, the areas in which the ferrite crystal orientation is homogeneous become very small (see section 6.1.2). So small, that they are confined within one lamella. Along the length of one lamella, multiple ferrite orientation domains occur. These small, differently oriented ferrite 'crystals' which are contained within one lamella, are all forced to deform in the same way, as imposed by the harder cementite lamellae. Because of this, no intergranular stresses can again develop.

At sufficiently larger strains all lamellae are oriented in approximately the same direction. This removes the first inhibiting factor described above. With the development of a strong macroscopic crystallographic texture, the ferrite crystal orientation also has to become more homogeneous over a larger area. This is also suggested by an EBSD scan presented in [64]. The second inhibiting factor described above is then also removed. Therefore, at sufficiently large strains, there must come a point where intergranular residual stress development becomes possible.

The onset of intergranular stress development is shifted to a larger strain in wire. This may be related to curling of the cementite lamellae. Curling imposes an additional deformation on the ferrite and forces all ferrite grains to curl, irrespective of their orientation with respect to the radial direction. This may delay the interaction between differently oriented grains. Curling can also result in more orientation fragmentation in ferrite, again making intergranular strain development more difficult and postponing it to larger strains.

Kriška [2] suggested that in this last stage, “the ferrite behaves as if the cementite is not present anymore”, allowing the partitioning between the different grain families. He further mentions that this could be the case if (1) the cementite is completely fragmented or dissolved or if (2) the mechanical properties of the two phases are not so different anymore. The current author likes the suggestion that ferrite behaves as if there is no cementite, but does not per-se agree with the proposed explanation.

Because the residual ferrite stress remains compressive at the point where intergranular residual stresses start to develop, complete fragmentation or dissolution of the cementite phase requires that the cementite phase be replaced by a ‘new’ hard phase. Such a new phase could be the interface-phase whose existence has been proposed in section 6.2.4. However, at the onset of stage 3 the residual lattice strain in this phase is still compressive. This means that it has at this point not yet completely replaced cementite. And, in any case, some ‘barrier-phase’ remains.

Option two might be possible if ferrite strain hardens enough to reach a strength comparable to that of cementite. However, if both phases have an equal flow stress, the residual stresses have to tend to zero. This is clearly in contradiction to the experimental evidence.

The statement that ‘ferrite behaves as if there is no cementite’, should rather be understood as the various ferrite grain families feeling the cementite in the same way. I.e. cementite, or another hard phase, still influences the ferrite strength, but does so to the same extent in all colonies. Only then will intergranular stresses be given a chance to develop.

8.1.5 Cementite vs. ferrite residual stress/strain

In addition to the residual stresses and strains in ferrite, those in cementite have also been determined. Because of the difficulty associated with measuring cementite diffraction peaks, especially at large deformations, the cementite residual stresses and strains are only available in the first two stages of the residual stress development. Qualitatively, the cementite data supports the view developed based on the ferrite data. Unfortunately, the inferior quality of the cementite diffraction peaks and the uncertainty in the cementite elastic constants (see section 6.2.2.2) did not allow to obtain a value for the cementite residual stress which is reliable enough to compare quantitatively with the ferrite residual stress. The difference between cementite residual stress calculated from the ferrite residual stress and the measured cementite residual stress, ranges from 100 to 1000 MPa. This compares to values of the residual stress on the order of 500, 1000 and 1500MPa in the TD, ND and RD directions, respectively. The best agreement is found in the rolling direction and the worst agreement in the transverse direction.

8.2 Intergranular strains in ferrite

So far, only the existence or non-existence of intergranular strains has been discussed, as well as a qualitative interpretation of their magnitude. It is now also instructive to look at the order of the intergranular strains, i.e. which grain family develops the largest or smallest residual lattice strain, and try to understand these observations.

Before analysing the results, it is good to have an idea of the elastic and plastic anisotropy of the various grain families. The stiffness along the loading direction, for a cubic, single crystal with an <hkl>-direction parallel to that loading direction, depends on the cubic elastic anisotropy factor A_{hkl} [120].

$$A_{hkl} = \frac{h^2k^2 + h^2l^2 + k^2l^2}{(h^2 + k^2 + l^2)^2}$$

The value of A_{hkl} for the various grain families is given in Table 8.1. It should be remarked that in a poly crystal, this dependence will only be accurate as long as no strong crystallographic texture is present [17]. However, for the current discussion, the picture presented by A_{hkl} will be sufficient.

The plastic anisotropy can be estimated from the Taylor factors (M) of the various grain families. The Taylor factors for a grain family with an <hkl>-

direction parallel to the loading direction have been calculated using the MTM-Taylor software developed by P. Van Houtte [121]. The results for both an axi-symmetric and a plain-strain deformation are given in Table 8.1. A higher Taylor factor indicates a higher resistance to plastic deformation.

Table 8.1: Cubic anisotropy factor (A_{hkl}), and Taylor factor for axi-symmetric and plain-strain deformation modes, for various <hkl>-grain families.

hkl-grain family	A_{hkl}	*M, axi-symm.*	*M, plain-strain*
<110>	0.25	3.182	3.349
<211>	0.25	2.734	3.368
<321>	0.25	2.903	3.328
<310>	0.09	2.474	2.666
<200>	0	2.121	2.330

The internal lattice strain development during a tensile test has been presented in section 6.3.2. It could be seen that the <200> grain family is elastically the most compliant one and that the <110> grain family is the stiffest one. This agrees well with the expected elastic anisotropy, and explains the higher internal strain in the <200> grain family upon yielding. With continued plastic deformation, it is expected that load will be transferred from the softer <200> and <310> grain families to the stronger <110> and <211> grain families. However, no such evolution can be observed in any of the figures presented in section 6.3.2 or Appendix E. This suggests that plastic anisotropy does not constitute a major contribution to the observed intergranular strains during loading.

After unloading, it is expected that the residual lattice strain will be less compressive in the stronger grain families as compared to the softer grain families. This is indeed what is observed for all samples. However, as pointed out in the previous paragraph, plastic anisotropy is not expected to play a decisive role. An alternative explanation has been suggested by Oliver et al. [17] in terms of elastic anisotropy. The cementite phase imposes a compressive stress on the ferrite phase during unloading. Under influence of this stress, the more compliant <200> and <310> grain families will then develop a larger residual strain as compared to the stiffer <110> and <211> grain families.

At this point, it should also be remarked that the internal lattice strain evolution measured as part of this work agrees entirely with the results available in literature [17,21–23,28,32]. Also the variations amongst the measured samples agrees with the various data reported in literature.

The residual lattice strain and stress development the ferrite phase of cold drawn and cold rolled pearlite has been presented in sections 6.2.1.1 and 6.2.2.1, respectively. The order of the intergranular residual stresses in the cold drawn wire corresponds to the order observed after a tensile test. The most compliant direction (<200>) exhibits the most compressive residual stress and the stiffest direction (<110>) exhibits the least compressive residual stress. At the large strains involved in cold drawing, this trend may further be reinforced by plastic anisotropy, which would lead to the same order of the residual stresses.

The intergranular residual lattice strains in cold rolled pearlite present a somewhat different picture. Up to a rolling strain of around 1, the same, expected order of the intergranular strains is observed. However, at larger rolling strains the order of the intergranular strains is completely reversed, as can be seen from Fig. 6.28 and Fig. 6.31. Because this occurs for both the P500 and P680 samples, this phenomenon is independent of the interlamellar spacing.

This remarkable difference between cold drawn and cold rolled pearlite must find its origin in the different deformation mode and the resulting differences in microstructure and crystallographic texture. It could also be linked to preferential strain hardening of some orientations as a result of cold rolling or the development of a larger volume fraction of interface ferrite (see sections 6.2.4 and 8.4.2). At this point, the exact origin of the reversal of the order of intergranular residual lattice strains in cold rolled sheet is not understood.

8.3 Strain gradients in pearlite

8.3.1 Break-down of the iso-strain assumption

The deformation behaviour of pearlite has often been interpreted based on an idealization of the microstructure into a sandwich. In this scenario, where the material consists of a stack of flat, well aligned ferrite and cementite lamellae, the iso-strain assumption holds. The total deformation in ferrite and cementite has to be equal in order to maintain geometric compatibility between both phases. The same approach has been followed in this work to simplify the modelling of the internal and residual stresses. However, the experimental evidence implies that this is a strong oversimplification which does not allow to capture the real deformation behaviour of pearlite.

The first evidence can be found in the recorded micrographs. While the microstructure is indeed lamellar and at strains higher than one, these are quite well aligned with the rolling plane, the microstructure does not at all resemble an ideal sandwich. In many locations the lamellae are bend, broken, fragmented or not there at all. Such an imperfect microstructure does not require both phases to deform according to the iso-strain assumption.

More evidence is presented by the in-situ neutron diffraction results. The RS-relieved sample has first been deformed to a strain of 1.1 and has its lamella aligned with the rolling plane. It can therefore be considered as a good sample with which to compare the results from the 2-D internal stress sandwich model. Both the experimentally recorded stress-strain curve and a plot of ferrite lattice strain vs. applied stress (Fig. 8.3) show only one deflection point. Comparing this to Fig. 7.12 makes it reasonable to assume that no cementite plasticity occurs up to fracture.

Under the assumption of a perfect sandwich, the cementite phase would thus have to deform elastically to a strain of 8%. The stress in the cementite phase would then be on the order of 17GPa. Such stresses are unreasonably high, even for cementite, and have never been reported in literature. Also the strain hardening of pearlite, predicted by the 2-D sandwich model would be much too high as a result of this. It must therefore be concluded that the iso-strain assumption doesn't hold in real pearlite.

The lack of a second deflection point in the stress-strain curve and lattice strain vs. applied stress plot, can also be explained by a gradual plastification of the cementite over the full strain interval of the tensile test (up to 8%), rather than non-plastifying cementite. In light of the inhomogeneity of the microstructure, such gradual plastification of cementite might indeed be possible, with conditions for plastic flow being fulfilled in some regions, but not in others. However, also in this scenario, the iso-strain assumption cannot hold. If all lamellae were subject to the same strain, the range over which cementite plastification occurs should be fairly limited.

The internal lattice strain in the ferrite phase of the RS-relieved sample continuously decreases past the yield point, until fracture. Results similar to those obtained here on sheet material, were obtained by Tomota et al. [22] on cold drawn pearlitic steel wire. The 2-D internal stress sandwich model developed in section 7.3 yields results which do not agree with this trend, indicating that the basic assumptions of the model, i.e. a sandwich microstructure and iso-strain deformation, are probably not correct. Another explanation would be that the ferrite undergoes strain softening during a tensile test. However, the current author cannot devise any mechanisms to explain such extensive strain softening.

Tomota et al. suggest that the decrease in lattice strain results from a strong stress transfer from the ferrite phase to the cementite phase. Such a stress transfer also takes place in the proposed sandwich model, however, the ferrite lattice strain continues to increase. To obtain a decreasing lattice strain, the cementite phase has to impose an additional compressive strain on the ferrite. Such a mechanisms has been described by Eshelby [122,123] for a hard and less deformable particle imbedded in a deforming matrix. Therefore, such strong stress transfer from one ferrite to cementite might also requires that they deform by a different amount, again illustrates that the microstructure should not be treated as a perfect sandwich and that the iso-strain assumption doesn't hold.

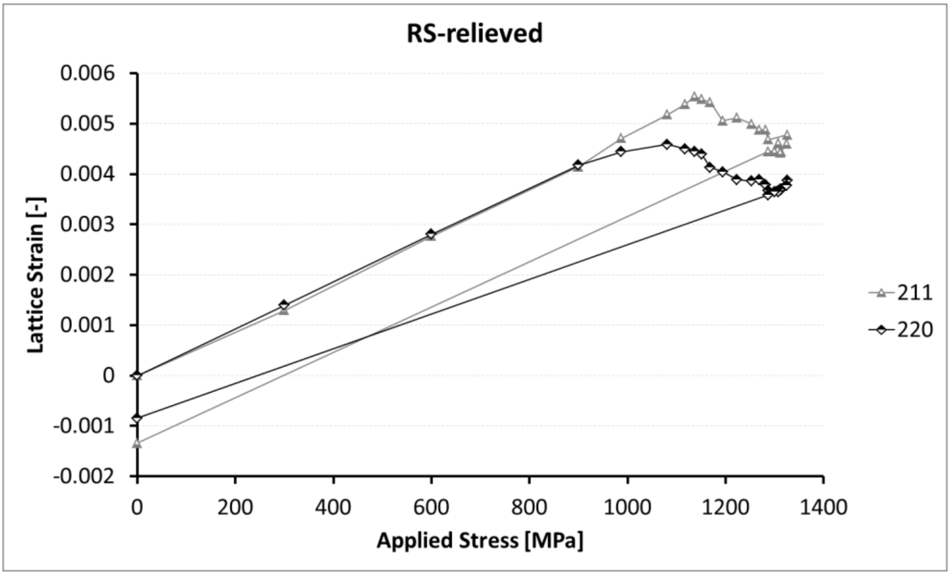

Fig. 8.3: Ferrite lattice strain as a function of applied stress during an in-situ tensile test on the stress relieved sample. Additional plot to illustrate the absence of cementite plasticity.

A last possible explanation for the decreasing internal ferrite lattice strain, incorporating the non-ideal microstructure, has been suggested by Van Houtte [49]. If the cementite lamellae are fragmented, the stress in the cementite builds up as a result of shear stresses acting on the ferrite-cementite interface. This mechanisms is described by the shear lag model [116]. The stress state in the lamellae is then a combination of a normal stress in the loading direction and a shear stress acting parallel to the plane of the lamellae. With increasing macroscopic tensile load, the shear stress in the lamellae will also increase. As a result, the stress state is moving along the yield locus from pure tension to points with a higher shear/normal stress ratio and plastic deformation can continue at a lower normal stress value.

Additional proof that the microstructure should not be considered as a sandwich is presented by the large residual stresses observed in the normal direction of cold rolled sheet, which are in agreement with earlier work by Seefeldt et al. [25]. Even at high rolling strains, where the cementite lamellae are well aligned with the rolling plane, the residual stresses remain. If the material was a perfect sandwich, no such stresses would exist.

Without the requirement for iso-strain, the ferrite lamellae are allowed to deform more than the cementite lamellae. One might then ask where this additional length of ferrite goes to. One possible solution would be to accommodate this additional ferrite elongation in colony boundaries or in the non-lamellar regions which are clearly observed in the real microstructure. Another possibility in a more lamellar region would be to have two subsequent cementite lamellae moving away from one another. The gap between those lamellae would then become larger and have to be filled up by ferrite. In other words, the ferrite bridge between two adjacent ferrite lamellae would be enlarged as is illustrated in Fig. 8.4. These accommodation mechanisms will introduce an additional amount of plastic deformation, either in the vicinity of ferrite bridges, or colony boundaries and non-lamellar regions, which can also contribute to the pearlite strain hardening.

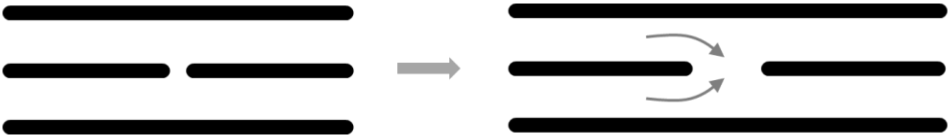

Fig. 8.4: Enlarging ferrite bridge between two ferrite lamellae as a consequence of cementite lamellae moving further apart.

The above discussion establishes that the lamellar microstructure of a real pearlitic steel cannot be considered as a sandwich. The two phases can therefore not be assumed to co-deform according to an iso-strain model. However, at the interfaces between ferrite and cementite compatibility does have to be maintained. The break-down of the iso-strain assumption therefore inevitably leads to the postulation of strain gradients in pearlite. In the following, the possible existence of such strain gradients will be considered in more detail.

8.3.2 Analysis of reversible line broadening

Significant peak broadening due to cold rolling has been observed in both the ferrite and cementite phase. Especially for the cementite phase, the peak broadening is remarkably strong already after the first rolling pass. At higher rolling strains, the peak broadening observed in the normal direction is to some extend reversed for the cementite phase. A similar reduction of the peak width in the normal direction was not observed for ferrite.

During in-situ tensile tests, the ferrite peak width was also seen to increase with the onset of plastic deformation. As the material is unloaded, a significant reduction in peak width is observed. This observation is more pronounced in a material with aligned lamellae. In the following, the possible contributions to peak broadening will be described shortly and it will be attempted to pin point which contributions can explain the experimental observations.

The first contribution to the peak width comes from instrumental broadening. As this contribution is constant and the interest here lies with the changes of the peak width, instrumental broadening will not be considered further.

Inhomogeneous deformation on the scale of the sample leads to macroscopic stress and strain gradients. When applying neutron diffraction, the recorded signal comes from grains throughout the entire sample cross-section. The macroscopic strain profile will therefore also contribute to peak broadening. Significant peak broadening was observed during both the in-situ and ex-situ neutron diffraction experiments. The macroscopic deformation during an in-situ tensile test should quite homogeneous within the gauge length, leading to a minimal macroscopic strain profile. As the broadening is significant for both the in-situ and ex-situ experiment, it is therefore reasonable to assume that the macro strain profile will not be the major contributor to peak broadening in either case.

Another possible contribution to peak broadening is size-broadening, i.e. a reduction of the coherently diffraction domain size. The EBSD scans presented in section 6.1.2 illustrate that size broadening will indeed be important for the cold rolled samples. However, it is unlikely that size broadening will be the major contribution for the smaller deformations reached in a tensile test. Additionally, size-broadening, which would result from the break-up of ferrite into smaller domains of homogeneous crystal orientation, cannot explain the observed reversibility of the peak broadening. The same can be said for any size-broadening that would result from a reduction of the ILS.

That leaves only strain-broadening to explain the reversible peak broadening. Strain-broadening comes from inhomogeneities in the elastic strain distribution on the scale of the grains. In the current context, a grain has to be considered as regions contribution to the same diffraction peak. Such inhomogeneities can result from the presence of dislocations, but can also be caused by elastic strain profiles within grains or by strain differences among similarly oriented grains. The contribution from strain-broadening can at least partially be reversible and will now be discussed further.

Unloading can lead to a decrease in the dislocation content and therefore a reduction of the peak width. Dislocations of opposite sign could annihilate with each other, while dislocations of the same sign can arrange themselves in walls to reduce the elastic strain fields associated with them. In a lamellar microstructure, dislocations are also known to bend out from the interfaces upon deformation and run back into the interfaces with unloading.

The peak width has been shown to be proportional to the square root of the dislocation density, $\sqrt{\rho}$, under a variety of different assumptions [124–128]. The FWHM of the 110 peak for the RS-relieved sample increases from 0.45 before loading to 0.575 before the first unloading cycle. During the unloading cycle a minimum value of 0.525 is reached for the FWHM. About 40% of the peak width gained during forward loading is thus again lost. The same is true for the second unloading cycle. The reduction in dislocation content can now be estimated. The proportionality between the FWHM and the dislocation density can be expressed as

$$\beta \approx C \cdot \sqrt{\rho} \tag{8.1}$$

in which C is a proportionality factor. Writing the dislocation densities before loading, before unloading and at the minimum peak width as ρ0, ρ1, and ρ2, respectively, the recovered dislocation density can be expressed as

$$\frac{\Delta\rho\ lost}{\Delta\rho\ gained} = \frac{\rho_1 - \rho_2}{\rho_1 - \rho_0} = \frac{{\beta_1}^2 - {\beta_2}^2}{{\beta_1}^2 - {\beta_0}^2} \tag{8.2}$$

For the example described above this results in 43% of the dislocation density gained during plastic tensile straining being lost again during the unloading cycle.

Such a strong decrease of the dislocation content seems unreasonable. Changes in dislocation density can therefore not be the only contribution to the strain-broadening observed here. An increase in dislocation density also cannot explain the very strong cementite peak broadening after the first rolling pass. TEM investigations don't provide any evidence for the storage of dislocations in cementite. It appears that the only other explanation that is left is the presence of significant intergranular or interlamellar elastic strain gradients. Upon relaxation of the externally applied load, these strain gradients can also decrease in magnitude, resulting in a decreasing peak width.

In the previous section it has been shown that strain gradients can exist because the iso-strain assumption doesn't hold. The discussion in the current section has led to the conclusion that strain gradients probably need to exist in order to explain the observed reversible peak broadening. In the next section, the possible origins of these strain gradients will be discussed and the experimental observations will be explained qualitatively.

8.3.3 Origins and consequences of strain gradients

The above discussion led to the conclusion that there must be elastic strain gradients in the material. These can have various origins, depending on the length scale considered, as will be discussed in the present section. It will also be shown that the strain gradients in cementite and ferrite are likely to have a different origin.

In general, strain gradients can exist between regions with different local flow stresses. It has already been shown that pearlite is a very inhomogeneous material. The as-patented material will have colonies with lamellae differently oriented with respect to the applied deformation. Each colony will therefore undergo a slightly different deformation and there will be a gradient of strain from one colony to its neighbour.

Similarly, after lamellae alignment, the microstructure contains regions with more or less fragmented lamellae. The local cementite volume fraction can also change from one region to another. This will again lead to local variations in the pearlite flow stress and the introduction of strain gradients.

These strain gradients will have both a plastic and an elastic component. The plastic component of the gradients results in the introduction of additional dislocations. This increase of the dislocation content will not only result in a contribution to the peak width. It may also provide an additional amount of strain hardening and influence the strength of pearlite. The differences in flow stress will also lead to differences in local elastic strain. This is the component of the strain-broadening which is probably more easily reversed. The strain gradients discussed in the above paragraphs are all strain gradients on the scale of the colony size, i.e. the microscopic length scale.

Another kind of strain gradients can exist, within the confines of a single lamella, i.e. the nanoscopic length scale. Because of the break-down of the iso-strain assumption, both phases can deform at a different rate. This will lead to a strain mismatch between the two phases. Assuming interface sliding is difficult due to the large area of the interface between two lamellae, a strain profile across the lamella is required in order to maintain compatibility at the interfaces. Such a profile is illustrated in Fig. 8.5 for pearlite subject to an external load. The gradient is perpendicular to the plane of the lamellae, but is mainly a gradient in the stress or strain component parallel to the plane of the lamellae and the direction of mismatch between the two phases.

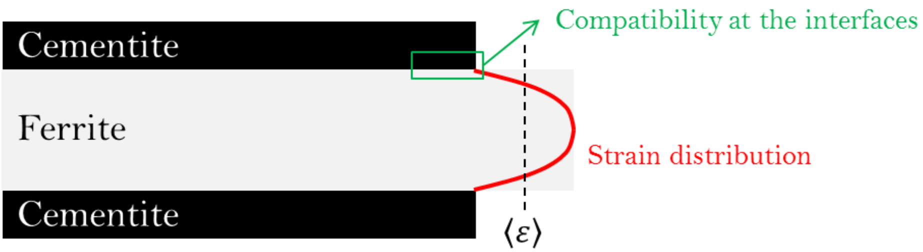

Fig. 8.5: Sketch of the interlamellar strain gradients which might exist in the ferrite phase of a pearlitic steel subject to an external load.

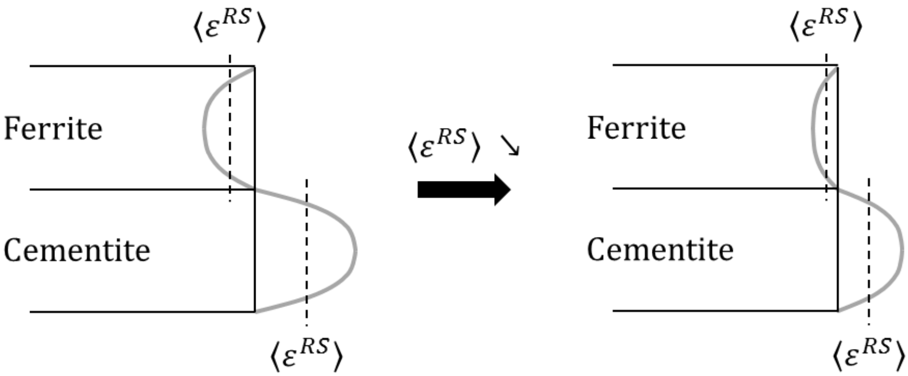

Fig. 8.6: Sketch of the interlamellar strain gradients which might exist in pearlite after removal of the externally applied load. The average residual strain as measured using diffraction techniques is indicated by $\langle\varepsilon^{RS}\rangle$. The reduction of the strain gradients with a smaller $\langle\varepsilon^{RS}\rangle$ is also shown.

A similar illustration of gradients in the residual elastic strain, after removal of the external load is shown in Fig. 8.6. It is also shown that, as the average residual strain in the lamella decreases, so will the extent of the strain gradient. This can explain why the peak width of the cementite diffraction profiles recorded in the normal direction decreases when the residual strain in that direction decreases, with the latter being a result of the rotation of the lamellae towards the rolling plane.

The presence of elastic strain gradients also explains why the peak broadening in the cementite phase is always much stronger than in the ferrite phase. From Fig. 8.6 it follows that the gradient in elastic strain is correlated to the average elastic strain in the lamella as well as to the thickness of the lamella. A small lamella thickness and a large average elastic strain, as are the case for cementite, result in a stronger elastic strain gradient.

If the same type of strain gradients exist in the ferrite phase, a similar decrease of the peak width in the normal direction should have been observed, as a result of the alignment of the lamellae and the accompanying reduction of the residual lattice strain in the normal direction. Additionally, during elastic tensile loading of the material such strain gradients would also develop and an increase of the peak width should be observed. However, neither phenomenon is observed. The strain gradients in pearlite must therefore be of a different kind.

In section 6.2.4 it has been illustrated that a dislocation rich interface-region might develop along the phase boundaries. The resulting gradient in dislocation density causes a gradient in flow stress across the thickness of the ferrite lamellae. Such a gradient in the material properties can then also cause a gradient in the elastic strain across the lamellae.

The above explanation could mean that at small strains, the plastic strain gradients in ferrite have not yet developed sufficiently to result in observable elastic strain gradients. As a consequence, the reduction of the lattice strain in the normal direction would not necessarily lead to a reduction of the diffraction peak width. This can be one of the reasons why the reversibility of the peak broadening is much less pronounced in the as-patented sample.

The decrease of the peak width in the RS-relieved sample can also be more pronounced because of the alignment of the lamellae. The strain profile in lamellae aligned with the loading direction will be larger in this direction, which is also the direction probed by the neutrons. Relaxation of the external load and strain profile will thus cause a stronger decrease of the peak width in these lamellae.

Finally, the explanation based on intra-lamellar variations in flow stress also captures why the peak broadening only starts after plastic deformation commences, even in the samples which were cold rolled before tensile straining. The regions with a higher dislocation density and flow stress will have the same elastic modulus as the centre of the ferrite lamellae. Therefore, during elastic loading, no strain gradient develops.

Elastic bending of the cementite lamellae forms another possible source of elastic strain gradients. The bending of the lamellae can be seen from the micrographs in section 6.1.1.3. In cold drawn wire a similar contribution can result from the curling of the lamellae around the drawing axis. For a couple of case studies, the stress resulting from elastic bending has been estimated based on the theory for elastic bending of a beam, as illustrated in Fig. 8.7.

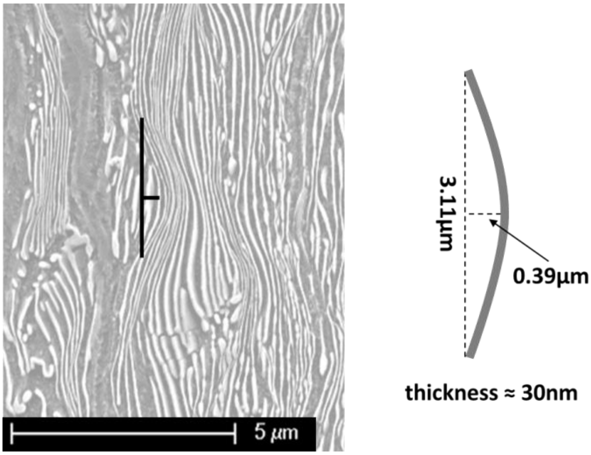

Fig. 8.7: Estimation of the stress due to elastic bending of the cementite lamellae, based on the theory for elastic bending of beams.

The maximum stress, i.e. at the outsides of the beam can be written as

$$\sigma = \frac{F \cdot l \cdot t}{4 \cdot I} \tag{8.3}$$

With F, l and t, respectively, the bending force, the length and the thickness of the beam. The bending force can be estimated as

$$F = \frac{f_{max} \cdot 48 \cdot E \cdot I}{l^3} \tag{8.4}$$

In which E is the Young's Modulus and f_{max} the maximum deflection of the beam. This finally yields the following expression for σ

$$\sigma = \frac{f_{max} \cdot 12 \cdot E \cdot t}{l^2} \tag{8.5}$$

Using the dimensions from Fig. 8.7 and a Young's Modulus of 210GPa gives a stress of about 3GPa. Other case studies all resulted in values in the range 3-4.5GPa. This stress has to be added to the 1-2GPa residual stress already present in the lamellae, reaching the range of 4-6GPa in which plasticity of the cementite phase could occur. It therefore is unreasonable to attribute all of the observed bending of the cementite lamellae to elastic bending. However, the obtained stress values do suggest that elastic bending may occur and could therefore contribute to the cementite peak broadening.

The discussion in this section illustrates that the peak broadening can at least partially be explained by the presence of strain gradients on the microscopic and nanoscopic length scales. Strain gradients will also exist on a macroscopic length scale, certainly for the cold rolled samples, but it has been discussed in section 8.3.2 that these are unlikely to be the major contribution to peak broadening. A detailed, quantitative analysis of the observed peak broadening based on the initial theories proposed by Williamson and Hall [129] or Warren and Averbach [113,130] would give more insight into the origins of this peak broadening. However, because of the many contributions to the peak broadening and the mathematical complexity of the theories, such an analysis would be quite time-consuming. It was not possible to perform the analysis within the current project and a quantitative analysis of the peak broadening is referred to future work.

8.4 Additional insights into the plastic deformation of pearlite

8.4.1 Onset of cementite plasticity

Strong indications for the plasticity of cementite have been provided through the microscopy study reported in section 6.1.1. The presented micrographs only clearly show cementite plasticity starting from a cold rolling strain of 0.92 on. However, the discussion in section 8.1.2 illustrated that cementite plasticity likely starts in the very first rolling passes. Such plasticity is then likely limited to the movement of dislocations across cementite lamellae, without any shape change observable with SEM.

On the other hand, the investigation of specimens subject to a tensile test provided evidence for widespread brittle fracture of the cementite lamellae. Likewise, the recorded stress-strain curves and ferrite lattice strains do not contain any evidence for cementite plasticity. This suggest that cementite deforms differently under rolling and drawing deformation as compared to tensile deformation.

Rolling or drawing can be accompanied by a significant hydrostatic compression, which can facilitate the plastic deformation of the hard cementite phase. During a tensile test, this hydrostatic component is absent. Plastic deformation of the cementite will then be more difficult, favouring brittle fracture.

8.4.2 Development of an interface-phase

As plastic deformation proceeds, dislocations are generated in the ferrite phase. These dislocations can move from one side of the lamella to the other or they can move as a hairpin along the length of the ferrite channel. In either case, dislocations will be deposited at or near the ferrite-cementite interface. As a result, the dislocation density will be higher at the interfaces as compared to the bulk of the ferrite. This statement is supported by microscopy evidence from literature [46,64,65,68].

Continuing this process of dislocation storage at the interfaces will first result in the introduction of a dislocation density gradient across the thickness of the ferrite lamellae. At high strains, the dislocation density at the interfaces may become so different from that in the bulk of the lamellae, that the ferrite at the interface will become significantly stronger. The transition from bulk-ferrite to interface-ferrite will be a gradual one.

The observation of the development of peak asymmetry has been shown to support this idea of interface-ferrite (section 6.2.4). In the preceding sections it has also been illustrated that the emergence of this interface-region can help to explain the observations related to reversible peak broadening.

The fact that the FWHM doesn't change too much with increasing rolling strain can also be linked to the above mechanism. If most dislocations are stored at the interfaces, the dislocation density in the 'bulk' of the ferrite lamellae might saturate after an initial increase at small strains. The dislocations stored in the interfaces will broaden the tails of the peaks and eventually cause asymmetry, but may not affect the FWHM, if the volume fraction of bulk-ferrite remains high enough.

The residual elastic strains estimated for the interface-ferrite evolve towards less compressive as compare to bulk-ferrite. At the largest rolling strains, the residual elastic strain even becomes tensile. This suggests that the interface-ferrite becomes so strong that, from the point of view of the residual elastic strains, it starts to behave as cementite. As such, a possible explanation for the continued pearlite strain hardening after cementite dissolution would be that the cementite phase is replaced by a dislocation rich ferrite region which can then still act as a barrier to long range dislocation movement.

The presence of the dislocation rich interface-region may also aid cementite dissolution by increasing the carbon diffusion rate or by increasing dislocation interaction with the cementite. The super saturation of carbon atoms in the vicinity of the cementite interface can then in turn contribute to the high strength of the interface-phase by pinning dislocations in place.

As has already been discussed previously, the presence of interface-ferrite can also influence the observed residual elastic strain evolution. The micro-phase residual strain in stage 3 increases slightly faster as compared to stage 2 for some directions, mainly 110. As the harder interface-ferrite develops, the volume fraction of 'bulk' ferrite decreases. As a result, to maintain the stress-balance, it has to carry a load of larger magnitude. In order for this load to continue to increase, the bulk ferrite has to continue to strain harden as well.

This strain hardening can be accounted for by the decreasing path length for dislocation movement, not only by a decreased ILS, but also but the growing interface-region. Additionally, as the residual elastic strain in the interface-ferrite evolves towards tension, it will take over part of the load of cementite. This could explain why a slight decrease in cementite RS is observed on cold drawn wire.

8.4.3 Cementite strain hardening

In section 8.1 it has been shown that some amount of cementite strain hardening must be allowed in order to explain the observed residual strain evolution. However, it has also been pointed out in section 3.2.2 that there is very little evidence for dislocation storage in cementite. This is attributed to the extreme thinness of the cementite lamellae. As a consequence dislocations are neither generated, nor stored in the cementite lamellae. They are rather generated at one interface and travel completely through the lamella to exit on the other side. It is thus the interaction with the ferrite phase that controls the cementite plasticity. Embedded cementite can therefore likely yield at stress values below its bulk strength.

The lack of storage of dislocations in cementite makes it necessary to develop a non-classical view on its strain hardening behaviour. Assume that any dislocations moving in the cementite are indeed (1) either generated at the interface as a result of stress concentrations or (2) originate from the ferrite and are transferred to the cementite. In the latter case, a residual dislocation segment is likely left in the interface to account for the difference in Burgers vector between the ferrite and cementite dislocations [131]. Such processes will therefore also change the interface structure. If the interface structure evolves from a semi-coherent interface towards a more incoherent interface [48], dislocation transfer and perhaps also nucleation will become more difficult. From this point of view, the increase in the cementite flow stress is controlled by the increased stress to introduce dislocations in cementite.

The type of dislocations that can be nucleated at the interface depends on the interface structure [132], and the same is likely true for the rate at which they can be nucleated. Because the interface structure may be changed as a direct result of dislocation being nucleated at the interface itself [133], strain hardening of the cementite may also result from the depletion of easy nucleation sources with ongoing deformation.

The development of the interface-ferrite can also result in apparent cementite strain hardening. As this region develops, a higher stress might be required to bring more dislocations from the 'bulk' ferrite to the interface. The harder interface-ferrite, which has a strength intermediate between the bulk-ferrite and cementite, will also reduce the misfit between ferrite and cementite. The stress concentrations at the interface will be spread out and reduced, making dislocation nucleation at cementite-ferrite interface more difficult.

From the above it follows that cementite strain hardening does not necessarily involve processes that could increase the strength of bulk cementite. It can involve any mechanism that results in an increased load bearing capacity of cementite. From that point of view, also alignment of the cementite lamellae with the loading direction can result in a strain hardening contribution as is required in terms of the proposed sandwich model.

Cementite strain hardening is thus not likely to be related to dislocation entanglement or pile-ups. Neither are any of the above proposed mechanisms related to the lamellae thickness. Any dislocation introduced into a cementite lamella will likely almost instantly traverse that lamella. It is therefore improbable that the cementite phase will exhibit the same exponential strain hardening as is generally accepted for the ferrite phase.

Because cementite does not really harden in the classical sense, i.e. the cementite itself does not really become ‘stronger’, but its load bearing capacity does increase, it might be more appropriate to talk about ‘apparent strain hardening’ of the cementite phase.

8.5 Applicability and use of the sandwich models

First of all it should be stressed that the developed sandwich models were never meant to quantitatively predict the measured lattice strains and calculated stresses. They were conceived as a result thinking about the reasons behind why and how residual stresses and strains develop. Consequently, they are merely a tool used in the analysis of the experimental results.

Nevertheless, it is interesting to recapitulate the most important assumptions that have been made. Firstly, there is the assumption of a perfect sandwich microstructure, leading to the iso-strain condition. It has already been pointed out in section 8.3.1 that this is an oversimplification of reality, where the lamellae were seen to be broken up in smaller fragments.

Strictly speaking, the model should also only be used at sufficiently large strains (>1) to justify a strong lamellae alignment. At small strains, and especially in the undeformed material where the lamellae alignment is uniformly distributed, only a small fraction of the colonies will have their lamellae aligned parallel to the rolling plane. The assumed strong alignment of the lamellae will lead to an over prediction of the residual strain value as compared to the initially randomly oriented colonies. This also means that no interlamellar shear of any kind, which may for example occur during rotation of the lamellae, is taken into account. Although it is difficult to estimate exactly how much of the material may be described as a sandwich, at strains larger than 1, at least more than half of the material should approximate a sandwich microstructure.

Secondly, the unloading of both phases has also been assumed to be linear. The in-situ neutron diffraction experiments which were performed illustrated that this also doesn't fit with reality. The origin of such non-linearity has not yet been elucidated, but it is clear that this would likely also lead to a somewhat different value of the residual stress.

Finally, the stress and strain state in the material have also been greatly simplified. This was done in order to maintain the intuitive nature of the models. A comparison with other, more complex models would be required in order to assess the true impact of this simplification.

Because the real in-situ strain hardening behaviour of the ferrite and cementite phase is not known, a couple of empirically chosen strain hardening behaviour were employed to generate results. Based on the discussion in this chapter it seems reasonable to assume exponential strain hardening for ferrite, but not for cementite. If the in-situ ferrite yield strength can be assumed to be of the same order of magnitude as pearlite yield strength, and allowing a sufficient amount of cementite strain hardening, curves similar to the green, dotted curve in Fig. 7.8 are obtained. These at least qualitatively capture the various stages in the residual stress and strain evolution observed experimentally.

For the cementite phase Voce strain hardening has been used. However, it is likely that at larger strains the saturating flow stress of the Voce law doesn't capture the in-situ cementite flow stress. On the other hand, it is at this point impossible to predict what kind of strain hardening behaviour would be better. Not only is the cementite strain hardening rather non-classical, as discussed in section 8.4.3, also processes such as cementite dissolution and brittle or ductile fragmentation of the cementite will influence its in-situ strain hardening behaviour. It is evident that, should a more realistic strain hardening law for cementite be available, the exact shape of the curves in Fig. 7.8 and others in Chapter 7 would be quite different. Still, it is the current authors strong conviction that sufficient cases have been investigated to justify the qualitative conclusions that have been drawn regarding the explanations behind the residual stress evolution in heavily deformed pearlite.

Although the list of limitations is long, the tool here developed was vital in coming to the conclusions that the cementite phase needs to strain harden to some extend and that the iso-strain assumption does not describe the real deformation behaviour of pearlite. Its simplicity can be considered to be both the greatest strength and greatest weakness of the sandwich model. As long as the model is used keeping this in mind, the current author believes the sandwich model can be a very powerful tool in thinking about the reasons behind experimental results.

9 Conclusions

The goal of the present research was to come to a better understanding of the residual stress development in multiphase, metallic alloys. In order to focus the research, one material was chosen as a case study. The main factors influencing this decision were the requirement for a relatively simple microstructure, the ability to buy and process the material, the knowledge already available in the department and the engineering importance of the material. Finally, the decision was made to study pearlitic steel.

Pearlite is a steel of eutectoid composition which has a lamellar microstructure if processed appropriately. With cold rolling or cold drawing these lamellae align themselves with the rolling plane or drawing direction, respectively. In the current study, samples subject to both rolling and drawing were investigated using various diffraction techniques in order to obtain the residual lattice strains and stresses that develop with increasing strain.

Although there are some differences between sheet and wire, in general three stages in the residual lattice strain development can be recognized.

- Stage 1: The residual lattice strain increases rapidly at small strains as the cementite phase starts to deform plastically. In this stage the magnitude of the residual lattice strain is likely controlled by the ferrite flow stress.
- Stage 2: The residual lattice strain maintains a nearly constant value and the intergranular strain development is very limited. In this stage the magnitude of the residual lattice strain is likely controlled by the difference in flow stress between ferrite and cementite. This led to the conclusion that cementite has to strain harden to some extent.
- Stage 3: Intergranular strain development becomes more pronounced. This is related to the completion of lamellar alignment and the evolution from small regions of homogeneous ferrite crystal orientation back to larger regions.

It can thus be seen that the residual micro-phase strain development is mainly controlled by the changing microstructure and the in-situ strain hardening behaviour of both phases.

A number of remarkable differences between cold rolled and cold drawn pearlite have also been observed. The increase of the residual lattice strain/stress is much steeper in stage 1 for the cold rolled sheet. The three stages start at a higher effective macroscopic strain for the cold drawn wire.

And, finally, for the cold rolled sheet, the order of the intergranular strains at high strains is reversed as compared to low strains. Such reversal has not been observed for wire. The origin of these differences has to be related to the differences in microstructure – curling in wire, more shear bands in sheet, different patenting treatment – and crystallographic texture, or be a consequence of the different deformation mode. While it has been attempted to explain the first two differences, no viable explanation was found for the intergranular strain reversal.

In-situ tensile tests were also performed on a number of samples. It could be seen that samples with a lamellar microstructure exhibit a more efficient load transfer from the ferrite to the cementite phase. Alignment of the lamellae with the loading direction further increases this load transfer, resulting in a continuous decrease of the ferrite lattice strain after the macroscopic yield point. It follows that alignment of the lamellae constitutes a significant contribution to the large strain work hardening of lamellar materials, by increasing the kinematic work hardening contribution.

Investigation of the diffraction peak widths was also performed for both the ex-situ and in-situ experiments. A strong increase of the peak width with cold rolling was observed, especially at small rolling strains. The peak broadening was much more pronounced in the cementite phase. As a result, after a rolling strain as small as 3% a large part of the cementite peaks could already no longer be observed. Part of this broadening was seen to be reversible. A similar observation was made for the ferrite phase, where the peak width during an in-situ tensile test decreased as a result of unloading.

In order to facilitate the analysis of the experimental results, an intuitive sandwich model was developed, starting from the assumption that the material can be idealized as a stack of alternating, flat ferrite and cementite plates. Using this tool, in combination with the microstructural observations that were made, the experimental results were investigated, leading to the following important conclusions regarding the deformation of pearlite:

- The co-deformation of the ferrite and cementite lamellae is not properly described by the iso-strain assumption. The idea of an idealized sandwich microstructure is a strong over simplification of reality which makes it impossible to capture the true deformation behaviour of pearlite.
- The hard cementite phase must undergo some amount of strain hardening. This is no strain hardening in the classical sense of the word, but is controlled by the transfer of dislocation across the interface and nucleation of cementite dislocations at the interface.

- Significant strain gradients of both an elastic and plastic nature exist within the material and on length scales varying from the sample size, over the colony size to the interlamellar spacing.

The development of a strong asymmetry of the ferrite peak profiles led to the postulation that a dislocation rich phase exists at the interface between ferrite and cementite. The strength and flow stress of this interface-ferrite may be significantly higher than that of bulk-ferrite. There will probably be a gradual transition in dislocation density from the bulk towards the interface. The existence of the interface-ferrite helped to explain both the residual lattice strain evolution and the introduction of strain gradients in the material.

Some inconsistencies arose in trying to calculate cementite residual stress from strains, based on cementite elastic constants found in literature. The latter are obtained from ab-initio calculations and should be applicable to bulk cementite. It has also been illustrated that the early onset of cementite plasticity and its strain hardening cannot be explained without accounting for the presence of the embedding ferrite phase. Consequently, the conclusion was drawn that the properties of in-situ cementite differ significantly from those of bulk cementite. The true, in-situ elastic and plastic behaviour of cementite might to a large extent be controlled by the surrounding ferrite phase.

By studying the residual and internal stress and strain evolution, some insight was gained in how the deformation of pearlite might proceed. At this point it is interesting to shortly summarise the view of the current author on the deformation of pearlite during cold rolling or drawing.

The cementite phase starts to deform plastically from the first rolling/drawing passes on. The plastification of cementite can occur over an extended strain range, due to the inhomogeneity of the microstructure. Plastic deformation is likely initiated by transfer of dislocations across the ferrite-cementite interface or the nucleation of cementite dislocations in the interface. It is therefore a direct result of the interaction between cementite and plastic deformation taking place in ferrite.

As deformation proceeds, the dislocation density in ferrite increases and the interlamellar spacing decreases. This results in an exponential strain hardening of the in-situ ferrite, which is reflected in the strain hardening of the composite as a whole. The generated dislocations are preferentially stored at the ferrite-cementite interface. This changes the interface structure, which may make the generation of cementite dislocations more difficult. As a result, the cementite also exhibit some kind of strain hardening.

Eventually, the dislocation density at the interfaces and the bulk of the ferrite is so different that a dislocation rich interface-region develops. This interface-ferrite has a strength in between that of cementite and bulk-ferrite. Any stress-concentrations which exist at the ferrite-cementite interface will thus be spread out. Dislocation nucleation at the cementite interfaces will then be impeded further, again contributing to cementite strain hardening.

Throughout these first stages of deformation, the strength of pearlite will be controlled by the barrier properties of cementite, which in turn gives ferrite its high in-situ strength. It has also been discussed that the inhomogeneity of the microstructure and the lamellar nature of the microstructure will introduce strain gradients in the material. The plastic component of these strain gradients will require the storage of additional dislocations which may further contribute to the high in-situ strength of ferrite.

At still higher deformation, cementite dissolution will commence and could eventually result in a loss of the cementite barriers. Nevertheless, pearlite continues to strain harden. This might be explained by the presence of the interface-ferrite. It is possible that the interface-ferrite facilitates cementite decomposition, but at the same time the carbon atoms that go into super saturation can further strengthen the interface-ferrite. The interface-ferrite can then gradually replace cementite as the barrier-phase. This may again be aided by the inhomogeneity of the microstructure which provides the required dislocations by the introduction of strong plastic strain gradients.

Some of the conclusions drawn regarding the residual stress development can be generalized to other multiphase materials. Firstly, it is important to realize that the evolution of the residual stresses is directly influenced by the combination of the strain hardening behaviours of the various phases. Secondly, reverse yielding of the soft phase is not a sufficient condition to obtain a saturation of the residual stress. This is only true if at the same time the strengthening of the soft phase is limited so as not to increase the reverse flow stress. Another possibility to obtain residual stress saturation, without reverse yielding of the soft phase, is to have such strain hardening behaviour in the phases that the difference in flow stress remains constant or slightly decreases. Finally, it should be remarked that, when studying lamellar materials, care should be taken in applying the iso-strain assumption.

A number of questions certainly still remain. The exact reasons behind the non-linearity of the tensile unloading curve and the associated decrease in peak width are not yet clear. The peak width was also seen to decrease past the point of zero applied stress, before increasing again. A reversal of the order of the intergranular strains was observed for cold rolled sheet, for which the underlying mechanisms have yet to be elucidated. The existence of strain gradients in the material has been postulated, but stronger evidence, based on a quantitative analysis of the diffraction peak broadening is still required. The requirement for cementite strain hardening has been deduced from the proposed sandwich model. While the current author strongly believes that this conclusion is merited, it is necessary to double check the viability of the sandwich model by the application of more sophisticated models that take into account the full 3D stress and strain state in the material. Finally, a couple of possible contribution to cementite strain hardening have been proposed. It is however clear that, to fully understand the deformation behaviour of pearlite, a lot of additional effort should be spend on understanding the *in-situ* cementite deformation behaviour from both an elastic and plastic point of view.

In final conclusion to the performed work, it can be said that the analysis of the residual stresses in a material can be used as a strong tool to learn more about the materials deformation behaviour. Here, this idea has been applied to pearlite, leading to new insights into its deformation behaviour.

10 Opportunities for future research

Although the current work has led to a number of interesting insights into the development of residual stresses and the deformation behaviour of pearlite, a lot of opportunities remains for future research. The main focus of these opportunities is in investigating pearlite further to learn more about this technologically interesting material, which will hopefully lead to even better material properties.

Strain gradients

A detailed analysis of the diffraction peak broadening in pearlite is required. The two most prominent contributions will be size and strain broadening. These need to be separated based on the available theories [113,129,130]. Once the strain broadening component has been obtained, it should be attempted to estimate the extent of the strain gradients in the material. It is obvious that this will not be a straight forward exercise, because of the complex microstructure and multiple contributions to strain broadening. In the ideal case, a subdivision should be made between the strain broadening contribution due to dislocations and the contribution due to spatial differences in elastic strain. Assumptions will inevitably have to be made regarding the origins of the strain broadening. This might be the crucial step in developing a quantitative theory on strain broadening in pearlite.

Alternatively, Transmission Kikuchi Diffraction (TKD) may be employed in an effort to get direct experimental evidence for the existence of interlamellar strain gradients. TKD is similar to EBSD, but is performed in transmission on a TEM foil, resulting in a spatial resolution on the order of 2-5 nm [134,135]. The technique itself is relatively straight forward and the measurements can be performed with a standard EBSD set-up. It is sample preparation which is the main difficulty, as has been experienced by the current author. By application of TKD to thin foils of deformed pearlite, it might be possible to observe small crystal rotations across the thickness of a single lamellae. This would likely required methods based on pattern diffusivity [136] or image cross-correlation [137–139] in order to visualise even very small misorientations. From these misorientations, plastic strain and dislocation densities might be calculated [140,141].

Modelling

The intuitive sandwich model which has been presented in this work has proven to be very useful to analyse experimental results and link those to the possible in-situ deformation behaviour of both phases. The proposed work-based solution could be used to add more phases to the material. As such, the influence of the emergence of a third interface-phase could be investigated. Alternatively, multiple phases could be defined representing different ferrite grain families.

In order to take into account the non-ideal microstructure of pearlite, a first step could be to apply the shear lag model [49,116] to the case of pearlite. This would allow to incorporate the transfer of stress between both phases along the interface and the gradual build-up of stress from the end of the cementite lamellae fragments to their middle. This inevitably means that multiple stress and strain components need to be taken into account, which could help explain the observed decrease of the ferrite lattice strain during an in-situ tensile test, as was hinted at in section 8.3.1. Additionally, the variation of lattice strain along the length of a cementite lamellae could give a contribution to the large peak broadening which was observed and might be estimated from the shear lag model.

It could also be checked whether the results from the sandwich model qualitatively agree with more sophisticated models in which the 3D stress and strain state is taken into account. With respect to modelling it should finally be remarked that in future attempts to model the large strain deformation of pearlite, cementite should not be considered as a purely elastic nor ideal plastic phase. An effort should rather be made to introduce some kind of strain hardening behaviour for cementite and investigate whether the results may fit with experimental observations.

In-situ phase properties

It has been shown that the properties of cementite deforming within pearlite, i.e. embedded in ferrite, may be quite different from those of bulk cementite. This is true for both the elastic an plastic behaviour of cementite. The effect of the embedding ferrite matrix should therefore be investigated. With respect to the plastic properties, this will likely also require taking into account the possibly changing interface structure. If it is possible to obtain the ferrite and cementite crystal orientations simultaneously by the application of TKD, a lot of information might be obtained regarding the interface.

It should also be attempted to get more information regarding the in-situ properties of ferrite. This might be done by doing tensile tests on samples deformed to various strains. If the composite yield is controlled by yielding of the softer phase, the flow stress of the soft phase can be estimated by subtracting the measured residual stress from the pearlite flow stress.

11 Bibliography

[1] Annual Crude Steel Production Archive, accessed 20 Apr. 2015. URL: http://www.worldsteel.org/statistics/statistics-archive/annual-steel-archive.html.

[2] Kriška M. X-Ray and Neutron Diffraction Stress Analysis in High Strength Steel Wire. KU Leuven, 2014.

[3] Dieter GE. Mechanical Metallurgy, SI metric . London: McGraw-Hill; 1988.

[4] He S, Van Bael A, Li SY, Van Houtte P, Mei F, Sarban A. Mater Sci Eng A 2003;346:101.

[5] Martinez-Perez ML, Mompean FJ, Ruiz-Hervias J, Borlado CR, Atienza JM, Garcia-Hernandez M, Elices M, Gil Sevillano J, Peng RL, Buslaps T. Acta Mater 2004;52:5303.

[6] Atienza JM, Ruiz-Hervias J, Martinez-Perez ML, Mompean FJ, Garcia-Hernandez M, Elices M. Scr Mater 2005;52:1223.

[7] Gibmeier J, Kornmeier J, Hofmann M. Citeseer 2009:279.

[8] Winholtz RA, Cohen JB. Metall Trans A 1992;23:341.

[9] Hanabusa T, Fukura J, Fujiwara H. Bull JSME 1969;12:931.

[10] Sinclair CW, Embury JD, Weatherly GC, Conlon KT. Philos Mag 2005;85:3137.

[11] Sinclair CW, Saada G, Embury JD. Philos Mag 2006;86:4081.

[12] Dakhlaoui R, Baczmański a., Braham C, Wroński S, Wierzbanowski K, Oliver EC. Acta Mater 2006;54:5027.

[13] Daymond MR, Hartig C, Mecking H. Acta Mater 2005;53:2805.

[14] Thilly L, Renault PO, Vidal V, Lecouturier F, Van Petegem S, Stuhr U, Van Swygenhoven H. Appl Phys Lett 2006;88:4.

[15] Vidal V, Thilly L, Van Petegem S, Stuhr U, Lecouturier F, Renault P-O, Van Swygenhoven H. Scr Mater 2009;60:171.

[16] Thilly L, Van Petegem S, Renault P-O, Lecouturier F, Vidal V, Schmitt B, Van Swygenhoven H. Acta Mater 2009;57:3157.

[17] Oliver EC, Daymond MR, Withers PJ. Acta Mater 2004;52:1937.

[18] Wilson DV, Konnan YA. Acta Metall 1964;12:617.

[19] Bonner NW, Molden GF, Webster PJ, Root JH, Thomas MH. Load-Sharing and Interphase Residual Microstresses in a High Carbon Pearlitic Steel, in:. Proc. Fifth Int. Conf. Residual Stress. - ICRS5. 1997.

[20] Young ML, Almer JD, Daymond MR, Haeffner DR, Dunand DC. Acta Mater 2007;55:1999.

[21] Daymond MR, Priesmeyer HG. Acta Mater 2002;50:1613.

[22] Tomota Y, Lukáš P, Neov D, Harjo S, Abe YR. Acta Mater 2003;51:805.

[23] Morooka S, Tomota Y, Suzuki T, Kamiyama T. Adv Mater Res 2007;15-17:912.

[24] Kanie A, Tomota Y, Torii S, Kamiyama T. ISIJ Int 2004;44:1952.

[25] Seefeldt M, Walentek A, Van Houtte P, Vrána M, Lukáš P. Mater Sci Forum 2006;525:375.

[26] Van Acker K, Root J, Van Houtte P, Aernoudt E. Acta Metall 1996;44:4039.

[27] Yahyaoui H, Sidhom H, Braham C, Baczmanski A. Mater Des 2014;55:888.

[28] Shinozaki T, Morooka S. Proc 3rd Int Conf Adv Struct Steels 2006.

[29] Hosford WF. Trans Met Soc AIME 1964;230:12.

[30] Gil Sevillano J, González D, Martinez-Esnaola JM. Mater Sci Forum 2007;550:75.
[31] Gil Sevillano J, Alkorta J, González D, Van Petegem S, Stuhr U, Van Swygenhoven H. Adv Eng Mater 2008;10:951.
[32] Weisser MA, Evans AD, Van Petegem S, Holdsworth SR, Van Swygenhoven H. Acta Mater 2011;59:4448.
[33] Jiang C, Srinivasan SG, Caro A, Maloy S a. J Appl Phys 2008;103.
[34] Nikolussi M, Shang SL, Gressmann T, Leineweber A, Mittemeijer EJ, Wang Y, Liu Z-K. Scr Mater 2008;59:814.
[35] Henriksson K, Nordlund K. Phys Rev B 2009;79:144107.
[36] Winholtz RA, Cohen JB. Mater Sci Eng A 1992;154:155.
[37] Suzuki T, Tomota Y, Isaka M, Moriai A, Minakawa N, Morii T. ISIJ Int 2004;44:1426.
[38] Li YJ, Choi P, Goto S, Borchers C, Raabe D, Kirchheim R. Acta Mater 2012;60:4005.
[39] Howell PR. Mater Charact 1998;40:227.
[40] Bhadeshia HKDH, Honeycombe RWK. Steels: Microstructure and Properties, third. Elsevier Ltd.; 2006.
[41] Juul Jensens D, Hansen N, Humphreys FJ. Effect of Metallurgical Parameters on the Textural Development in Fcc Metals and Alloys, in:. Eight Int. Conf. Textures Mater. 1988.
[42] Kong XW, Engler O, Lücke K. Textures Microstruct 1991;14-18:1215.
[43] Dunst D, Dendievel R, Mecking H. Mater Sci Forum 1994;157-162:665.
[44] Humphreys FJ. Textures in Two-Phase Metals, in:. Elev. Int. Conf. Textures Mater. 1996.
[45] Read HG, Reynolds WTJ, Hono K, Tarui T. Scr Mater 1997;37:1221.
[46] Goto S, Kirchheim R, Al-Kassab T, Borchers C. Trans Nonferrous Met Soc China 2007;17:1129.
[47] Languillaume J, Kapelski G, Baudelet B. Acta Mater 1997;45:1201.
[48] Fang F, Zhao Y, Liu P, Zhou L, Hu X, Zhou X, Xie Z. Mater Sci Eng A 2014;608:11.
[49] Van Houtte P. Personal Communication. 2015.
[50] Zelin M. Acta Mater 2002;50:4431.
[51] Zhang X, Godfrey A, Hansen N, Huang X, Liu W, Liu Q. Mater Charact 2010;61:65.
[52] Embury JD, Fisher RM. Acta Metall 1966;14:147.
[53] Langford G. Metall Trans A 1977;8:861.
[54] Wang Y-T, Adachi Y, Nakajima K, Sugimoto Y. Acta Mater 2010;58:4849.
[55] Danoix F, Julien D, Sauvage X, Copreaux J. Mater Sci Eng A 1998;250:8.
[56] Sauvage X, Copreaux J, Danoix F, Blavette D. Philos Mag A 2000;80:781.
[57] Takahashi J, Tarui T, Kawakami K. Ultramicroscopy 2009;109:193.
[58] Li YJ, Choi P, Borchers C, Westerkamp S, Goto S, Raabe D, Kirchheim R. Acta Mater 2011;59:3965.
[59] Gridnev VN, Gavriljuk VG. Phys Met 1982;4:531.
[60] Gavriljuk VG. Mater Sci Eng A 2003;345:81.
[61] Bolling GF, Richman RH. Metall Trans 1970;1:2095.
[62] Mellor BG, Edmonds DV. Metall Trans A1 1977;8A:763.
[63] Pearson DD, Verhoeven JD. Metall Mater Trans A 1984;15:1037.

[64] Zhang X, Godfrey A, Hansen N, Huang X. Acta Mater 2013;61:4898.
[65] Zhang X, Godfrey A, Huang X, Hansen N, Liu Q. Acta Mater 2011;59:3422.
[66] Tagashira S, Sakai K, Furuhara T, Maki T. ISIJ Int 2000;40:1149.
[67] Gil Sevillano J. J Phys III 1991;1:967.
[68] Dollar M, Bernstein IM, Thompson AW. Acta Metall 1988;36:311.
[69] Zhang XD, Godfrey A, Liu W, Liu Q. Mater Sci Technol 2011;27:562.
[70] Porter DA, Easterling KE, Smith GDW. Acta Metall 1978;26:1405.
[71] Fasiska EJ, Jeffrey GA. Acta Crystallogr 1965;19:463.
[72] Fruchart D, Chaudouet P, Fruchart R, Rouault A, Senateur JP. J Solid State Chem 1984;51:246.
[73] Umemoto M, Liu ZG, Takaoka H, Sawakami M, Tsuchiya K, Masuyama K. Metall Mater Trans A 2001;32:2127.
[74] Umemoto M, Todaka Y, Tsuchiya K. Mater Sci Forum 2003;426-432:859.
[75] Terashima T, Tomota Y, Isaka M, Suzuki T, Umemoto M, Todaka Y. Scr Mater 2006;54:1925.
[76] Webb WW, Forgeng WD. Acta Metall 1958;6:462.
[77] Inoue A, Ogura T, Masumoto T. Metall Trans A 1977;8:1689.
[78] Inoue A, Ogura T, Masumoto T. Scr Metall 1977;11:1.
[79] Keh AS. Acta Metall 1963;11:1101.
[80] Maurer K, Warrington DH. Philos Mag 1967;15:321.
[81] Gil Sevillano J. Mater Sci Eng 1975;21:221.
[82] Gil Sevillano J. Wire J Int 2011.
[83] Kuhlmann-Wilsdorf D. Metall Trans 1970;1:3173.
[84] Embury JD, Hirth JP. Acta Metall Mater 1994;42:2051.
[85] Gil Sevillano J. On the Yield and Flow Stress of Lamellar Pearlite, in:. Strength Met. Alloy. Aachen, Germany: 1979.
[86] Janecek M, Louchet F, Doisneau-Cottignies B, Bréchet Y. Philos Mag A 2000;80:1605.
[87] Zhang RF, Wang J, Beyerlein IJ, Misra A, Germann TC. Acta Mater 2012;60:2855.
[88] Elwazri AM, Wanjara P, Yue S. Mater Sci Eng A 2005;404:91.
[89] Hauk VM, Oudelhoven RWM, Vaessen GJH. Metall Trans A 1982;13:1239.
[90] Ridley N. Metall Mater Trans A 1984;15:1019.
[91] Noyan IC, Cohen JB. Residual Stress: Measurement by Diffraction and Interpretation. New York: 1987.
[92] Van Houtte P, De Buyser L. Acta Metall 1993;41:323.
[93] Daymond MR. J Appl Phys 2004;96:4263.
[94] Kriška M, Tacq J, Acker K Van, Seefeldt M, Petegem S Van. J Phys Conf Ser 2012;340:012101.
[95] Genzel C, Denks IA, Gibmeier J, Klaus M, Wagener G. Nucl Instruments Methods Phys Res Sect A Accel Spectrometers, Detect Assoc Equip 2007;578:23.
[96] Stuhr U. Nucl Instruments Methods Phys Res Sect A Accel Spectrometers, Detect Assoc Equip 2005;545:319.
[97] Stuhr U, Spitzer H, Egger J, Hofer A, Rasmussen P, Graf D, Bollhalder A, Schild M, Bauer G, Wagner W. Nucl Instruments Methods Phys Res Sect A Accel Spectrometers, Detect Assoc Equip 2005;545:330.

[98] Arnold O, Bilheux JC, Borreguero JM, Buts a., Campbell SI, Chapon L, Doucet M, Draper N, Ferraz Leal R, Gigg M a., Lynch VE, Markvardsen a., Mikkelson DJ, Mikkelson RL, Miller R, Palmen K, Parker P, Passos G, Perring TG, Peterson PF, Ren S, Reuter M a., Savici a. T, Taylor JW, Taylor RJ, Tolchenov R, Zhou W, Zikovsky J. Nucl Instruments Methods Phys Res Sect A Accel Spectrometers, Detect Assoc Equip 2014;764:156.

[99] Akeroyd F, Ansell S, Antony S, Arnold O, Bekasovs A, Bilheux J, Borreguero J, Brown K, Buts A, Campbell S, Champion D, Chapon L, Clarke M, Cottrell S, Dalgliesh R, Dillow D, Doucet M, Draper N, Fowler R, Gigg MA, Granroth G, Hagen M, Heller W, Hillier A, Howells S, Jackson S, Kachere D, Koennecke M, Le Bourlot C, Leal R, Lynch V, Manuel P, Markvardsen A, McGreevy R, Mikkelson D, Mikkelson R, Miller R, Nagella S, Nielsen T, Palmen K, Parker PG, Pascal M, Passos G, Perring T, Peterson PF, Pratt F, Proffen T, Radaelli P, Rainey J, Ren S, Reuter M, Sastry L, Savici A, Taylor J, Taylor RJ, Thomas M, Tolchenov R, Whitley R, Whitty M, Williams S, Zhou W, Zikovsky J. Mantid: Manipulation and Analysis Toolkit for Instrument Data. Computer Program; 2013.

[100] Hofmann M, Schneider R, Seidl G a., Rebelo-Kornmeier J, Wimpory RC, Garbe U, Brokmeier HG. Phys B Condens Matter 2006;385-386:1035.

[101] Walentek A, Seefeldt M, Verlinden B, Aernoudt E, Van Houtte P. J Microsc 2006;224:256.

[102] Takahashi T, Ponge D, Raabe D. Steel Res Int 2007;78:38.

[103] Guo N, Liu Q. J Microsc 2012;246:221.

[104] Kriška M, Tacq J, van Acker K, Seefeldt M. Mater Sci Forum 2013;768-769:327.

[105] Kriska M, Tacq J, Van Acker K, Seefeldt M. J Heat Treat Mater 2014;69:97.

[106] Tacq J, Kriška M, Seefeldt M. Mater Sci Forum 2013;768-769:380.

[107] Rendle D. J Forensic Sci 1981;26:343.

[108] Rayne JA, Chandrasekhar BS. Phys Rev 1961;122:1714.

[109] Jiang C, Srinivasan SG. Nature 2013;496:339.

[110] Ledbetter H. Mater Sci Eng A 2010;527:2657.

[111] Laszlo F, Nolle H. J Mech Phys Solids 1959;7:193.

[112] Stuart H, Ridley N. J Iron Steel Inst 1966;204:711.

[113] Warren BE. Prog Met Phys 1959;8:147.

[114] Ungar T, Mughrabi H, Rönnpagel D, Wilkens M. Acta Metall 1984;32:333.

[115] Mughrabi H, Ungar T, Kienle W, Wilkens M. Philos Mag A 1986;53:793.

[116] Clyne TW, Withers PJ. An Introduction to Metal Matrix Composites. Cambridge: Cambridge University Press; 1993.

[117] Bultheel A. Inleiding Tot de Numerieke Wiskunde, 1st ed. ACCO; 2006.

[118] Chakrabarty J. Theory of Plasticity. New York: McGraw-Hill; 1987.

[119] Walentek A, Seefeldt M, Verlinden B, Aernoudt E, Van Houtte P. Mater Sci Eng A 2008;483-484:716.

[120] Nye JF. Physical Properties of Crystals. Oxford: Oxford University Press; 1985.

[121] Van Houtte P. Textures Microstruct 1988;8-9:313.

[122] Eshelby JD. Proc R Soc London, Ser A - Math Phys Sci 1957;241:376.

[123] Eshelby JD. Proc R Soc London, Ser A - Math Phys Sci 1959;252:561.

[124] Krivoglaz MA, Ryaboshapka KP. Fiz Met i Metalloved 1963;15:18.

[125] Wilkens M. Fundemental Asp Dislocation Theory 1970;317:1195.
[126] Vermeulen AC, Delhez R, de Keijser TH, Mittemeijer EJ. J Appl Phys 1995;77:5026.
[127] Krivoglaz MA. Scattering of X-Ray and Neutrons in Crystals with Dislocations, in:. X-Ray Neutron Diffr. Non-Ideal Cryst. 1996.
[128] Scardi P, Leoni M, Delhez R. J Appl Crystallogr 2004;37:381.
[129] Williamson GK, Hall WH. Acta Metall 1953;1:22.
[130] Warren BE, Avenbach BL. J Appl Phys 1950;21:595.
[131] Raabe D, Choi P, Li Y, Kostka A, Sauvage X, Lecouturier F, Hono K, Kirchheim R, Pippan R, Embury D. MRS Bull 2010;35:982.
[132] Wang J, Kang K, Zhang RF, Zheng SJ, Beyerlein IJ, Mara N a. Jom 2012;64:1208.
[133] Beyerlein IJ, Mara NA, Wang J, Carpenter JS, Zheng SJ, Han WZ, Zhang RF, Kang K, Nizolek T. JOM 2012;64:1192.
[134] Keller RR, Geiss RH. J Microsc 2012;245:245.
[135] Trimby PW. Ultramicroscopy 2012;120:16.
[136] Wilkinson A, Dingley D. Acta Metall Mater 1991;39:3047.
[137] Wilkinson AJ. Ultramicroscopy 1996;62:237.
[138] Wilkinson AJ. Scr Mater 2001;44:2379.
[139] Wilkinson AJ, Meaden G, Dingley DJ. Superlattices Microstruct 2009;45:285.
[140] Kamaya M, Wilkinson AJ, Titchmarsh JM. Nucl Eng Des 2005;235:713.
[141] Kamaya M. Mater Charact 2009;60:125.
[142] Bearden JA. Rev Mod Phys 1967;39:78.
[143] Hubbell JH, Seltzer SM. Tables of X-Ray Mass Attenuation Coefficients and Mass Energy-Absorption Coefficients from 1 keV to 20 MeV for Elements Z = 1 to 92 and 48 Additional Substances of Dosimetric Interest, accessed 3 Jul. 2012. URL: http://www.nist.gov/pml/data/xraycoef/index.cfm.

APPENDICES

A. General evolution of the microstructure with cold rolling

The evolution of the microstructure with cold rolling strain is illustrated here for a sample isothermally transformed at 680°C. Micrographs representative for the bulk of the samples are shown. The figures represent samples cold rolled to strain of 0, 0.12, 0.96, 1.44 and 1.98, in that order. For all images, the rolling direction is vertical and the normal direction horizontal. Note that the scale of the pictures changes with increasing strain. This cannot be avoided if the distinguishing features of the microstructure are to remain visible.

The first two figures illustrate that the microstructure doesn’t change much after the first few percent of rolling strain. At a strain of 0.96 however, it can clearly be seen that ILS and lamellae themselves become thinner and align with the rolling direction. Additionally, bending of the lamellae can be seen which is cause by the onset of shear banding. These features become more distinct with increasing rolling strain. For a more detailed discussion of the main microstructural features, see section 6.1.

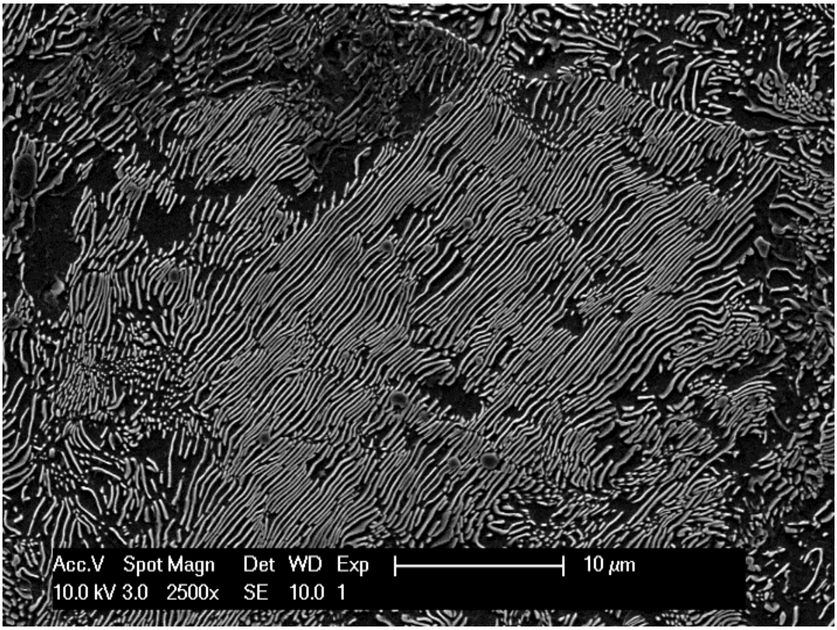

Fig. A.1: SEM micrograph of an undeformed pearlitic steel sample, isothermally transformed at 680°C.

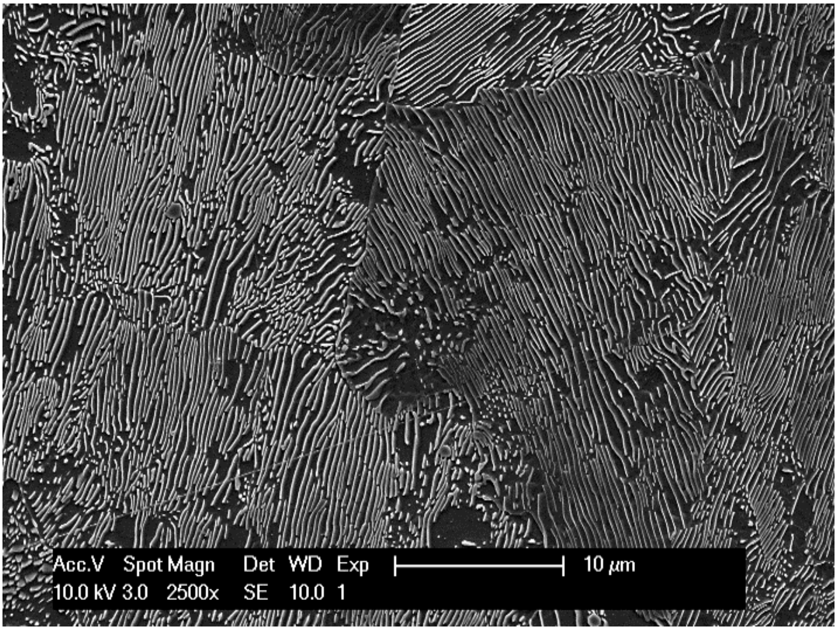

Fig. A.2: SEM micrograph of a pearlitic steel sample, isothermally transformed at 680°C and cold rolled to a strain of 0.12.

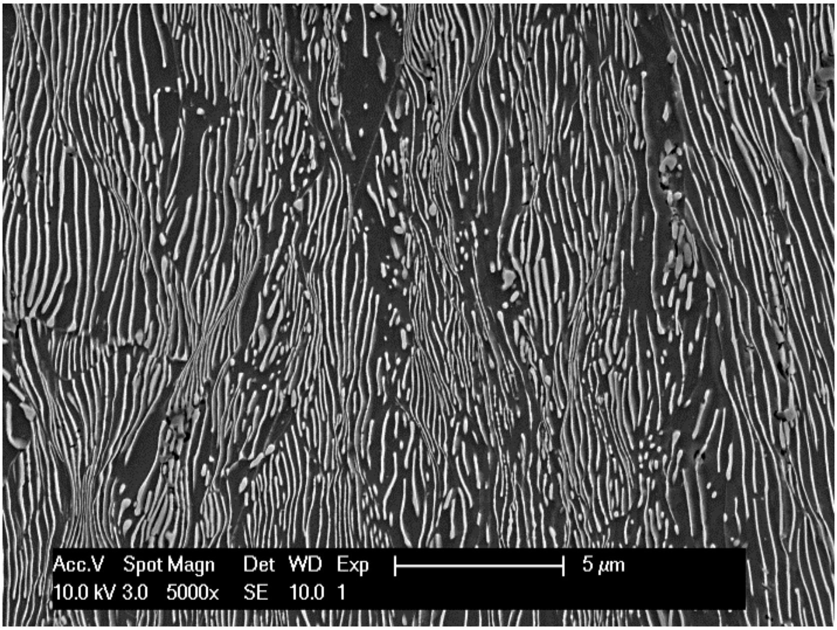

Fig. A.3: SEM micrograph of a pearlitic steel sample, isothermally transformed at 680°C and cold rolled to a strain of 0.96.

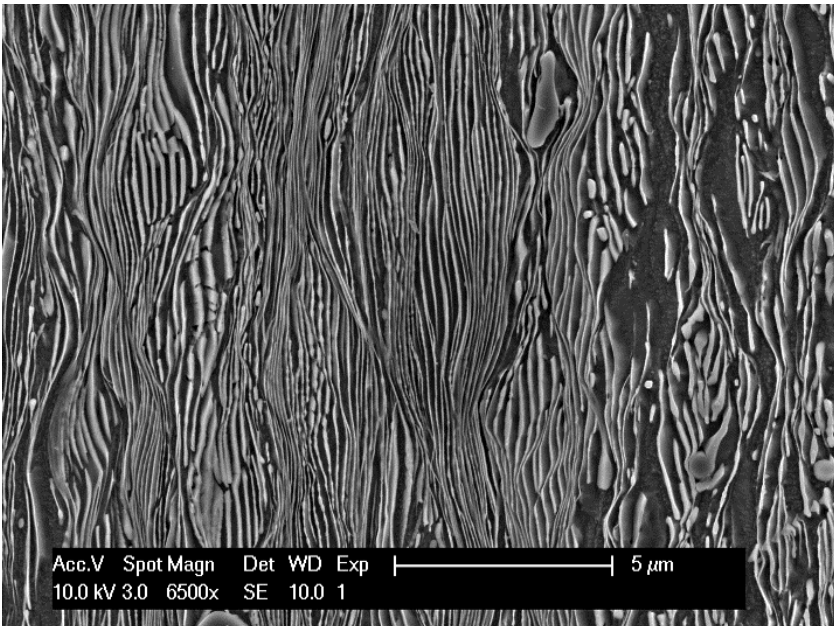

Fig. A.4: SEM micrograph of a pearlitic steel sample, isothermally transformed at 680°C and cold rolled to a strain of 1.44.

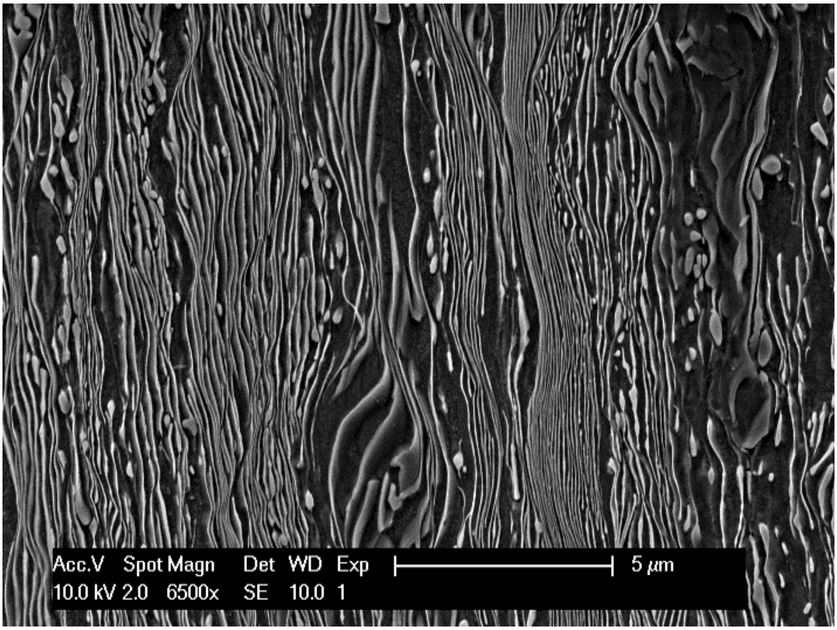

Fig. A.5: SEM micrograph of a pearlitic steel sample, isothermally transformed at 680°C and cold rolled to a strain of 1.98.

B. Residual surface stresses (X-ray diffraction)

The total residual stresses at the surface of the cold rolled pearlitic steel sheet were measured using laboratory X-ray diffraction. These results did not lead to any new conclusions and were not used in processing any of the other data. They are presented here, in appendix, for the sake of the interested reader and in order to document them for possible future reference.

$\mathrm{Sin}^2\psi$ measurements were performed using the in-house laboratory X-ray diffraction set-up. The ferrite 211 diffraction peak was used to determine the lattice strains. Chromium radiation with a wavelength of ~2.29Å [142] was used, resulting in a 2θ angle of ~156.2°, resulting in good strain sensitivity.

The residual stress was only determined in the rolling direction ($\varphi = 0°$). Nine ψ angles were used, ranging from -45° to 45°. Due to the relatively low peak intensity, especially at higher rolling strains, each measurement point took about one hour. To evaluate the homogeneity of the samples along their length, and to increase the statistical relevance of the experiment, up to five points were measured along the length of the rolled strip. All measurements were performed in the centre of the strip (with respect to the transverse direction).

No surface treatments were applied to the rolled sheets in order to not influence the residual stresses present. Based on the wavelength of the used Cr radiation and the absorption coefficient of iron [143], the penetration depth was found to be ~10μm. The measured stress is therefore the total stress at the surface of the material.

The stresses were calculated using isotropic diffraction elastic constants as were available in the 'Analyze'® software ($\frac{1}{2}S_2 = 5.81E^{-6}MPa^{-1}$, $-S_1 = 1.27E^{-6}MPa^{-1}$). The stress components perpendicular to the sample surface were assumed to be negligible and set to zero. This may be an over simplification however. A penetration depth of 10μm is large compared to the scale of the lamellar microstructure. It is therefore possible that there are non-zero micro-phase stress components in the normal direction. Nevertheless, the assumption is made because it was not possible to perform $\sin^2\psi$ measurements for three φ angles, as would be required to obtain the complete stress tensor.

Measurements were done on three sample sets, each with a different starting ILS. The obtained stresses are surface stresses and are thus a combination of micro-phase stresses and macro-stresses, i.e. the total phase stress is measured.

The stresses were measured on 2-5 different position along the length of each sheet. The stresses measured on the same side show variation of around 20-30 MPa. This variation might be linked to the imperfection of the rolling process which results in variations of the sheet thickness along its length. The local residual surface stress will also depend on the local conditions of lubrication, roll quality and different rolling parameters such as rolling speed and reduction. Variations in these conditions along the length of a sheet can cause the observed variation in RS-value. The variations are not due to experimental errors in the RS-determination. The RS was measured on the same position multiple times to check the experimental error, which is on the order of less than 10 MPa. The rolling strain and residual stress values reported in the following, are the averages along the length of the sheet.

There is a large difference in stress between the two sides of the sheet, with the stress on one side being significantly higher (Fig. B.1) than the stress on the other side (Fig. B.2). The trend in the surface stress evolution is also different for both sides. On the high stress side, quick saturation is observed, while the lows stress side exhibits a linear increase of the residual surface stress up to a cold rolling strain of around 1.5. The high stress side corresponds to the side of the plate which has a rougher surface finish. This suggests that the difference between both sides is controlled by the quality of the rolls used during cold rolling. It follows that the macro stress profile will also be non-symmetric. Because the plates were turned upside down after each rolling pass, it further suggests that the residual stress in the top 5μm of the material is mainly the result of the last rolling pass.

Although there are differences between both sides of the sheet, there are also similarities. Firstly, the total surface stress eventually seems to saturate on both sides of the sheet. Secondly, it can be see that the absolute value of the residual stress increases with decreasing ILS, suggesting that a higher strength of the composite material leads to a higher total phase stress.

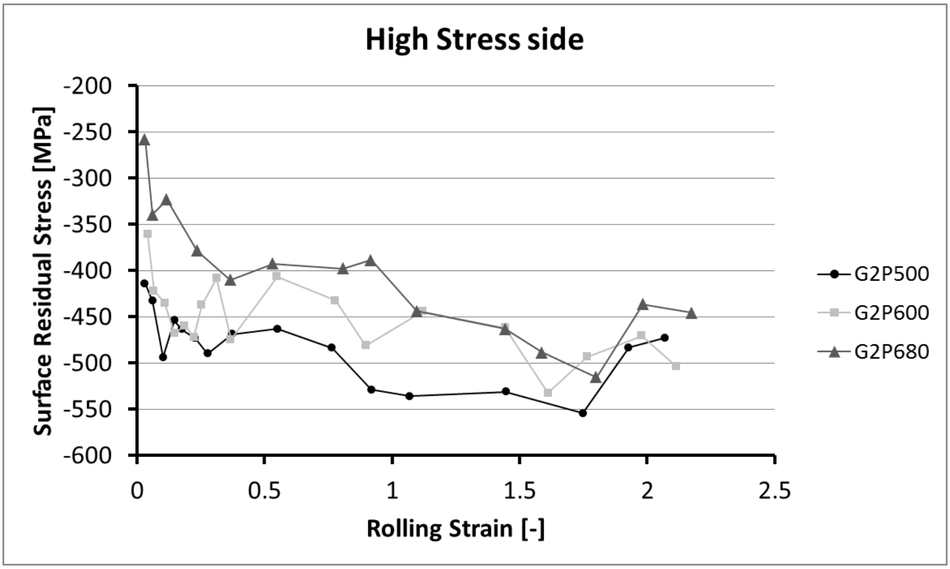

Fig. B.1: Total residual stress measured on the surface of three sets of cold rolled sheets, each with a different starting interlamellar spacing (see Table 4.2). This graphs corresponds to the rougher side of the sheets and exhibits higher stress values (more negative).

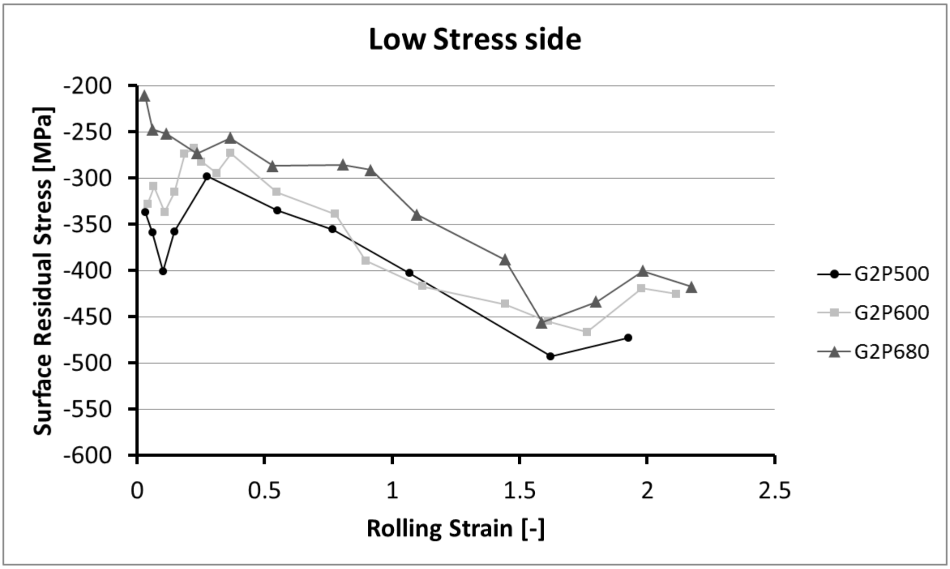

Fig. B.2: Total residual stress measured on the surface of three sets of cold rolled sheets, each with a different starting interlamellar spacing (see Table 4.2). This graphs corresponds to the smoother side of the sheets and exhibits lower stress values (less negative).

C. Lattice strains and stresses for P680 samples

In this appendix, the lattice strains and stresses as obtained from the neutron diffraction measurements at the POLDI beamline at the PSI are given for the P680 sample set. The experiment leading to this data, as well as some of the plots presented here have been discussed in section 6.2.2.1. The other plots are qualitatively similar to those obtained for the P500 sample set, which is presented in section 6.2.2.1, and need no separate discussion. They are shown here for the sake of completeness.

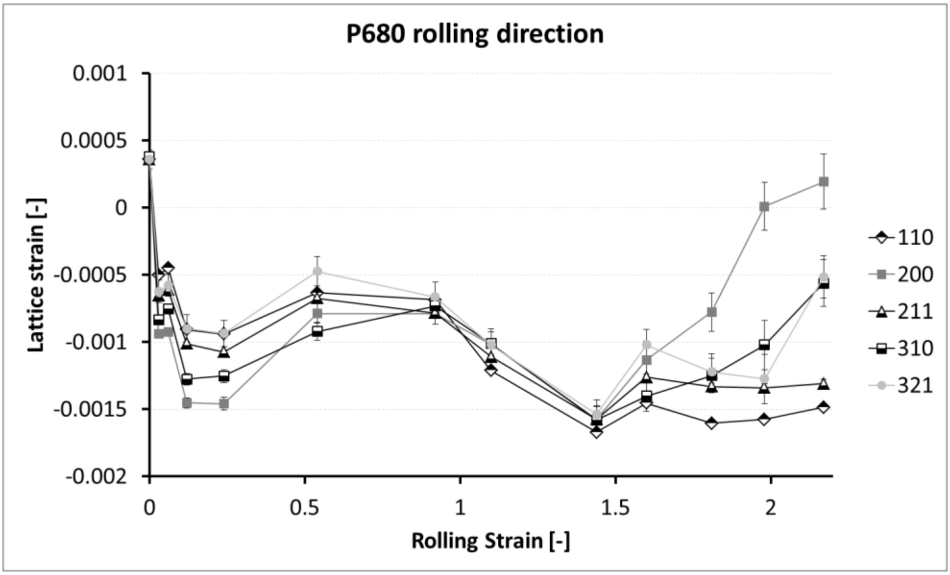

Fig. C.1: Lattice strain for various ferrite grain families as a function of cold rolling strain. The lattice strains were obtained from peak positions measured in the rolling direction, on the P680 samples. When the error bars are not visible, they are of the same size as the data symbols.

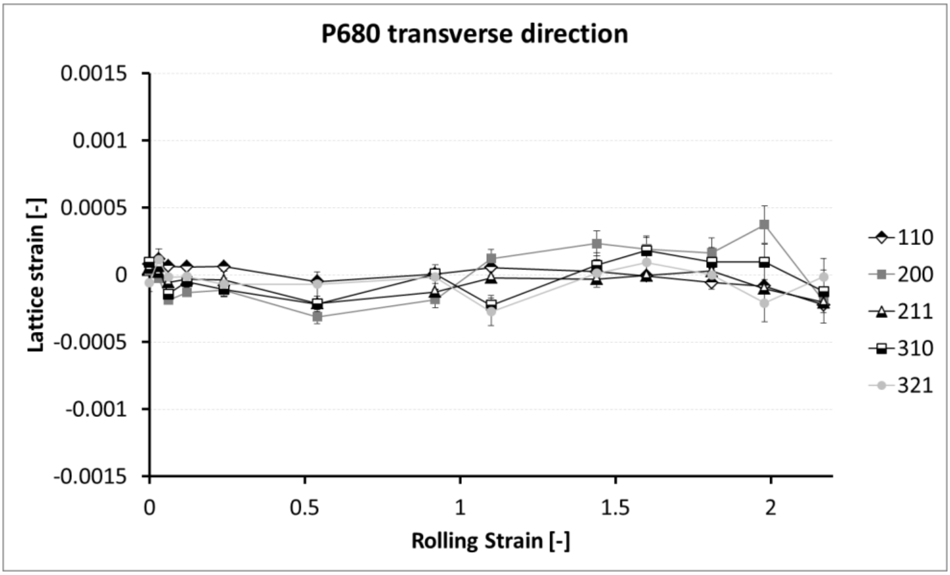

Fig. C.2: Lattice strain for various ferrite grain families as a function of cold rolling strain. The lattice strains were obtained from peak positions measured in the transverse direction, on the P680 samples. When the error bars are not visible, they are of the same size as the data symbols.

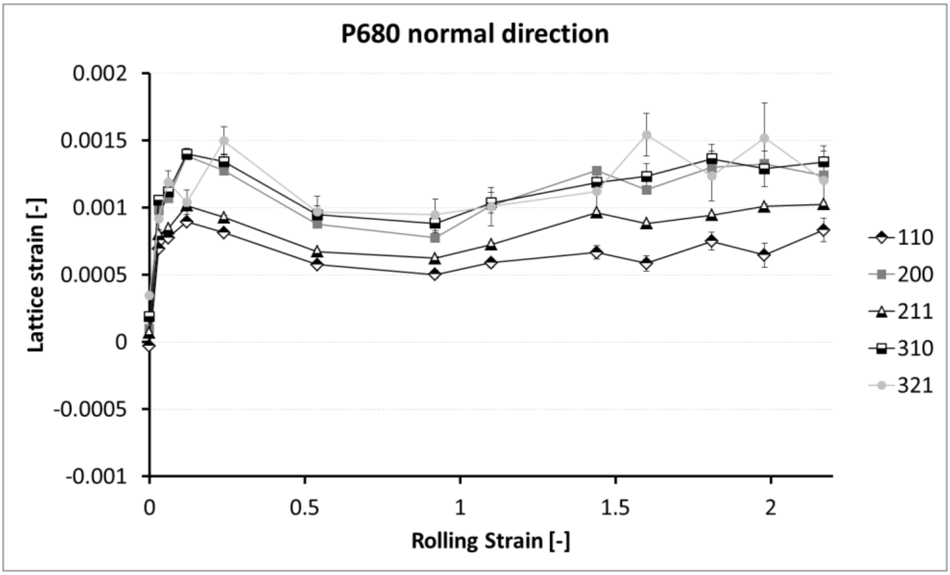

Fig. C.3: Lattice strain for various ferrite grain families as a function of cold rolling strain. The lattice strains were obtained from peak positions measured in the normal direction, on the P680 samples. When the error bars are not visible, they are of the same size as the data symbols.

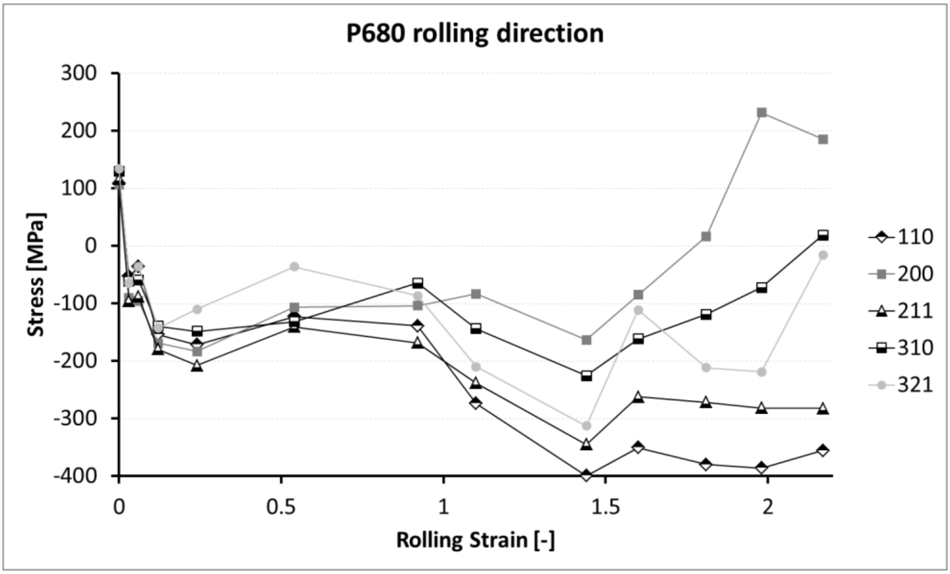

Fig. C.4: Residual stress for various ferrite grain families as a function of cold rolling strain. The lattice strains were obtained from peak positions measured in the rolling direction, on the P680 samples.

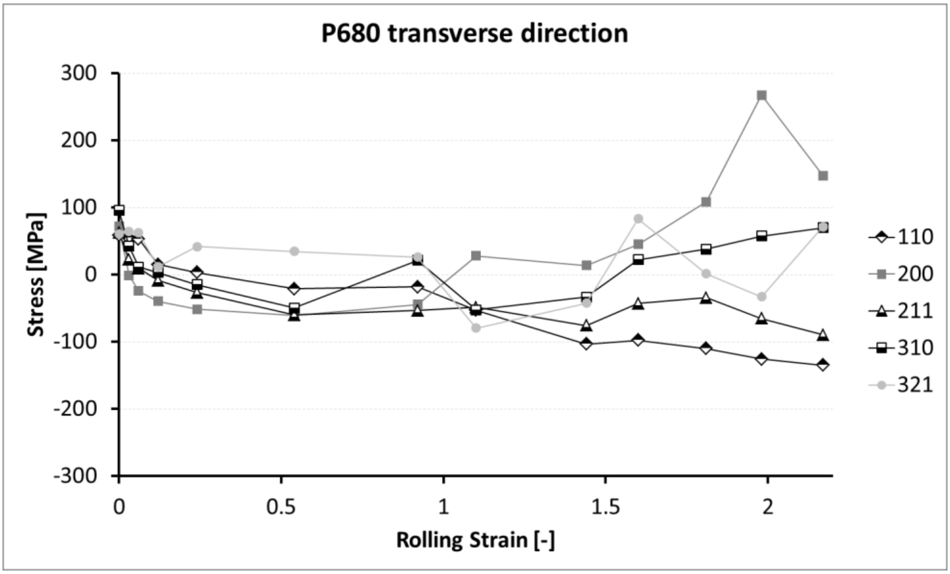

Fig. C.5: Residual stress for various ferrite grain families as a function of cold rolling strain. The lattice strains were obtained from peak positions measured in the transverse direction, on the P680 samples.

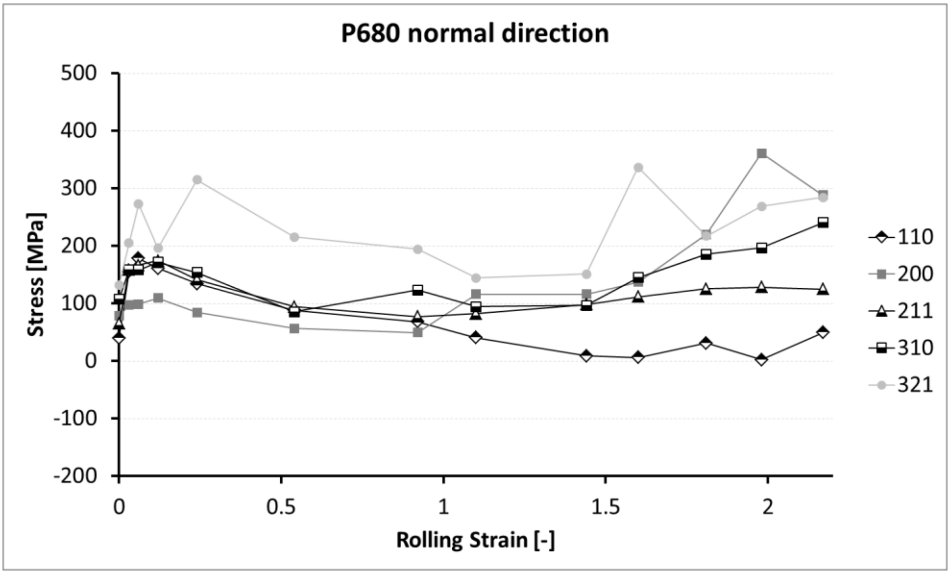

Fig. C.6: Residual stress for various ferrite grain families as a function of cold rolling strain. The lattice strains were obtained from peak positions measured in the normal direction, on the P680 samples.

D. <110> ferrite lattice strain and stress measured at MLZ

The <110> ferrite lattice strains and stresses obtained at MLZ in Garching were very similar to the lattice strains obtained at PSI, which are presented and discussed in section 6.2.2.1. They are shown here in order to allow the reader to verify this conclusion. Due to time considerations, the strain in the TD could not be measured for all samples. However, to be able to calculate the stress, a value of the TD strain is required. For those samples for which the strain in the TD direction was not measured, the average value of the TD strain observed in the previous rolling passes was adopted. This is believed to be a reasonable assumption as it could be seen from the PSI measurements that the lattice strain in the TD remains nearly constant.

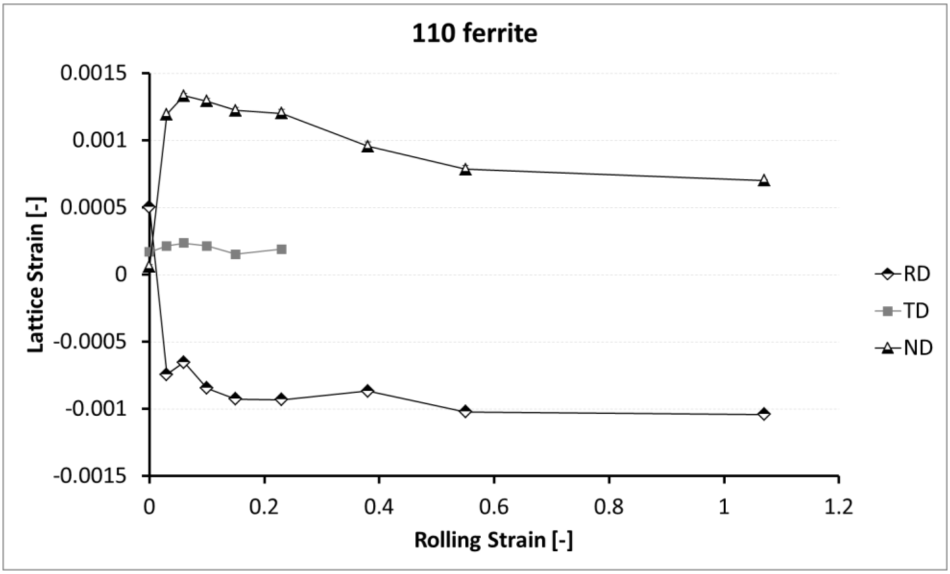

Fig. D.1: <110>-ferrite lattice strain as a function of cold rolling strain, measured using neutron diffraction. The material was isothermally transformed at 500°C prior to rolling. The lattice strains are shown for the three principle directions of the cold rolled sheet. Error bars have been plotted, but they are of the same size as the data symbols.

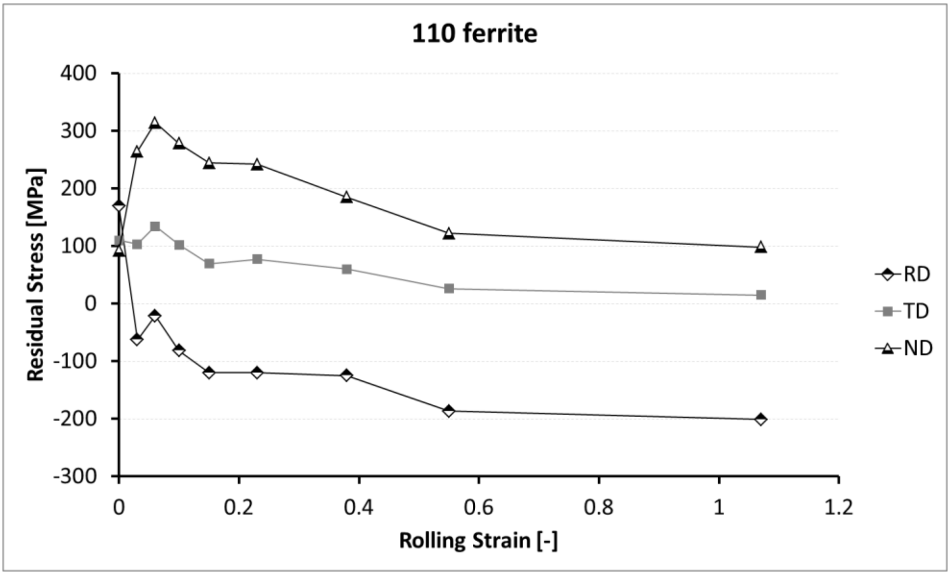

Fig. D.2: Residual stress for the <110>-ferrite reflection as a function of cold rolling strain. The stresses were obtained from the measured strain by application of the principle directions method.

E. Additional plots in-situ neutron diffraction experiments

In-situ tensile tests were performed under neutron diffraction. The results of these experiments are discussed in section 6.3. For clarity and the sake of completeness, additional plots are presented here.

The engineering stress-strain curves presented in section 6.3 are the ex-situ curves recorded prior to the in-situ experiments. The stress-strain curves recorded during the in-situ neutron diffraction experiment are shown in Fig. E.1. Each neutron diffraction measurement was performed at constant extensometer strain and is characterized by a drop of the stress. This indicates that some amount of relaxation by creep occurs while holding at constant strain. In Fig. E.2, Fig. E.3 and Fig. E.4 the lattice strain evolution in the as-rolled, stress relieved and spheroidised samples are given.

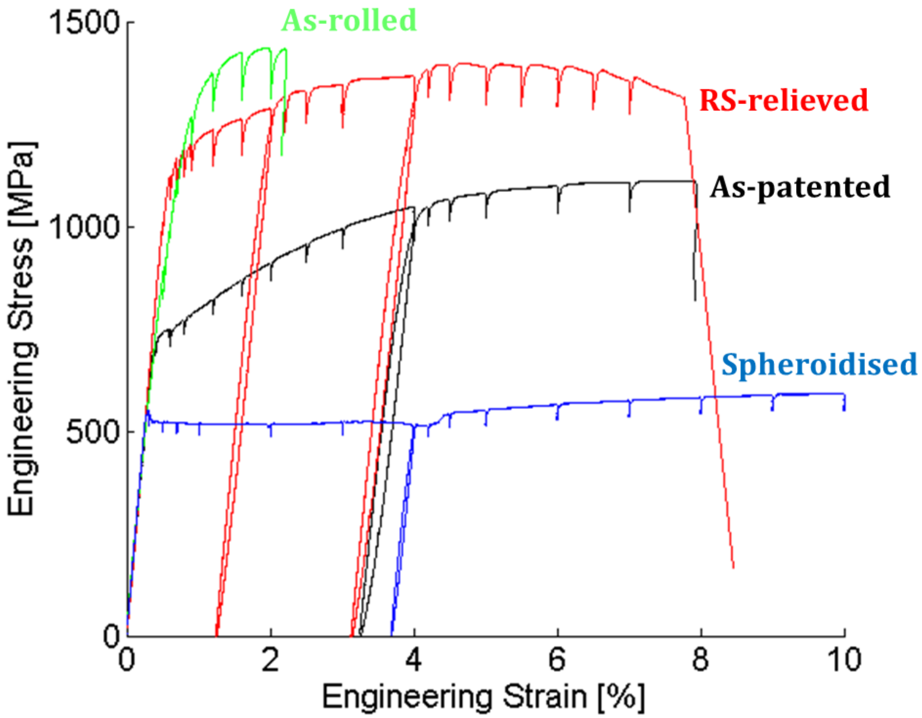

Fig. E.1: In-situ engineering stress-strain curves for the four different samples described in section 6.3.

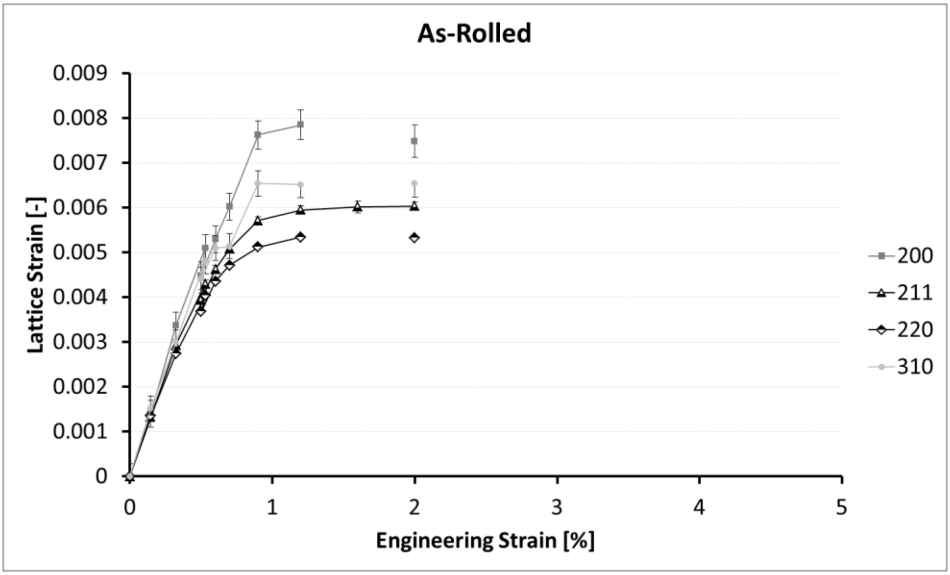

Fig. E.2: Ferrite lattice strain in the loading direction as a function of macroscopic tensile strain, for the as-rolled sample. The lattice strain for all four measured ferrite grain families is shown. Error bars are shown, but are of the same size as the data symbols for the <220> and <211> reflections.

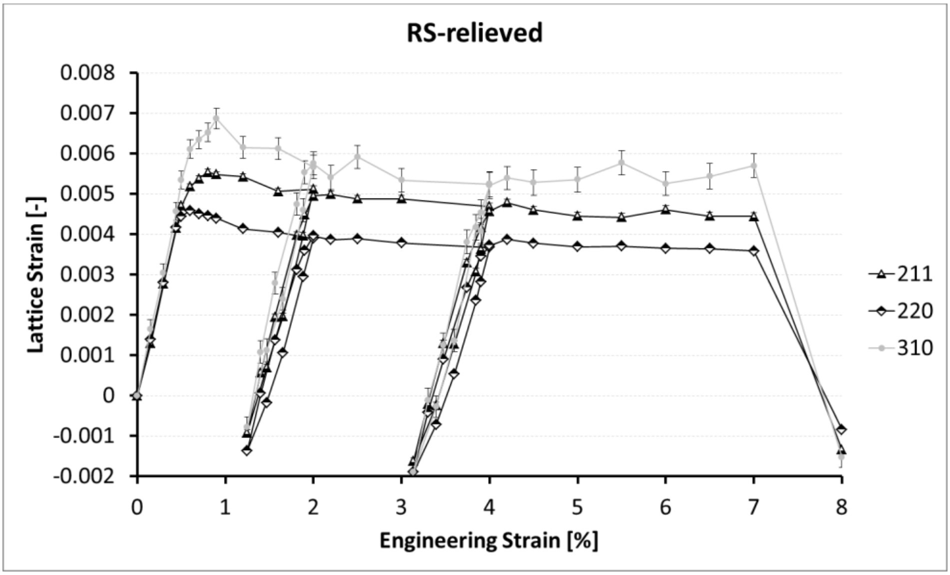

Fig. E.3: Ferrite lattice strain in the loading direction as a function of macroscopic tensile strain, for the stress relieved sample. The lattice strain for all four measured ferrite grain families is shown. Error bars are shown, but are of the same size as the data symbols for the <220> and <211> reflections.

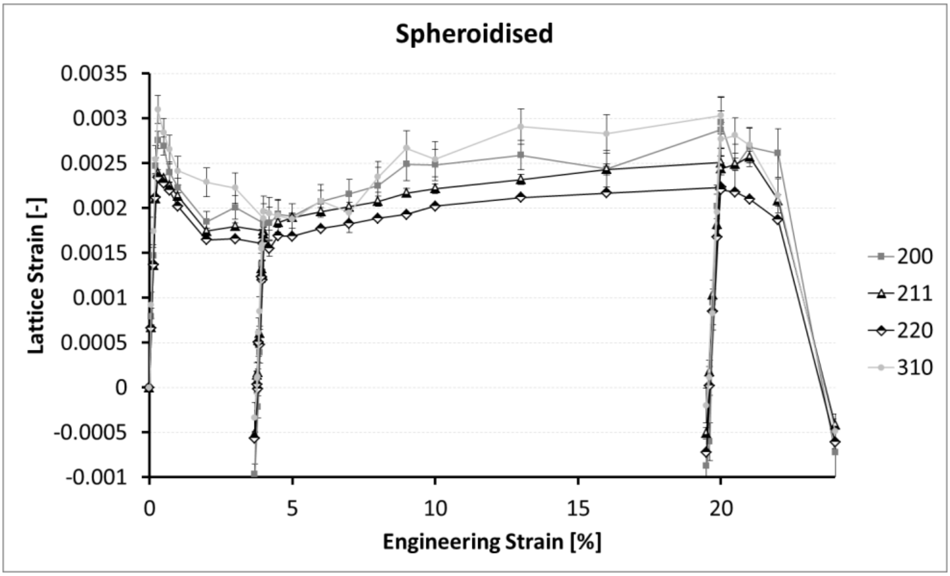

Fig. E.4: Ferrite lattice strain in the loading direction as a function of macroscopic tensile strain, for the spheroidised sample. The lattice strain for all four measured ferrite grain families is shown. Error bars are shown, but are of the same size as the data symbols for the <220> and <211> reflections.

F. 1-D residual stress sandwich model: displacement based approach

In section 7.2.2, the residual stresses which remain after loading and unloading a two-phase material with a lamellar sandwich microstructure are calculated. The calculation is based on simply following the evolutions of the lattice strains in both phases during the loading and unloading cycle. Here, the same procedure is applied, but instead of following the strains, the displacements are followed. From these displacements the strains and stresses can then be calculated. The method presented here is completely analogue to the one proposed in section 7.2.2 and the obtained solution to the problem is also identical. However, after implementation of both solutions, the one based on the displacements has been shown to converge faster. Therefore, this method is also elaborated here.

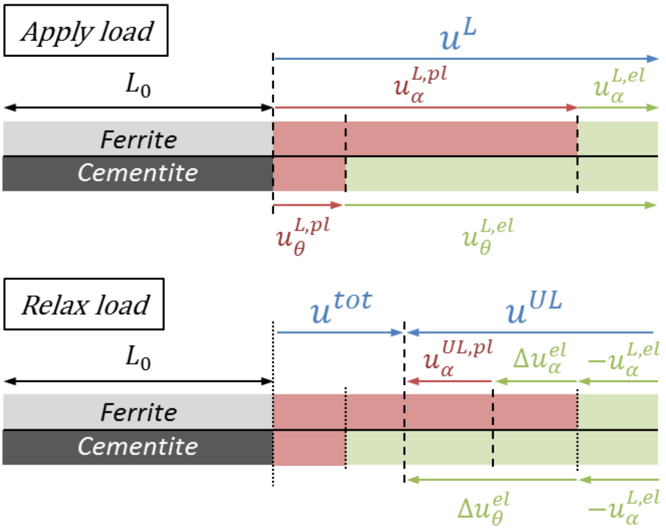

Fig. F.1: Illustration and definition of the displacements occurring during loading and unloading of a two-phase lamellar sandwich material subjected to an external load, parallel to the alignment direction of the lamellae. After unloading the material reaches an equilibrium elongation which is characterized by the high dashed line in the lower sketch.

The solution process is divided in two steps: a loading step and an unloading step. The displacements occurring during both steps are illustrated and defined in Fig. F.1. The basic assumptions under which the calculations are performed are also similar to the strain based approach:

- The total displacement u_i^{tot} is under all circumstances equal in both phases.

- The stress, strain and displacements are only considered in the loading direction. All other dimensions are not taken into account.
- The true stress-strain curves for both materials are assumed to be known and representative for the in-situ behaviour of the phases in the composite material.

Loading step

The total loading displacement in the ith phase can be decomposed in an elastic and plastic portion.

$$u^L = u_i^{L,pl} + u_i^{L,el} \tag{F.1}$$

The superscripts *L*, *el* and *pl* refer to the loading step, elastic and plastic strain, respectively. The subscript *i* refers to the ith phase.

The same can be done for the total loading strain.

$$\varepsilon^L = \varepsilon_i^{L,pl} + \varepsilon_i^{L,el} \tag{F.2}$$

Based on the definitions of the displacements, these three strains can now be written as:

$$\varepsilon_i^{L,pl} = \ln\left(\frac{L_0 + u_i^{L,pl}}{L_0}\right) \tag{F.3}$$

$$\varepsilon_i^{L,pl} = \ln\left(\frac{L_0 + u_i^{L,pl} + u_i^{L,el}}{L_0 + u_i^{L,pl}}\right) \tag{F.4}$$

$$\varepsilon^L = \varepsilon_i^{L,pl} + \varepsilon_i^{L,el} = \ln\left(\frac{L_0 + u^L}{L_0}\right) \tag{F.5}$$

Using the stress-strain curves of both phases, the stress in both phases after loading can be obtained from the loading strain ε^L. The elastic and plastic parts of the loading strain in each phase are then given by

$$\varepsilon_i^{L,el} = \frac{\sigma_i^L}{E_i} \tag{F.6}$$

$$\varepsilon_i^{L,pl} = \varepsilon^L - \varepsilon_i^{L,el} \tag{F.7}$$

The elastic and plastic parts of the displacement are finally obtained from equations F.3 and F.4.

$$u_i^{L,pl} = L_0 \exp\left(\varepsilon_i^{L,pl}\right) - L_0 \tag{F.8}$$

$$u_i^{L,el} = \left(L_0 + u_i^{L,pl}\right) \exp\left(\varepsilon_i^{L,el}\right) - \left(L_0 + u_i^{L,pl}\right) \tag{F.9}$$

Unloading step

The unloading exists in removing the imposed deformation u^L. As a result the material will exhibit a spring back. The first part of the spring back consists of a displacement equal in magnitude to the elastic displacement $u_\alpha^{L,el}$ in the ferrite phase. At this stage the ferrite doesn't contain any forward elastic strain anymore, while the cementite phase is still in a state of elastic tension. The cementite will want to relax further, thereby compressing the ferrite. Whether the ferrite will be compressed purely elastically or also plastically, depends on the magnitude of the elastic stress remaining in the cementite after elastically unloading the strain $u_\alpha^{L,el}$.

Definition of displacements and strains

From Fig. F.1 it can be seen that the total elastic unloading displacement in the i^th^ phase is equal to:

$$u_i^{UL,el} = -u_\alpha^{L,el} + \Delta u_i^{el} \tag{F.10}$$

$u_i^{UL,el}$ has a negative value. The total unloading displacement is then

$$u^{UL} = u_i^{UL,pl} + u_i^{UL,el} = u_i^{UL,pl} - u_\alpha^{L,el} + \Delta u_i^{el} \tag{F.11}$$

All the required strains can now be written in terms of the displacements. The unloading strain can then be written as

$$\varepsilon^{UL} = \varepsilon_i^{UL,pl} + \varepsilon_i^{UL,el} = \ln\left(\frac{(L_0 + u^L) + u^{UL}}{L_0 + u^L}\right) \tag{F.12}$$

The plastic unloading strain in the i^th^ phase is defined as

$$\varepsilon_i^{UL,pl} = \ln\left(\frac{L_0 + u_i^{L,pl} + u_i^{UL,pl}}{L_0 + u_i^{L,pl}}\right) \tag{F.13}$$

The elastic unloading strain is somewhat more difficult to define. An expression for $\varepsilon_i^{UL,el}$ can be found starting from eq. 7.11 from which it can be seen that

$$\Delta\varepsilon_i^{el} = \varepsilon^{UL} - \varepsilon_i^{UL,pl} + \varepsilon_\alpha^{L,el} \tag{F.14}$$

All the terms can be written in terms of displacements, and taking into account eq. F.10, it follows that

$$\Delta\varepsilon_i^{el} = \ln\left(\frac{L_0 + u_i^{L,pl} + u_i^{L,el} + u_i^{UL,pl} - u_\alpha^{L,el} + \Delta u_i^{el}}{L_0 + u_i^{L,pl} + u_i^{L,el} - u_\alpha^{L,el}} \cdot \frac{L_0 + u_i^{L,pl}}{L_0 + u_i^{L,pl} + u_i^{UL,pl}}\right)$$

For the ferrite and cementite phases, respectively, this translates to

$$\Delta\varepsilon_\alpha^{el} = \ln\left(\frac{L_0 + u_\alpha^{L,pl} + u_\alpha^{UL,pl} + \Delta u_\alpha^{el}}{L_0 + u_\alpha^{L,pl} + u_\alpha^{UL,pl}}\right) \tag{F.15}$$

$$\Delta\varepsilon_\theta^{el} = \ln\left(\frac{L_0 + u_\theta^{L,pl} + u_\theta^{L,el} - u_\alpha^{L,el} + \Delta u_\theta^{el}}{L_0 + u_\theta^{L,pl} + u_\theta^{L,el} - u_\alpha^{L,el}}\right) \tag{F.16}$$

From eq. F.14 and taking into account that $\varepsilon^{UL} = \varepsilon_i^{UL,pl} + \varepsilon_i^{UL,el}$, from which it can be deduced that

$$\varepsilon_i^{UL,el} = -\varepsilon_\alpha^{UL,el} + \Delta\varepsilon_i^{el} \tag{F.17}$$

Writing this down in terms of displacements and using the fact that $u_\alpha^{L,pl} = u_i^{L,pl} + u_i^{L,pl} - u_\alpha^{L,el}$ it is found that

$$\varepsilon_i^{UL,el} = \ln\left(\frac{L_0 + u_i^{L,pl}}{L_0 + u^L} \cdot \frac{L_0 + u_i^{L,pl} + u_i^{L,el} + u_i^{UL,pl} - u_\alpha^{L,el} + \Delta u_i^{el}}{L_0 + u_i^{L,pl} + u_i^{UL,pl}}\right)$$

As a proof for the derivation of the above expression, $\varepsilon_i^{UL,el}$ and $\varepsilon_i^{UL,pl}$ can be added up. Doing so will indeed yield the same result as eq. F.12.

The total strain after loading and unloading can finally be expressed as

$$\varepsilon^{tot} = \varepsilon^L + \varepsilon^{UL} = \ln\left(\frac{L_0 + u^L + u^{UL}}{L_0}\right) \tag{F.18}$$

Based on the above expressions, the total strain can also be decomposed in an elastic and a plastic part.

$$\begin{aligned} \varepsilon^{tot} &= \left(\varepsilon_i^{L,pl} + \varepsilon_i^{L,el}\right) + \left(\varepsilon_i^{UL,pl} + \varepsilon_i^{UL,el}\right) \\ &= \left(\varepsilon_i^{L,pl} + \varepsilon_i^{UL,pl}\right) + \left(\varepsilon_i^{L,el} + \varepsilon_i^{UL,el}\right) \\ &= \varepsilon_i^{tot,pl} + \varepsilon_i^{tot,el} \end{aligned}$$

In which the elastic and plastic part of the total strain are, in terms of the displacements:

$$\varepsilon_i^{tot,pl} = \ln\left(\frac{L_0 + u_i^{L,pl} + u_i^{UL,pl}}{L_0}\right) \tag{F.19}$$

$$\varepsilon_i^{tot,el} = \ln\left(\frac{\left(L_0 + u_i^{L,pl} + u_i^{UL,pl}\right) + u_i^{L,el} + u_i^{UL,el}}{L_0 + u_i^{L,pl} + u_i^{UL,pl}}\right) \tag{F.20}$$

It is these latter strains, the total elastic strains in both phases after unloading, which we are finally interested in. It is from these trains that the residual stress can be calculated using Hooke's law.

Implementation of the model

A solution for the residual stress can be found under the conditions that (1) the strain in both phases has to be equal after unloading and (2) that the stress equilibrium equation has to be fulfilled.

The first condition, i.e. co-deformation, translates into

$$\varepsilon_\theta^{tot,el} + \varepsilon_\theta^{tot,pl} = \varepsilon_\alpha^{tot,el} + \varepsilon_\alpha^{tot,pl} \tag{F.21}$$

Equations F.19 and F.20 can be used to write eq. F.21 in terms of displacements. Simplifying the expression taking into account that $u_\theta^{UL,pl}$ equals zero and that the total loading displacement is the same in both phases yields

$$u_\theta^{UL,el} = u_\alpha^{UL,pl} + u_\alpha^{UL,el}$$

From Fig. F.1 it can be seen that this is indeed what was expected. Using eq. F.10 the equal strain condition can finally be written as

$$\Delta u_\theta^{el} = u_\alpha^{UL,pl} + \Delta u_\alpha^{el} \tag{F.22}$$

The stress balance can be written in terms of the total elastic strain in both phases after unloading.

$$E_\alpha \cdot \varepsilon_\alpha^{tot,el} \cdot (1 - V_\theta) + E_\theta \cdot \varepsilon_\theta^{tot,el} \cdot V_\theta = 0 \qquad \text{(F.23)}$$

Equation F.20 can be used to write this in terms of displacements. It can then be seen that equations F.22 and F.23 contain three unknown variables: Δu_θ^{el}, Δu_α^{el} and $u_\alpha^{UL,pl}$. To solve the problem, a last relationship between these variables is needed.

The strains $\Delta\varepsilon_\alpha^{el}$ and $\varepsilon_\alpha^{UL,pl}$ are linked through the reverse flow curve of the ferrite phase, as can be seen from Fig. 7.2. Inspection of eq. F.13 and eq. F.15 shows that this results in a relation between Δu_α^{el} and $u_\alpha^{UL,pl}$, as long as the shape of the reverse flow curve is known. Because an analytical solution to the problem is impossible except for very simple flow curve definitions, in the following an iterative solution procedure will be proposed.

However, before doing so, three more expressions need to be derived. First, by evaluating eq. F.20 for the ferrite phase, taking into account eq. F.10, and comparing to eq. F.15, it can be seen that

$$\varepsilon_\alpha^{tot,el} = \Delta\varepsilon_\alpha^{el} \qquad \text{(F.24)}$$

Secondly, from Fig. 7.2 it can be seen that $\Delta\varepsilon_\alpha^{el}$ can be obtained from the reverse flow curve of the ferrite phase if the unloading strain is known.

$$\Delta\varepsilon_\alpha^{el} = \frac{\sigma_\alpha^{UL}}{E_\alpha} \qquad \text{(F.25)}$$

Thirdly, the plastic unloading strain in the ferrite phase can be written as

$$\varepsilon_\alpha^{UL,pl} = \varepsilon^{UL} - \Delta\varepsilon_\alpha^{el} + \varepsilon_\alpha^{L,el} \qquad \text{(F.26)}$$

This expression can easily be proven by elaborating all it in terms of displacements and comparing to eq. F.13.

The solution procedure is illustrated in Fig. F.2. A starting value for u^{UL} is chosen. The iterative loop is then started until evaluation of the equilibrium equation is possible. If the left hand side is larger than zero, there is still too much tension in the material and a larger absolute value for u^{UL} should be chosen. On the other hand, if the left hand side is smaller than zero, there is too much compression and a smaller absolute value for u^{UL} should be chosen. If the left hand side of the equilibrium equation approaches zero, the correct solution to the problem was found.

At that point the total elastic strains in the material can be used to compute the residual stresses by applying Hooke's law. The amount of reverse yielding in the ferrite phase can be found by evaluating the expression for $\varepsilon_\alpha^{UL,pl}$ (eq. F.13).

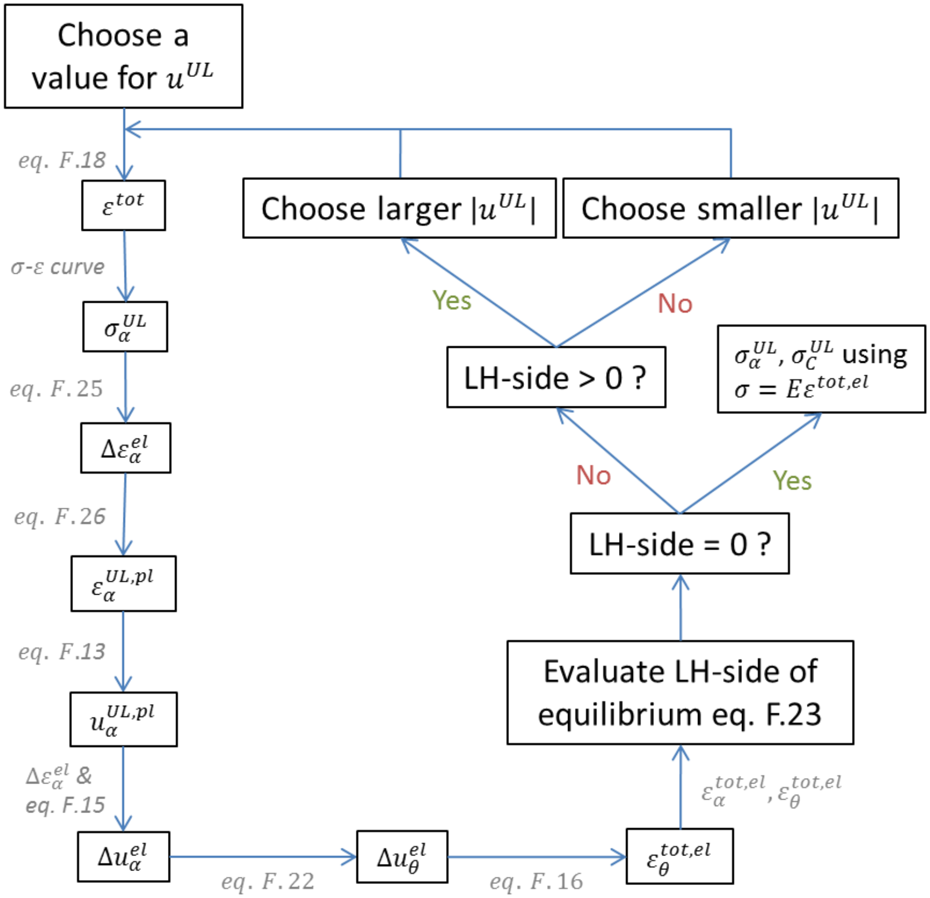

Fig. F.2: Iterative solution scheme for the 1-D residual stress sandwich model, based the Stress/Strain solution. The followed approach starts from a displacement description of all strains. The unloading displacement u^{UL} is the parameter that needs to be optimized in order to fulfil the equilibrium equation.

G. Calculation of the plastic strain state in the 2-D internal stress sandwich model

Using the normality rule (eq. G.1) and the conservation of volume (eq. G.2), the three components of the plastic deformation state can be calculated based on the knowledge of $\varepsilon_{eq}^{pl,\alpha}$. The calculation is required for the implementation of the 2-D internal stress sandwich model and the derivation will be given here. To aid the reader, the normality rule and conservation of volume have been repeated.

$$\frac{\varepsilon_{22}^{pl,\alpha}}{\varepsilon_{11}^{pl,\alpha}} = \frac{2\sigma_{22}^{\alpha} - \sigma_{11}^{\alpha}}{2\sigma_{11}^{\alpha} - \sigma_{22}^{\alpha}} \tag{G.1}$$

$$\varepsilon_{11}^{pl,\alpha} + \varepsilon_{22}^{pl,\alpha} + \varepsilon_{33}^{pl,\alpha} = 0 \tag{G.2}$$

First, $\varepsilon_{22}^{pl,\alpha}$ and $\varepsilon_{33}^{pl,\alpha}$ can be written in terms of $\varepsilon_{11}^{pl,\alpha}$ by manipulating eq. G.1 and G.2.

$$\varepsilon_{22}^{pl,\alpha} = \left(\frac{2\sigma_{22}^{\alpha} - \sigma_{11}^{\alpha}}{2\sigma_{11}^{\alpha} - \sigma_{22}^{\alpha}}\right)\varepsilon_{11}^{pl,\alpha} \tag{G.3}$$

$$\varepsilon_{33}^{pl,\alpha} = -\left(1 + \frac{2\sigma_{22}^{\alpha} - \sigma_{11}^{\alpha}}{2\sigma_{11}^{\alpha} - \sigma_{22}^{\alpha}}\right)\varepsilon_{11}^{pl,\alpha} \tag{G.4}$$

The equivalent plastic strain

$$\varepsilon_{eq}^{pl,\alpha} = \sqrt{\frac{2}{3}\left({\varepsilon_{11}^{pl,\alpha}}^2 + {\varepsilon_{22}^{pl,\alpha}}^2 + {\varepsilon_{33}^{pl,\alpha}}^2\right)}$$

can now also be expressed in terms of $\varepsilon_{11}^{pl,\alpha}$ by substituting eq. E.3 and E.4.

$$\varepsilon_{eq}^{pl,\alpha} = \sqrt{\frac{2}{3}\left({\varepsilon_{11}^{pl,\alpha}}^2 + \left(\frac{2\sigma_{22}^{\alpha} - \sigma_{11}^{\alpha}}{2\sigma_{11}^{\alpha} - \sigma_{22}^{\alpha}}\right)^2 {\varepsilon_{11}^{pl,\alpha}}^2 + \left(1 + \frac{2\sigma_{22}^{\alpha} - \sigma_{11}^{\alpha}}{2\sigma_{11}^{\alpha} - \sigma_{22}^{\alpha}}\right)^2 {\varepsilon_{11}^{pl,\alpha}}^2\right)}$$

It follows that the absolute value of $\varepsilon_{11}^{pl,\alpha}$ can be calculated from

$$\left|\varepsilon_{eq}^{pl,\alpha}\right| = \sqrt{\frac{2}{3}\cdot\left(\varepsilon_{eq}^{pl,\alpha}\right)^2\cdot\left[1 + \left(\frac{2\sigma_{22}^{\alpha} - \sigma_{11}^{\alpha}}{2\sigma_{11}^{\alpha} - \sigma_{22}^{\alpha}}\right)^2 + \left(1 + \frac{2\sigma_{22}^{\alpha} - \sigma_{11}^{\alpha}}{2\sigma_{11}^{\alpha} - \sigma_{22}^{\alpha}}\right)^2\right]^{-1}}$$

The sign of $\varepsilon_{11}^{pl,\alpha}$ can be found from inspecting the normality rule.

$$\operatorname{sign}\left(\varepsilon_{11}^{pl,\alpha}\right) = \operatorname{sign}\left(2\sigma_{11}^{\alpha} - \sigma_{22}^{\alpha}\right)$$

CURRICULUM VITAE

Jeroen TACQ
Born: 22-11-1988,Roeselare
Nationality: Belgian
Contact: jeroen.tacq@outlook.com

Education

Oct. 2011-Nov. 2015	Ph.D. in Materials Engineering, KU Leuven, Department MTM
Sept. 2009-July 2011	Master of Materials Engineering, Metals and Ceramics, KU Leuven, Department MTM
Sept. 2006-July 2009	Bachelor of Materials Engineering, KU Leuven, Department MTM

Experience

Aug. 2015-Current	R&D Engineer at Maes Jonker, Izegem, Belgium
Oct. 2011-Nov. 2015	Researcher at KU Leuven, Department MTM, Leuven, Belgium
Dec. 2010	Bekaert Experience 2010, Paris, France
Aug.-Sept. 2010	Summer job as research assistant at KU Leuven, Department MTM, Leuven, Belgium
June-Aug. 2009	Internship at Bekaert Technology Centre (BTC), NV Bekaert, Zwevegem, Belgium

List of Publications

M. Kriška, J. Tacq, K. Van Acker, M. Seefeldt, S. Van Petegem, *Neutron and X-ray diffraction study of residual and internal stress evolution in pearlitic steel during cold wire drawing.* Journal of Physics: Conference Series, 2012.

M. Kriška, J. Tacq, K. Van Acker, M. Seefeldt, *Assessment of total residual stress evolution and microstructure changes in pearlitic steel during wire drawing.* In Asiasteel International Conference, 2012, Beijing, China.

M. Kriška, J. Tacq, K. Van Acker, M. Seefeldt, *Evolution of residual micro phase and orientation dependent stresses during cold wire drawing.* Material Science Forum 768-769, 2014, 327-334.

J. Tacq, M. Kriška, M. Seefeldt, *Synchrotron diffraction study of the cementite phase in cold drawn pearlitic steel wires.* Materials Science Forum 768-769, 2014, 380-387.

J. Tacq, M. Kriška, M. Seefeldt, *Residual stress in the cementite phase of cold drawn pearlite.* Journal of Heat Treatment and Materials 69, 2014, 64-70.

M. Kriška, J. Tacq, K. Van Acker, M. Seefeldt, *Microstructure and properties of pearlitic steel during cold wire drawing: A residual stress perspective.* Journal of Heat Treatment and Materials 69, 2014, 97-105.

J. Debehets, J. Tacq, A. Favache, P. Jacques, J. Seo, B. Verlinden, M. Seefeldt, *Analysis of the variation in nanohardness of pearlitic steel: Influence of the interplay between ferrite crystal orientation and cementite morphology.* Materials Science and Engineering A, Structural Materials: Properties, Microstructure and Processing 616, 2014, 99-106.

Publications under preparation

J. Tacq, J. Pilch, B. Verlinden, M. Seefeldt, *Load transfer and strain gradients in pearlite investigated by means of in-situ neutron diffraction.* (Manuscript finished, ready for submission)

J. Tacq, T. Panzner, S. Van Petegem, M. Hofmann, B. Verlinden, M. Seefeldt, *Micro phase residual strains as footprints of the deformation behaviour of a lamellar material – The case of cold rolled pearlite.* (Manuscript finished, ready for submission)

J. Tacq, B. Verlinden, M. Seefeldt, *Development of a dislocation rich interface layer in heavily cold deformed lamellar pearlite.* (Draft of manuscript finished)